RATIONAL DESIGN OF CONJUGATED POLYMERS FOR ORGANIC SOLAR CELLS
BASED ON STRUCTURE-PROPERTY RELATIONSHIPS

Jeromy James Rech

A dissertation submitted to the faculty at the University of North Carolina at Chapel Hill in partial fulfillment of the requirements for the degree of Doctor of Philosophy in the Department of Chemistry in the College of Arts and Sciences.

Chapel Hill
2021

Approved by:

Frank A. Leibfarth

Aleksandr V. Zhukhovitskiy

James F. Cahoon

Gerald J. Meyer

Wei You

ABSTRACT

Jeromy James Rech: Rational Design of Conjugated Polymers for Organic Solar Cells Based
on Structure-Property Relationships
(Under the direction of Wei You)

Conjugated polymers have a long history of exploration and use in organic solar cells,
and over the last twenty-five years, marked increases in the solar cell efficiency have been
achieved. With the remarkable advances in the efficiency of organic solar cells, the need to
distill key structure-property relationships for semiconducting materials cannot be
understated. The fundamental design criteria based on these structure-property relationships
will help realize low-cost, scalable, and high efficiency materials. This dissertation details
design strategies for both small molecule fused-ring electron acceptors and functionalized
donor-acceptor copolymer electron donors. First, a series of fused-ring electron acceptors
with structural differences will be investigated (such as extending the conjugated core,
changing the solubilizing side chains, adding electron withdrawing groups, etc.) and key
design criteria will be derived. This will lead to a model which outlines the key requirements
in order for a small molecule fused-ring electron acceptor to exhibit high efficiency.
Afterwards, new methodologies to prepare conjugated polymer donors will be explored in
the context of structure-property relationships. A common polymer backbone will be
functionalized with various modifications including fluorine substituents, nitrogen
heteroatoms, and cyano substituents; and the location and number of these modifications will
be explored. A complete investigation on the structure-property relationship for each

functionalization will be undertaken, and the optical, electrochemical, morphological, and photovoltaic impact of each substituent detailed. Furthermore, the limits of these functionalizations will be investigated, and key design rationale will be developed. Finally, while many of these conjugated materials exhibit high performance, the cost and synthetic complexity of these materials is also too large. For that reason, a redesigned synthesis of a high-performance conjugated polymer which offers an 86% reduction in the materials cost will be highlighted. The insights gained from this dissertation can aid in the design on new donor and acceptor materials to obtain high efficiencies and make polymer-based organic solar cells competitive for industrial processing.

ACKNOWLEDGEMENTS

There is a long list of people who deserve my upmost gratitude. I have such an amazing support network which constantly encourages me and makes me strive to be the best version of myself. If this amazing group of people were stripped away, there would be no chance that I would be here today. Thank you!
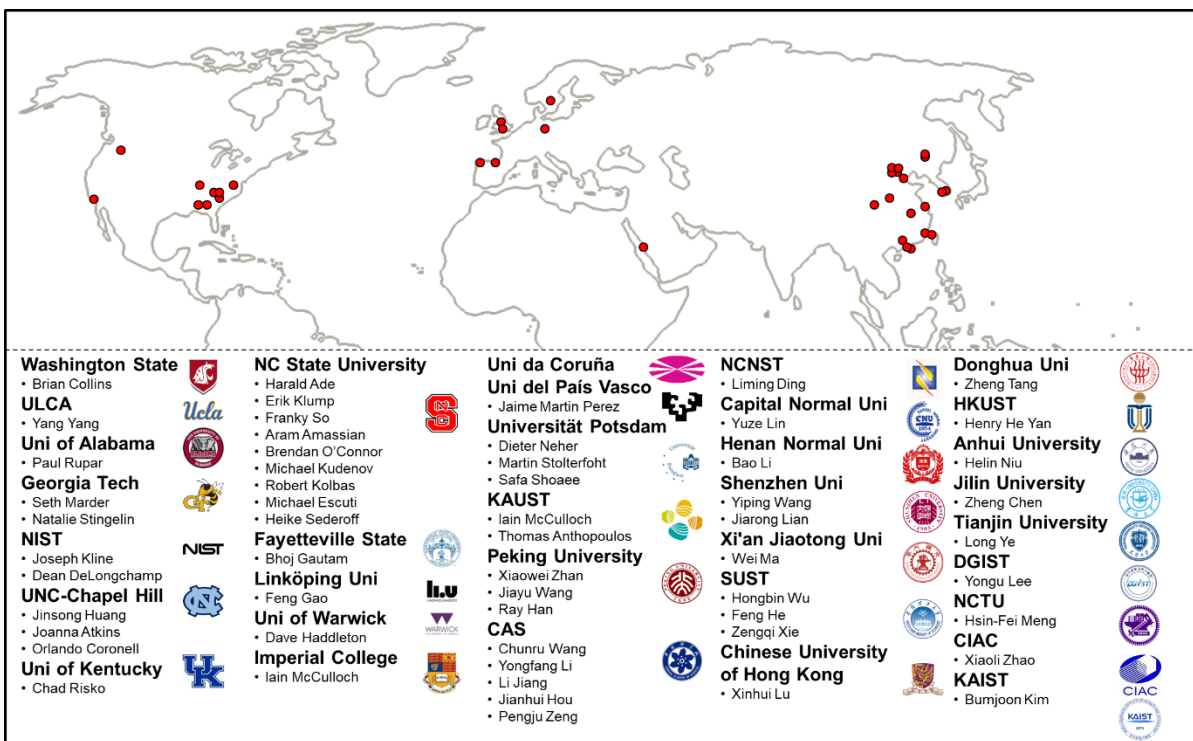
I would first like to thank my research advisor, Professor Wei You. When I was first visiting UNC back in 2016, his energy and positivity was so refreshing, and his passion for research excited me. After working in his lab during the summer, I knew that this was a location which I wanted to spend the next five years. Wei was more than just a mentor – he is a friend. When I joined his lab, I had a deficient background on organic chemistry, but his patience, optimism, and guidance (both in and out of the lab) has helped me become the chemist that I am today. Wei constantly created opportunities to help me succeed and taught me so much about how to be a good research mentor.

Next, I would like to thank a few specific people in the lab. I will start with Dr. Qianqian Zhang: when I first started working in the lab, I had absolutely no organic chemistry laboratory skills, and she taught me so much and had such patience with the numerous stupid questions I would constantly ask. Qianqian's passion and work ethic would rub off on me and help me establish my own work ethic that led me through graduate school. Next, I need to thank Dr. Liang Yan. Beyond testing thousands of devices for me, Liang has taught me a great deal of fundamental physics about semiconductors and photovoltaics over

the past five years. Also from the device lab, a close friend, Dr. Nicole Bauer, deserves much gratitude. My first major project was to design new acceptors based on a TCF-moiety, and I made so many brand new fused-ring electron acceptors based on this structure – all of which turned out to be a horrible device (see Chapter 2 for why). However, even in the slew of failed device after failed device, Nicole's positivity and encouragement helped me fly through my first two years of graduate school. Of course, I must say a big "Thank You!" to all my former and current labmates (such as Dr. Ian VonWald, Dr. Allison Kelly, Dr. SungYun Son, Dr. Joji Tanaka, Stephanie Samson, Kyle Cushman, Xiaowei Zhong, and others) who are always helpful and make the lab such a great place to work in.

In a similar vein, I could not have been successful without the amazing help and support of many collaborators. Organic Solar Cells is one of the most interdisciplinary fields which I have ever witnessed, as seen with my publications that are filled with synthetic chemists, material scientists, device physics, engineers, etc. I have also been honored to have been included on so many publications over the past few years based on rich collaborations. There are so many labs which have done such great work with some of my polymers, and it is so exciting to see their creativity! I have organized a map below which includes a mark for each university – and you can easily see that I have had the great opportunity to work with so many labs across the world! Below I have also listed the names of the lead professors in each collaboration, but I also need to thank their postdocs, graduate students, and others who helped test my materials. One set of collaborations I want to specifically highlight is OrACEL (Organic and Carbon Electronics Labs) at North Carolina State University (NCSU). I have been able to closely work with so many great folks from Dr. Harald Ade and Dr.

Brendan O'Connor's labs (such as Dr. Nrup Balar, Dr. Long Ye, Yuan Xiong, Dr. Masoud Ghasemi, Somayeh Kashani, Ronald Booth, Pratik Sen, Eshwar Ravishankar, and others).

Washington State
- Brian Collins

ULCA
- Yang Yang

Uni of Alabama
- Paul Rupar

Georgia Tech
- Seth Marder
- Natalie Stingelin

NIST
- Joseph Kline
- Dean DeLongchamp

UNC-Chapel Hill
- Jinsong Huang
- Joanna Atkins
- Orlando Coronell

Uni of Kentucky
- Chad Risko

NC State University
- Harald Ade
- Erik Klump
- Franky So
- Aram Amassian
- Brendan O'Connor
- Michael Kudenov
- Robert Kolbas
- Michael Escuti
- Heike Sederoff

Fayetteville State
- Bhoj Gautam

Linköping Uni
- Feng Gao

Uni of Warwick
- Dave Haddleton

Imperial College
- Iain McCulloch

Uni da Coruña
Uni del País Vasco
- Jaime Martin Perez

Universität Potsdam
- Dieter Neher
- Martin Stolterfoht
- Safa Shoaee

KAUST
- Iain McCulloch
- Thomas Anthopoulos

Peking University
- Xiaowei Zhan
- Jiayu Wang
- Ray Han

CAS
- Chunru Wang
- Yongfang Li
- Li Jiang
- Jianhui Hou
- Pengju Zeng

NCNST
- Liming Ding

Capital Normal Uni
- Yuze Lin

Henan Normal Uni
- Bao Li

Shenzhen Uni
- Yiping Wang
- Jiarong Lian

Xi'an Jiaotong Uni
- Wei Ma

SUST
- Hongbin Wu
- Feng He
- Zengqi Xie

Chinese University of Hong Kong
- Xinhui Lu

Donghua Uni
- Zheng Tang

HKUST
- Henry He Yan

Anhui University
- Helin Niu

Jilin University
- Zheng Chen

Tianjin University
- Long Ye

DGIST
- Yongu Lee

NCTU
- Hsin-Fei Meng

CIAC
- Xiaoli Zhao

KAIST
- Bumjoon Kim

I would also like to thank Professor Frank Leibfarth, Professor Aleksandr Zhukhovitskiy, Professor James Cahoon, and Professor Gerald Meyer for serving on my final defense committee; and Professor Theo Dingemans for serving on my preliminary oral defense committee. I appreciate your commitment, comments, and encouragements throughout my time here at the University of North Carolina at Chapel Hill.

Next, I want to thank my best friend, Lisa Janes. From the little side lab at Lewis University in 2013 to almost every night over Discord – you have always been there for me! You are the one person who I can talk to about absolutely everything. We started our very first exploration into research together – playing around with fryer grease and making "biodiesel." And through so many projects at Lewis – biodiesel, CMP, and water filtration – we muddled through together. I was not prepared to fail in research experiments, and that

fear of failure (amongst other things) made research miserable at times. However, through thick and thin, good times and bad, we always supported and helped each other. Without someone like you by my side, I do not think I could be where I am today. You are incredibly smart and passionate, and this always drove me to improve myself. I know that life can suck at times, but having you as a friend makes so many things more bearable; I am so blessed to have someone like you in my life and am so excited to see what is next for the both of us!

Finally, I need to thank my family (Mom, Dad, Josh, Jessica, Max, and my grandparents) for encouraging and supporting me in whatever I chose to do. This journey would not have been possible without your emotional (and occasional) financial support. I always knew that you believed in me and wanted the best for me. Growing up, you taught me to dream big and so many core principles which guided me to where I am today.

PREFACE

This dissertation includes seven main chapters which have components which include previously published work. Chapter 1 serves as a mini-review which highlights some key structure-property relationships established through collaboration articles including those found in: the *Journal of Materials Chemistry A*,[1] *Chemistry of Materials*,[2] *Materials Chemistry Frontiers*,[3] *Materials Chemistry Frontiers*,[4] *Journal of Materials Chemistry A*,[5] *Materials Chemistry Frontiers*,[6] *Acta Physico-Chimica Sinica*,[7] *Small Structures*,[8] and *Advanced Energy Materials*.[9] Chapter 2 highlights work that was published in a special themed edition of *Materials Chemistry Frontiers* on Non-Fullerene Acceptors for Organic Solar Cells.[10] Chapter 3 transitions the focus onto the conjugated polymer and the impact on molecular weight, summarizing two articles in *ACS Applied Polymer Materials* and *Chemistry of Materials*.[11,12] Chapter 4 describes the impact of fluorinated thiophene linkers on the performance of conjugated polymers based on my *Macromolecules* paper.[13] Chapter 5 shifts to a different electron withdrawing group, a cyano substituent, as described in our *ACS Applied Polymer Materials* work.[14] Chapter 6 focuses on my publication which was featured in *ACS Applied Polymer Materials* in a special issue on High Efficiency Polymers for Solar Cell Applications and was also featured on the cover art for the issue.[15] Finally, my work on low cost polymers which was published in *Chemistry of Sustainable Chemistry*, which was both a VIP article and part of an invited contribution on Advanced Organic Solar Cells, is summarized in Chapter 7.[16] Texts are reproduced with permission (see footnotes).

TABLE OF CONTENTS

LIST OF TABLES

LIST OF FIGURES

LIST OF SCHEMES

LIST OF CHARTS

LIST OF ABBREVIATIONS AND SYMBOLS

1D	One Dimensional
2D	Two Dimensional
2TF	3,3'-difluoro-2,2'-bithiophene
4FT	Monofluorinated (in the 4-position) Thiophene unit
Å	ångström (10^{-10} m)
Abs	Absorbance
ADA	Acceptor-Donor-Acceptor
AFM	Atomic Force Microcopy
Ag	Silver
Al	Aluminum
ALS	Advanced Light Source (Berkeley)
AM 1.5G	Air Mass of 1.5 Global (standard solar spectrum)
APCI	Atmospheric Pressure Chemical Ionization
arb	arbitrary (units)
BDD	Benzodithiophenedione
BHJ	Bulk Heterojunction
BHT	Butylated hydroxytoluene (stabilizer)
BnDT	Benzodithiophene
Br	Bromine
^{13}C	Carbon-13 isotope
Ca	Calcium
CB	Chlorobenzene

CDCl$_3$	Deuterated Chloroform
CF	Chloroform
CN	Cyano
COS	Crack Onset Strain
CT	Charge Transfer
CuSCN	Copper (I) thiocyanate
CV	Cyclic Voltammetry
Đ	Dispersity
Δ	Delta (change in)
D:A	Donor:Acceptor
DArP	Direct Arylation Polymerization
DCB	Dichlorobenzene
DCM	Dichloromethane
DFT	Density Functional Theory
dFT	Difluorinated Thiophene unit
DIO	1,8-diiodooctane
DMA	Dynamic Mechanical Analysis
DMF	Dimethylformamide
DMSO	Dimethyl Sulfoxide
DIAD	Diisopropyl azodicarboxylate
DSC	Differential Scanning Calorimetry
ε_o	Permittivity of Free Space (8.85×10^{-12} F/m)
ε_r	Dielectric Constant of the material

E'	Storage Modulus
E"	Loss Modulus
E_{CT}	Energy of the Charge Transfer State
E_f	Elastic Modulus
E_g	Band Gap
E_{opt}	Optical Band Gap
EtOAc	Ethyl Acetate
Et_2O	Diethyl Ether (aka DEE)
ESI	Electrospray ionization
ETL	Electron Transport Layer
EtOH	Ethanol
eq	equivalence (molar)
EQE	External Quantum Efficiency
eV	Electronvolts (1.602×10^{-19} J)
^{19}F	Fluorine-19 isotope
F	Fluorine
Fc	Ferrocene
Fc^+	Ferrocenium ion
FF	Fill Factor
FREA	Fused Ring Electron Acceptor
FWHM	Full Width at Half Maximum
g	Paracrystalline disorder parameter
G_c	Fracture Energy

GIWAXS	Grazing Incident Wide Angle X-Ray Scattering
^{1}H	Proton
H	Hydrogen
HCl	Hydrochloric Acid
HNO$_3$	Nitric Acid
HOMO	Highest Occupied Molecular Orbital
HT-GPC	High Temperature Gel Permeation Chromatography
HTL	Hole Transport Layer
ICT	Intramolecular Charge Transfer
IDT	Indacenodithiophene
IDTT	Indacenodithienothiophene
IP	In-Plane
IPA	Isopropyl Alcohol
IPCE	Incident Photon to Charge carrier Efficiency
ITO	Indium Tin Oxide
INCN	2-(3-oxo-2,3-dihydroinden-1-ylidene)malononitrile
J	Current Density
J$_o$	Dark Current Density
J$_{ph}$	Photocurrent Density
J$_{ph,sat}$	Saturated Photocurrent Density
J$_{SC}$	Short Circuit Current Density
k(n)	Nongeminate Recombination Rate Coefficient
k$_b$	Boltzmann Constant (1.380649×10^{-23} J/K)

λ_{max}	Absorption maximum
λ_{onset}	Absorption onset
LDA	Lithium diisopropylamide
LUMO	Lowest Unoccupied Molecular Orbital
m	Slope
Mn	Number Average Molar Mass
Mw	Weight Average Molar Mass
MeOD	Deuterated Methanol
MeOH	Methanol
Me_3SnCl	Trimethyltin chloride
$MgSO_4$	Magnesium Sulfate
mmol	Millimoles
MoO_3	Molybdenum trioxide
MS	Mass Spectroscopy
MW	Molecular Weight
n-BuLi	*n*-butyl lithium
NaCl	Sodium Chloride
$NaHCO_3$	Sodium Bicarbonate
NaOH	Sodium Hydroxide
NBS	*N*-bromosuccinimide
NDI	Naphthalene diimide
NFA	Non-fullerene Acceptor
NFSI	N-fluorobenzenesulfonimide

NMR	Nuclear Magnetic Resonance
NREL	National Renewable Energy Laboratory
OEG	oligio (ethylene glycol)
OFET	Organic Field Effect Transistor
OOP	Out-Of-Plane
opt	Optical
OPV	Organic Photovoltaic
OSC	Organic Solar Cell
P(E,T)	Charge Collection Probability
PCE	Power Conversion Efficiency
PDI	Perylene diimide
PEDOT:PSS	Poly(3,4-ethylenedioxythiophene) polystyrene sulfonate
PG	Protecting Group
PL	Photoluminescence
PLQE	Photoluminescence Quantum Efficiency
PMI	Process Mass Intensity
P(o-tol)$_3$	Tri($ortho$-toluene)phosphine
PPh$_3$	Triphenyl phosphine
PSC	(all) Polymer Solar Cell
Pt	Platinum
q$_{xy}$	Scattering Vector (momentum transfer) in the xy plane
q$_z$	Scattering Vector (momentum transfer) in the z plane
RMS	Root Mean Square

RPM	Revolutions Per Minute
RPV	Resistance Dependent Photovoltage
RSoXS	Resonant Soft X-Ray Scattering
S	Sulfur
SC	Synthetic Complexity
SCLC	Space Charge Limited Current
T	Temperature
τ	Lifetime
T_d	Decomposition Temperature (5% weight loss)
tan δ	loss factor = E''/E'
TAZ	Benzotriazole
TBAF	Tetra-n-butylammonium fluoride
TCB	Trichlorobenzene
TCF	Tricyanovinyldihydrofuran
TGA	Thermogravimetric Analysis
THF	Tetrahydrofuran
TIPS	Triisopropylsilane
TMS	Trimethylsilane
Tol	Toluene
TPC	Transient Photocurrent
TPV	Transient Photovoltage
μ_e	Electron Mobility
μ_h	Hole Mobility

UV	Ultraviolet Light
V_{eff}	Effective Voltage
V_{OC}	Open Circuit Voltage
Vis	Visible Light
w/w	weight per weight (concentration)
XRD	X-Ray Diffraction
$ZnCl_2$	Zinc (II) Chloride
ZnO	Zinc Oxide
$/W_p$	Dollars per Watt peak (energy cost)

INTRODUCTION

Petroleum, natural gas, and coal still make up the majority of energy sources throughout the world (over 80% in 2016, according to the U.S. Energy Information Administration), and the impact and sustainability of these fossil fuels have dire consequences on our world. Because of the environmental implications, the demand for clean, renewable energy has driven the development of new technologies such as solar energy. Sunlight has the highest theoretical potential to meet the earth's renewable energy needs. The majority of commercial solar panels are based on monocrystalline silicon, which have drawbacks, such as harsh and energy extensive processing condition, high cost, and poor mechanical robustness. Many of these shortcomings can be addressed by using organic semiconductors.

The first organic semiconductor was accidentally discovered in 1975 when a visiting scientist in Hideki Shirakawa's lab added too much Ziegler-Natta catalyst to acetylene during a polymerization. Instead of the expected black powder, pieces of silvery polyacetylene film were produced; historically, materials with a metallic sheen could conduct electricity, which led to an exploration on the materials conductivity.[17] After a lecture at the Tokyo Institute of Technology, Shirakawa and Alan MacDiarmid met over a cup of green tea and talked about conductive materials. After Shirakawa showed this silvery polymer which was serendipitously created, he was invited to join a collaboration with MacDiarmid and Alan Heeger at the University of Pennsylvania.[18] This group of three (MacDiarmid, Heeger, and

Shirakawa) would receive the Nobel Prize in Chemistry in 2000 for the discovery and development of conductive polymers.

Years later, Alan Heeger would team up with Fred Wudl (University of California at Santa Barbara) and Niyazi Sarıçiftçi (Johannes Keplet University at Linz, Austria) to create the first polymer solar cell in 1993 (published the very same week I was born) based on a bilayer device with polymer donor MEH-PPV (poly[2-methoxy-5-(2-ethylhexyloxy)-1,4-phenylenevinylene]) and electron acceptor buckminsterfullerene (C_{60}). While charge transfer was observed, low efficiencies (0.04%) were measured due to the short lifetime and diffusion length of the generated exciton.[19] To fix this issue, Fred Wudl would add a solubilizing group to buckminsterfullerene to create a new electron acceptor called PCBM (phenyl-C61-butyric acid methyl ester) in 1995.[20] This allowed for the polymer and acceptor to be mixed in the casting solution and create a bulk heterojunction (BHJ), which is a continuous interpenetrating network of the two materials that can allow for more efficient charge separation. This new device architecture would significantly boost the efficiency of the MEH-PPV:PCBM blend over 2% efficiency.[21]

These initial works create the entirely new field of organic solar cells (OSCs), which has rapidly grown over the past 25 years. OSCs have been extensively researched because of their low cost, flexibility, light weight, semi-transparency, and ease of processing on an industrial scale, making them candidates to help supply the world's energy needs.[22–31] Besides these key advantages, OPVs also include less environmental impact during manufacturing processes and operations and have a short energy payback time in comparison to other photovoltaic technologies.[32–34]

Still to this day, OSCs typically utilize the same BHJ active layer morphology discovered back in 1995, which is a continuous interpenetrating network of two materials: an electron donor and electron acceptor.[35,36] Common electron donors include donor-acceptor conjugated copolymers, while the electron acceptor can either be a fullerene derivative (such as PCBM)[37] or a non-fullerene acceptor (such as ITIC).[38] This dissertation will discuss in great details and evolution and structure-property relationships in both conjugated polymers and non-fullerene acceptors. In the BHJ, photons are absorbed by the active components from the incident sunlight, and this energy is used to form an exciton, a Coulombically bound electron-hole pair.[39,40] This exciton is then dissociated into free charge carriers at the donor-acceptor (D-A) interface, and the separated electron and hole travel through the respective domains to be collected at the electrodes.[41–43]

When judging the performance of an OSC, there are three important parameters to consider: short-circuit current density (J_{SC}), open-circuit voltage (V_{OC}) and fill factor (FF). The J_{SC} is the current density at which the voltage across the solar cell is equal to zero and gives the maximum current output for the device. V_{OC} is the maximum voltage of the device and occurs when the current is equal to zero. Fill factor is the ratio of maximum power output of the cell to the product of the J_{SC} and V_{OC}. These parameters can be determined by measuring photocurrent as a function of applied bias and creating a plot of the current density vs. voltage (J-V curve), as shown in **Figure I**. The combination of these parameters (divided by the incident power) make up the power conversion efficiency (PCE), which is a descriptor of the efficiency of the solar cell.
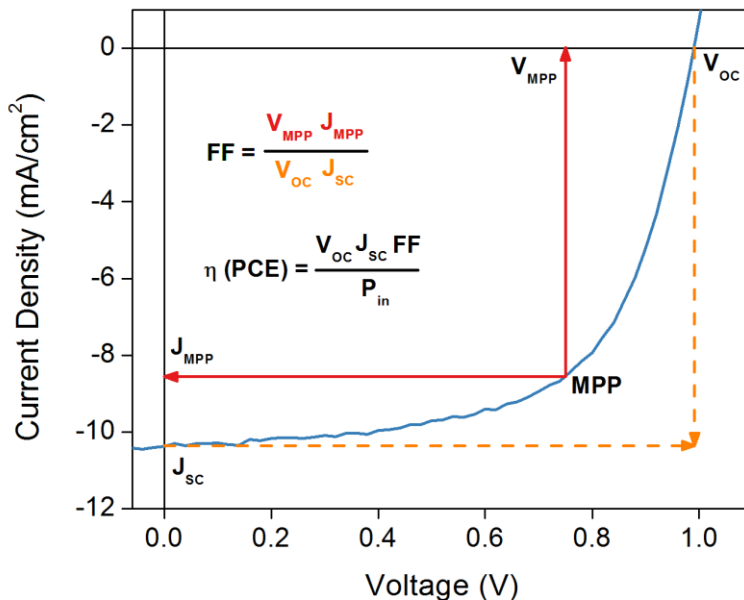
Figure I: Example *J-V* curve highlighting key OPV parameters

The major focus of this dissertation is to understand the structure-function

relationship between the synthesis of new materials for OSCs (i.e., molecular engineering)

and the corresponding device performance (i.e., J_{SC}, V_{OC}, *FF*, and PCE). While PCBM

demonstrated impressive results in the past, fullerenes tend to aggregate in a thin film over

time, causing an unstable morphology that can result in a short lifetime of the device.

Furthermore, fullerenes absorb very little visible light and have relatively fixed energy levels,

which limit the efficiencies which can be obtained. To address these shortcomings new types

of electron acceptors have been developed which are classified as non-fullerene acceptors

(NFAs). Chapters 1 will highlight the history and development of small molecule fused-ring

electron acceptors (FREAs), and Chapter 2 will provide a deep-dive into the impact of the

end groups of the NFA materials.

For conjugated polymers, methods to boost the efficiency include adjusting polymer

backbone, developing new donor and acceptor moieties, tuning the solubilizing side chains,

and incorporating substituents.[44–50] Amongst those strategies, incorporating proper

substituents on high-performance polymers is of special interest to further improve the

properties of polymers without modifying the essential backbones of polymers. Chapter 3

will highlight the polymerization methods and the impact on the polymer molecular weight

on the performance and mechanical properties of the solar cell blend. Then Chapters 4-6 will

investigate the impact of various substituents such as fluorine (Chapter 4), cyano (Chapter 5),

and mixed systems (Chapter 6). Finally, the cost and scalability for conjugated polymers will

be addressed in Chapter 7. Altogether, this creates a framework to design new materials

which can further push organic solar cells towards commercialization.

CHAPTER 1: Structure-Property Relationships for Fused Ring Electron Acceptors Learned through Collaboration during the "ITIC Gold Rush"

1.1 Introduction

The efficiency of bulk heterojunction (BHJ) organic solar cells (OSCs) has recently observed a surge in record high efficiency (over 16% for single junction and over 17% for tandem devices),[51–58] largely from the emergence of non-fullerene acceptors (NFAs).[38,51–53,56,59–62] Along with the benefits of solution processability, low cost, and semi-transparency, OSC blends with NFAs can now achieve efficiencies higher than those of fullerene-based blends due to their complementary absorption and tunable energy levels.[63–70] The most common class of NFAs are fused-ring electron acceptors (FREAs), which often have a characteristic acceptor-donor-acceptor (A-D-A) architecture, such as ITIC (i.e., 3,9-bis(2-methylene-(3-(1,1-dicyanomethylene)-indanone))-5,5,11,11-tetrakis(4-hexylphenyl)-dithieno[2,3-d:2′,3′-d′]-s-indaceno[1,2-b:5,6-b′]-dithiophene).[38] ITIC was first reported by Xiaowei Zhan's group in 2015, and ITIC and its derivatives have become the center of focus for many research groups.[56,71–77]

Following the successful demonstrating of the new ITIC small molecule acceptor which could surpass PCBM efficiency when blended with donor polymer of PTB7-Th, a "gold rush" began with many groups synthesizing brand new derivatives of ITIC. This is graphically depicted in **Figure 1.1** via a keyword search on Web of Science; the figure depicts the number of times "non-fullerene acceptor" (left, red) and "organic solar cell" (right, black) was used in publications over the past eight years. After the initial major

publications in 2015 demonstrated that FREAs could achieve higher efficiency than PCBM, there is a huge increase in the number of publications in the following years. Conversely, the number of publications on has remained relatively constant during this period, which demonstrates the NFA growth features are not from natural growth in publishing community.
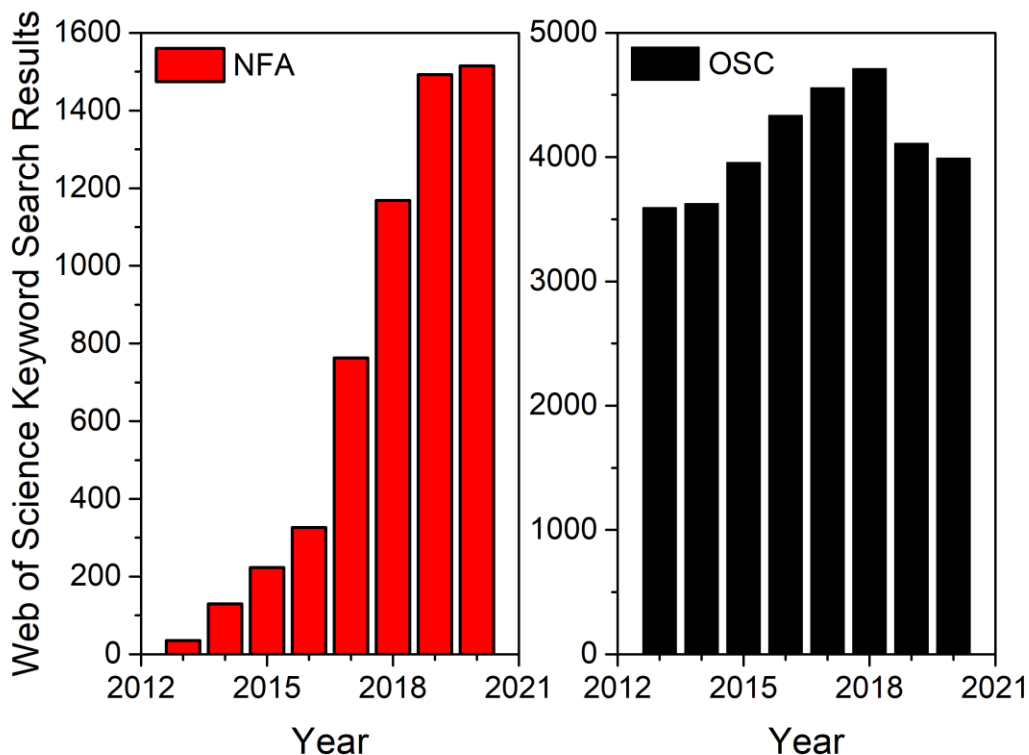
Figure 1.1 – The number of publications on "Non-Fullerene Acceptor" and "Organic Solar Cells" per year based on Web of Science keyword search

The majority of my doctoral studies where within this time frame which experienced a huge increase in non-fullerene acceptors. Fortuitously, with many labs designing new electron acceptors, the demand for p-type polymers to pair with the new acceptors was very high and I had the opportunity to provide my materials to research groups across the world. From these various collaborations, I have been co-author on a variety of publications with a very diverse set of FREAs. In the following sections, a select series of these publications are reviewed and some important structure-property relationships are demonstrated.

1.2 Modifying Donor Core: Extending the Core with Benzenes [1]

One year after the original ITIC publication, Xiaowei Zhan's lab reported a smaller version of ITIC which has a five fused ring indacenodithiophene (IDT) core instead of the original indacenodithienothiophene (IDTT) seven fused ring core. This new acceptor was called IDIC and possessed similar properties with ITIC. Furthermore, when paired with donor polymer of PDBT-T1, the resulting solar cells had an 8.71% efficiency, which was the highest polymer:small molecule acceptor blend efficiency at the time.[78] Along with the high efficiency, this blend was also attractive as the IDT core had a much simpler synthetic route.

Two years later, Xiaowei Zhan revisited this IDIC small molecule in a collaboration with our lab. Inspired by work just published by Yongsheng Chen's lab which used a naphthalene-based core,[79] we systematically investigated the impact of extending the donor core from a benzene to a naphthalene unit. The naphthalene ring has larger π-conjugation and rigid structure, which we hoped would lead to reduced energetic disorder and strong intermolecular interactions – and thus more efficient charge transport. **Chart 1.1** shows the chemical structure of IDIC and the new extended IHIC.
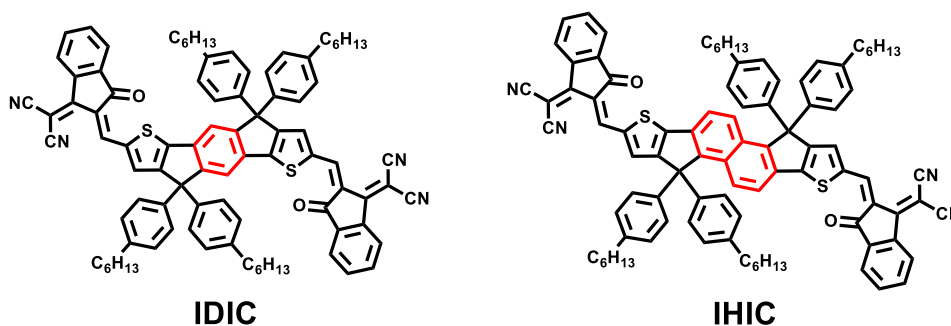
Chart 1.1 – Chemical Structures of IDIC and IHIC

Compared to the benzene core of IDIC, the naphthalene-based IHIC showed larger π-conjugation with stronger intermolecular π-π stacking (3.53 vs 3.45 Å respectively), as measured through grazing-incident wide-angle X-ray scattering (GIWAXS). Furthermore, IHIC had both up-shifted energy levels (i.e., higher LUMO), which can lead to a larger V_{OC}, and higher electron mobilities, a combination which increases the solar cell efficiency. As summarized in **Table 1.1**, the FTAZ:IHIC blend had an increase in J_{SC}, V_{OC}, and *FF* that led to a champion device efficiency of nearly 9% (compared to the 7% of the IDIC acceptor).

Table 1.1 – Photovoltaic characteristics of the FTAZ:FREA blends.

FREA	Abs onset (nm)	HOMO (eV)	LUMO (eV)	μ_e (x10$^{-4}\frac{cm^2}{V\,s}$)	J_{sc} (mA/cm^2)	V_{oc} (V)	FF (%)	PCE (%)
IDIC	743	-5.51	-3.81	1.5	13.5 ± 0.1	0.894 ± 0.005	58.1 ± 1.2	**7.05 ±** 0.17
IHIC	732	-5.47	-3.75	3.0	14.2 ± 0.2	0.947 ± 0.005	66.4 ± 0.6	**8.91 ±** 0.16

This work offered a simple strategy which can increase the efficiency of a small molecule acceptor, and since this publication, there have been various other groups which also reported new FREAs which utilized this same strategy, some of which have achieved solar cell efficiencies over 13%.[80–84] However, there are also other methods to extend the rigid core, which we will explore in the next section.

1.3 Modifying Donor Core: Extending the Core with Thiophenes [2]

Three months after the IDIC/IHIC publication, we published another collaboration with Xiaowei Zhan's lab which aimed to similarly extend the core. This time, however, from the original IDT core, we symmetrically added extra fused thiophene rings to the end of the

---

[2] This section includes a summary of an article in *Chemistry of Materials*. The original citation is as follows: Shuixing Dai, Yiqun Xiao, Peiyao Xue, **Jeromy James Rech**, Kuan Liu, Zeyuan Li, Xinhui Lu, Wei You, Xiaowei Zhan. "Effect of Core Size on Performance of Fused-Ring Electron Acceptors." *Chemistry of Materials*, **2018**, 30 (15), 5390-5396.

donor core. This resulted in four new materials with five, seven, nine, and eleven fused ring cores, which were named as F5IC, F7IC, F9IC, and F11IC for simplicity. The chemical structure for each acceptor is shown in **Chart 1.2**. Note, the end group of these FREAs is slightly different as they are fluorinated, more details on this can be found in section 1.7 below.
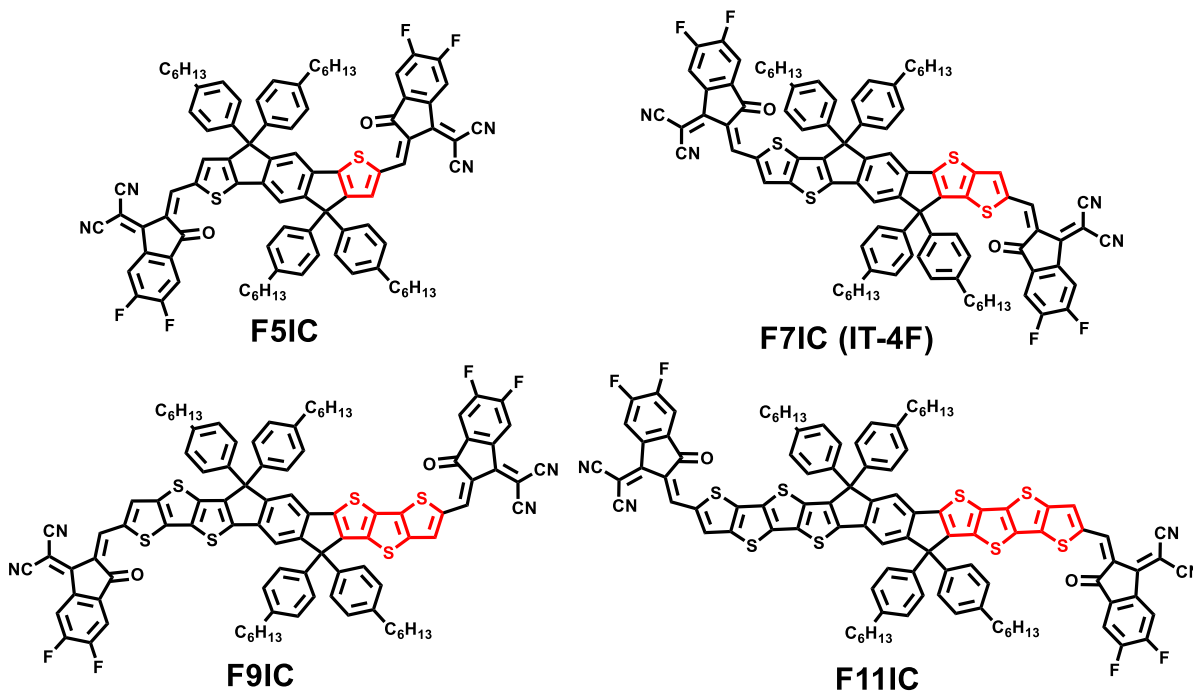
Chart 1.2 – Chemical Structures of F5IC, F7IC, F9IC, AND F11IC. Note, F7IC is commonly known as IT-4F

While the synthesis of these acceptors is complex, the final materials show clear trends and impact from the extension of the donor core. The first notable difference is the light absorption of these materials; as the core is extended, the absorption onset shifts to the right and the bandgap of the FREA shrinks. Based on the electrochemical data, this is primarily attributed to an increasing HOMO energy level. Also, similar to the IDIC vs IHIC study, increasing the length of the donor core led to an increase in packing efficiency, as the π-π stacking decreased for the larger cores, as found from the q_z peak in GIWAXS measurements. This is also manifested in the mobility data where the electron mobility scales

with the donor core length, as shown in **Table 1.2**. The combination of red-shifted

absorption, up-shifted energy levels, more favorable morphology, and increased charge

carrier mobilities all culminated in an increase in performance with larger core size.

Furthermore, from light intensity data, increasing the core size also seemed to decrease the

amount of bimolecular recombination observed in each blend.

Table 1.2 – Photovoltaic characteristics of the FTAZ:FREA blends.

FREA	Abs onset (nm)	HOMO (eV)	LUMO (eV)	μ_e (x$10^{-4} \frac{cm^2}{V\,s}$)	J_{sc} (mA/cm^2)	V_{oc} (V)	FF (%)	PCE (%)
F5IC	756	-5.82	-4.05	0.8	14.49 ± 0.39	0.703 ± 0.012	52.0 ± 1.7	**5.3** ± 0.3
IT-4F	795	-5.74	-4.01	1.5	18.30 ± 0.19	0.741 ± 0.011	57.5 ± 2.6	**7.8** ± 0.4
F9IC	832	-5.52	-3.97	1.7	19.72 ± 0.52	0.856 ± 0.017	67.7 ± 1.3	**11.4** ± 0.3
F11IC	844	-5.44	-3.94	14.0	Limited solubility in casting conditions			

As seen in **Table 1.2**, there is no solar cell data for the F11IC acceptor. While the

material is slightly soluble in common OSC solvents, it cannot be dissolved in appropriate

concentrations for solution casting of the bulk heterojunction. However, 5% of F11IC can be

added to each binary mixture to form a ternary blend with FTAZ, FnIC, and F11IC (where n

= 5, 7, or 9). For each of these ternary blends, the efficiency is higher than the parent binary

blend, attributed primarily to an increase in J_{SC}. The champion ternary blend of

FTAZ:F9IC:F11IC exhibited a 12.6% solar cell efficiency. Beyond the impact of the core

extension, this work also demonstrates the solubility limits of the IDT-based FREAs – with

only two branching side chain positions, a maximum of ten fused rings can be achieved; any

larger rings likely need to have additional solubilizing side chains in order to be solution

processable.

1.4 Modifying Donor Core: Adding Oxygen Heteroatoms [3]

In the previous two sections, various structural changes where highlighted which included adding additional thiophene and benzene rings to the donor core of IDIC. There is also a rich literature of works which change around the core rings, investigate isomers of these structures, and change out moieties (for example, replacing the benzene core with a thienothiophene, like changing IDIC to 4TIC, shown in **Chart 1.3**). However, most of the early FREA literature after the discovery of ITIC revolved around small changes to the building blocks and adding functional groups to the end group acceptor (more on that in section 1.7). This made a collaboration with Liming Ding's lab of interest to the field as the change in chemical structure was more unique. As shown in **Chart 1.3**, we reported new FREAs which included a carbon-oxygen-bridged ladder type acceptor.

For this collaboration, we reported a new FREA called CO$_i$6IC, which incorporated a bridging oxygen at the location of the side chain. When compared to 4TIC,[80] which would be the analogue without the C-O bridge, a red shift in absorption and up-shift in the LUMO is observed. This can increase the J_{SC} and V_{OC}, which resulted in an overall increase in the performance, from 7.8% to 8.4%. There was a strong decrease in the electron mobility, however, this did not negatively impact the solar cell performance. A summary of key data is available in **Table 1.3**.

---

[3] This section includes a summary of an article in *Materials Chemistry Frontiers*. The original citation is as follows: Ting Li, Honghong Zhang, Zuo Xiao, **Jeromy J. Rech**, Helin Niu, Wei You and Liming Ding. "A carbon-oxygen-bridged hexacyclic ladder-type building block for low-bandgap nonfullerene acceptors." *Materials Chemistry Frontiers*, **2018**, 2 (4), 700-703.
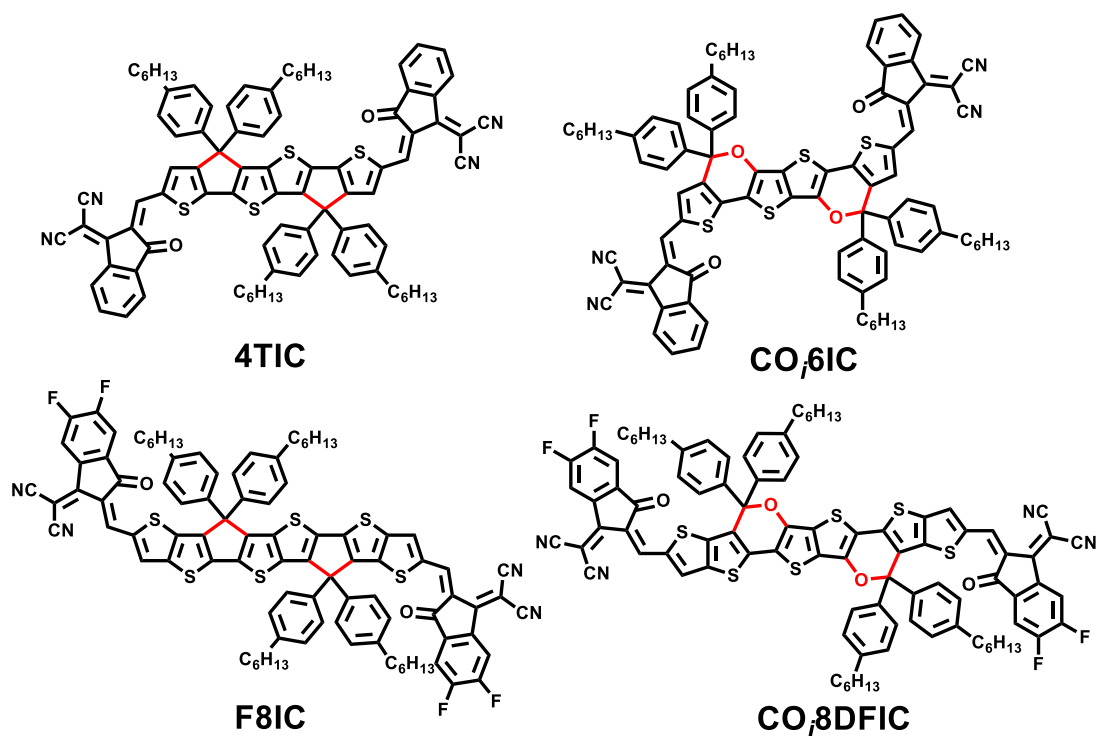
Chart 1.3 – Chemical Structures of 4TIC, CO$_i$6IC, F8IC, and CO$_i$8DFIC

Table 1.3 – Photovoltaic characteristics of the polymer:FREA blends.

FREA	**Abs onset (nm)**	**HOMO (eV)**	**LUMO (eV)**	**μ_e (x10^{-4} $\frac{cm^2}{V\,s}$)**	**J_{sc} (mA/cm²)**	**V_{oc} (V)**	**FF (%)**	**PCE (%)**
4TIC	898	-5.45	-3.93	8.3	17.10 ± 0.34	0.744 ± 0.008	60.9 ± 0.2	**7.77 ±** 0.30
CO$_i$6IC	903	-5.57	-3.86	0.7	17.45	0.82	59.0	**8.43**
F8IC	976	-5.43	-4.00	7.7	23.3 ± 0.9	0.642 ± 0.003	70.0 ± 0.7	**10.4 ±** 0.4
CO$_i$8DFIC	984	-5.50	-3.88	3.9	28.2	0.70	71.0	**14.1**

While these changes might seem minor, this work served as the foundation for a new record high efficiency blend. Based on the proof of concept from this work, Liming Ding's lab would go on to make a derivative called CO$_i$8DFIC, which had an expanded donor core (add two more fused thiophene rings, one to each end – similar to what we demonstrated in section 1.4) and functionalized end group. This combination, when paired with a more appropriate polymer donor would hold the record for highest efficiency organic solar cell with over 14% efficiency for a period of time during 2018.[85,86] Compared to the non C-O

bridge analogue named F8IC,[87,88] the same trends (red shifted for increase in J_{SC} and higher

LUMO for increase in V_{OC}) are observed. Both chemical structures and summary of key data

for F8IC and CO$_i$8DFIC are shown in **Chart 1.3** and **Table 1.3**. Towards the end of that

year, Liming Ding also used the same material in a tandem organic solar cell and achieved a

remarkable 17.3% efficiency.[89] These follow-up works strongly demonstrate the value

which can be offered from using a C-O bridging unit.

1.5 Modifying Donor Core: Adding 2D Conjugation [4]

Another interesting design motif was published in collaboration with Xiaowei Zhan's

lab in 2019 which aimed at understanding the impact of conjugation which was orthogonal to

the backbone. As shown in sections 1.2 and 1.3, extending the donor core (through the

addition of benzene and thiophene units) can greatly impact the optoelectronic and

photovoltaic properties – this extension is along the backbone. The question remained, what

happens if conjugation is extended in the cross direction (i.e., off the backbone), which we

termed as 2D-conjugation? An example of this would be the "1D" ITIC compared to the

"2D" ITIC-2D, as shown in **Chart 1.4**. Note, we are not claiming the ITIC is one

dimensional, simply that the conjugation is along a single axis along the backbone.

---

[4] This section includes a summary of an article in *Materials Chemistry Frontier*. The original citation is as follows: Jiayu Wang, Yiqun Xiao, Wei Wang, Cenqi Yan, **Jeromy Rech**, Wei You, Xinhui Lu, and Xiaowei Zhan. "Pairing 1D/2D-conjugation donor/acceptors towards high-performance organic solar cells." *Materials Chemistry Frontier*, **2019**, 3, 276-283.
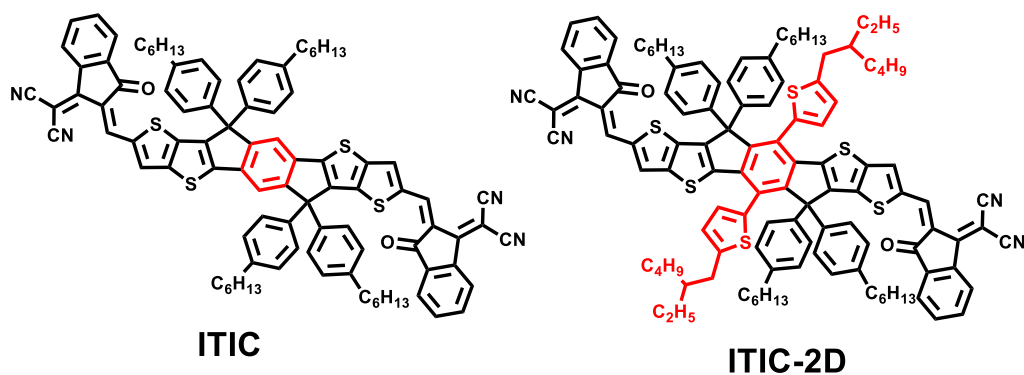
Chart 1.4 – Chemical Structures of ITIC and ITIC-2D

The optoelectronic data, summarized in **Table 1.4**, show that 2D conjugation can red-shift the absorption and slightly decrease the optical bandgap. However, the changes in morphology are more telling. The 2D conjugated side chains on the acceptor induce self-aggregation which lead to a larger acceptor domain size. This means that by tuning the directionality of conjugation (1D vs 2D), the crystallinity and miscibility of the blend can be partially tuned. This combination can result in a decrease in biomolecular recombination and a more favorable morphology, which in turn results in the improved PCE, summarized below.

Table 1.4 – Photovoltaic characteristics of the FTAZ:FREA blends.

FREA	Abs onset (nm)	HOMO (eV)	LUMO (eV)	μ_e $(x10^{-4} \frac{cm^2}{V\,s})$	J_{sc} (mA/cm^2)	V_{oc} (V)	FF (%)	PCE (%)
ITIC	800	-5.48	-3.84	2.0	16.06 ± 0.36	0.922 ± 0.003	56.2 ± 0.4	**8.32 ±** 0.19
ITIC-2D	810	-5.43	-3.80	4.1	18.63 ± 0.26	0.922 ± 0.003	62.0 ± 0.6	**10.65 ±** 0.20

One important comparison also includes considering the conjugation of the donor polymer. FTAZ would be consider a "1D" polymer from the above definition, so an FTAZ-derivative polymer like J71 (structure in Appendix A), which has "2D" conjugation but otherwise similar properties would be interesting to explore. From the combination of the 4 possible blends (1D:1D of FTAZ:ITIC, 1D:2D of FTAZ:ITIC-2D, 2D:1D of J71:ITIC, and

2D:2D of J71:ITIC-2D) the blends with mixed systems (one 1D and one 2D material) exhibited the highest performance (10-11%) while similar blends (1D:1D or 2D:2D) showed lower performance (8-9%). This creates an interesting discovery which requires more investigation; however, it seems that cross-conjugation (i.e., having one "1D" and one "2D" material) can be an effective way to adjust the miscibility and morphology of the active layer and achieve better performance.

1.6 Modifying Donor Core: Extension Through Dimerization – Link Effect [5]

From section 1.3, it was shown that a large donor core can be a great method to achieve higher performance, but the largest acceptor of F11IC was insoluble. This means that additional side chains need to be added in order to solution process F11IC. Furthermore, the synthetic route to make the larger ladder cores becomes increasingly complex. To circumvent these problems, during 2020, we published another collaboration with Xiaowei Zhan, this time looking at dimers of IDIC. Instead of building up a huge ladder core, dimerizing the five fused core of IDIC can be a facile approach to obtain an 10 fused ring donor core. However, the question arose, how does the link pattern (i.e., single, double, or triple bond) impact the FREA? To answer this question, three new IDIC dimers were made with different link patterns and their structures are summarized in **Chart 1.5**.

---

[5] This section includes a summary of an article in the *Journal of Materials Chemistry A*. The original citation is as follows: Guilong Cai, Yiqun Xiao, Mengyang Li, **Jeromy James Rech**, Jiayu Wang, Kuan Liu, Xinhui Lu, Zheng Tang, Jiarong Lian, Pengju Zeng, Yiping Wang, Wei You, and Xiaowei Zhan. "Effect of Link Pattern on Fused-Ring Electron Acceptor Dimers." *Journal of Materials Chemistry A*, **2020**, 8 (27), 13735-13741.
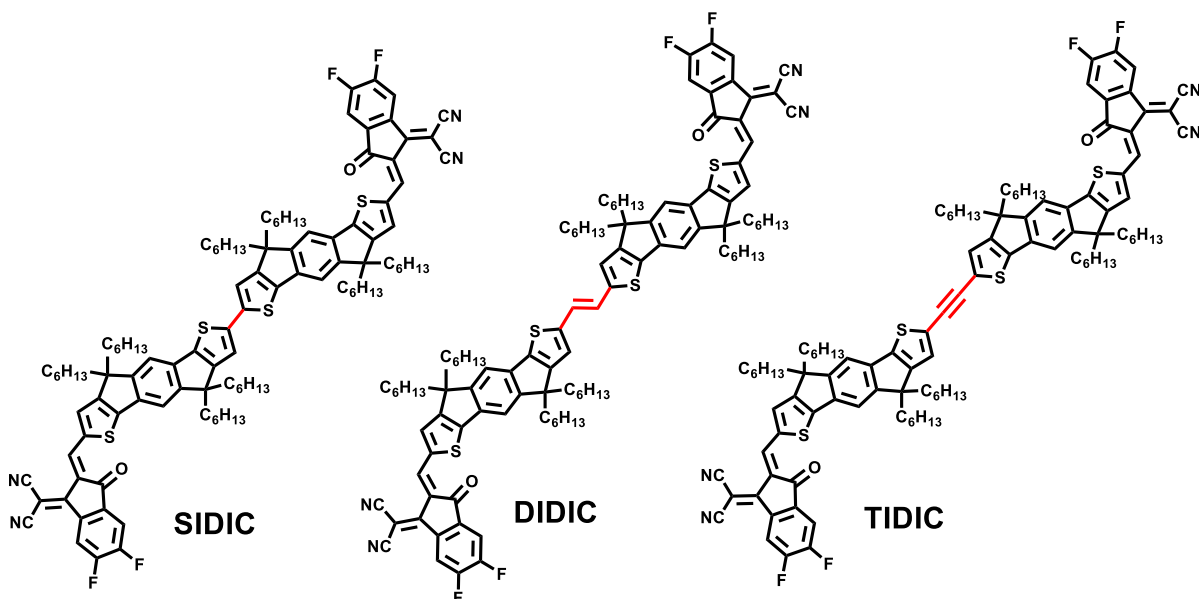
Chart 1.5 – Chemical Structures of SIDIC, DIDIC, and TIDIC

While all three acceptors have similar molar attenuation coefficients and LUMO energy, the link pattern has a large impact on the absorption window; compared to the single bond linkage of SIDIC, the double bond of DIDIC results in a small red-shift while the triple bond of TIDIC has a strong blue-shift. Typically, blue-shifting would result in a smaller J_{SC} value; however, while TIDIC has the smallest absorption range, the FTAZ:TIDIC blend had the strongest EQE over 80%. Further investigation revealed the high electron mobility of TIDIC, **Table 1.5**, which translated to the highest charge collection efficiency (99%). This combination results in a much-improved J_{SC}.

Table 1.5 – Photovoltaic characteristics of the FTAZ:FREA blends.

FREA	Abs onset (nm)	HOMO (eV)	LUMO (eV)	μ_e (x10^{-4} $\frac{cm^2}{V\,s}$)	J_{sc} (mA/cm^2)	V_{oc} (V)	FF (%)	PCE (%)
SIDIC	867	-5.43	-3.88	2.9	17.9 ± 0.30	0.858 ± 0.005	68.4 ± 1.4	**10.5 ±** 0.3
DIDIC	886	-5.44	-3.91	1.4	17.1 ± 0.28	0.817 ± 0.001	64.0 ± 1.0	**8.9 ±** 0.3
TIDIC	800	-5.59	-3.88	11.0	20.6 ± 0.44	0.869 ± 0.006	70.7 ± 1.4	**12.7 ±** 0.2

To understand why the double bond linked DIDIC blend had the worst efficiency, the morphology was explored. DIDIC was the most crystalline acceptor with the highest rotation barrier. This led to poor miscibility with FTAZ and a 35% larger domain size. This combination results in more charge carrier recombination and lower performance. So in this particular series, the triple bond linkage (TIDIC) resulted in the highest performance for the dimer systems by decreasing the crystallization while maintaining high mobility, and this might suggest an interesting design motif for others to explore in the future.

There is very little work being done to explore dimer acceptors outside of naphthalene diimides (NDIs) and perylene diimides (PDIs);[90–92] however, all of these dimers (which are not fused) normally use a single bond link pattern. NDI and PDI based dimer acceptors also typically have lower performance compared to ITIC derivatives and tend to crystallize very easily. This can create an opportunity to potentially increase the efficiency of these systems by exploring different link patterns, such as a triple bond.

1.7 Modifying End Groups: Adding Substituents (F, OMe) [6]

Of all the variations in FREAs published in the past six years, the most common location for functionalization is the electron withdrawing INCN (2-(3-oxo-2,3-dihydroinden-1-ylidene)malononitrile) end-group. Of the possible changes to the base INCN pendant group, adding electron donating or withdrawing substituents were the most commonly explored. A perfect example of this comes from a collaboration with Xiaowei Zhan in 2018. In that work, three new derivatives of ITIC-Th (which has slightly different side chains, see

---

[6] This section includes a summary of an article in *Materials Chemistry Frontiers*. The original citation is as follows: Zeyuan Li, Shuixing Dai, Jingming Xin, Lin Zhang, Yang Wu, **Jeromy Rech**, Fuwen Zhao, Tengfei Li, Kuan Liu, Qiao Liu, Wei Ma, Wei You, Chunru Wang and Xiaowei Zhan. "Enhancing performance of electron acceptor ITIC-Th via tailoring end groups." *Materials Chemistry Frontiers*, **2018**, 2 (3), 537-543.

section 1.9 for more details) were synthesized with one fluorine group, two fluorine groups, and one methoxy group on each INCN acceptor. The chemical structures for each FREA are depicted in **Chart 1.6**.
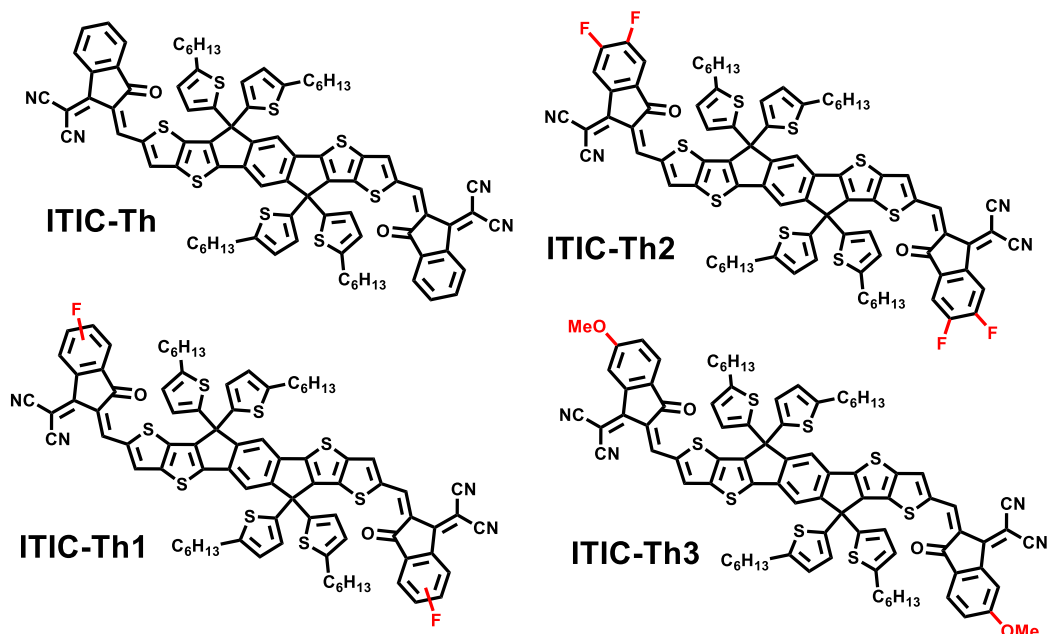
Chart 1.6 – Chemical Structures of ITIC-Th, ITIC-Th1, ITIC-Th2, and ITIC-Th3

To begin with, the electron withdrawing fluorine substituent causes a red shift in absorption and deepens the HOMO and LUMO levels (ITIC-Th vs ITIC-Th1). The impact of the second fluorine (ITIC-Th2) continues to shift in the same direction, however, with diminished impact. As summarized in **Table 1.6**, these effects have counteractive effects. A red-shift in absorption will often increase the J_{SC} as the acceptor can harvest photons from a larger selection of the sun's wavelength; however, a deeper LUMO level results in more loss and a smaller V_{OC}. Because these two effects are opposite, it is difficult to predict the impact on performance and much of it will come down to recombination and morphology. In the case of the mono-fluorinated ITIC-Th1, the massive increase in J_{SC} overrides the V_{OC} loss, and the FTAZ:ITIC-Th1 blend can achieve an improved efficiency near 12%.

Upon addition of the second fluorine, ITIC-Th2 has a decrease in performance. The additional drop in V_{OC} is only met with a small increase in the J_{SC}. While the ITIC-Th2 is red-shifted compared to ITIC-Th1, an inferior morphology leads to more recombination and a slightly smaller current. The ITIC-Th2 has the lowest crystallinity and larger domain size, making it harder to split excitons. This shows the careful balance in functionalization, as the second fluorine group offers no benefits in terms of solar cell efficiency.

Alternatively, an electron donating methoxy group can be used, such as the case with ITIC-Th3. Much like with the case of fluorination, the functionalization of the INCN end group has a delicate balance. The electron donating methoxy increases the bandgap and causes a strong blue shift, which will limit the J_{SC}; however, the LUMO level is also up-shifted which can allow for a much higher V_{OC}. In the case of the single methoxy group, the increase in voltage can override the loss in current and result in a net improvement in the performance of the solar cell.

Table 1.6 – Photovoltaic characteristics of the FTAZ:FREA blends.

FREA	Abs onset (nm)	HOMO (eV)	LUMO (eV)	μ_e (x10^{-4} $\frac{cm^2}{V\,s}$)	J_{sc} (mA/cm^2)	V_{oc} (V)	FF (%)	PCE (%)
ITIC-Th	775	-5.66	-3.93	1.6	15.67 ± 0.23	0.915 ± 0.003	61.1 ± 0.9	**8.7 ±** 0.15
ITIC-Th1	800	-5.74	-4.01	3.5	19.22 ± 0.18	0.847 ± 0.002	72.6 ± 0.3	**11.9 ±** 0.10
ITIC-Th2	805	-5.75	-4.07	5.1	16.97 ± 0.25	0.748 ± 0.004	69.3 ± 0.8	**8.9 ±** 0.15
ITIC-Th3	760	-5.67	-3.73	7.2	16.26 ± 0.13	0.960 ± 0.003	68.1 ± 0.3	**10.6 ±** 0.15

This same trend can also be seen with a series of C-O bridge FREAs which we reported with Liming Ding. As shown in **Chart 1.7**, a series of acceptors with varying fluorination on the end group where explored. Similarly, as summarized in **Table 1.7**, the bandgap consistently decreases upon fluorination, as shown by the red-shifted absorbance.

This allows for harvesting of more low energy photons and this increases the J_{SC}, from 17 to 21 mA/cm^2 when comparing the two extremes. However, the fluorine also deepens the HOMO and LUMO energy level, and this results in a lower drop in the V_{OC}. In this specific series, the single fluorinated end group of CO$_i$6FIC resulted in the highest performance by balancing the increase in current with decrease in voltage.
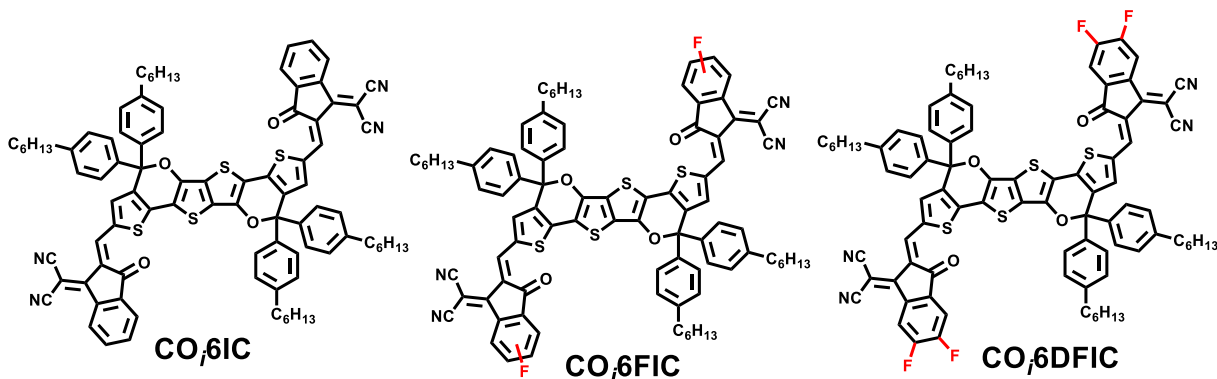
Chart 1.7 – Chemical Structures of CO$_i$6IC, CO$_i$6FIC ,and CO$_i$6DFIC

Table 1.7 – Photovoltaic characteristics of the FTAZ:FREA blends.

FREA	Abs onset (nm)	HOMO (eV)	LUMO (eV)	μ_e (x10$^{-4}\frac{cm^2}{V\,s}$)	J_{sc} (mA/cm^2)	V_{oc} (V)	FF (%)	PCE (%)
CO$_i$6IC	905	-5.57	-3.86	0.7	17.45	0.82	59.0	**8.43**
CO$_i$6FIC	925	-5.60	-3.93	2.1	19.38	0.75	62.6	**9.12**
CO$_i$6DFIC	947	-5.64	-4.04	1.3	20.98	0.67	58.9	**8.25**

Further understanding of the fluorine impact can also be understood by comparing FREAs which will be introduced in future sections (1.9 and 1.10, *vide infra*), which are summarized in **Table 1.8**. Each odd entry (grey colored) in a non-functionalized FREA, and the subsequent entry (white colored) is the fluorinated version of the same FREA. In all four of these pairs, the fluorinated version includes two fluorines per end group. Across each of the pairs, the J_{SC} consistently increases upon fluorination of the end group, matching the same assertions as previously described. Also, there is a large decrease in the V_{OC} based on

21

the impact which the fluorine substituents have on the energy levels. In these four pairs, the FF is also improved and this results in an overall increase in the efficiency of the solar cell.

Table 1.8 – Photovoltaic characteristics of the FTAZ:FREA blends.

FREA	Abs onset (nm)	HOMO (eV)	LUMO (eV)	μ_e $(x10^{-4}\frac{cm^2}{V\,s})$	J_{sc} (mA/cm^2)	V_{oc} (V)	FF (%)	PCE (%)
ITIC	800	-5.48	-3.84	2.0	16.06 ± 0.36	0.922 ± 0.003	56.2 ± 0.4	**8.3 ±** 0.2
IT-4F	795	-5.74	-4.01	1.5	18.30 ± 0.19	0.741 ± 0.011	57.5 ± 2.6	**7.8 ±** 0.4
ITIC-Th	775	-5.66	-3.93	1.6	15.67 ± 0.23	0.915 ± 0.003	61.1 ± 0.9	**8.7 ±** 0.2
ITIC-Th2	805	-5.75	-4.07	5.1	16.97 ± 0.25	0.748 ± 0.004	69.3 ± 0.8	**8.9 ±** 0.2
INIC	790	-5.46	-3.90	0.9	13.96 ± 0.05	0.961 ± 0.009	55.5 ± 3.0	**7.5 ±** 0.3
F9IC	785	-5.50	-3.92	1.0	20.00 ± 0.16	0.863 ± 0.009	65.2 ± 3.2	**11.3 ±** 0.4
INIC4	838	-5.52	-4.00	1.7	15.42 ± 0.13	0.952 ± 0.003	64.9 ± 2.8	**9.5 ±** 0.2
FINIC	821	-5.56	-4.02	8.3	20.35 ± 0.20	0.855 ± 0.010	73.7 ± 1.0	**12.8 ±** 0.2

Therefore, from the results summarized in **Tables 1.6 – 1.8**, it appears the end group fluorination can be a valuable strategy to increase the efficiency of the solar cell blend, but one should be careful using this approach. The functionalization consistently increases the J_{SC} but decreases the V_{OC}, so the FF and morphology are often the tie breaker to see if the functionalization results in a net increase or decrease of the solar cell efficiency.

1.8 Modifying End Groups: Extending with Benzenes [7]

Along with adding substituents (such as methyl groups, fluorine atoms, and methoxy groups), other end group modifications include extending the benzene unit to a naphthalene

---

[7] This section includes a summary of an article in *Acta Physico-Chimica Sinica*. The original citation is as follows: Peiyao Xue, Junxiang Zhang, Jingming Xin, **Jeromy Rech**, Tengfei Li, Kaixin Meng, Jiayu Wang, Wei Ma, Wei You, Seth Marder, Ray Han, and Xiaowei Zhan. "Effects of Terminal Groups in Third Components on Performance of Organic Solar Cells." *Acta Physico-Chimica Sinica*, **2019**, 35 (3), 275-283.

unit. It has been proposed that the primary charge pathway from one acceptor to the next is through the close π-π stacking of the end groups – a claim which we investigate at great lengths in Chapter 2. Based on this, having a large planar aromatic end group, such as naphthalene, might help increase the intermolecular interactions between acceptors and result in better charge transfer between acceptors. This claim was investigated with a collaboration with Xiaowei Zhan in 2018.

IDIC   **IDNC**
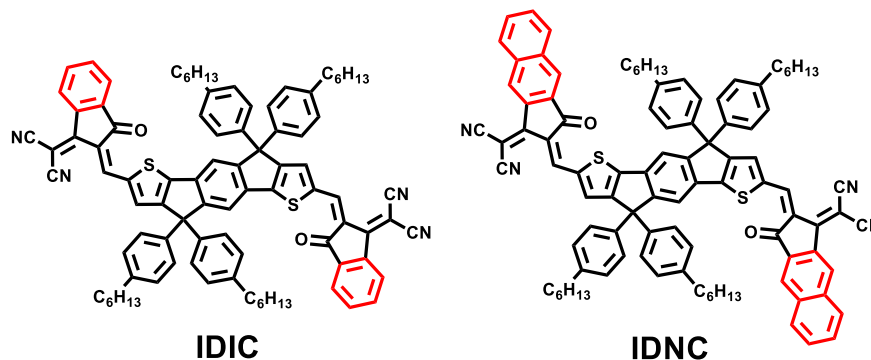
Chart 1.8 – Chemical Structures of IDIC and IDNC

A new derivative of IDIC was synthesized with a naphthalene end unit; the chemical structure for IDNC is shown in **Chart 1.8**. One of the first notable differences between to the two acceptors is the large red shift (~60 nm) seen when extending to the larger end group. Furthermore, the charge carrier mobility also increases, likely from the stronger intermolecular interactions possible from the extended end group. This combination results in a very large 40% increase in the current density, and while the VOC decreases from the deeper LUMO energy level, the overall efficiency increases compared to the IDIC control. Key data is summarized in **Table 1.9**.

Table 1.9 – Photovoltaic characteristics of the FTAZ:FREA blends.

FREA	Abs onset (nm)	HOMO (eV)	LUMO (eV)	μ_e (x$10^{-4}\frac{cm^2}{V\,s}$)	J_{sc} (mA/cm^2)	V_{oc} (V)	FF (%)	PCE (%)
IDIC	719	-5.51	-3.81	0.6	13.6 ± 0.23	0.917 ± 0.005	58.9 ± 2.1	**7.33** ± 0.17
IDNC	779	-5.65	-3.92	0.9	18.6 ± 0.25	0.810 ± 0.001	60.7 ± 0.5	**9.13** ± 0.10

1.9 Modifying Side Chains: Phenyl vs Thienyl

There are a few main functions of the hexylphenyl side chains: (1) to provide solubility in common organic solvents to allow for solution processing, (2) to limit π-π stacking of the donor core, creating an isolated and protected charge transport pathway, and (3) to adjust the crystallinity of the acceptor without interrupting the conjugation of the backbone. These can be met with various options, including the common hexylphenyl side chains seen in IDIC and ITIC, through a sp^3 carbon which bridges the fused ring core. However, we have also explored a thiophene based side chains with further collaborations with Xiaowei Zhan. The chemical structure of the ITIC series with two different types of side chains is shown in **Chart 1.9**, with key data shown in **Table 1.10**.
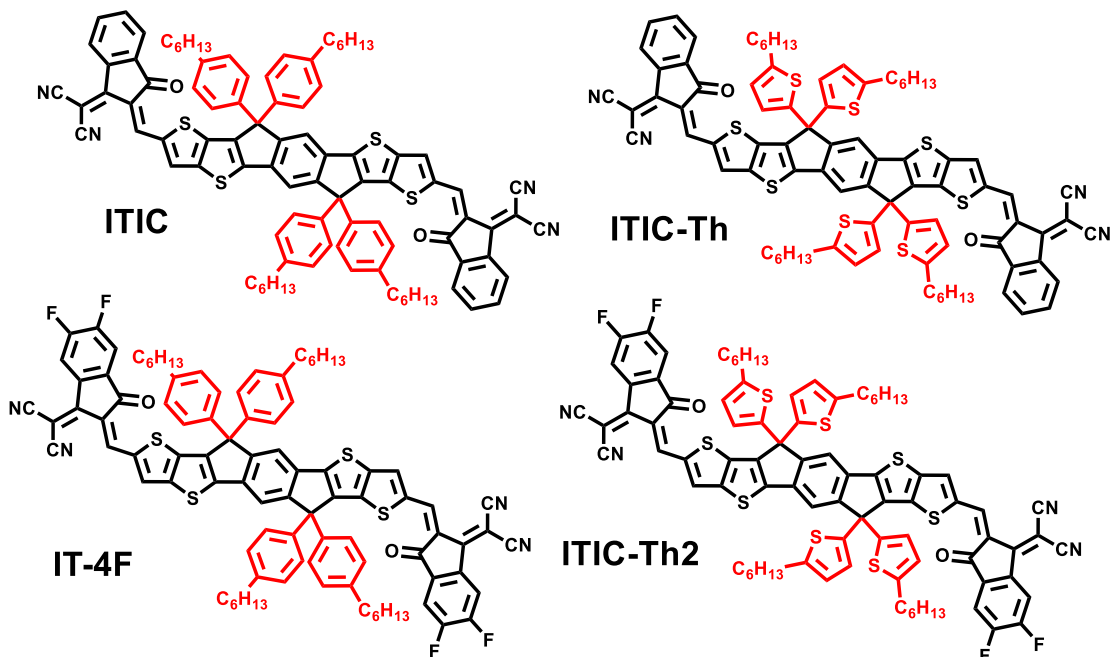
Chart 1.9 – Chemical Structures of ITIC, ITIC-Th, IT-4F, and ITIC-Th2

Table 1.10 – Photovoltaic characteristics of the FTAZ:FREA blends.

FREA	Abs onset (nm)	HOMO (eV)	LUMO (eV)	μ_e (x10^{-4} $\frac{cm^2}{V\,s}$)	J_{sc} (mA/cm^2)	V_{oc} (V)	FF (%)	PCE (%)
ITIC	800	-5.48	-3.84	2.0	16.06 ± 0.36	0.922 ± 0.003	56.2 ± 0.4	**8.3 ±** 0.2
ITIC-Th	775	-5.66	-3.93	1.6	15.67 ± 0.23	0.915 ± 0.003	61.1 ± 0.9	**8.7 ±** 0.2
IT-4F	795	-5.74	-4.01	1.5	18.30 ± 0.19	0.741 ± 0.011	57.5 ± 2.6	**7.8 ±** 0.4
ITIC-Th2	805	-5.75	-4.07	5.1	16.97 ± 0.25	0.748 ± 0.004	69.3 ± 0.8	**8.9 ±** 0.2

Unlike the previous sections, the primary difference if seen in the fill factor. The thienyl-based side chains are able to tune the crystallinity of the acceptor to result in a better morphology and this, in turn, results in an improved *FF*. This is seen in both the ITIC and IT-4F case study, where the *FF* increases (from 56 to 61 and 58 to 69%, respectively) for both materials. There is a slight decrease in the J_{SC} and comparable V_{OC}s, but the overall efficiency tracks with the changes to the fill factor. A similar trend is also seen in the organic field effect transistor realm with the works of Iain McCulloch.[93]

1.10 Modifying Side Chains: Effect of Fluorination [8]

Thus far, there has been a lot of discussion and research into understanding the fluorine impact on fused ring electron acceptors, but these works have all focused on the end group acceptor moiety. This led us to consider the impact that fluorination had on the device performance when the fluorine substituent was added to the side chain. Published with Xiaowei Zhan, four FREAs where synthesized and explored, as shown in **Chart 1.10**. Of

---

[8] This section includes a summary of an article in *Small Structures*. The original citation is as follows: Shuixing Dai, Jiadong Zhou, Tsz-Ki Lau, **Jeromy Rech**, Kuan Liu, Zengqi Xie, Xinhui Lu, Wei You and Xiaowei Zhan. "Effects of Fluorination Position on Fused-Ring Electron Acceptors." *Small Structures*, **2020**, 1 (2) 2000006.

these materials, fluorine atoms were added to the phenyl unit of the side chain in a meta-position to the linkage to the donor core.
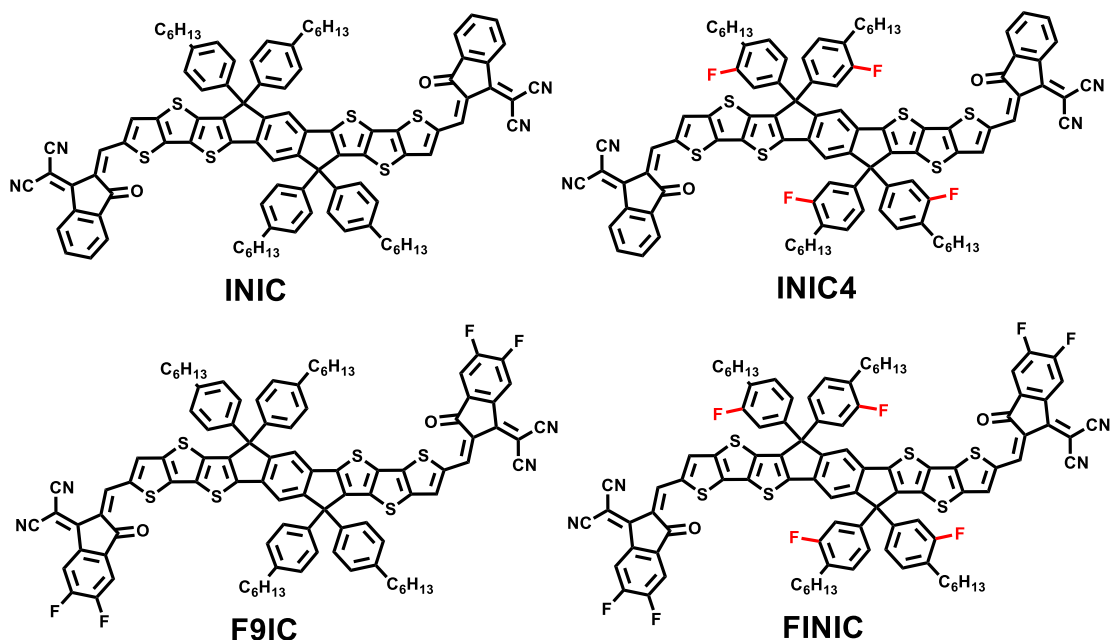
Chart 1.10 – Chemical Structures of INIC, INIC4, F9IC, and FINIC

When the fluorine atom is added to the side chain, the impact is different from results summarized previously with fluorinated end groups. The addition of the fluorine does still cause a red-shift in absorption, with a slight increase in the current density; however, the drop in V_{OC} upon fluorination is much smaller, as shown in **Table 1.11**. Furthermore, the fluorine tunes the crystallinity of the acceptor and there is a very notable increase in the FF, which ultimate leads to impressive increases in the solar cell efficiency.

Table 1.11 – Photovoltaic characteristics of the FTAZ:FREA blends.

FREA	Abs onset (nm)	HOMO (eV)	LUMO (eV)	μ_e $(\times 10^{-4} \frac{cm^2}{V\,s})$	J_{sc} (mA/cm^2)	V_{oc} (V)	FF (%)	PCE (%)
INIC	790	-5.46	-3.90	0.9	13.96 ± 0.05	0.961 ± 0.009	55.5 ± 3.0	**7.5 ±** 0.3
INIC4	838	-5.52	-4.00	1.7	15.42 ± 0.13	0.952 ± 0.003	64.9 ± 2.8	**9.5 ±** 0.2
F9IC	785	-5.50	-3.92	1.0	20.00 ± 0.16	0.863 ± 0.009	65.2 ± 3.2	**11.3 ±** 0.4
FINIC	821	-5.56	-4.02	8.3	20.35 ± 0.20	0.855 ± 0.010	73.7 ± 1.0	**12.8 ±** 0.2

The fluorination impact is best shown through morphology data. GIWAXS scans show that all acceptors adapt a face-on orientation, but the fluorinated FREAs have 1.3 Å larger lamella packing and 0.1 Å smaller π-π stacking. The crystalline correlation lengths are also higher for both of the fluorinated acceptors as well. This combination can explain the higher mobility and lower recombination (as measured through light intensity studies) for the fluorinated materials. This strategy of adding fluorine to the side chains, while more synthetically complex, is a creative way to enjoy benefits of fluorine substituent while minimizing the negative consequences; the champion device of FTAZ:FINIC also exhibited a high 13% solar cell efficiency.

1.11 Conclusion [9]

Various structure-property relationships for fused ring electron acceptors have been discussed, and one collaboration with Chunru Wang's lab demonstrates a nice combination of these. Published in *Advanced Energy Materials*, we introduced a new FREA which was called IDCIC, shown in **Chart 1.11**. This acceptor had (1) an extended core with a total of ten fused rings (with both extra benzene and thiophene units), (2) added solubility from hexyl side chains, and (3) fluorinated end groups. This combination resulted in a solar cell with nearly 14% efficiency, which in 2018 was one of the highest reported values. One important drawback is the synthetic pathway for this molecule is very long and complex for this material, making it difficult to make in large quantities.

---

[9] This section includes a summary of an article in *Advanced Energy Materials*. The original citation is as follows: Dan He, Fuwen Zhao, Jingming Xin, **Jeromy James Rech**, Zhixiang Wei, Wei Ma, Wei You, Bao Li, Li Jiang, Yongfang Li and Chunru Wang. "A Fused Ring Electron Acceptor with Decacyclic Core Enables over 13.5% Efficiency for Organic Solar Cells." *Advanced Energy Materials*, **2018**, 8 (30), 1802050.
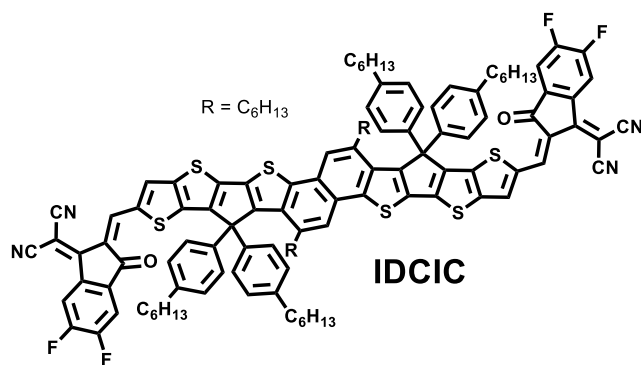
Chart 1.11 – Chemical Structures of IDCIC

To summarize a few key structure-property relationships which have been demonstrated through the collaborations described in this chapter: (1) Extending the fused ring donor core increases the charge carrier mobility and raises the frontier molecular orbitals, which allows for a higher V_{OC}. Some precautions should be taken, as the solubility decreases with extended length, with a max of 9-10 fused rings being able to solubilized without the need for additional side chains. (2) Functionalization of the end groups should be done carefully. The common technique of fluorination results in a red-shifted absorption and higher J_{SC}, but also pulls down the LUMO energy level and decreases the V_{OC}. (3) The side chains can offer more than just solubility; tuning the structure of the side chain is an effective method to modify the crystallinity and morphology of the FREA and can be a facile method to increase the *FF*.

CHAPTER 2: The Crucial Role of End Group Planarity for Fused-Ring Electron Acceptors in Organic Solar Cells [10]

2.1 Introduction

In the previous chapter, various structure-property relationships of fused ring electron acceptors (FREAs) were highlighted. While device efficiencies have shown great improvement, the structural changes in new FREAs have become increasingly minor and the locations for new functionalization are becoming sparse. In short, the field has become saturated with ITIC and its derivatives, which has limited the synthesis of new and novel structures. In particular, the acceptor moiety, 2-(3-oxo-2,3-dihydroinden-1-ylidene)malononitrile (INCN), has only seen minor development. However, it is important to note that some of these changes have shown substantial improvements in the BHJ device efficiency, such as IT-M and IT-4F,[94,95] compared to the original ITIC. Indeed, these works have pushed the efficiency levels forward in great strides, but to continue forward at this pace, new materials will need to be explored, and understanding the molecular engineering requirements of FREAs is vital to this process.

Analyzing the shared structural features of notably high-performing FREAs can offer clues on the molecular engineering requirements. These include: (a) A-D-A architecture for

---

[10] Parts of this chapter previously appeared as an article in the *Materials Chemistry Frontiers*. Reprinted with permission from Chinese Chemical Society, Institute of Chemistry of Chinese Academy of Sciences, and the Royal Society of Chemistry. The original citation is as follows: Jeromy J. Rech, Nicole Bauer, David Dirkes, Joseph Kaplan, Zhengxing Peng, Huotian Zhang, Long Ye, Shubin Liu, Feng Gao, Harald Ade, and Wei You. "The Crucial Role of Steric Hindrance for the End Group of Fused-Ring Electron Acceptors for Organic Solar Cells." *Materials Chemistry Frontiers*, **2019**, *3* (8), 1642-1652.

tunability of band gap and energy levels; (b) conjugated ladder core to serve as an intermolecular charge transport channel; (c) alkyl side chains connected to a tetrahedral carbon on the donor unit to increase solubility, processability, and prevent excessive aggregation; (d) planar exposed electron deficient end groups that can form charge transport channels with neighboring acceptor molecules, presumably via the end-group interaction between different FREAs.[24,63,96–98,64–70,76] However, a more in-depth understanding of these requirements is lacking. For example, there have been many studies on the synthesis and performance of new FREAs,[1,3,101–103,6,7,51,61,62,72,99,100] but little work has focused on the molecular packing of these materials (i.e., requirement (d) above). To obtain high efficiency, OSC electron acceptors need a high electron mobility in order to extract electrons from the active layer and transport them to the cathode before they recombine. It is thought that the high electron mobility exhibited by small molecule NFAs is a result of close π-π stacking between neighboring acceptor end groups, which facilitate intermolecular π-orbital interactions and form charge transport pathways across neighboring NFA molecules.[76,96]

Based on the shared structural features, a few groups have proposed diagrams to show the molecular packing of FREAs;[24,97,98] however, the direct observation and limits of these models have often not been tested. For example, charge transport between acceptors is believed to occur at the FREAs acceptor end groups, and the distance between acceptor end groups (i.e., π-π stacking distance) needs to be sufficient for charge transport to occur. Values for efficient charge transport are often estimated to be within the 3-4 Å range, but most models don't offer further insight on this distance requirement. These models come in part from grazing-incidence wide-angle X-ray scattering (GIWAXS) measurements, which typically show lamellar and π-π stacking in FREAs, but this information alone lacks the

details needed for a complete understanding. Very recently, Lu and co-workers used measurements such as GIWAXS to experimentally illustrate the formation of charge transport pathways via the interactions of the INCN end groups of ITIC and ITIC-Th.[104] This work serves as a strong example to validate the design of such models. While each model shows this favorable π-π stacking of the INCN end groups as the charge pathway between two acceptors, none include the limits of this interaction (i.e., maximum π-π stacking distance possible while maintaining efficient charge transport). Understanding the limits of the packing is important to the design of new NFAs, as clear structural design criterion can streamline the development of new high performance FREAs.

As previously mentioned, there was no strict consensus on the specific values of distance that FREAs would have to reach in order to achieve high performance in OPVs; thus, we conducted a quick literature survey of a large variety of high performance FREAs,[26,32,108–117,51,118–123,72,77,99,100,105–107] and organized the data on π-π stacking distance in **Figure 2.1a**. The π-π stacking distance was reported for each of these materials through crystal structure, neat XRD, or GIWAXS measurement, and a table summarizing these values along with the chemical structures of each FREA is shown in **Table 2.1** and **Chart 2.1**. It is important to note that these values come from the neat, small molecule only films; once blended with a donor polymer, the range of π-π stacking distances varies based on the miscibility and interaction between the components of the active layer. Nevertheless, **Figure 2.1a** clearly shows that high performance FREA-based blends reported in literature display a close π-π stacking distance of ~ 3.5 Å between acceptor end units forming the charge transport pathways. This very narrow distribution of distance between end groups of these FREAs, centering around 3.5 Å, presents an interesting and important question: Is this

distance, ~ 3.5 Å, a prerequisite or key criterion in designing new FREAs? Or, if everything else was equal, would a significant deviation from this distance of 3.5 Å lead to a decrease in photovoltaic performance? To address these questions, we designed a new sterically hindered FREA (i.e., IDTCF, structure in **Figure 1b**) which would have a π-π stacking distance outside the range shown by current high performance FREAs (~ 3.3 Å to ~ 3.7 Å). By further studying the tolerance with the end group interaction, a sharper understanding of the molecular design requirements can help facilitate the design of new high performance NFAs.
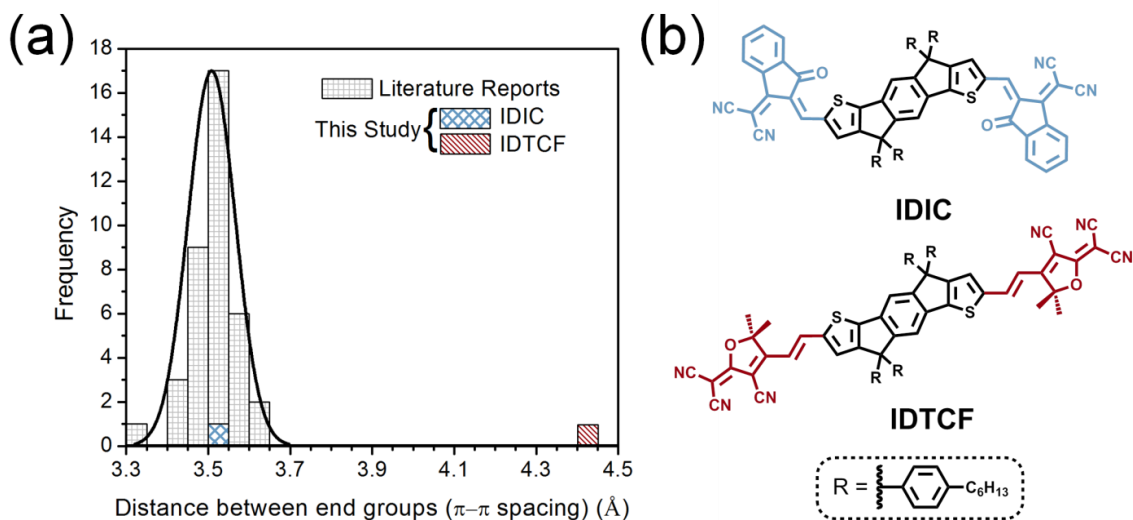
Figure 2.1 – (a) Histogram of π-π spacing distances reported in literature of high performance FREAs and (b) chemical structures of fused-ring electron acceptors
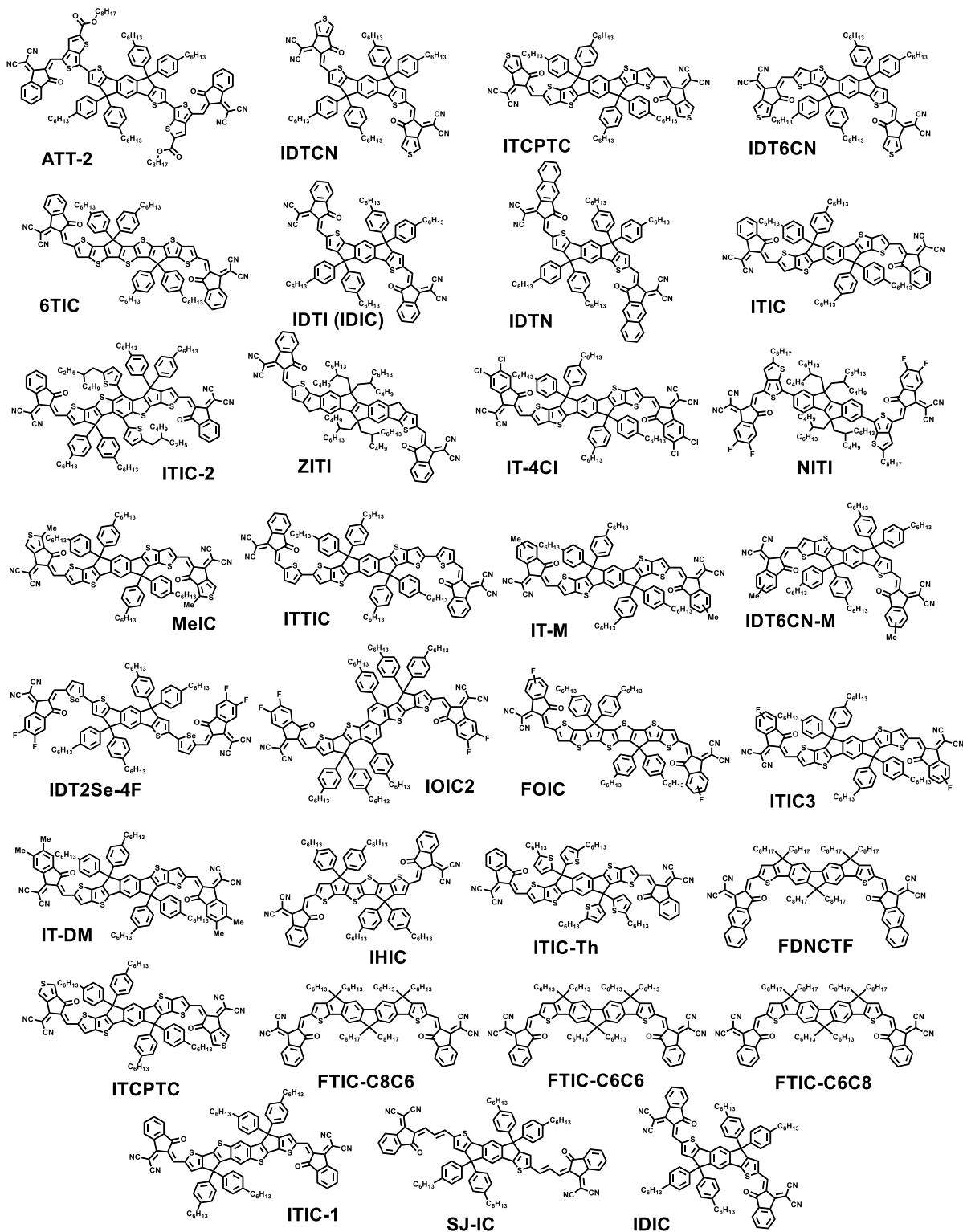
Chart 2.1 – Chemical structures for each of the various high performance fused-ring electron acceptors (FREAs) used in the literature survey of end-group π-π stacking distances

Table 2.1 – Literature survey of end-group π-π stacking distances in high performance FREAs

Entry	FREA	PCE (%)	π-π stacking distance (Å)	Reference
1	ATT-2	9.58	**3.5**	[105]
2	IDTCN	6.4	**3.53**	[106]
3	ITCPTC	10.74	**3.53**	[106]
4	IDT6CN	9.27	**3.49**	[106]
5	IDT6CN-M	11.20	**3.51**	[106]
6	6TIC	11.07	**3.59**	[107]
7	IDTN	12.2	**3.53**	[100]
8	IDTI (IDIC)	7.4	**3.55**	[100]
		11.3	**3.52**	[120]
		6.95	**3.47**	[122]
9	ITIC	11.41	**3.58**	[108]
		11.34	**3.5**	[111]
		10.21	**3.53**	[115]
10	ITIC-1	8.54	**3.5**	[109]
11	ITIC-2	11.0	**3.5**	[109]
12	ZITI	13.04	**3.43**	[110]
13	IT-4Cl	13.45	**3.51**	[51]
14	NITI	12.74	**3.43**	[112]
15	ITCPTC	11.63	**3.6**	[77]
16	MeIC	12.54	**3.5**	[77]
17	ITTIC	9.12	**3.57**	[72]
18	FTIC-C8C6	10.45	**3.48**	[113]
19	FTIC-C6C6	9.75	**3.45**	[113]
20	FTIC-C6C8	11.12	**3.48**	[113]
21	IDT2Se-4F	11.19	**3.33**	[114]
22	IOIC2	12.3	**3.65**	[84]
23	FOIC	12.0	**3.51**	[116]
24	ITIC3	8.0	**3.49**	[116]
25	IT-M	12.05	**3.5**	[117]
26	IT-DM	11.25	**3.5**	[117]
27	IHIC	10.6	**3.49**	[118]
		9.77	**3.51**	[119]
28	ITIC-Th	8.10	**3.51**	[123]
		10.9	**3.49**	[32]
		9.75	**3.49**	[121]
29	FDNCTF	10.9	**3.4**	[26]
30	SJ-IC	9.27	**3.59**	[122]

Herein, we present two FREAs, IDIC and IDTCF (structures in **Figure 2.1b**), with distinct chemical structures that produce different π-π stacking distances between the FREA end groups and show that the chemical structure of the end groups are indeed responsible for the π-π stacking distances seen in these FREAs. The increased stacking distance was expected to have a strong limit on the end group interaction, which would significantly impact the device performance. IDTCF is a new A-D-A-type FREA which consists of an indacenodithiophene (IDT) donor core and two tricyanovinyldihydrofuran (TCF) acceptor end groups. Unlike the INCN end group in the case of IDIC, the TCF end group in IDTCF has two methyl substituents which are out of the plane of the backbone, making it more difficult for the IDTCF to pack closely. Given the same IDT core and A-D-A structure, IDIC and IDTCF have similar optical and electrochemical properties, but IDTCF has a larger intermolecular π-π stacking distance (4.40 Å) due to steric hindrance from the out-of-plane methyl substituents. The hindered packing of IDTCF extends the minimum packing distance by ~ 1 Å; however, the device performance for the IDTCF-based OPV device is drastically (~10 ×) lower than that of IDIC-based one. The origin of the different efficiencies for each acceptor was carefully analyzed, and our results clearly manifest the importance of close π-π stacking distance and planarity of the end groups of FREAs, providing an important design criterion to consider when developing new FREAs for higher device efficiencies.

2.2 Results and Discussion

2.2.1 Synthesis

The chemical structure for each acceptor material in this study is depicted in **Figure 2.1b**, and the full synthetic route for each of the FREAs (IDTCF and IDIC) is shown in **Scheme 2.1** (in 2.4 Experimental section at end of chapter). The indacenodithiophene (IDT)

core, INCN, and TCF acceptor end groups were synthesized according to previous literature reports,[1,38,124] and a Knoevenagel condensation between IDT and INCN or TCF afforded the IDIC or IDTCF in 75% and 52% yields, respectively. The structure of each FREA was confirmed by nuclear magnetic resonance (NMR) (**Figure 2.14** and **Figure 2.15**) and mass spectroscopy (see 2.4 Experimental), and each FREA showed good solubility in common solvents such as chloroform, toluene, and chlorobenzene.

2.2.2 Photovoltaic Performance

We first explored the relationship between photovoltaic performance and end group stacking distance by pairing each acceptor with a wide bandgap donor polymer, FTAZ,[125] in bulk heterojunction (BHJ) solar cells. Devices were prepared with an inverted architecture of ITO/ZnO/FTAZ:Acceptor/MoO$_3$/Al, a donor:acceptor (D:A) ratio of 1:1, and chlorobenzene as the solvent. Details of solvent optimization can be found in **Table 2.2**.

Table 2.2 – Photovoltaic characteristics of the FTAZ:IDIC and FTAZ:IDTCF solar cells in various different solvents [CF = chloroform; CB = chlorobenzene; Tol = toluene].

Acceptor	Solvent	J_{sc} (mA/cm^2)	V_{oc} (V)	FF (%)	PCE (%)
	CF	7.48 ± 0.19	0.876 ± 0.004	40.9 ± 1.1	2.68 ± 0.06
IDIC	CB	10.79 ± 0.18	0.954 ± 0.004	50.6 ± 1.5	5.21 ± 0.19
	Tol	8.29 ± 0.81	0.944 ± 0.008	43.1 ± 1.0	3.37 ± 0.33
	CF	1.51 ± 0.11	0.738 ± 0.008	39.9 ± 0.4	0.44 ± 0.04
IDTCF	CB	2.10 ± 0.12	0.705 ± 0.034	39.6 ± 1.8	0.59 ± 0.06
	Tol	1.25 ± 0.10	0.737 ± 0.009	41.5 ± 0.6	0.38 ± 0.03

Representative *J-V* curves are displayed in **Figure 2.2a**, and the photovoltaic characteristics are outlined in **Table 2.3**. From these results, it is clear that the IDIC-based devices outperform those based on IDTCF. IDIC-based devices show a higher short-circuit current (J_{SC}), open-circuit voltage (V_{OC}), and fill factor (*FF*), leading to an overall power conversion efficiency (PCE) nearly ten times greater than that of the IDTCF-based ones. The

external quantum efficiency (EQE) of each blend was also measured, and is shown in **Figure 2.2b**. Both devices have a broad EQE response; however, FTAZ:IDIC has a much higher EQE response than FTAZ:IDTCF, with maximum values reaching ~55 % and ~15 %, respectively.
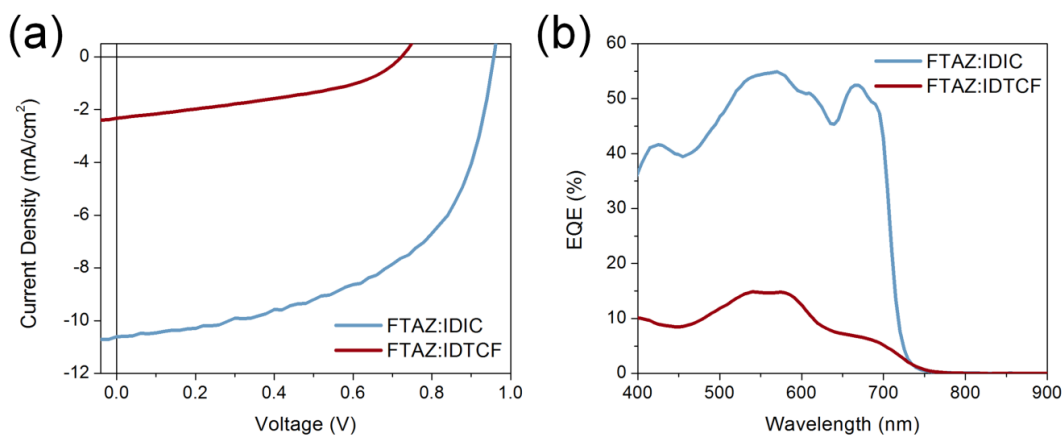
Figure 2.2 – (a) Representative *J-V* curves and (b) EQE spectra for the FTAZ:IDIC and FTAZ:IDTCF devices

Table 2.3 – Photovoltaic characteristics of FTAZ:IDIC and FTAZ:IDTCF solar cells

Acceptor	J_{SC} (mA/cm^2)	V_{OC} (V)	*FF* (%)	PCE (%)
IDIC	10.79 ± 0.18	0.954 ± 0.004	50.6 ± 1.5	5.21 ± 0.19
IDTCF	2.10 ± 0.12	0.705 ± 0.034	39.6 ± 1.8	0.59 ± 0.06

We also synthesized two additional FREAs with an indacenodithienothiophene (IDTT) core, yielding ITIC and ITTCF, whose chemical structures are shown in **Figure 2.3a**. From the *J-V* curves, shown in **Figure 2.3b**, with each of these new FREAs paired with FTAZ in BHJ solar cells, it is clear that the same decrease in performance is seen for all materials with the hindered TCF acceptor moiety. This finding can eliminate any performance decrease due to the choice in the donor core.
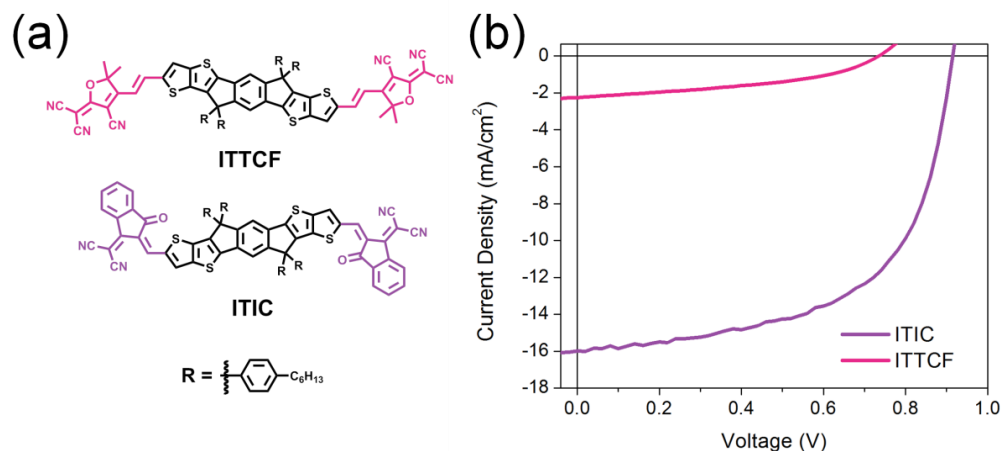
Figure 2.3 – (a) Chemical structure for ITIC and ITTCF electron acceptors and (b) representative *J-V* curve for each acceptor paired with FTAZ

From these results, it is clear that the structural changes in IDTCF (i.e., compared with the structure of IDIC) are detrimental to the performance of BHJ solar cells, likely due to the hindered packing of the TCF end groups (the only structural difference between IDTCF and IDIC). To further corroborate this claim and disclose more detailed structure-property correlation, we explored the electrochemical, optical, and morphological properties of each FREA.

2.2.3. Optical and Electrochemical Properties

We then investigated the electrochemical properties of these materials, using cyclic voltammetry (CV) to measure their highest occupied molecular orbital (HOMO) and lowest unoccupied molecular orbital (LUMO) levels. The CV curves are displayed in **Figure 2.4a**, and the energy levels are summarized in **Figure 2.4b**. As there is a decrease in V_{OC} for the IDTCF-based device, and the V_{OC} is generally related to the energy difference between the LUMO of the acceptor and the HOMO of the donor, an understanding of these energy levels would provide insight into this decrease of V_{OC}. However, both FREAs have a similar LUMO level (– 3.99 eV for IDIC and – 3.98 eV for IDTCF), which would suggest that the

38

lower V_{OC} and performance for the IDTCF-based device is not due to a difference in energetics, but to some other underlying cause. This V_{oc} loss will be further discussed in 2.2.6 Charge Transport.
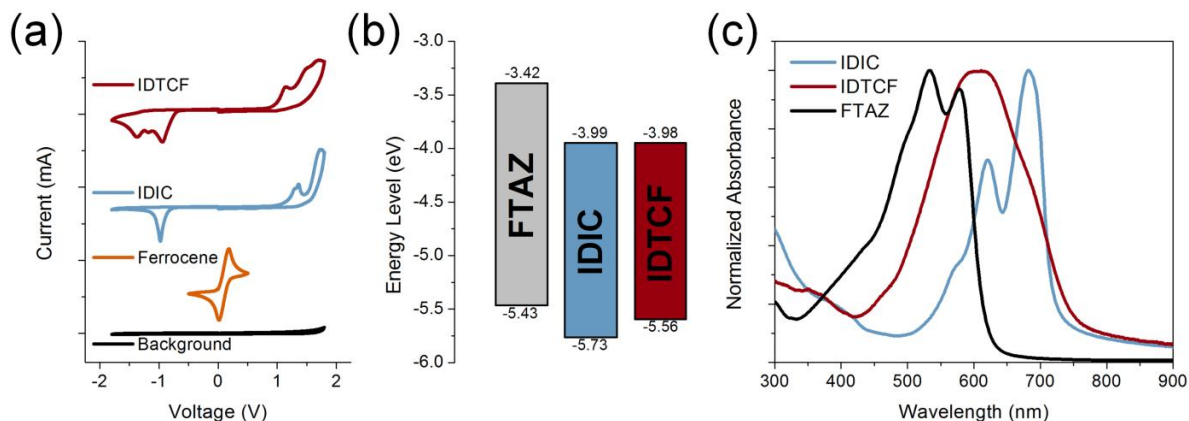
Figure 2.4 – (a) Electrochemical measurements of HOMO and LUMO through cyclic voltammetry, (b) HOMO/LUMO energy diagram from CV results, and (c) Thin film UV-Visible absorbance spectrum of each of the materials studied

To explore the decrease in the J_{SC} for the IDTCF-based device, we studied the optical properties of the FREAs. The absorption spectra for IDIC and IDTCF in solution and thin films are shown in **Figure 2.5a** and **Figure 2.4c**, respectively. The IDIC molecule shows a strong intramolecular charge transfer (ICT) band at 682 nm, with weaker shoulder absorption at 620 nm. Meanwhile, the IDTCF molecule shows a broader absorption with a maximum absorbance at 610 nm. The full width at half maximum (FWHM) for IDIC and IDTCF are 106 nm and 184 nm, respectively. We previously claimed the methyl substituents on the acceptor moiety of the IDTCF molecule increase the steric hindrance and make packing more difficult, which would lead to a large ensemble of orientations which are present for IDTCF at any given point in time, as illustrated by the 1.7 times larger FWHM. Conversely, the IDIC has a more crystalline structure, resulting in fewer conformations, and therefore a smaller FWHM. Nevertheless, both FREAs have similar optical bandgaps, determined by the

absorption onset, which helps corroborate the claim that the TCF and INCN end groups have similar electron withdrawing strength.
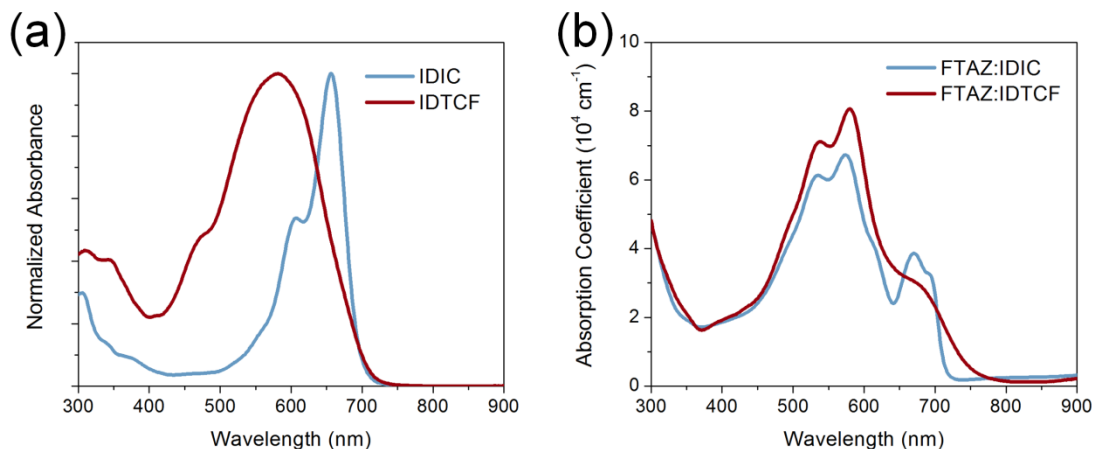
Figure 2.5 – (a) Dilute solution UV-Vis for each FREA dissolved in chloroform and (b) full device absorption coefficient for each FTAZ:FREA blend

The donor polymer, FTAZ, on the other hand, has the strongest absorbance from 400-600 nm, which is complementary to the absorption of the IDIC molecule. The IDTCF molecule, however, has more overlap in its absorption with that of FTAZ. This is further illustrated in the entire device absorbance, shown in **Figure 2.5b**. While there is less absorbance in the range beyond 600 nm for IDTCF blend, the absorption coefficient of both the FTAZ:IDTCF and FTAZ:IDIC are similar across the entire range. Therefore, absorption difference alone cannot account for the observed huge difference between the J_{SC} value of the FTAZ:IDTCF device and that of the FTAZ:IDIC one (**Table 2.3**). In fact, the much diminished EQE response in the region of 400 nm to 600 nm in the FTAZ:IDTCF device (**Figure 2.2b**) – where the FTAZ polymer would contribute the most – indicate that there would exist significant issues with either charge generation, charge transport, or both in the FTAZ:IDTCF device.

2.2.4 Computational Modeling

To further understand the interactions between the electron acceptors, we utilized computation and modeling to explore the closest packing of both FREAs. We performed density functional theory (DFT) calculations at the DFT wB97XD/6-31G(d) level of theory using Gaussian 16 package, version A03. We modeled both a single FREA molecule and a dimer system for both IDIC and IDTCF, and to reduce the computation time yet still maintain the chemical structure, the hexyl side chain was replaced with a methyl substituent. **Figure 2.6a** and **Figure 2.6c** represent the most stable conformation of both the single units, and the methyl substituents of TCF are highlighted in red. The IDTCF has a minimum energy conformation which is planar, as illustrated in **Figure 2.6c**, while the IDIC has a slight bending at the end groups. However, in the dimer system of IDIC, this slight twist is matched by the next acceptor unit, which allows the IDIC molecules to tightly pack. **Figure 2.6b** shows the dimer system for IDIC, and the distance between the INCN end groups was calculated to be 3.58 Å. This value is further corroborated within literature reports, where GIWAXS measurements of films of neat IDIC show an in-plane (IP) π-π stacking distance of 3.45 Å.[1] In the dimer system of IDTCF, shown in **Figure 2.6d**, the FREAs show more twisting and an expanded π-π stacking distance of 3.84 Å. It is important to note that this is the closest packing that is possible for the IDTCF acceptors, and the distance between end groups can be even larger in real films. Additionally, this modeling was only done with a dimer system, so the effects from more IDTCF molecules are unknown. However, these results already begin to demonstrate the impact of the steric bulk from the methyl groups of the TCF acceptor moiety.
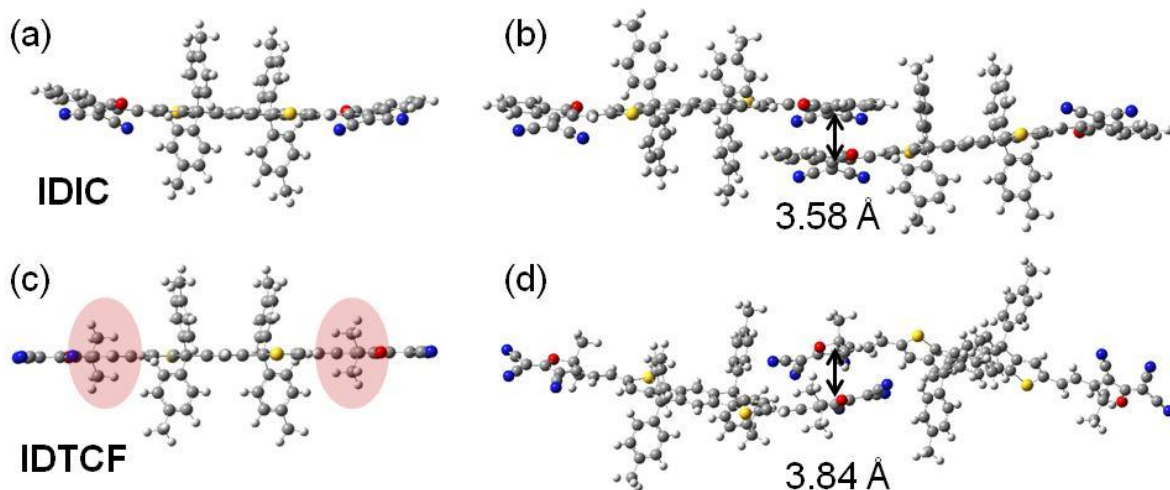
Figure 2.6 – Minimized energy conformation for (a) IDIC unit, (b) IDIC dimer, (c) IDTCF unit, and (d) IDTCF dimer. Additionally, the closest packing of the FREAs was shown to be (b) 3.58 Å for IDIC and (d) 3.84 Å for IDTCF
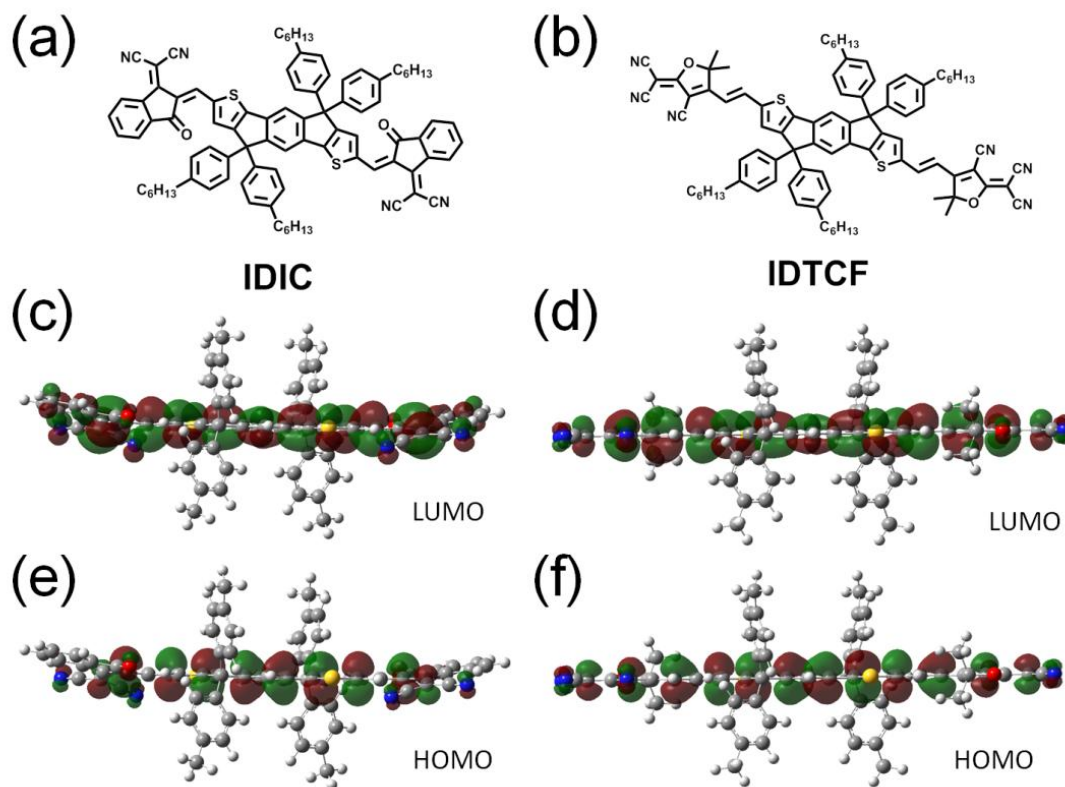
Figure 2.7 – Chemical structure of (a) IDIC and (b) IDTCF, including the (c) LUMO and (e) HOMO of IDIC next to the (d) LUMO and (f) HOMO of IDTCF

Furthermore, the computed electron distributions at the ground and excited states of both FREAs are provided in **Figure 2.7**. The electron distributions, showing the HOMO and LUMO energy levels, for both IDIC and IDTCF show a similar distribution of electron density across each molecule, which further confirms the previous claim that both FREA end groups have similar electron withdrawing strength when paired with the IDT core.

2.2.5 Packing of Molecules in Thin Films

If there is a difference in the packing, as indicated by the previous DFT calculations, we would expect to see a difference in the order and crystallinity of the materials. The hindered IDTCF small molecule was unable to form appropriate single crystals for analysis, so we utilized X-ray diffraction and GIWAXS measurements to explore these properties. We began by performing X-ray diffraction (XRD) measurements of spun-cast samples for each of the neat small molecule films, as illustrated in **Figure 2.8**. To begin with, **Figure 2.8a** is the out-of-plane (OOP) XRD scan for each FREA. For IDIC, we identified two lamella scattering peaks at 3.3° and 5.0° two theta peaks shown in **Figure 2.8a**. This further confirms the packing and semi-crystalline nature of IDIC. In contrast, IDTCF shows no scattering signal in the OOP direction. This lack of signal helps further support the claim that the out-of-plane methyl substituents on the TCF end group disrupt the packing required for efficient charge transport. Next, **Figure 2.8b** is the in-plane (IP) XRD scan for each FREA. Similar to the OOP scan, IDTCF shows no peaks, which again suggests no ordering in the film. In the case of IDIC, a small peak is observed; however, the XRD signal which would correspond to π-π stacking, was not identified. Overall, the XRD data clearly illustrates a loss of ordering for the FREA containing the hindered TCF group, further supporting the claim that IDTCF is unable to pack and form charge transport pathways.
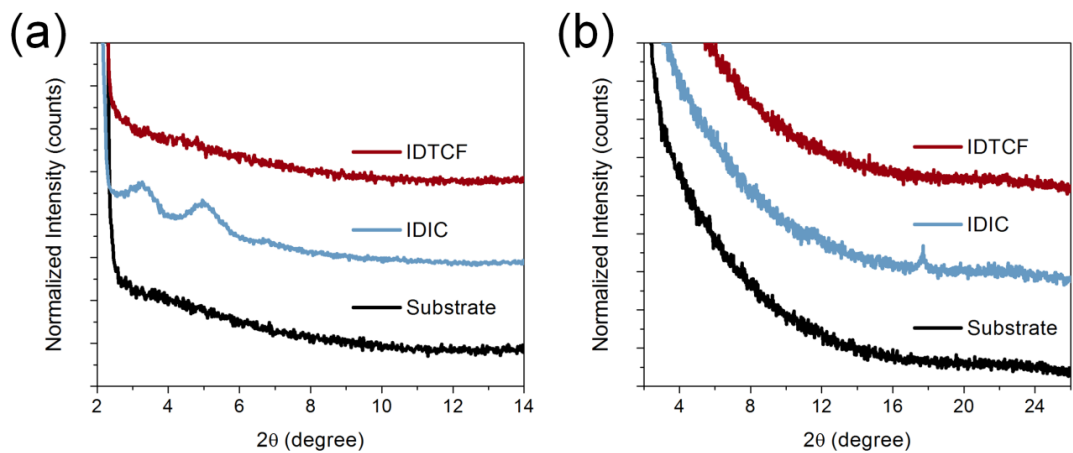
Figure 2.8 – (a) Out-of-plane and (b) in-plane XRD scattering spectra for each acceptor, including blank substrate
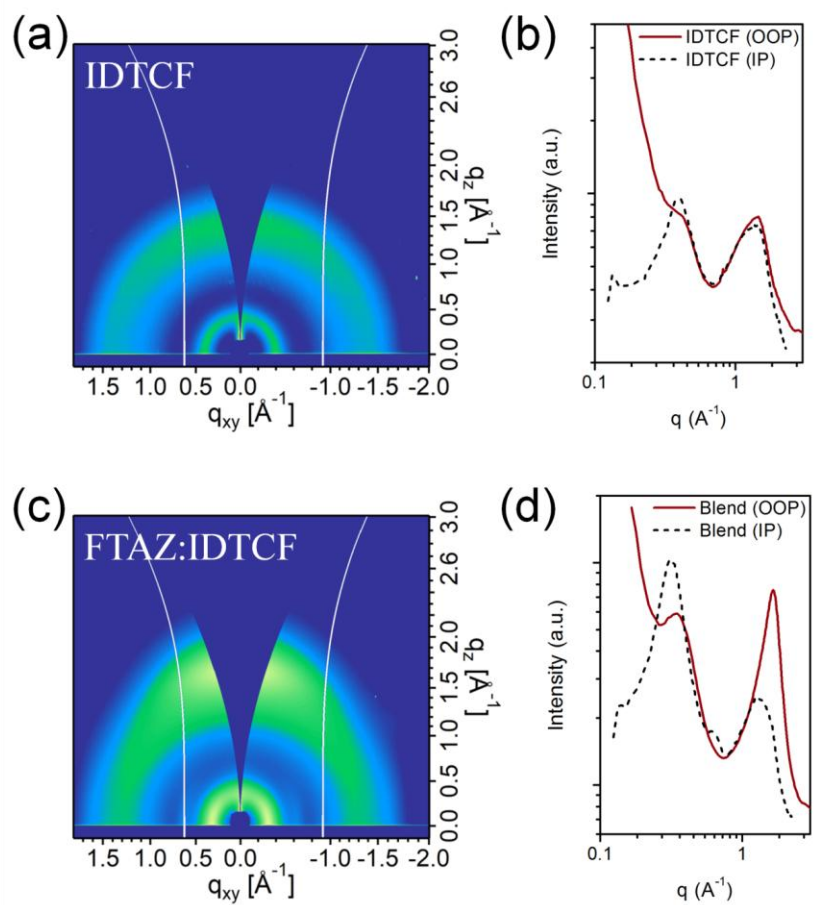
Figure 2.9 – (a,c) 2D GIWAXS pattern and (b,d) in-plane (IP) and out-of-plane (OOP) profiles of neat IDTCF film and FTAZ:IDTCF blend film

To confirm the larger π-π stacking distance, we also measured the molecular packing and texture through synchrotron radiation-based GIWAXS.[126] We previously reported both neat IDIC and FTAZ:IDIC blends with GIWAXS,[1] and the neat IDTCF and blend with FTAZ are shown in **Figure 2.9**. In the neat IDTCF case, the GIWAXS pattern illustrates a random orientation for IDTCF, as shown by the diffuse halo in **Figure 2.9a**, which further corroborates the XRD data. The π-π stacking is shown by the (010) peak in the OOP, at $q = 1.43$ Å^{-1}, corresponding to a 4.40 Å π-π stacking distance. This value is significantly larger than that of the (010) peak of IDIC, at $q = 1.82$ Å^{-1} peak, which corresponds to a π-π stacking distance of 3.45 Å. Additionally, when IDTCF is blended with FTAZ (**Figure 2.9c** & **2.9d**), the (010) peak of the blend system shifts to $q = 1.38$ Å^{-1}, which corresponds to a π-π stacking distance of 4.56 Å.

The next interesting point is to look at the changes that occur to the packing of FTAZ when blended with IDTCF. In the in-plane blend film, the FTAZ contributes to the signals at $q = 0.32$ Å^{-1} and $q = 0.63$ Å^{-1}, which are (100) and (200) peaks. In the OOP direction, when FTAZ is blended with a high performance non-fullerene acceptor, the (010) peak was located between $q \sim 1.7\text{-}1.8$ Å^{-1} (3.5-3.7 Å),[2,6,7,9,62] however, for the FTAZ:IDTCF blend film, the (010) peak is shifted to $q = 1.65$ Å^{-1}, which corresponds to a larger π-π stacking distance of 3.81 Å. This illustrates that the IDTCF acceptor also disrupts the packing of FTAZ, which may lower the hole mobility of FTAZ (*vide infra*).

The GIWAXS results clearly illustrate that the end group packing is expanded by ~ 1 Å from the out of plane methyl substituents of TCF, and compared to the materials outlined in the literature survey conducted at the beginning of this work, the 4.40 Å π-π stacking distance of IDTCF is outside the range seen in high performance FREAs. Additionally, as

both IDIC and IDTCF have similar optical and electrochemical properties, with the only difference being the additional sterics of the TCF acceptor group, we show the importance of the planarity of the end group acceptor moieties and the impact on device performance.

2.2.6 Charge Transport

While IDIC and IDTCF have stark differences in device performance (e.g., J_{SC}, V_{OC}, and FF), their optical and electrochemical properties are similar, indicating that inferior charge transfer and/or charge transport in the IDTCF-based device may be causing the lower performance; each of which can be attributed to the inferior packing which was outlined in the previous section. In many OPV systems, bimolecular recombination has been shown to be the dominant recombination mechanism, thus limiting charge transport and efficiency.[127–129] Furthermore, we have established that the IDTCF molecules have poor packing attributed to the out-of-plane methyl substituents, which could lead to recombination issues. One technique to probe the recombination mechanism is to look at the light intensity dependence of both J_{SC} and V_{OC}. It has been established that the slope value (m) of the light intensity plots can help elucidate the key recombination mechanisms present in the solar cell.[130] For example, in a semi-log plot of V_{OC} vs. light intensity, a slope of 1 kT/q indicates that bimolecular recombination is the major loss mechanism under open-circuit conditions. Values less than 1 kT/q signify surface recombination,[131,132] and as the slope approaches 2 kT/q, trap-assisted recombination becomes the dominant recombination mechanism.[133,134] In **Figure 2.10b**, the slopes for both the FTAZ:IDIC and FTAZ:IDTCF blends are very close to 1 kT/q, which indicates that bimolecular is dominant in terms of non-geminate recombination mechanisms. Next, J_{SC} is known to have a power law dependence on light intensity, such that the slope of the log-log plot of J_{SC} vs. light intensity indicates the strength of bimolecular

recombination under short-circuit conditions. When the slope is close to unity, only weak

bimolecular recombination is present, which is what we find for both FTAZ:IDIC and

FTAZ:IDTCF blends in **Figure 2.10a**. Consequently, the light intensity data in **Figure 2.10**

illustrate that both IDIC and IDTCF containing blends have very similar and low bimolecular

recombination. This unexpected result suggests that the issue may be with geminate

recombination, which will be further explored with photoluminescence studies.
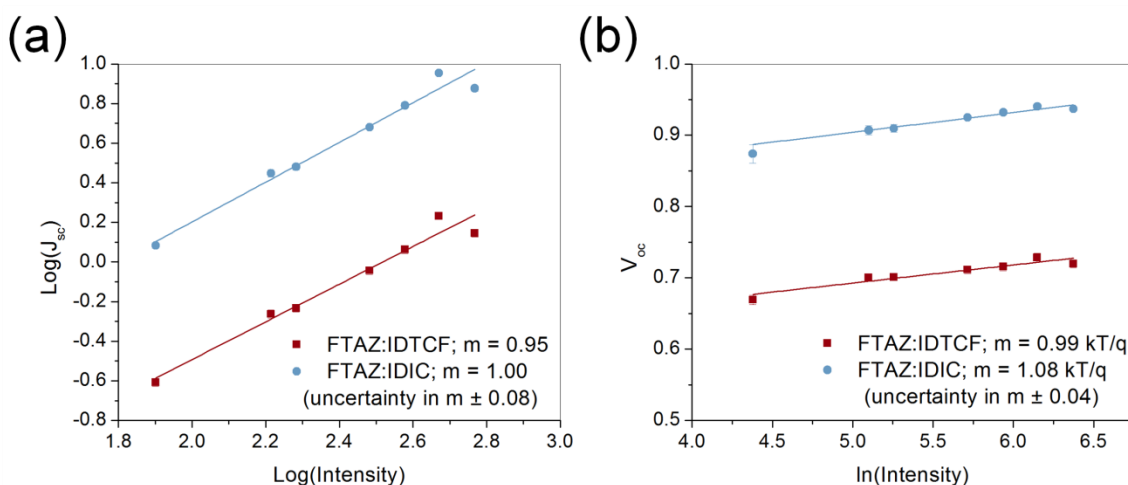
Figure 2.10 – Light intensity dependence of (a) short-circuit current and (b) open-circuit voltage for both FTAZ:IDIC and FTAZ:IDTCF blends

To explore the charge transfer from FTAZ to the acceptors, we measured the

photoluminescence (PL) quenching of each blend (**Figure 2.11**). Both IDIC (**Figure 2.11a**)

and IDTCF (**Figure 2.11c**) are able to quench the photoluminescence of FTAZ nearly

completely (>95%), indicating efficient exciton dissociation in both blends. This suggests

that a key step in charge generation, from exciton to the charge transfer (CT) state, is not a

major issue in either the IDIC- or IDTCF-based device when FTAZ absorbs the incident

photon. However, we cannot rule out the possibility of losing mobile charge carriers due to

loss mechanisms including recombination to the ground state from the CT state.
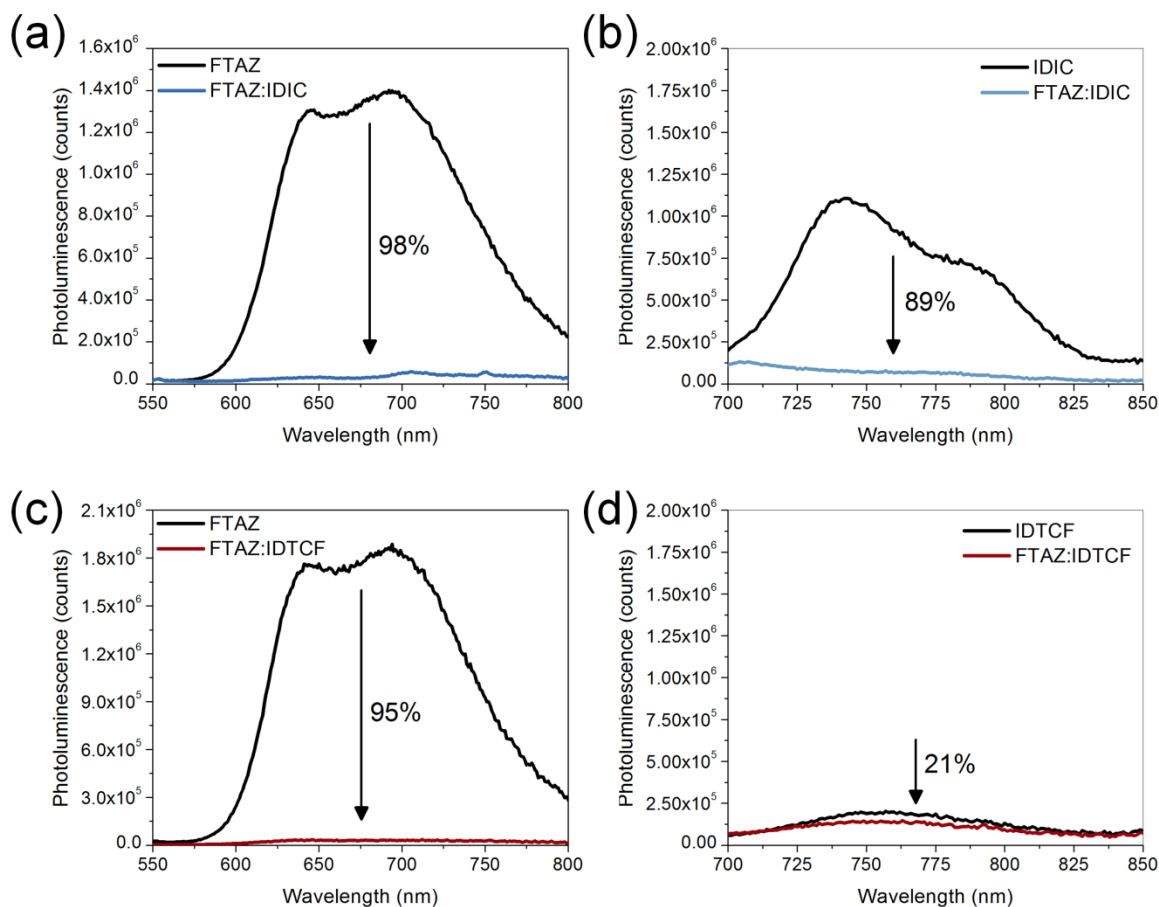
Figure 2.11 – (a) Photoluminescence (PL) of neat FTAZ and FTAZ:IDIC blend films excited at 500 nm, (b) PL of neat IDIC and FTAZ:IDIC blend films excited at 650 nm, (c) PL of neat FTAZ and FTAZ:IDTCF blend films excited at 480 nm, (d) PL of neat IDTCF and FTAZ:IDTCF blend films excited at 650 nm

Next, as both IDIC and IDTCF play a role in absorbing incident photons and thus generating excitons, we explore the charge transfer from the acceptors to FTAZ through photoluminescence quenching as well. Unlike the previous case, there is a distinct difference in the PL quenching when looking at the acceptor excitation. To begin with, in the FTAZ:IDIC case (**Figure 2.11b**) there is strong quenching of the IDIC fluorescence by FTAZ (~90%). However, for FTAZ:IDTCF (**Figure 2.11d**) there is very poor quenching of the IDTCF fluorescence (~20%). It is important to note that the overall PL of IDTCF is lower in **Figure 2.11** because of the excitation wavelength. For the excitation of the acceptor, a

higher wavelength was needed to avoid any absorbance of the incident photons by FTAZ, therefore, just a shoulder of IDTCF was excited. The neat films of both IDIC and IDTCF display strong PL when excited at a more optimal wavelength, as demonstrated by their similar photoluminescence quantum efficiency (PLQE), which will be explored further in the next section. Most importantly, the inability of FTAZ to quench the photoluminescence of IDTCF suggests that geminate recombination is a major issue in the FTAZ:IDTCF blend.

We also measured the PLQE for each of the materials. The PLQE is the quantum efficiency for the photoluminescence process (i.e., number of photons emitted/number of photons absorbed). In the case of neat IDIC and IDTCF, both have similar PLQE around 3%, as shown in **Table 2.4**. These values are appropriate for similar organic materials. Neat FTAZ films also have strong PL, but even lower PLQE (0.3%). The PL spectra for each are shown in **Figure 2.12**. When looking at the blend films, FTAZ:IDIC has no PLQE, which further illustrates the strong quenching of FTAZ PL by IDIC; however, in the case of FTAZ:IDTCF, a PLQE similar to that of neat FTAZ is found (0.4%). This agrees with the poor quenching observed in the previously discussed PL experiments, and indicates that there may be an issue with charge transfer in the FTAZ:IDTCF system, which could lead to increased geminate recombination.

Table 2.4 – Photoluminescence Quantum Efficiency (PLQE) Summary – excited at 532 nm

	FTAZ:IDIC	**FTAZ:IDTCF**	**FTAZ**	**IDIC**	**IDTCF**
PLQE	0.0%	0.4%	0.3%	3.3%	3.0%
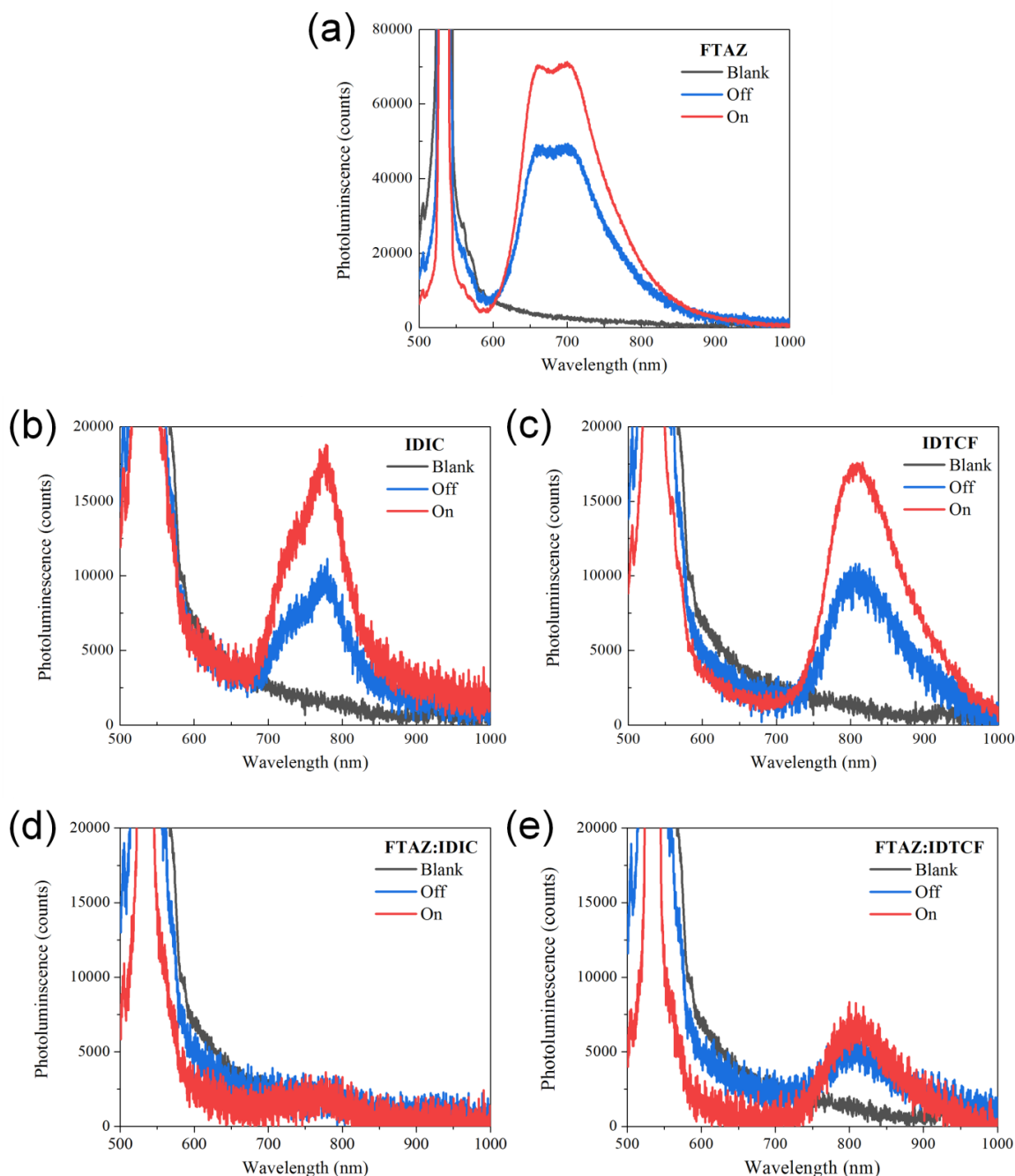
Figure 2.12 – (a) PL spectra of neat FTAZ excited at 532 nm, (b) PL spectra of neat IDIC excited at 532 nm, (c) PL spectra of neat IDTCF excited at 532 nm, (d) PL spectra of FTAZ:IDIC blend film excited at 532 nm, (e) PL spectra of FTAZ:IDTCF excited at 532 nm

Note: Quantifying PLQE requires three measurements: (1) in the ***blank*** experiment the laser is directed into the integrating sphere with no sample mounted (2) in the ***off*** experiment the sample is excited indirectly by the light scattered from the integrating sphere wall (3) in the ***on*** experiment the sample is excited directly by the laser beam

Through these photoluminescence experiments (summarized in **Table 2.5**), we have identified that geminate recombination may be a major issue for the FTAZ:IDTCF system. Therefore, while both FTAZ and IDTCF have the ability to absorb incident photons and generate excitons, there is not much interaction between the two materials, likely caused by the sterics of the IDTCF acceptor. Due to this lack of interaction, the excitons are more likely to undergo geminate recombination rather than splitting into free charge carriers, which would contribute to the much lower J_{sc} and *FF* measured for the IDTCF-based devices.

Table 2.5 – Summary of photoluminescence studies

Blend	Photoluminescence quench efficiency @ donor excitation	Photoluminescence quench efficiency @ acceptor excitation	Photoluminescence Quantum Efficiency (PLQE)
FTAZ:IDIC	97.7 %	89.4 %	0.0 %
FTAZ:IDTCF	95.5 %	21.1 %	0.4 %

The poor packing and interaction observed in the FTAZ:IDTCF system can also have an effect on the charge transport in the device. To explore the charge transport properties of these materials, we measured the mobility of the blends via the space charge limited current (SCLC) method. We have previously studied the hole and electron mobility for the FTAZ:IDIC blend, which were measured to be 1.5×10^{-4} and 2.6×10^{-5} cm^2 V^{-1} s^{-1}, respectively.[1] For the IDTCF-based blend, hole- and electron-only devices were fabricated with the structure of ITO/PEDOT:PSS/FTAZ:IDTCF/MoO$_3$/Al and ITO/ZnO/FTAZ:IDTCF/Ca/Al, respectively. The hole mobility of the FTAZ:IDTCF blend was measured to be 7.9×10^{-6} cm^2 V^{-1} s^{-1}, which is over two orders of magnitude lower than the hole mobility generally observed for FTAZ-based blends.[1–4,6,7,9,135,136] Recall that the GIWAXS results found that IDTCF disrupts the packing of the FTAZ chains as seen by the larger (010) peak in the blend film. This effect will directly hinder the hole transport and

would contribute to the low J_{SC} value observed for the FTAZ:IDTCF device. For the electron mobility, the measured dark current was extremely low, and a mobility value was not able to be determined (i.e., could not reach SCLC range). This implies that the electron transport is even more hindered than the hole transport, and the actual mobility value is likely of an even lower order of magnitude ($< 10^{-6}$ cm^2 V^{-1} s^{-1}). The poor electron transport could be due to the disrupted packing of IDTCF molecules, stemming from the steric hindrance imparted by the methyl groups on the TCF unit.
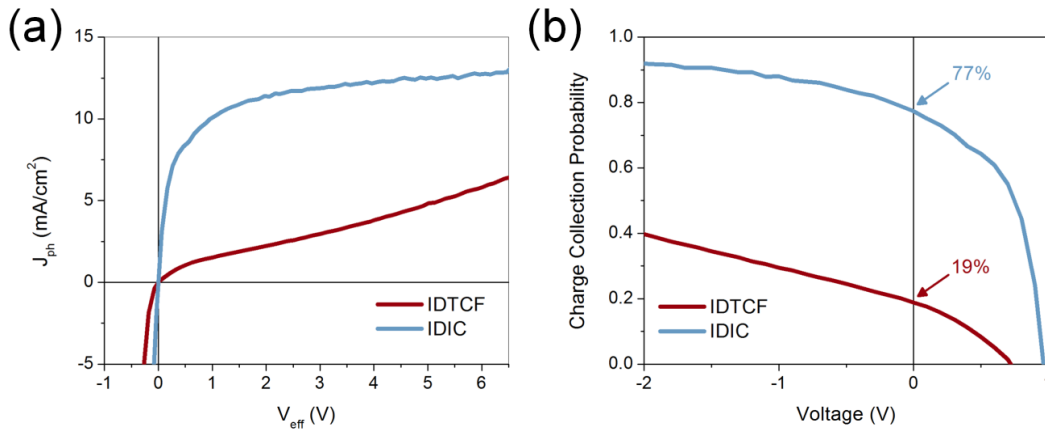
Figure 2.13 – (a) Photocurrent density and (b) charge collection probability (P(E,T)) of FTAZ:IDIC and FTAZ:IDTCF based solar cells

Finally, we studied the charge collection by looking at the charge collection probability (P(E,T)) for each blend (**Figure 2.13**). Experimentally, the photocurrent density (J_{ph}) was first measured as a function of the effective voltage (V_{eff}) (**Figure 2.13a**).[137] The photocurrent density is defined as the difference between the current densities in the dark and under illumination. The charge collection probability can then be calculated by dividing J_{ph} by the saturation photocurrent ($J_{ph,sat}$). From **Figure 2.13a**, it is clear that for the IDTCF-based device, the photocurrent continues to rise (i.e., doesn't saturate) even at high voltages (> 6 V), suggesting that charges are still being extracted. Generally, at higher applied

voltages all generated excitons would split into free charge carriers which are subsequently collected at the electrodes, leading to a saturation of the photocurrent. The fact that charges are still not completely extracted at such high voltage values for the FTAZ:IDTCF device demonstrates the poor charge transfer that occurs in the devices containing IDTCF as an acceptor, which we have previously highlighted as a major issue in this system. Additionally, at the short-circuit condition, the IDIC-based device has a much higher P(E,T) than that of the IDTCF-based device, 77% vs. 19%, respectively (**Figure 2.13b**). These results indicate that the charge collection process is far more efficient in the IDIC system. There have been multiple works that explore the effect of charge collection on device performance, and it has clearly outlined that issues with charge collection results in V_{OC} loss.[133,138–140] Therefore, the low charge collection probability observed for the FTAZ:IDTCF device can also help explain the lower V_{OC} measured for this system compared to FTAZ:IDIC.

2.3 Conclusion

In summary, a hindered fused-ring electron acceptor, IDTCF, was developed to probe the impact of sterics at the acceptor end groups on the performance of non-fullerene acceptor (NFA) based BHJ solar cells. Compared to the control FREA of IDIC, IDTCF showed similar optical and electrochemical properties; however, the photovoltaic performance of IDTCF was ten times lower than that of IDIC. XRD, GIWAXS, and DFT calculations illustrated a difference in packing (π-π stacking) of these materials, and from a literature search of current high-performance FREAs, a common value of ∼ 3.5 Å was found for π-π stacking. GIWAXS measurements show that the IDTCF molecule has a larger π-π stacking distance of 4.40 Å compared to the 3.45 Å of IDIC. We identify geminate recombination and charge collection issues as the major mechanisms that cause the poor performance of the

FTAZ:IDTCF system. Overall, these experiments provide a good explanation for the superior performance of IDIC-based devices compared to IDTCF. Particularly, we illustrated the importance of planarity of the end group acceptor moieties of FREAs, as even a methyl substituent out of the plane is enough to disrupt the packing and drastically decrease the device performance. Ultimately, this is one of the first works to concretely establish planarity and close packing as part of the design requirements for non-fullerene acceptors.

2.4 Experimental Details

2.4.1 Synthesis of IDIC and IDTCF

Scheme 2.1 – Reaction scheme for the synthesis of IDIC and IDTCF
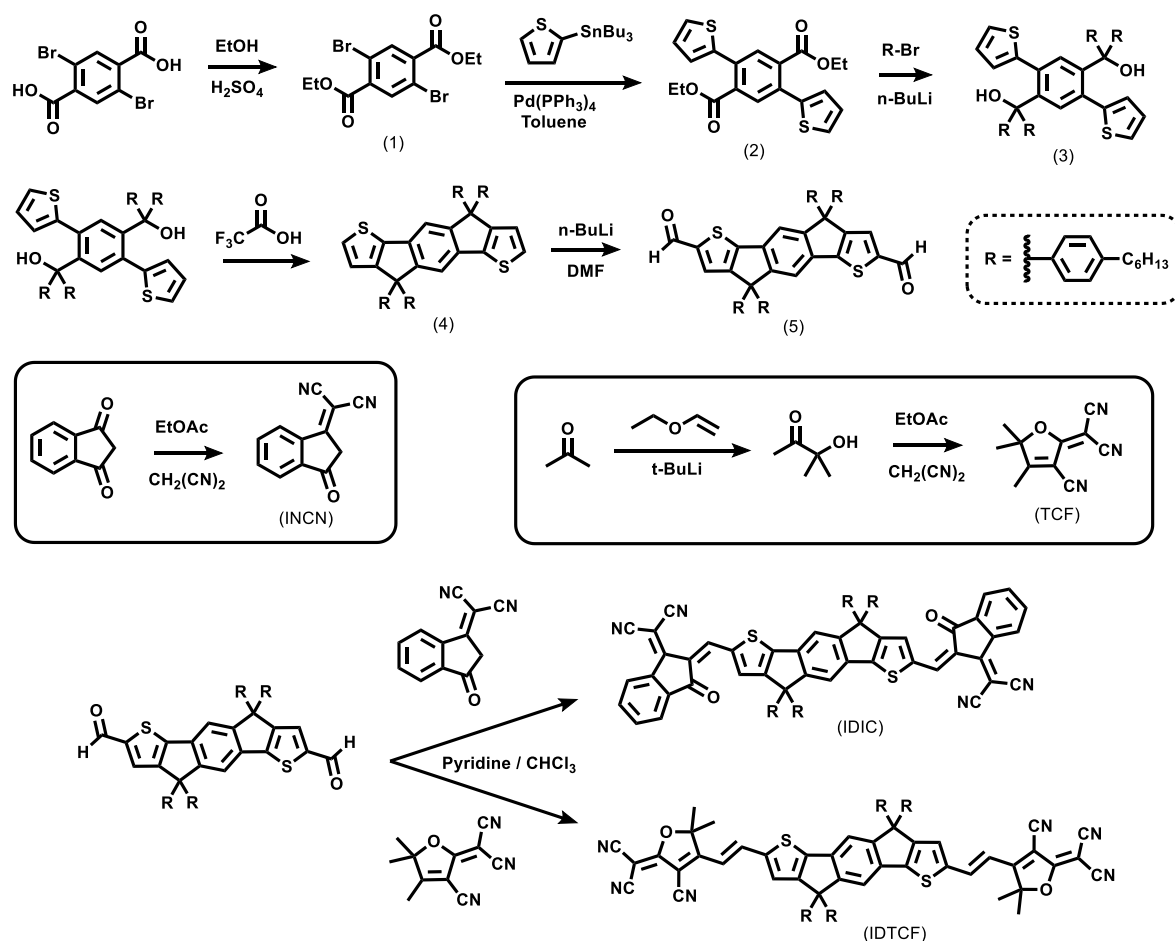
All chemicals were purchased from commercial source (Sigma-Aldrich, Fisher, Matrix, etc.) and were used as received except when specified. THF was distilled over sodium and benzophenone before use. For reactions under argon, the glassware was evacuated and refilled with argon for three times and charged with reactants.

Synthesis of Diethyl-2,5-dibromoterephthalate (**1**): Commercially available 2,5-dibromoterephthalic acid (1.0 eq, 46.3 mmol) was dissolved in ethanol (400 mL). Concentrated sulfuric acid (4.0 eq, 185.2 mmol) was added, and the resulting mixture was stirred under reflux for 3 days and then cooled to room temperature. The mixture was concentrated via rotary evaporation and run through a short silica plug with DCM as elutent. A white solid was collected after recrystallization in ethanol (yield = 69%). ^{1}H NMR (400 MHz, CDCl$_3$, ppm) δ: 8.02 (s, 2H), 4.42 (q, J=7.14 Hz, 4H), 1.42 (t, J=7.13 Hz, 6H). ^{13}C NMR (101 MHz, CDCl$_3$) δ: 164.07, 136.26, 135.57, 119.91, 62.19, 13.98.

Synthesis of Diethyl-2,5-di(thiophen-2-yl)terephthalate (**2**): To a solution of diethyl-2,5-dibromoterephthalate (1.0 eq, 10 mmol) and Pd(PPh$_3$)$_4$ (0.04 eq, 0.37 mmol) in anhydrous toluene (50 mL) was added 2-(tributylstannyl)thiophene (2.2 eq, 22 mmol). The reaction mixture was heated to reflux under argon atmosphere overnight before being cooled to room temperature. The mixture was poured into water (200 mL) and extracted with Et$_2$O (4 times, 100 mL each). The combined organic phase was washed with water and dried over MgSO$_4$. After concentration, column chromatography (1:1 DCM:hexane) was used to isolate the white solid (yield = 47%). ^{1}H NMR (400 MHz, CDCl$_3$, ppm) δ: 7.83 (s, 2H), 7.41 (dd, J=4.8, 1.4 Hz, 2H), 7.10-7.13 (m, 4H), 4.24 (q, J=7.2 Hz, 4H), 1.18 (t, J=7.2 Hz, 6H). ^{13}C NMR (101 MHz, CDCl$_3$) δ: 167.8, 138.2, 133.7, 133.2, 130.7, 128.6, 128.0, 127.6, 60.9, 14.1.

Synthesis of (2,5-di(thiophen-2-yl))-1,4-phenylene)bis(bis(4-hexylphenyl)methanol)

(**3**): The reactive side chain was first prepared by slowly adding 2.5 M *n*-butyllithium in hexane (5.4 eq, mmol) to a solution of 1-bromo-4-hexylbenzne (5.4 eq, 18.6 mmol) and anhydrous THF (20 mL) at −78 °C. The flask was kept stirring at −78 °C in a dry ice/acetone bath for 2 hours. Diethyl-2,5-di(thiophen-2-yl)terephthalate (1.0 eq, 3.4 mmol) was dissolved in anhydrous THF and the solution was added dropwise, under the protection of argon. The reaction vessel was slowly warmed to room temperature and stirred overnight. The reaction mixture was poured into water and extracted with ethyl acetate (3 times, 50 mL each). The combined organic phase was washed with water and dried over $MgSO_4$. The product was concentrated with rotary evaporation and no further purification was completed to the crude material.

Synthesis of 4,4,9,9-tetrakis(4-hexylphenyl)-4,9-dihydro-s-indaceno[1,2-b:5,6-b']dithiophene (**4**): The crude product of compound 3 was charged into three-neck flask. After adding trifloroacetic acid (0.1 mL) in methylene chloride (10 mL), the mixture was stirred for 1 hours at room temperature. After pouring into water, the mixture was extracted with ethyl acetate (three times, 100 mL each). The combined organic phase was washed with water and dried over $MgSO_4$. After concentration, the resulting crude compound was purified by column chromatography (10:1 hexane:DCM) to give light yellow solid (yield = 60%). ^{1}H NMR (400 MHz, $CDCl_3$, ppm) δ: 7.42 (s, 2H), 7.23 (d, J=4.9 Hz, 2H), 7.15 (d, J=8.3 Hz, 8H), 7.04 (d, J=8.3 Hz, 8H), 6.99 (d, J=4.9 Hz, 2H), 2.59 – 2.50 (m, 8H), 1.37 – 1.24 (m, 28H), 0.91 – 0.83 (m, 4H). ^{13}C NMR (101 MHz, $CDCl_3$) δ: 156.05, 153.60, 142.81, 141.89, 141.68, 135.65, 128.48, 128.08, 127.72, 123.23, 117.69, 62.45, 35.39, 31.56, 31.16, 28.98, 22.43, 13.92.

Synthesis of 4,4,9,9-tetrakis(4-hexylphenyl)-4,9-dihydro-s-indaceno[1,2-b:5,6-b']dithiophene-2,7-dicarbaldehyde (**5**): In a dry round-bottomed flask, compound 4 (1.0 eq, 0.14 mmol) was dissolved in anhydrous THF (25 mL) and placed under an argon atmosphere. The solution was cooled to −78 °C with a dry ice/acetone bath and stirred while 2.5 M *n*-butyllithium in hexane (2.6 eq, 0.36 mmol) was added dropwise. The mixture was stirred for one hour at −78 °C, and then anhydrous DMF (10.0 eq, 1.38 mmol) was added dropwise. The reactant was warmed to room temperature and stirred overnight. The reaction mixture was poured into water (100 mL) and extracted with DCM (5 times, 50 mL each). The combined organic phases where washed with water and dried with $MgSO_4$ and concentrated. The resulting crude compound was purified by column chromatography (3:2 hexane:DCM) to give a yellow solid (yield = 61%). ^{1}H NMR (400 MHz, $CDCl_3$, ppm) δ: 9.83 (s, 2H), 7.65 (s, 2H), 7.59 (s, 2H), 7.11 (m, 16H), 2.56 (t, J=7.7 Hz, 8H), 1.62–1.53 (m, 8H), 1.36–1.26 (m, 24H), 0.87 (t, J=6.9 Hz, 12H). ^{13}C NMR (101 MHz, $CDCl_3$) δ: 182.52, 156.67, 154.87, 150.12, 145.94, 141.79, 140.21, 135.44, 131.65, 128.47, 127.48, 118.33, 62.34, 35.38, 31.53, 31.13, 28.93, 22.42, 13.91.

Synthesis of 2-(3-oxo-2,3-dihydro-1H-inden-1-ylidene)malononitrile (**INCN**): Indane-1,3-dione (1.0 eq, 13.7 mmol) and malononitrile (2.0 eq, 27.4 mmol) were dissolved in absolute ethanol (35 mL), and then anhydrous sodium acetate (1.3 eq, 17.8 mmol) was added while stirring. After 50 min, the mixture was poured into cold water (400 mL), and acidified to pH 1–2 by addition of the hydrochloric acid. The precipitate was filtered and recrystallized from glacial acetic acid (yield = 76%). ^{1}H NMR (400 MHz, $CDCl_3$, ppm) δ: 8.66 (d, J=7.8 Hz, 1H), 7.99 (m, 2H), 7.83-7.92 (m, 2H), 2.09 (s, 2H). ^{13}C NMR (101 MHz, $CDCl_3$) δ: 194.18, 165.69, 135.13, 125.51, 1.24.20, 111.48, 111.57, 78.67, 42.70.

Synthesis of 2-(3-cyano-4,5,5-trimethylfuran-2(5H)-ylidene)malononitrile (**TCF**):

Ethyl vinyl ether (1.4 eq, 14 mmol) was added to anhydrous THF (30 mL) under the

protection of argon. The mixture was cooled to −78 °C with a dry ice/acetone bath and stirred

while 2.0 M *tert*-butyllithium in heptane (1.2 eq, 12 mmol) was slowly added dropwise. The

reaction mixture was warmed to room temperature for 30 minutes, then cooled back to −78

°C with a dry ice/acetone bath. Dry acetone (1.0 eq, 10 mmol) was added via syringe and the

reaction mixture was allowed to slowly warm to room temperature overnight. A 20 mL

mixture of 1:1 methanol:water was added dropwise and then followed with 2 mL of

concentrated HCl. The reaction mixture was stirred under the protection of argon for 2 hours.

Afterwards, the reaction mixture was concentrated to orange oil. No further purification steps

where done on the hydroxy-ketone species. In a dry round bottom flask, malononitrile (2.0

eq, 20 mmol) and sodium ethoxide (1.0 eq, 10 mmol) where dissolved in anhydrous ethanol

(30 mL) under the protection of argon. After stirring for 2 hours, the crude product was

added and the reaction mixture stirred overnight. The reaction mixture was concentrated to a

dark orange sludge, which was neutralized with 6 M HCl (10 mL). The crude product was

washed with water (10 mL) and collected via filtration. The pale yellow solid was washed

with minimal amounts of water and dried in the oven overnight (yield = 66%). ^{1}H NMR (400

MHz, CDCl$_3$, ppm) δ: 2.36 (s, 3H), 1.63 (s, 6H). ^{13}C NMR (101 MHz, CDCl$_3$) δ: 182.48,

175.15, 110.99, 110.36, 108.94, 104.83, 99.73, 24.39, 14.19.

Synthesis of 2,2'-((2Z,2'Z)-((4,4,9,9-tetrakis(4-hexylphenyl)-4,9-dihydro-s-

indaceno[1,2-b:5,6-b']dithiophene-2,7-diyl)bis(methaneylylidene))bis(3-oxo-2,3-dihydro-1H-

indene-2,1-diylidene))dimalononitrile (**IDIC**): INCN (6.9 eq, 0.38 mmol) was added into the

mixture of compound 5 (1.0 eq, 0.06 mmol) in chloroform (15 mL) and pyridine (0.5 mL)

mixture; the reactant was purged with argon for 30 min and then refluxed overnight. After cooling to room temperature, the reaction was poured into methanol and the precipitate was filtered off. The crude product was purified by column chromatography (2:1 chloroform:hexane) to give a metallic purple solid (yield = 75%). ^{1}H NMR (400 MHz, CDCl₃, ppm) δ: 8.90 (s, 2H), 8.69 (d, J=8.0 Hz, 2H), 7.92 (d, J=7.1 Hz, 2H), 7.80 – 7.69 (m, 8H), 7.16 – 7.09 (m, 16H), 2.58 (t, J=7.9 Hz, 8H), 1.60 (m, 8H), 1.32 – 1.26 (m, 24H), 0.90 – 0.86 (m, 12H). ¹³C NMR (101 MHz, CDCl₃) δ: 188.21, 180.83, 160.42, 158.92, 157.79, 157.77, 142.19, 141.30, 140.15, 138.30, 136.93, 136.71, 135.07, 134.36, 128.61, 127.47, 69.28, 62.82, 35.39, 31.55, 31.13, 29.54, 28.91, 22.42, 13.93. Mass Spec: $C_{90}H_{83}N_4O_2S_2$ $[M+H]^+$, m/z = 1315.59157, mass error = –2.8 ppm.
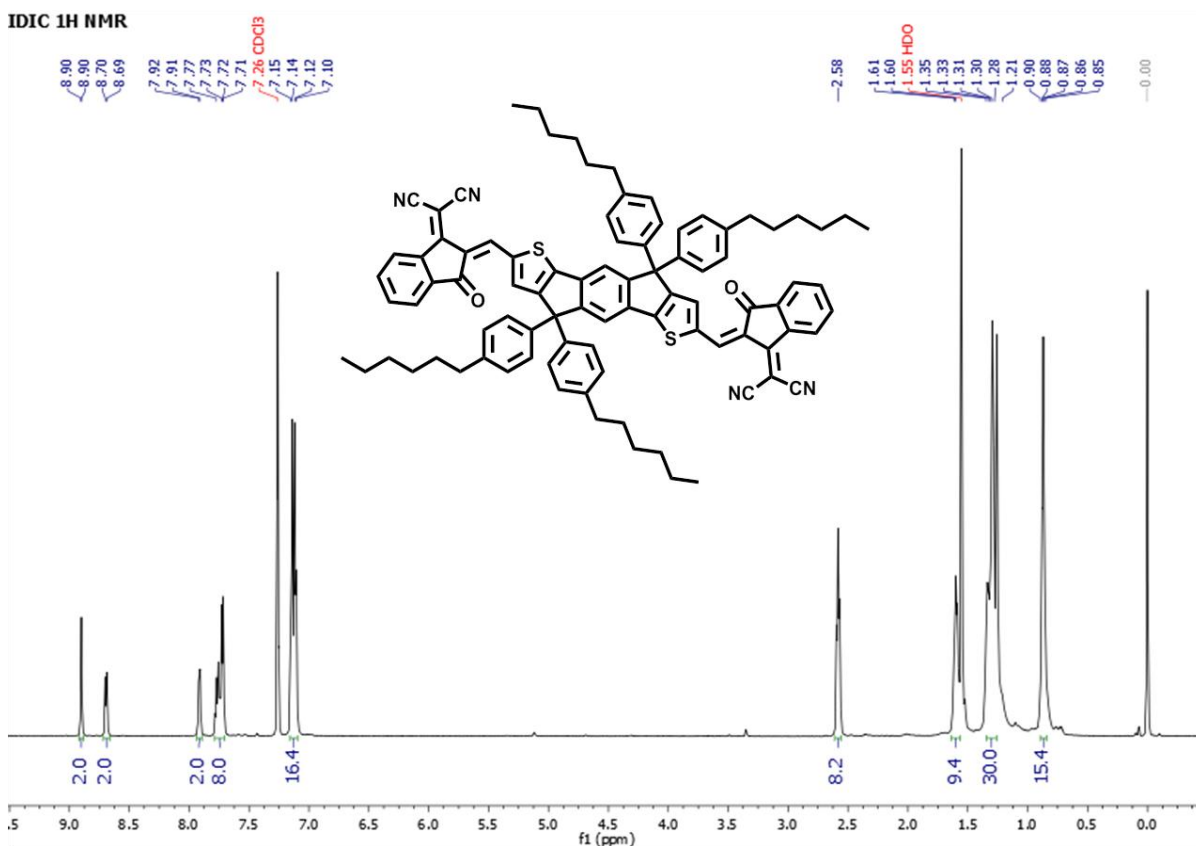
Figure 2.14 – ^{1}H NMR for IDIC

59

Synthesis of 2,2'-(((1E,1'E)-(4,4,9,9-tetrakis(4-hexylphenyl)-4,9-dihydro-s-indaceno[1,2-b:5,6-b']dithiophene-2,7-diyl)bis(ethene-2,1-diyl))bis(3-cyano-5,5-dimethylfuran-4(5H)-yl-2(5H)-ylidene))dimalononitrile (**IDTCF**): TCF (6.9 eq, 0.38 mmol) was added into the mixture of compound 5 (1.0 eq, 0.06 mmol) in chloroform (5 mL) and pyridine (15 mL) mixture; the reactant was purged with argon for 30 min and then refluxed for 48 hours. After cooling to room temperature, the reaction was poured into methanol and the precipitate was filtered off. The crude product was purified by column chromatography (chloroform eluting) to give a blue-purple solid (yield = 52%). ^{1}H NMR (400 MHz, CDCl$_3$, ppm) δ: 7.76 (d, J=15.9 Hz, 2H), 7.53 (s, 2H), 7.38 (s, 2H), 7.10 (m, 16H), 6.66 (d, J=15.8 Hz, 2H), 2.57 (t, J=7.8 Hz, 8H), 1.73 (s, 12H), 1.60 (m, 8H), 1.25 – 1.37 (m, 24H), 0.87 (t, J=6.9 Hz, 12H).^{13}C NMR (101 MHz, CDCl$_3$) δ: 194.12, 162.82, 144.95, 140.17, 138.21, 136.90, 134.71, 130.64, 128.77, 127.60, 94.66, 92.37, 69.14, 66.19, 50.20, 35.56, 31.70, 31.34, 29.10, 26.25, 22.60, 18.60, 14.10. Mass Spec: C$_{88}$H$_{89}$N$_6$O$_2$S$_2$ [M+H]$^+$, *m/z* = 1325.64624, mass error = −1.5 ppm.
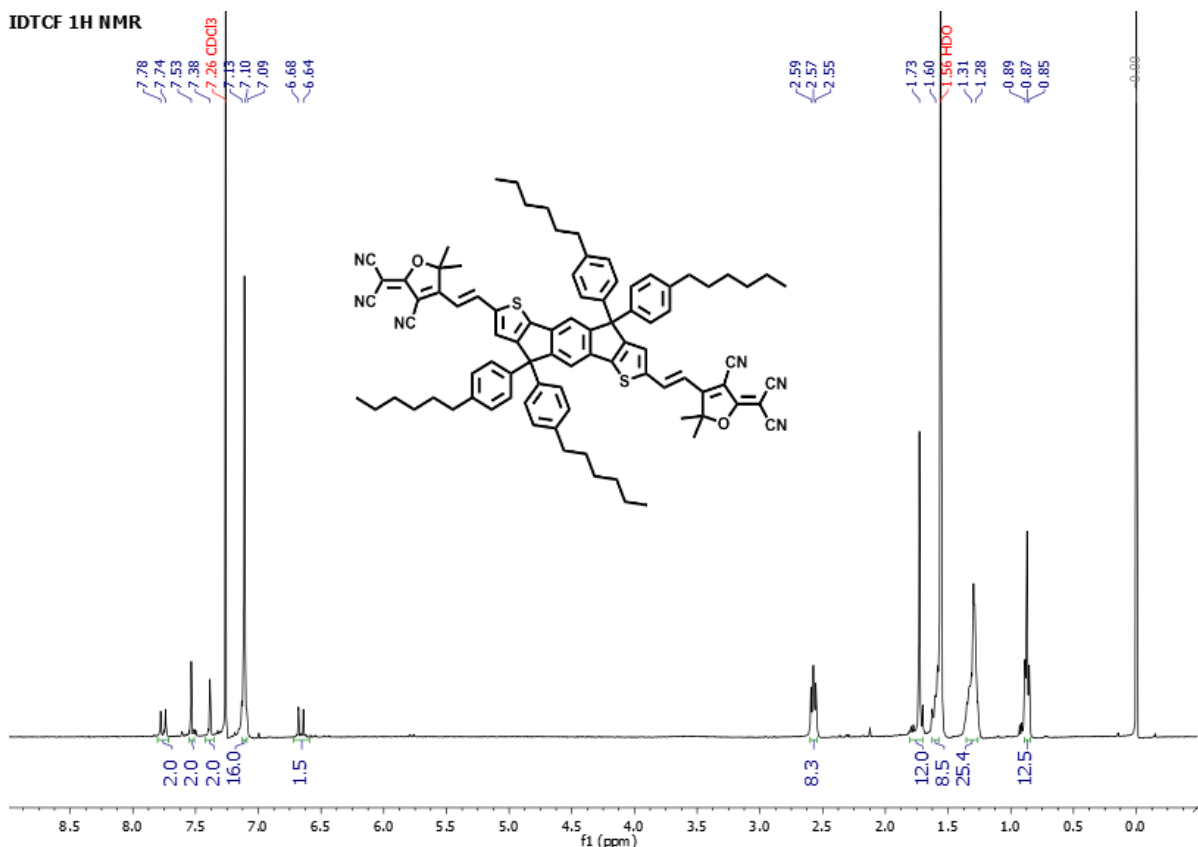
Figure 2.15 – ^{1}H NMR for IDTCF

2.4.2 Characterization Details

^{1}H and ^{13}C nuclear magnetic resonance (NMR) measurements were recorded with Bruker DRX spectrometers (400 MHz). Mass Spectrometry was run on a ThermoScientific Q Exactive HF-X mass spectrometer and analyzed via Xcalibur (ThermoFisher). UV-Visible absorption spectra were obtained with a Shimadzu UV-2600 spectrophotometer. A Rigaku SmartLab was used for high-resolution X-ray diffractometer (XRD) measurements.

CV measurements were carried out on thin films using a Bioanalytical Systems (BAS) Epsilon potentiostat with a standard three-electrode configuration. A three electrode cell of a glassy carbon working electrode, Ag/Ag$^+$ reference electrode, and Pt counter electrode were used. Films of the FREAs were drop-cast onto the glassy carbon electrode

from hot chloroform solution (2 mg/mL, with tetrabutylammonium hexafluorophosphate added at 100 wt%) and dried using a heat gun. 0.1 M solution of tetrabutylammonium hexafluorophosphate in anhydrous acetonitrile was used as a supporting electrolyte. Scans were carried out under argon atmosphere at a scan rate of 100 mV/s. The reference electrode was calibrated using a ferrocene/ferrocenium redox couple.

Solar cell devices were tested under AM 1.5G irradiation calibrated with an NREL certified standard silicon solar cell. Current density-voltage curves were measured via a Keithley 2400 digital source meter.

GIWAXS measurements were performed at beamline 7.3.3 [Ref 27] at the ALS. The 10 KeV X-ray beam was incident at a grazing angle of 0.13 degree. The scattered X-rays were detected using a 2D area detector (Pilatus 1M). All measurements were conducted under He atmosphere to reduce air scattering.

2.4.3 Device Fabrication

Solar cells were fabricated on glass substrates with patterned indium doped tin oxide (ITO). ITO substrates were cleaned via sonication in deionized water, acetone and isopropyl alcohol for fifteen minutes each, followed by UV-ozone treatment for 15 minutes. The ZnO precursor solution was prepared by dissolving 1 g of zinc acetate dihydrate and 0.28 g of ethanolamine in 10 mL of 2-methoxyethanol. The solution was stirred overnight, and then spun cast onto the cleaned ITO at 4000 rpm for 30 s, then baked at 150°C for 30 minutes in air. The substrates were then transferred into a nitrogen filled glovebox. FTAZ:Acceptor solutions (FTAZ:IDIC or IDTCF=1:1, 6 mg/mL FTAZ) in chlorobenzene were prepared and spuncast onto the ZnO. The solar cells were finished by evaporation of 10 nm MoO_3 and 70 nm of aluminum, with a device area of 13 mm^2.

CHAPTER 3: Controlling the Molecular Weight of Conjugated Polymers: Impact of Photovoltaic and Mechanical Properties [11,12]

3.1 Introduction

The previous chapters highlighted some important developments in fused-ring electron acceptors, along with some impressive solar cell efficiencies. The focus will now switch to the conjugated polymer electron donor which is paired with these electron acceptors. One of the key chemical structures which I have worked extensively on is a benzotriazole (abbreviated as TAZ) acceptor moiety. The TAZ building block has unique and highly tunable features which make it appropriate for use in organic solar cells. For example, solubilizing side chains can be added selectively on the N-2 position of the triazole which can allow for processability without inducing steric hindrance along the polymer backbone. The 5 and 6 positions (located on the "bottom" of the benzene farthest from the triazole) can be functionalized with a wide variety of substituents (such as fluorine, nitrogen and cyano) which can further tune the polymer properties.[141] One of our most successful

---

[11] Parts of this chapter previously appeared as an article in *ACS Applied Polymer Materials*. Reprinted with permission from © 2021 American Chemical Society. The original citation is as follows: Stephanie Samson, **Jeromy Rech**, Lorena Perdigón-Toro, Zhengxing Peng, Safa Shoaee, Harald Ade, Dieter Neher, Martin Stolterfoht, and Wei You. "Organic Solar Cells with Large Insensitivity to Donor Polymer Molar Mass across All Acceptor Classes." *ACS Applied Polymer Materials*, **2020**, 2 (11), 5300-5308.

[12] Parts of this chapter previously appeared as an article in *Chemistry of Materials*. Reprinted with permission from © 2021 American Chemical Society. The original citation is as follows: Nrup Balar, **Jeromy James Rech**, Reece Henry, Long Ye, Harald Ade, Wei You, and Brendan T. O'Connor. "The Importance of Entanglements in Optimizing the Mechanical and Electrical Perfromance of All-Polymer Solar Cells." *Chemistry of Materials*, **2019**, 31 (14), 5124-5132.

semiconducting materials is a copolymer with a benzodithiophene (BnDT) donor moiety and a fluorinated benzotriazole (FTAZ) acceptor moiety.[125,142] PBnDT-FTAZ (also commonly called FTAZ) achieved a high hole mobility on the order of 10^{-3} cm^{2}V^{-1}s^{-1}, and when paired with phenyl-C61-butyric acid methyl ester (PCBM), the resulting solar cell achieved over 7% efficiency. More recently with the advent of fused ring electron acceptors, FTAZ based solar cells have achieved over 13% efficiency.[143,144] A summary of some of the structural variations of the TAZ core we have reported is shown in **Figure 3.1**, along with the solar cell efficiencies published with PCBM.[13,14,125,135,136,141,145–148] We have also explored some of these materials with FREAs and achieved even higher efficiencies, but we want to include direct comparisons for each structural modifications, so a consistent control acceptor of PCBM was used for each of these blends.
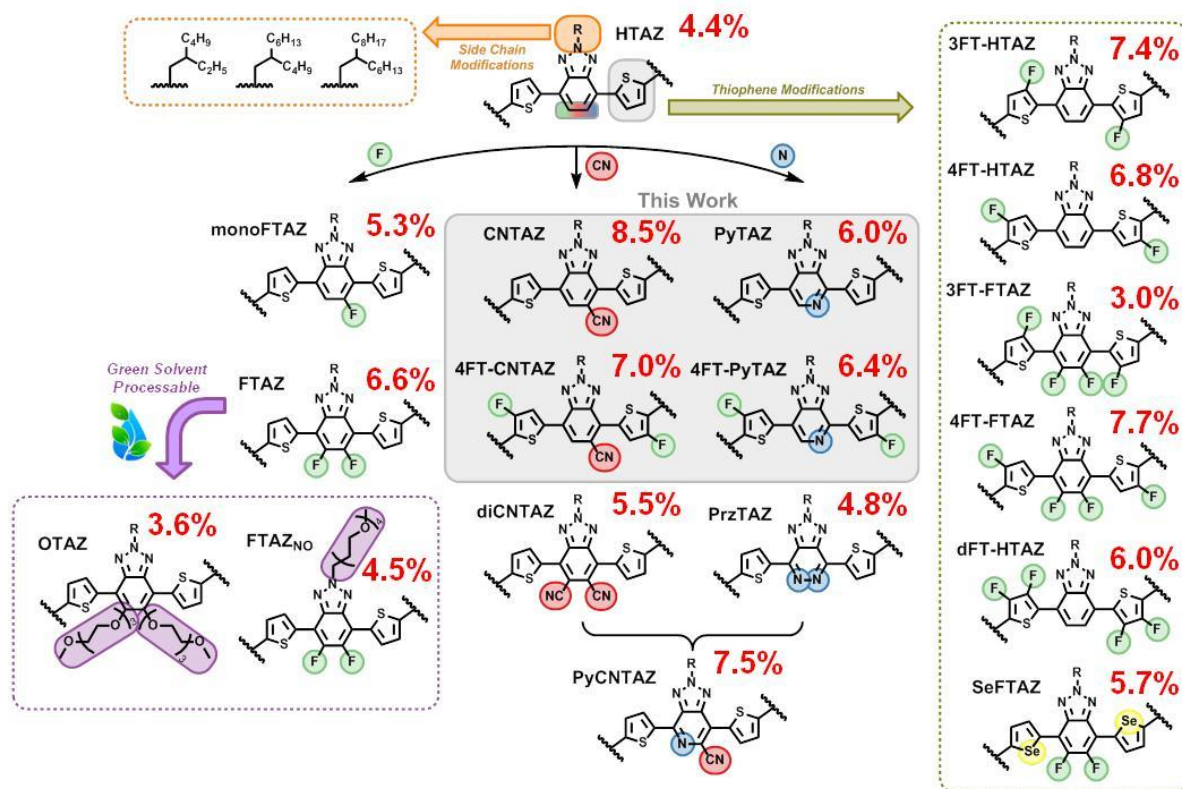
Figure 3.1 – Chemical structures of various TAZ-based acceptor moieties. Each was polymerized with the same BnDT donor moiety. The average PCE for polymer:PCBM blend is included in red.

The molecular weight of polymers is perhaps the most important property of a given polymer, which separates polymers from small molecules. Typically, a high molecular weight is required to impart polymers with desirable physical properties, such as thermal stability and mechanical strength.[149,150] Conjugated polymers for bulk heterojunction (BHJ) solar cells are no exception. It has long been recognized that the molecular weight (e.g., number average molar mass, M_n) of conjugated polymers in BHJ blends has a strong influence in the device performance of such solar cells.[151–154] The M_n of donor polymers affects both the donor properties (e.g., mobility,[155] absorbance,[12] and glass transition temperature[156]) and BHJ morphology[157] (e.g., domain size and composition,[155,158–160] structure,[161] and surface texture[162,163]). Moreover, the nature and severity of the effects of M_n of a given donor polymer on the performance of BHJ devices can vary from one system to the other when the nature of paring acceptor (as required by BHJ) is changed from fullerene derivatives, to non-fullerene based acceptors (including fused ring electron acceptors and polymer acceptors).[164,165]

These studies, regardless of the acceptor type, often found that there is some intermediate M_n range for the donor polymer which affords optimal photovoltaic properties, with performance falling off as a consequence of suboptimal morphology.[153,155,159,166–169] In addition, this optimal M_n range is dependent not only on the chemical nature of the donor polymer, but also on the acceptor that is paired with the specific donor in a BHJ blend. For example, consider BHJ OSCs utilizing the prototypical donor polymer, poly(3-hexylthiophene) (i.e., P3HT). When $PC_{61}BM$ (a fullerene derivative) was used, the maximum power conversion efficiency (PCE) of such BHJ devices was found at a M_n of ~30 kg/mol for P3HT.[153,166–168] In cases where a FREA acceptor was used, the trend between the M_n of

65

P3HT and PCE can be similar, as with O-IDTBR, or very different, as with EH-IDTBR.[164] Furthermore, despite P3HT's ubiquity, there is no reported study on the effects of the M_n of P3HT on the BHJ system where P3HT was paired with a polymer acceptor, though such system had been reported as early as 2007.[170] In fact, to our knowledge, no studies have been done comparing the effects of M_n of the same donor polymer on BHJ solar cells across the three different types of acceptors from fullerene derivatives, to FREAs, to polymer acceptors. Such studies would disclose the differences and similarities of the impact of donor M_n across the three acceptor classes, and provide further insights on the fundamental reason why such differences and similarities would occur.

Throughout this chapter, we will discuss the polymerization conditions which allow for the control of the molecular weight of the conjugated polymer. Using FTAZ as a model polymer, the photovoltaic properties will be explored with fullerene (PCBM) and non-fullerene small molecule (ITIC) and polymer (N2200) acceptors. An in-depth investigation will reveal the trends in the common characterizes for an organic solar cell. Finally, the mechanical properties of an all-polymer solar cell blend (FTAZ:N2200) will be investigated. This will culminate in a comprehensive understanding of the molecular weight impact on relevant properties needed to create a light weight and mechanically robust FTAZ-based organic solar cell.

3.2 Controlling Molecular Weight during Polymerization

The polymerization of FTAZ (**Scheme 3.1**), along with other donor-acceptor copolymers, is a common step-growth polymerization which can be described by the Carothers equation. In order for the Carothers equation to effectively describe the polymerization, and thus predict the molar mass, both the monomers and palladium catalyst

must have very high purity and are recrystallized multiple times prior to use, as we described

in detail in our earlier work.[158] As there are two monomers, the Carothers equation can

control the molar mass by changing the monomer ratio (r; $0 < r \leq 1$); the extent of the

reaction (p) is assumed to be near completion (p = 0.993) based on our previous experiences.

Pleasingly, the measured M_n from high temperature gel permeation chromatography (HT-

GPC) is close to the theoretical molar mass (**Table 3.**). This observation not only verifies the

validity and success of using the Carothers equation in our case, more importantly, the

obtained series of FTAZ polymers with different yet controlled M_n offer an excellent system

for our study. All FTAZ polymers in this molar mass range are soluble in common

processing solvents of chloroform, chlorobenzene, and toluene (with the assistance of heat).
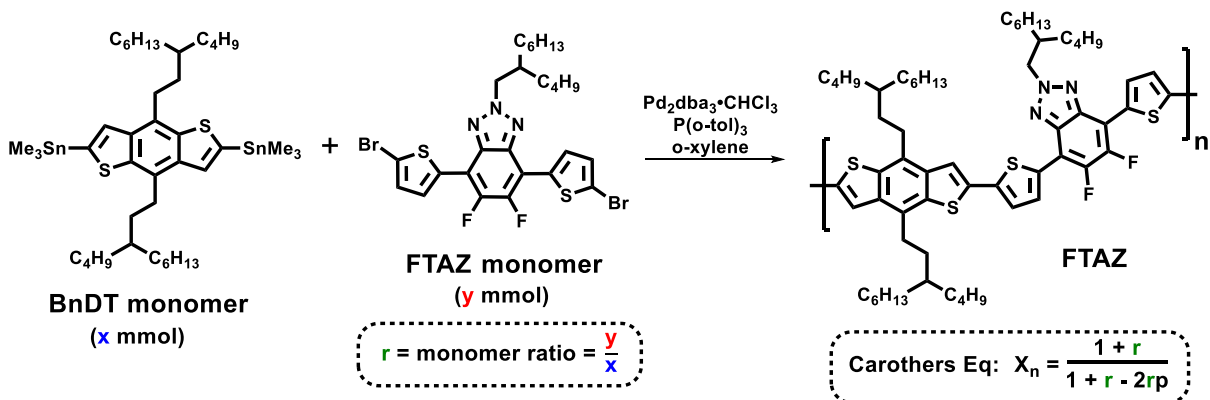
Scheme 3.1 – The polymerization reaction (Stille polycondensation) between the BnDT moiety and FTAZ moiety to form the donor FTAZ polymer. The molar mass is controlled via the Carothers equation, which depends on the ratios of the two monomers (r) and the extent of reaction (p), with the latter assumed to be near unity (p=0.993) in our case.

BnDT monomer (see below), FTAZ monomer (see below), Pd₂(dba)₃·CHCl₃ (1.9-2.0

mg, 0.002 mmol, 0.02 eq.) and P(o-tol)₃ (4.9-5.0 mg, 0.016 mmol, 0.16 eq.) were charged

into a 10 mL vial designed for microwave reactor. The mixture was evacuated and refilled

with argon for three cycles before addition of anhydrous o-xylene under an argon stream.

The reaction was heated up to 200 °C and held at that temperature for 10 min in a CEM

microwave reactor. After the polymerization, the crude polymer was dissolved in hot

chlorobenzene and precipitated into stirring methanol. The collected polymer was extracted

via a Soxhlet extractor with ethyl acetate, hexanes, and chloroform. The polymer solution in

chloroform was concentrated under reduced pressure/rotavap, and the polymer

was redissolved into a minimal amount of hot chlorobenzene and precipitated into methanol.

The polymer was then collected via vacuum filtration and formed a thin metallic golden

colored film, which was then dried under vacuum. Note: the molar mass of the polymer can

be controlled by tuning the ratio of the BnDT and FTAZ monomers, as shown in **Table 3.1**.

Table 3.1 – Measured FTAZ number-average molar mass and dispersity.

FTAZ	BnDT eq / mg		FTAZ eq / mg		Yield mg / %		M_n (kg/mol)	Đ
10K	1.20	79.4	1.0	48.5	80	100	**7.5**	2.02
30K	1.07	94.4	1.0	64.5	102	93	**28.5**	1.82
40K	1.04	91.5	1.0	64.5	105	98	**40.9**	1.96
60K	1.02	89.8	1.0	64.7	104	98	**60.1**	1.89
100K	1.01	88.9	1.0	64.5	105	100	**105.2**	1.94
120K	1.00	88.0	1.0	64.7	97	93	**116.9**	1.91

3.3 Correlating Molecular Weight and Solar Cell Performance

3.3.1 Overall Trends between Molecular Weight and Photovoltaic Properties

In order to determine the effect of donor M_n on the efficiency of our model

FTAZ:acceptor system, various BHJ blends were fabricated: (1) fullerene acceptor:

FTAZ:PCBM (1:2 w/w) with a device architecture of ITO/PEDOT:PSS/FTAZ:PCBM/Ca/Al,

with an active layer thickness of ~250 nm; (2) polymer acceptor: FTAZ:N2200 (1:1 w/w)

with a device architecture of ITO/ZnO/FTAZ:N2200/MoO₃/Al, with an active layer

thickness of ~110 nm; and (3) small molecule acceptor: FTAZ:ITIC (1:1 w/w) with the

device architecture of ITO/ZnO/FTAZ:ITIC/MoO₃/Al, with an active layer thickness of ~ 90

nm. The resulting photovoltaic characteristics under one-sun conditions are visualized in

Figure 3.2.
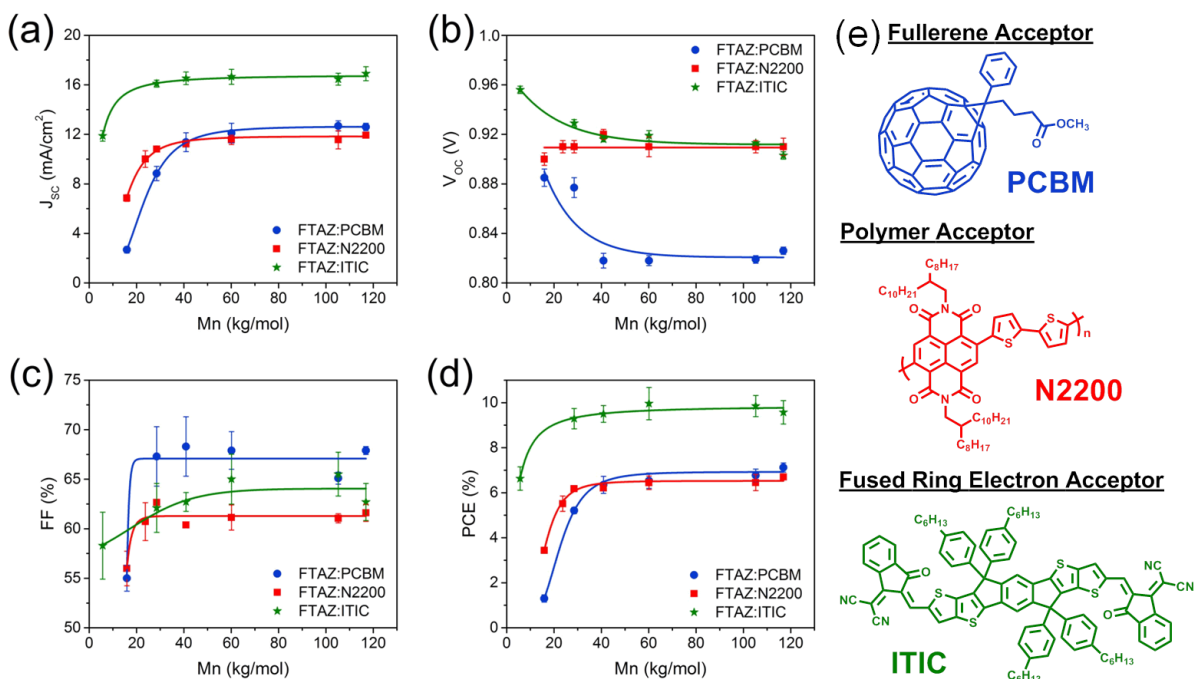
Figure 3.2 – Trends in photovoltaic figures of merit with increasing M_n for FTAZ:PC$_{61}$BM, FTAZ:N2200, and FTAZ:ITIC systems: (a) J_{SC}, (b) V_{OC}, (c) FF, and (d) PCE. The chemical structure for each electron acceptor is shown in (e). The exact same polymer batches of FTAZ were used for all three systems from 30K – 120K. The solid lines are guides to the eyes.

Overall, the power conversion efficiency (PCE), short-circuit current density (J_{SC}), open-circuit voltage (V_{OC}), and fill factor (*FF*) of devices are *insensitive* to changes in the M_n of FTAZ between ~30–100 kg/mol. The all polymer solar cell and fullerene blend exhibit similar efficiencies (~7%), but the FREA blend with ITIC can reach nearly 10%. However, at very low M_n, PCE, J_{SC}, and (to some extent) *FF* increase between 10 kg/mol and 30 kg/mol; in contrast, V_{OC} decreases in this range. To further understand the origin in these changes, an in-depth investigation into the device physics and morphology will be done on a model system of FTAZ:ITIC.

3.3.2 Why does low M_n FTAZ blends have lower J_{SC} and FF?

   To begin with, J_{SC} (**Figure 3.2a**) increases more than 30% between 10K and 30K

FTAZ then plateaus. In fact, the rather dramatic increase of J_{SC} from 10K to 30K is the

primary cause for the noticeably increased PCE from 10K to 30K. It is worth noting that this

trend is also previously observed in FTAZ:PC$_{61}$BM[158] and FTAZ:N2200[12] systems.

Absorption trends of the blend films can be found in **Figure 3.3**, where all systems show

similar and high attenuation coefficients. Previous measurements of neat FTAZ films reveal

slight increases in attenuation coefficient with increasing M_n; however, these differences are

not enough to account for the drastic change in J_{SC} beyond 30 kg/mol.[12] Furthermore,

external quantum efficiency (EQE) measurements show similar response profiles for all M_n;

however, the maximum response for the 10K polymer based BHJ device is only ~ 50% as

opposed to ~ 70% for higher M_n polymers, which is consistent with the observed J_{SC} trend

with the M_n.
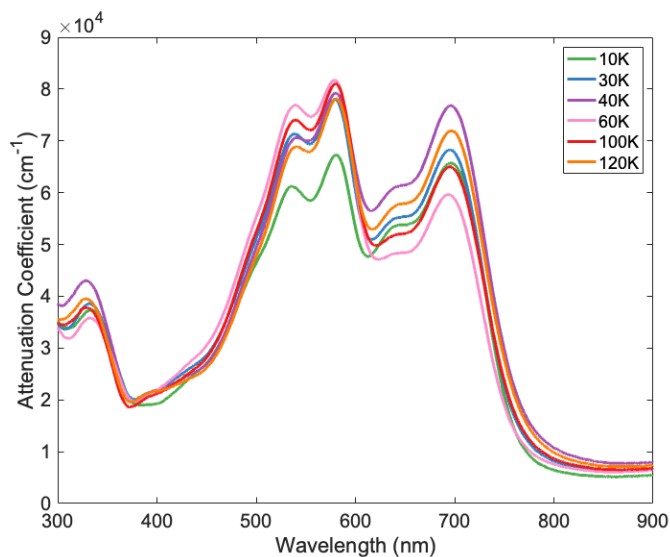
Figure 3.3 – Absorption spectra for FTAZ:ITIC blend films
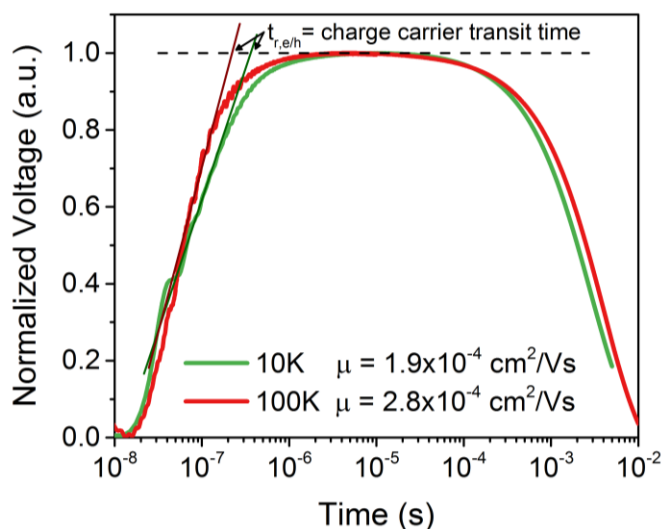
Figure 3.4 – Resistance dependent photovoltage measurements used to measure charge carrier mobility in the blend films. The transients indicate balanced transport.

Next, the *FF* (**Figure 3.2c**) also increases over the probed M_n range. Again, an increase is seen between 10K and 30K. Minor increases in *FF* are seen thereafter, with a slight decrease at very high M_n. We note that this increase in *FF* between 10K and 30K, also seen in previous studies on FTAZ,[12,158] cannot be strongly attributed to differences in mobility with M_n, because resistance dependent photovoltage (RPV)[171] (**Figure 3.4**) shows that mobility is only modestly affected by M_n (1.9×10^{-4} cm^2/V·s for 10K vs. 2.8×10^{-4} cm^2/V·s for 100K). This is consistent with previous studies.[12,158] Furthermore, the entanglement M_n as determined through elastic modulus measurements lies slightly below 30 kg/mol.[12] Though entanglement can hinder polymer crystallization,[167] it also increases the incidence of tie chains between crystalline domains.[151] These connections ensure charge transport between crystalline domains,[172] in line with our observed trends in mobility in this and in previous studies.[158] However, the increase in mobility between low and high M_n FTAZ alone is not enough to explain such a marked increase in J_{SC} and *FF* after 10K.

71
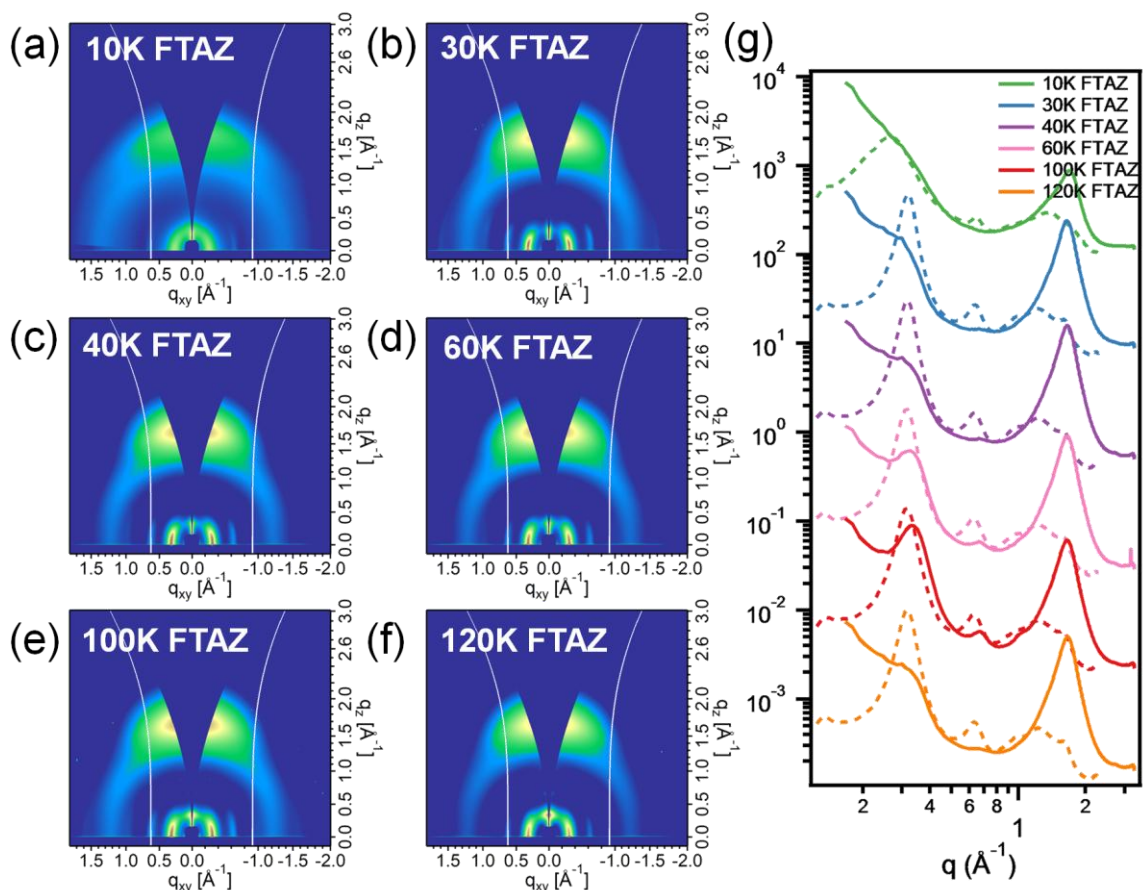
Figure 3.5 – (a-f) 2D GIWAXS patterns and (g) line-cuts out-of-plane (solid) and in-plane (dashed) for FTAZ films with M_n of (a) 10, (b) 30, (c) 40, (d) 60, (e) 100, and (f) 120 kg/mol.

As the OPV characteristics are heavily dependent on morphology,[173] we explored the bulk molecular packing and texture using synchrotron radiation-based grazing incidence wide angle X-ray scattering (GIWAXS) and resonant soft X-ray scattering (RSoXS). GIWAXS was used to extract molecular-scale morphological information both in and out of the sample plane,[174,175] and the collected scattering provides information such as π-π stacking distance, lamellar spacing, film texture, and crystallinity.[175] 2D GIWAXS patterns of neat FTAZ films (**Figure 3.5**) revealed relatively low crystallinity with a lamellar stacking peak at $q = 0.3$ Å^{-1} in-plane (corresponding to a spacing distance of 20.9 Å) and π-π stacking peaks at $q \sim 1.7$ Å^{-1} out-of-plane (corresponding to a spacing distance of 3.7 Å). Though

morphology was largely similar between the higher M_n FTAZ, the neat 10K FTAZ film is

markedly less ordered, indicative of less preferential packing. Moreover, the in-plane

stacking peaks are stronger for higher M_ns, suggesting an enhanced preference for the face-on

orientation.
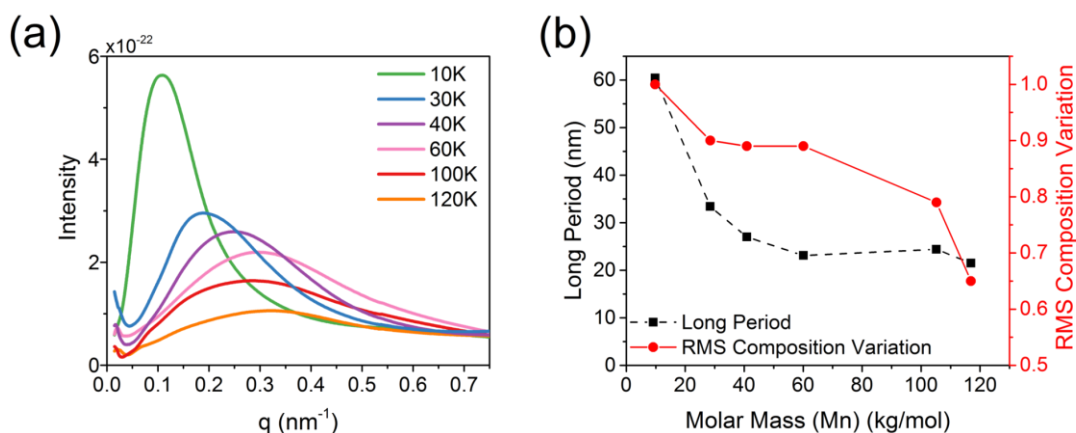
Figure 3.6 – (a) Thickness-normalized RSoXS profiles extracted at 283.4 eV and (b) long period (domain spacing) and RMS composition variation (domain purity) for FTAZ:ITIC blends with varying donor M_n.

As GIWAXS primarily probes molecular-scale contrast variations (particularly,

molecular packing), RSoXS was used to probe mesoscale morphological information in the

sample plane regarding overall domain characteristics.[176] Here, we extract the long period,

or center-to-center domain spacing, and the relative composition variations of the active layer

(formerly called domain purity). Using a representative blend of FTAZ:ITIC, by RSoXS each

different M_n FTAZ:ITIC blend demonstrated a single size distribution (**Figure 3.6a**). In

addition, long period and relative composition variations (**Figure 3.6b**) decreased with

increasing M_n. The 10K polymer blend had the largest domain spacing at ~ 60 nm, while

larger M_n polymers had domain spacings around ~ 20 nm. As exciton diffusion length is ~ 10

nm,[177] the large spacing in the 10K FTAZ batch hinders charge separation. Furthermore, the

relative composition variations show that the 10K blend has the purest domains. Because the

10K blend has both the largest and purest domains, this can result in reduced exciton splitting and will result in a large J_{SC} loss. In addition, domain purity is typically reflected in FF,[178] where excessively impure domains can lead to increased bimolecular recombination[117,179–181] and excessively pure domains can lead to isolated charge traps.[180] On the other hand, more mixed domains provide increased interfacial area and percolation pathways beneficial for charge separation and transport, affecting both J_{SC} and FF. The J_{SC} and FF of the 10K polymer is significantly lower than those of higher M_n polymers despite the high relative domain purity of 10K FTAZ blends. This suggests that the 10K blend's domains may be excessively pure, potentially limiting exciton separation into free carriers. The ultimate effect of the 10K blend's overly-large and pure domains is a reduced exciton dissociation efficiency, lowering J_{SC}. On the other hand, domain purity and spacing were remarkably similar for the intermediate M_n polymers, though domain purity decreased slightly for the largest M_n polymers. This may have contributed to the slight decrease in FF seen at very high M_n. The relatively strong phase segregation in very low M_n FTAZ blends was also observed in the FTAZ:$PC_{61}BM$ system but not in the FTAZ:N2200 system. We speculate that low M_n, particularly when the M_n below the entanglement M_n, could facilitate aggregation of the small molecular acceptors. In contrast, the use of a polymer acceptor may hinder the aggregation of the donor due to the chain entanglements of the acceptor. Despite differences at very low donor M_n, morphology for all three systems was reasonably invariant for a large range of moderate FTAZ M_n.

In summary, morphological studies reveal that the excessively large and pure domains present in 10K FTAZ blend devices contributed to the markedly low J_{SC} at low M_n. As M_n is increased to intermediate values between 30 kg/mol and 100 kg/mol, 2D GIWAXS patterns,

long period and relative composition variations become relatively constant. While morphological studies have provided insight into our observed J_{SC} and FF trends, the V_{OC} remains unexplained. A hint from the morphology measurements lies in the relative composition variations, as the domain purity affects recombination and thus V_{OC}. To clarify the V_{OC} trend, we turn to device physics measurements.

3.3.3 Why does low M_n FTAZ blends have higher V_{OC}?

Unlike J_{SC} and *FF*, V_{OC} (**Figure 3.2b**) appears to decrease with increasing M_n, with the most dramatic changes seen at low M_n, and at intermediate M_n, V_{OC} plateaus. V_{OC} is primarily dependent on the energy offset between the donor's highest-occupied molecular orbital (HOMO$_D$) and the acceptor's lowest unoccupied molecular orbital (LUMO$_A$), but it is also affected by recombination dynamics.[182,183] The bandgap of FTAZ is not affected by M_n as previously demonstrated by Li et al.[158] and confirmed here with cyclic voltammetry (CV) measurements (**Figure 3.7a**). Moreover, the bandgap of the BHJ blend obtained by EQE$_{PV}$ differentiation (dEQE/dE) does not apparently depend on the M_n of FTAZ (**Figure 3.7b**).
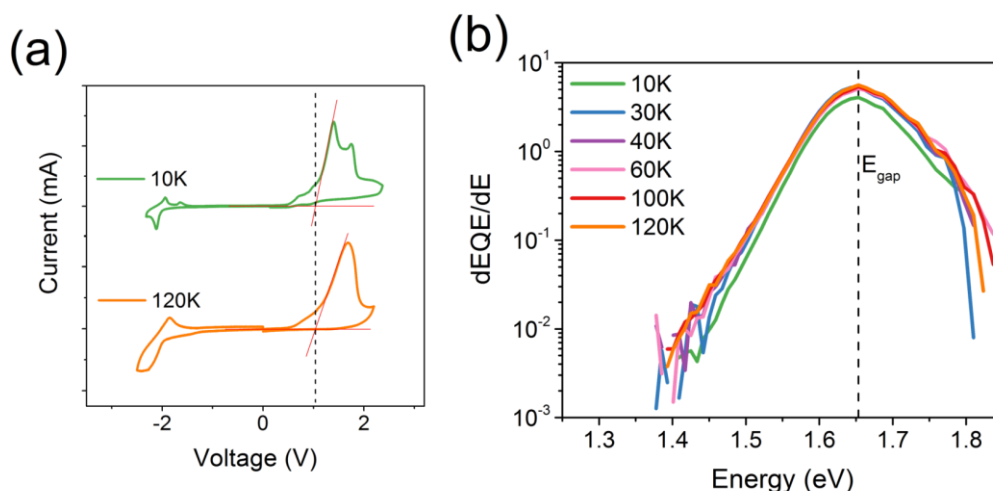
Figure 3.7 – Methods of FTAZ bandgap measurement, (a) cyclic voltammetry and (b) EQE$_{PV}$ derivative

In order to further investigate this V_{OC} loss, we probed recombination mechanisms of the devices, since the recombination losses typically account for the main loss of V_{OC}.[184] Recombination can be probed by measuring the dependence of J-V characteristics on light intensity. The J_{SC} may have a power law scaling with light intensity (I), $J_{SC} \propto I^{\alpha}$. For relatively low light intensities,[185,186] such as the one sun condition, α is typically between 0.9 and 1.[187] Ideally, $\alpha = 1$, signifying that carriers are swept out before recombination at short-circuit,[133] although this does not allow to exclude first-order recombination losses.[188] Nevertheless, $\alpha \sim 1$ means that recombination losses scaling with the second-order of the light intensity are absent.[185,186] On the other hand, V_{oc} can be described by the following equation:

$$V_{OC} = \frac{nkT}{q} \ln \left(\frac{J_{SC}}{J_0} + 1 \right) \qquad (\text{eq 3.1})$$

where kT is the thermal energy, q is the electric charge and J_0 is the dark saturation current density. Here, the ideality factor n accounts for the deviation from the ideal bimolecular recombination. Experimentally,[133] the slope of V_{OC} vs. $\ln(I)$ can be used to determine n, where I is the light intensity. A slope of unity (i.e., $n = 1$) typically indicates that the bimolecular recombination is dominant. Deviations from $n = 1$ indicate the presence of a competing recombination processes of different order. For example, $n \leq 1$ suggests the presence of surface recombination and that the V_{OC} saturates to the built-in voltage, $1 \leq n \leq 2$ implies a combination of bimolecular and trap-assisted recombination, and $n = 2$ indicates that trap-assisted recombination is dominant.[132,189]
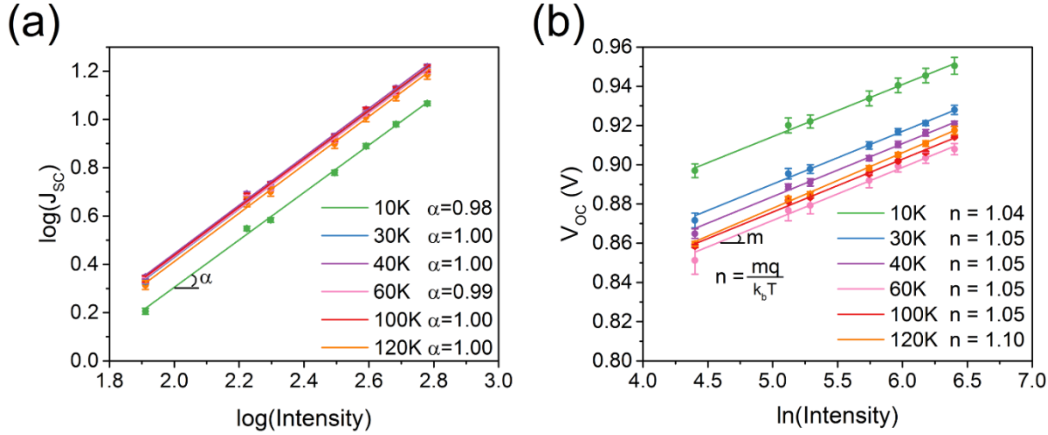
Figure 3.8 – Light intensity measurements for investigating recombination in FTAZ:ITIC blend films. (a) Log-log fitting of J_{SC} vs light intensity (W/m^2) to probe for deviations from weak bimolecular recombination. (b) Semi-log fitting of V_{OC} vs. light intensity (W/m^2) to determine recombination order.

In our system, from the log-log plot of J_{SC} vs. I (**Figure 3.8a**) and semi-log plot of V_{OC} vs. I (**Figure 3.8b**), α and n were found to be ~ 1 for all values of M_n, except for a slight increase in n for 120K FTAZ. This increase in n may have contributed to the slight decrease in FF observed for very high M_n and is also in line with the observed decrease in domain purity. Overall, the light intensity dependence of J_{SC} and V_{OC} indicates that bimolecular recombination is the dominant mechanism for all M_n blends, but it is relatively weak at J_{SC} conditions.
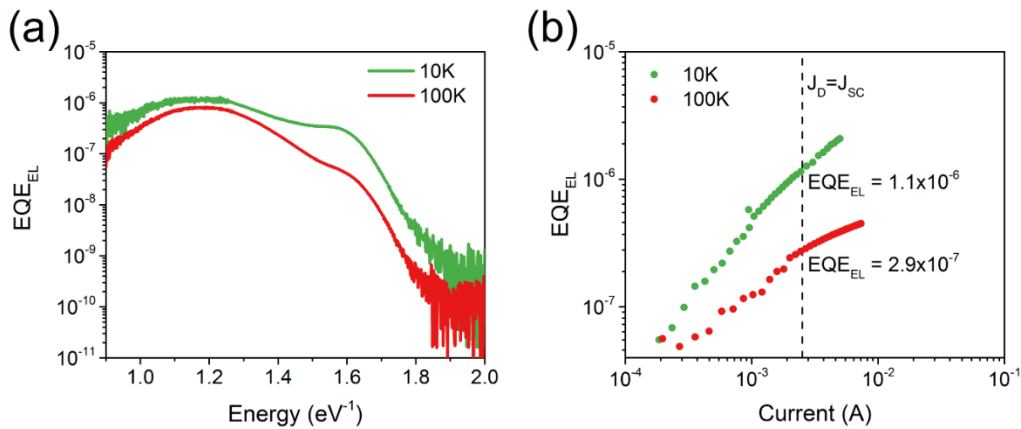
Figure 3.9 – Electroluminescence spectra of 10K and 100K FTAZ polymer blends (a) against photon energy and (b) against injection current. The EQE$_{EL}$ for energy loss calculations is taken at an injected current equivalent to the J_{SC} relevant to open-circuit conditions. The graph shows that the EQE$_{EL}$ is approximately ~3.8 smaller in the 100K FTAZ organic solar cell blend.

To further classify these V_{OC} losses (ΔV_{OC}) from recombination, we can divide ΔV_{OC} into unavoidable radiative ($\Delta V_{OC,rad}$) and avoidable non-radiative ($\Delta V_{OC,nr}$) losses. For this study, the ΔV_{OC}s of 10K and 100K FTAZ (i.e., the M_ns resulting in the lowest and highest PCEs, respectively) were explored. $\Delta V_{OC,nr}$ can be determined experimentally through EQE_{EL} (**Figure 3.9**) using

$$\Delta V_{OC,nr} = -\frac{kT}{q} ln(EQE_{EL}). \qquad (\text{eq 3.2})$$

EQE_{EL} is taken at an injected current such that $J_{inj}(V_{OC}) = J_{SC}$ as $\Delta V_{OC,nr}$ should be evaluated under conditions similar to open-circuit under illumination.[190] Furthermore, the V_{OC} can be calculated by first determining its value in the limit of only radiative recombination ($V_{OC,rad}$),

$$V_{OC,rad} = \frac{kT}{q} ln\left(\frac{J_{SC}}{J_{0,rad}} + 1\right), \qquad (\text{eq 3.3})$$

then subtracting the calculated $\Delta V_{OC,nr}$,

$$V_{OC} = V_{OC,rad} - \Delta V_{OC,nr} = \frac{E_{CT}}{q} + \frac{kT}{q} ln\left(\frac{J_{SC}h^3 c^2}{fq2\pi(E_{CT}-\lambda)}\right) + \frac{kT}{q} ln(EQE), \qquad (\text{eq 3.4})$$

where the first two terms in the rightmost expression comprise $V_{OC,rad}$.[191] $J_{0,rad}$ is the radiative current density in the dark due to the blackbody radiation and can be determined by extending the EQE_{PV} using the EL spectra (**Figure 3.10**).[192,193] Differences in the non-radiative losses account for the majority of the V_{OC} difference between the 10K and 100K FTAZ blends.

Table 3.2 shows that the 10K FTAZ blend has a lower $J_{0,rad}$ and higher EQE_{EL} than the 100K FTAZ blend, meaning that relatively high V_{OC} of the 10K FTAZ blend can thus be attributed to the reduced non-radiative losses using **Equation 3.4**
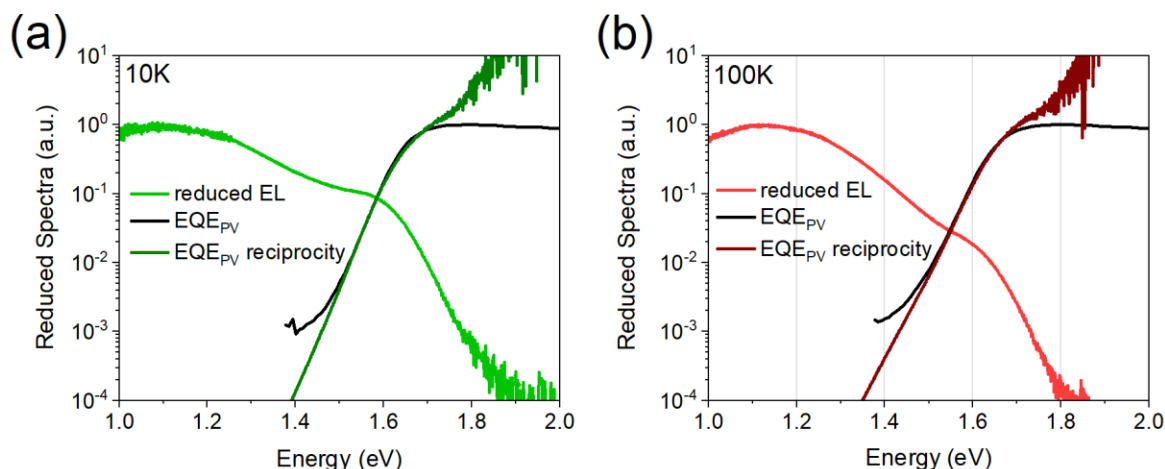
Figure 3.10 – Reduced EQE$_{PV}$ and EL spectra for determination of the charge transfer (CT) state, according to the work of Vandewal and coworkers.[190] Unfortunately, the CT energy could not be determined due to overlap with ITIC singlet emission (shoulder at ~1.6 eV).[194] EQE$_{PV}$ reciprocity is the extension of the spectrum from the calculation of EL/blackbody spectrum.

Table 3.2 – Parameters used for the calculation of energy losses based on measured EQE$_{EL}$.

FTAZ	J_{SC} (A/m^2)	$J_{0,rad}$ (A/m^2)	EQE$_{EL}$	$V_{OC, rad}$ (V)	$\Delta V_{OC,nr}$ (V)	V_{OC} (V) meas.	V_{OC} (V) calc.
10K	140	3.3×10^{-20}	1.1×10^{-6}	1.29	0.36	0.92	0.93
100K	170	1.5×10^{-19}	2.9×10^{-7}	1.26	0.39	0.90	0.87

Morphologically, the difference in V_{OC} losses may potentially stem from the large and relatively pure domains of the 10K FTAZ blends, where the decreased D:A interfacial area results in decreased radiative[195] and non-radiative[196] recombination. Voltage losses can also be related to the charge transfer state energy (E_{CT}) through **Equation 3.4**.[197] However, E_{CT} is difficult to determine due to overlap of the EQE$_{PV}$ with what we ascribe as the singlet emission from the FREA, ITIC at ~1.6 eV[194] (**Figure 3.10**). The appearance of a contribution from the singlet excitons in the electroluminescence spectra of both blends points to a significant hybridization between charge transfer states and the first excited singlet, which has been shown for a number of organic blends.[198] Hybridization results in

increased luminescence of the CT state and thereby a decrease in the non-radiative recombination losses.[198] In the case of the 10K and 100K FTAZ blends, the evidence of a stronger singlet "shoulder" in the EL (**Figure 3.9**) suggests a larger coupling to singlet excitons in the 10K FTAZ device, which according to the work of Eisner *et al.*,[198] explains the higher EQE_{EL} values obtained. As for the $J_{0,rad}$, **Figure 3.10** still suggests that E_{CT} could be at slightly higher energies in the 10K FTAZ blend, which could explain the lower $J_{0,rad}$ value and hence the slightly smaller radiative recombination losses.

3.4 Mechanical Properties in Polymer:Polymer Semiconducting Blends

From the previous section, the highest performance blend was FTAZ:ITIC, and this theme (i.e., use of a fused-ring electron acceptor) has recently been consistent throughout literature. However, while the performance values are high, blends with small molecule acceptors tend to exhibit poor thermomechanical stability,[199] due to either the diffusion of the acceptor into the bulk heterojunction, resulting in unstable morphology and thus leading to performance degradation, or the small molecule acts to vitrify the mixed amorphous domains resulting in mechanically brittle films.[200,201] However, BHJs with all-polymer blends (such as FTAZ:N2200) are expected to be morphologically stable, a characteristics associated with their macromolecular nature that limits diffusion. All-polymer films are also expected to be tougher due to the long aspect ratio of polymers allowing for the distribution of load across the length of the chains and through chain entanglements.[202] Based on the aforementioned qualities of all-polymer blends, blending two semiconducting polymers will likely result in a mechanically robust active layer. This has been generally observed, supported by reports that all-polymer solar cells (all-PSCs) exhibit improved mechanical properties compared to their polymer:FREA counterpart.[203,204] All-PSCs have also been

improving in performance with power conversion efficiencies (PCEs) exceeding 11%.[205] Thus, all-PSCs are a promising approach to achieve thermally and mechanically stable, high efficiency organic solar cells.

However, the improved mechanical behavior of the all-PSCs is not guaranteed and they can be mechanically fragile.[206] Mechanical failure may be due to a number of features including constituent polymers being glassy, poor intermolecular interactions, and unfavorable segregation behavior. The previously observed fragility was partially attributed to the low molecular weights (MWs) of the constituent polymers. The importance of MW on mechanical behavior has also been found in polymer–fullerene systems where Bruner and Dauskardt reported that the increase in the MW of P3HT significantly increased the fracture energy (G_c) of P3HT:PCBM BHJs.[207] However, increasing the MW of P3HT resulted in a drop in the power conversion efficiency. All-PSCs, on the other hands have been reported with a positive correlation between MW and PCE.[208] Inspired and motivated by these results, we attempt to understand the role of polymer MW on the mechanical behavior of all-PSCs.

3.4.1 Trends from Dynamic Mechanical Analysis

Dynamic Mechanical Analysis (DMA) is a powerful tool to study thermal transition temperatures associated with mechanical relaxations in polymers. It is particularly useful in the case of donor–acceptor-type conjugated copolymers, such as FTAZ, which do not show clear thermal transitions with the more commonly used differential scanning calorimetry (DSC). The storage modulus (E') and tan(δ) for the neat polymer films are given in **Figure 3.11**. In the DMA scans, there is a clear drop in E' for the FTAZ films near −25 °C for all MWs considered. Using the peak in tan(δ) to define this thermal transition, the FTAZ

samples exhibit transitions in the range of −26 to −20 °C with a marginal drop in the

transition temperature with an increase in MW. There is also a subtle thermal transition that

is more clearly observed in the low-MW samples at approximately 30 to 40 °C. Thus, we

consider the transition near −20 °C to be a sub-transition and label it as T_β and label the

transition near 40 °C as T_α in **Figure 3.11a**. For FTAZ, the cumulative drop in E' is relatively

small for a glass transition given its low crystallinity. There is also no clear MW dependence

of the thermal transitions, which is a common feature of a glass transition.[209,210] Thus,

neither transition fits a classical view of a glass transition, and the physical origin of the

observed thermal transitions represent a complex relaxation behavior that requires further

study outside the scope of this report. Similar to FTAZ, N2200 was found to have a thermal

transition at −21 °C. While the origin of the transition temperatures requires further study,

the fact that they are near or below room temperature shows that the films are viscoelastic at

room temperature, which gives the potential for significant toughness as long as the criterion

that sufficient intermolecular interactions are met.
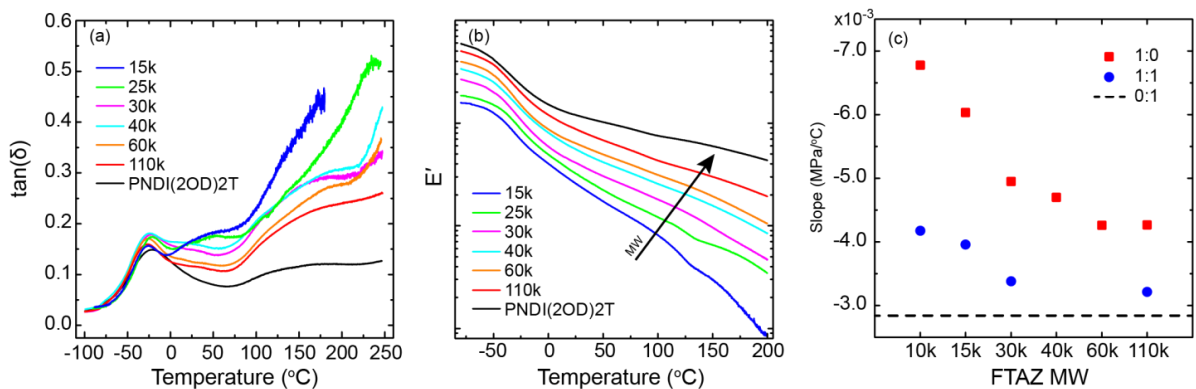
Figure 3.11 – (a) tan(δ) and (b) storage modulus of CB-dropcast neat FTAZ samples of different molecular weights and N2200 measured from the DMA temperature sweeps. (c) The slope of the semi log storage modulus vs. temperature plots of the neat and the blend samples.

The thermal transitions measured by the DMA can generally be divided into three

regions: (1) glassy region where the polymer chains are frozen and exhibit very little

movement, (2) transition region where the side chain or the polymer backbone relaxes, and (3) rubbery plateau where the polymer chains are very mobile. The length and the slope of the rubbery plateau is dependent upon entanglement of polymer chains where higher entanglement density of polymer chains restricts the drop in storage modulus (E') and flattens its temperature dependence. The change in E' of the neat FTAZ films are plotted in **Figure 3.11b**. The slope of the rubbery plateau for the different MW FTAZ films is given in **Figure 3.11c**, showing that there is a sharp drop in the slope with increasing MW from the 15k to the 30k films. With increasing MW there continues to be a drop in the slope but to a smaller extent. This suggests that the entanglement molecular weight for FTAZ is near ~30k. Similarly, we observe a decrease in slope of the rubbery plateau in the blend films with increasing MW as shown in **Figure 3.11c**, and the slopes in the rubbery plateau are lower than the neat FTAZ films owing to the presence of N2200. From the above observations, it can be argued that there is a very limited or absence of interchain interactions in the form of entanglement among the donor-donor and donor-acceptor polymer chains in the blend films with 10k and 15k.
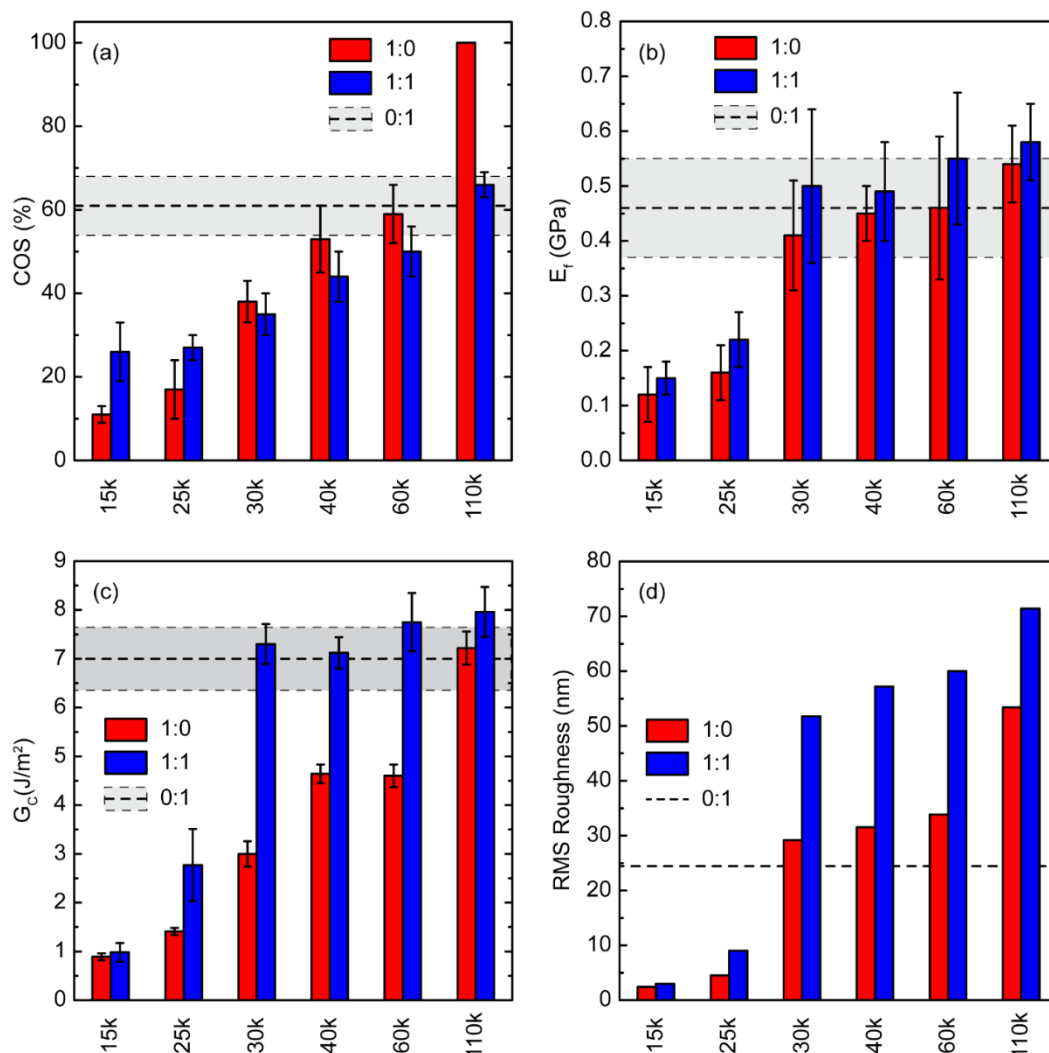
Figure 3.12 – (a) Crack onset strain, (b) elastic modulus, and (c) fracture energy of the neat and the blend films with different molecular weights of FTAZ. The COS of the neat 110k film does not have an error bar as all the films were stretched to 100% without any crack formation. (d) Root mean square roughness of the fractured neat and blend films of different MWs of FTAZ.

3.4.2. Film on Elastomer Characterization

The ductility of the films was probed by crack onset strain (COS) measurements, with results for the neat and blend films given in **Figure 3.12a**. The neat FTAZ films are found to exhibit a monotonic increase in COS with MW, where the MW of 15k has a COS of ~10% and the COS for 120k exceeds 100%. These results are similar to the increase in elongation at break with increasing MW that is observed in polymers in conventional tensile tests. As

discussed in the previous section, FTAZ at all MWs is viscoelastic at room temperature, and hence this trend is attributed to an increase in polymer chain length and entanglements, which allows the chains to slide past one another, preventing chain scission and preventing crack formation at chain ends. The high-MW N2200 films exhibit a COS of ~60%. The blend films follow a similar trend of increase in COS with the MW of FTAZ. For low-MW FTAZ blends, the COS of the blend was found to be slightly higher than the neat FTAZ films, likely due to the interaction of the brittle FTAZ with the more ductile high-MW N2200. In the moderate MW FTAZ blend films, the COS track well with the neat FTAZ COS. For the blend film with 120k, the COS was found to be closer to the COS of neat N2200 films, which became the limiting polymer.

The elastic modulus (E_f) of the films, measured using a wrinkling metrology approach, is plotted in **Figure 3.12b**. It was observed that the neat 15k and 25k films exhibited substantially lower elastic moduli compared to the higher-MW variants. These results are consistent with the general trend that the elastic modulus of polymers increases with MW until surpassing several times the entanglement MW where the elastic modulus tends to plateau.[211] A similar observation has been made experimentally and computationally in other conjugated polymer systems.[211,212] This suggests that the FTAZ entanglement M_n is below 30 kg mol^{-1}. This is consistent with the unique diffraction and thermal transition behavior observed for the low-MW FTAZ, where the lack of entanglements allows for the proposed chain-extended aggregate conformation. A similar trend in E_f with the MW was found in the blend films, where the 15k and 25k blend films were found to have a lower E_f than the higher-MW films. The blend films exhibited

marginally higher stiffness compared to the neat films of respective FTAZ variants but generally fell within the uncertainty of the measurements.

3.4.3. Trends in Cohesive Fracture Energy

The fracture energies of the neat and blend films are plotted in **Figure 3.12c**, as measured by four-point bending tests. The neat FTAZ films had a monotonic increase in G_c from 0.89 to 7.22 J m^{-2} when going from the 15k to 120k films, indicating improved cohesion with the increase in MW. The fracture energy of the N2200 film was found to be 7.00 J m^{-2}. In polymer thin films, G_c is often associated with the size of the plastic zone, which forms ahead of the crack tip in the form of crazes or local yielding. The presence of a plastic zone can be inferred by studying the fracture surface. We examined the surfaces by atomic force microscopy (AFM) and observed that the roughness of the fracture surface tracked well with the increase in G_c, where the RMS roughness of the fractured surface is given in **Figure 3.12d**, determined from the AFM scans. The low-MW FTAZ (15k) films had a relatively smooth fracture surface indicative of little plastic deformation near the crack tip. In these films, it was also observed that the crack propagated close to the Ca interface. This crack location is attributed to the low fracture resistance of the polymer, which prevents the crack from getting arrested within the bulk of the film before it propagates in the plane of the film during the four point bending tests. Conversely, in films with 25k and higher-MW FTAZ, the crack propagation was observed to be in the middle of the film. It should be noted that the four point bending test architecture was different than the OPV device stack. The device was an inverted architecture with ZnO interface layer, whereas the four point bending test employed a conventional device stack with a PEDOT:PSS layer. This was done to directly compare the fracture energy to COS, which was for films also cast on PEDOT:PSS.

In addition, this approach eliminated the use of the rougher ZnO layer in the fracture tests that may influence fracture behavior.[213] Despite of the different architecture, the crack propagation takes place through the active layer capturing film cohesion.

3.5 Conclusions

As demonstrated throughout this chapter, the molecular weight of the conjugated polymer can have very large impact on the end device. By changing the monomer feed ratio, the M_n of FTAZ can be effectively predicted through the Carothers equation. A series of FTAZ batches from 10-120K M_n were synthesized and paired with the fullerene acceptor of PCBM and non-fullerene acceptors of ITIC (a fused-ring electron acceptor/small molecule) and N2200 (polymer).

To understand the trends in the photovoltaic properties, we explored a model system of FTAZ:ITIC in great detail. Our results show that increases in FF and J_{SC} from 10K to 30K are primarily attributed to improved morphology. This morphology is consistent for blend films utilizing 30K or greater FTAZ. A modest increase in mobility is observed despite reduced phase purity, while a smaller long period and more oriented morphology allows for more efficient exciton dissociation and charge transport. Low M_n blends demonstrate higher V_{OC}, which plateaus at intermediate M_n and remains constant. Given the identical band gaps of the neat FTAZ polymers, the increasing energy loss from 10K to 100K is ascribed to lower radiative and non-radiative energy losses in the case of the lower M_n. In summary, together with our earlier works,[12,158] this study demonstrates a single donor polymer which, when blended with prototypical fullerene (PC$_{61}$BM), polymer (N2200), or FREA (ITIC) acceptors, demonstrates reduced sensitivity of photovoltaic and morphological characteristics over a remarkably wide range of M_n. Though the effects of donor FTAZ M_n observed in this

study may not be universal across all possible acceptors, these results suggest it is possible to achieve efficient and reproducible OPVs with varying acceptor types without the need for stringent M_n control during synthesis, as long as the donor polymer has a sufficiently high M_n. However, the origin of this broad M_n insensitivity is not yet known. The results of the overarching study can serve as a stepping stone for future work to correlate chemical structure to the observed behavior.

Furthermore, all-polymer solar cells (such as FTAZ:N2200) have the potential for superior stability and mechanical properties compared to small molecular acceptor blends. The results observed from the DMA, the COS, the E_f, and the G_c experiments complement one another and show a dramatic change in the mechanical behavior of the neat FTAZ and the blend films moving from 25K to 30K and higher. This behavior can be attributed to a significant increase in donor–donor and donor–acceptor entanglements. It can also be deduced that the entanglement MW of FTAZ is below 30 kg/mol. This matches the photovoltaic responses described as well. We have demonstrated the FTAZ is a great candidate for flexible devices, as it can be strained to over 100% without forming cracks.

CHAPTER 4: Utilizing Difluorinated Thiophene Units to Improve Performance of Polymer Solar Cells [13]

4.1 Introduction

The continued efficiency improvements for OSCs is due in part to the development of new conjugated organic materials and blending strategies (e.g., ternary blend),[214–218] and a both popular and reliable method to improve device efficiency is fluorination of conjugated polymers.[46,125,137,219–221] Fluorine is both the smallest electron withdrawing group (van der Waals radius of 1.35 Å) and the most electronegative element ($\chi_r = 3.98$).[222–224] Therefore, when added along the polymer backbone, fluorine offers negligible steric hindrance and deepens energy levels, while maintaining a similar band gap.[145,224,225] Another advantage to fluorination is an increase in inter- and intra-molecular interactions (e.g., F···H, F···S, F···π), which have demonstrated to favorably change the polymer backbone planarity as well as the packing in OSC devices.[135,226–229] Most high performance conjugated polymers used in OSCs are copolymers with a characteristic "donor-*linker*-acceptor-*linker*" alternating architecture; therefore, the location of fluorination needs to be considered.

While the donor moiety *can* be fluorinated to improve the photovoltaic performance of the devices, in many cases, adding fluorine substituents to the donor moiety show detrimental impact in device performance.[219,230] However, one fluorinated donor moiety

---

[13] Parts of this chapter previously appeared as an article in *Macromolecules*. Reprinted with permission from © 2021 American Chemical Society. The original citation is as follows: **Jeromy J. Rech**, Liang Yan, Zhengxing Peng, Shuixing Dai, Xiaowei Zhan, Harald Ade, and Wei You. "Utilizing Difluorinated Thiophene Units to Improve Perfromance of Polymer Solar Cells." *Macromolecules*, **2019**, 52 (17), 6523-6532.

which has consistently performed well is 3,3'-difluoro-2,2'-bithiophene (2TF).[47,49,231–238] Compared to a non-fluorinated bithiophene donor moiety, the 2TF has been shown to have a higher torsional barrier, which promoted a planar structure with enhanced π-π interactions, and results in improved morphology of the bulk heterojunction blend and photovoltaic properties of the corresponding devices.[49,234] There have also been a few studies that investigated the fluorination of the solubilizing side chains of conjugated polymers. Therein fluorination seems to generally increase mobilities, suppress triplet formation and charge recombination, and slightly improve thermal stability: which can be attributed in all cases to fluorine interactions increasing ordering the side chains into a more optimal orientation.[239–244] However, because of the limited scope of materials made with fluorinated side chains, a complete understanding on the impact of this approach is still elusive. Given the electron-withdrawing nature of fluorine, it is not surprising that the most common fluorination location is the electron deficient acceptor moiety. We have previously demonstrated with our FTAZ polymer that fluorine substituent on the benzotriazole acceptor moiety increased all three major device characteristics: open circuit voltage (V_{OC}), short circuit current density (J_{SC}), and fill factor (FF).[46,125] The increase in V_{OC} was due to the deepening of the highest occupied molecular orbital (HOMO) level from the electron withdrawing strength of the fluorine substituent, and a higher hole mobility allowed for improvements in both J_{SC} and FF. This same trend has been demonstrated by many other polymer systems in literature as well.[146,245–248]

While fluorination of the acceptor moiety has been established as a valuable technique to increase the OSC device performance, a limitation of this approach is that not all acceptor moieties have locations for fluorination. A notable example would be the

benzodithiophenedione (BDD) acceptor moiety in the commonly used PBDB-T polymer.[249] Moreover, in order to synthesize a new fluorinated acceptor moiety, typically a new synthetic route needs to be developed beginning with a fluorinated starting material; this *de novo* synthesis increases the number of steps/time required to make the final polymer. Therefore, to circumvent these issues, fluorination on one final location should be considered: the conjugated linker (often thiophene) that connects the donor and acceptor moieties together. The idea of fluorinating thiophene units has shown success in the donor moiety of 2TF (*vide supra*), and in various mono-fluorinated thiophene units (3FT and 4FT) which we used to link benzodithiophene donor moieties and benzotriazole acceptor moieties.[135] Therein, we demonstrated that relocating the fluorine substituent from acceptor moiety to the thiophene linker maintained the advantageous properties from fluorination. There have been multiple other reports which have explored using mono-fluorinated thiophene units,[223,250] but there are very few reports for OSC polymers which simultaneously utilize fluorination at both the 3' and 4' position of the thiophene linker, i.e., a difluorinated thiophene (dFT) unit.

Throughout the literature, dFT units have a prominent place in the realm of organic thin-film transistors (OFETs). There are numerous reports which utilize dFT units in conjugated polymers to achieve high OFET mobilities.[228,251–259] For example, Wenping Hu's lab reported an OFET polymer containing dFT units with mobilities over 6 cm^2 V^{-1} s^{-1} and on/off ratio over 10^5, which makes it among the highest values in OFETs fabricated on a flexible substrate.[260] However, of the reports that use dFT units in OSCs,[261–266] the impact of fluorination remains ambiguous. For example, Kazuo Takimiya's lab used a difluorinated thiophene unit in their PNTz polymers, and compared to the mono-fluorinated version, there was a sharp decrease in performance (10.5% vs 6.5%), which is attributed to increased

91

recombination – the polymers containing the dFT unit had much lower solubility and thus formed crystallites.[261] Conversely, when Martin Heeney's lab incorporated the dFT unit into their germanium containing polymers, they observed a 50% improvement in efficiency, attributed to a substantially higher hole mobility and deeper energy levels.[262,263] Furthermore, there have not been any reports of a dFT containing conjugated polymer that was paired with non-fullerene acceptors (NFAs), even as NFAs have rapidly boosted the performance of OSCs within the past few years.[31,63,64,143,267,268]

To further understand the impact of fluorination, in particular, the dFT unit, we designed and synthesized a new conjugated polymer, dFT-HTAZ, which differs from the original HTAZ polymer[125] by having two difluorinated thiophene linkers (see **Scheme 4.1** for structures of HTAZ and dFT-HTAZ). The incorporation of the dFT units maintained the optical properties while lowering the energy levels of the dFT-HTAZ polymer by ~ 0.4 eV, which allowed for a much improved V_{OC} value of ~ 1 V in the dFT-HTAZ based devices. While multiple electron acceptors were considered and tested, the champion device of dFT-HTAZ:ITIC-Th1 reached an efficiency of ~ 10 %, which is nearly 3× that of the non-fluorinated HTAZ:ITIC-Th1 blend. As most OSC polymers have thiophene linkers, we envision that strategically using the dFT units can serve as an effective method to increase OSC performance in many conjugated polymer systems.

4.2 Results and Discussion

4.2.1. Synthesis of monomers and polymers

HTAZ was synthesized according to literature procedures,[125,135] and the synthetic pathway for dFT-HTAZ is depicted in **Scheme 4.1**. The starting material, tetrabromothiophene (**1**) can be prepared straightforwardly by reacting thiophene with excess

liquid bromine, however recrystallization is necessary before the next reaction can proceed. As the desired locations for fluorination is on the less reactive 3' and 4' positions of thiophene, (**1**) must first be protected at the 2' and 5' positions with trimethylsilyl (TMS) groups to render (**2**). Once purified, (**2**) was then treated with *n*-butyllithium (*n*-BuLi) and underwent electrophilic fluorination with N-fluorobenzenesulfonimide (NFSI) to offer (**3**); however, the order of addition is very important. Adding 2 mole equivalence of *n*-BuLi then 2 equivalence of NFSI resulted in unacceptably low yields (<10%). Fortunately, we discovered that the yield for this reaction could be improved by adding small amount of *n*-BuLi and NFSI in several portions rather than all at once. Multiple different orders of addition were explored and are summarized in the SI. Next, selective deprotection and bromination of the 5' position of (**3**) can be achieved in one pot with *N*-bromosuccinimide (NBS). The desired precursor (**4**) can then be made through lithium-halogen exchange followed by stannylation. Product (**4**) is a key immediate, since it can be paired with any acceptor moiety of choosing via Stille Coupling. In our case, the fluorinated thiophene units were attached through a Stille cross-coupling reaction between (**4**) and a brominated benzotriazole (**5**) to yield the monomer precursor (**6**). The final step to produce the dFT-HTAZ monomer (**7**) is to remove the TMS protecting group and brominate at that location, which can be done similarly to step 1 in converting (**3**) to (**4**). The resulting monomer was recrystallized multiple times to yield a high purity yellow crystalline powder appropriate for polymerization. Finally, the monomers (TAZ monomer and BnDT monomer) were subjected to a microwave assisted Stille polycondensation to yield the target polymers, HTAZ and dFT-HTAZ.
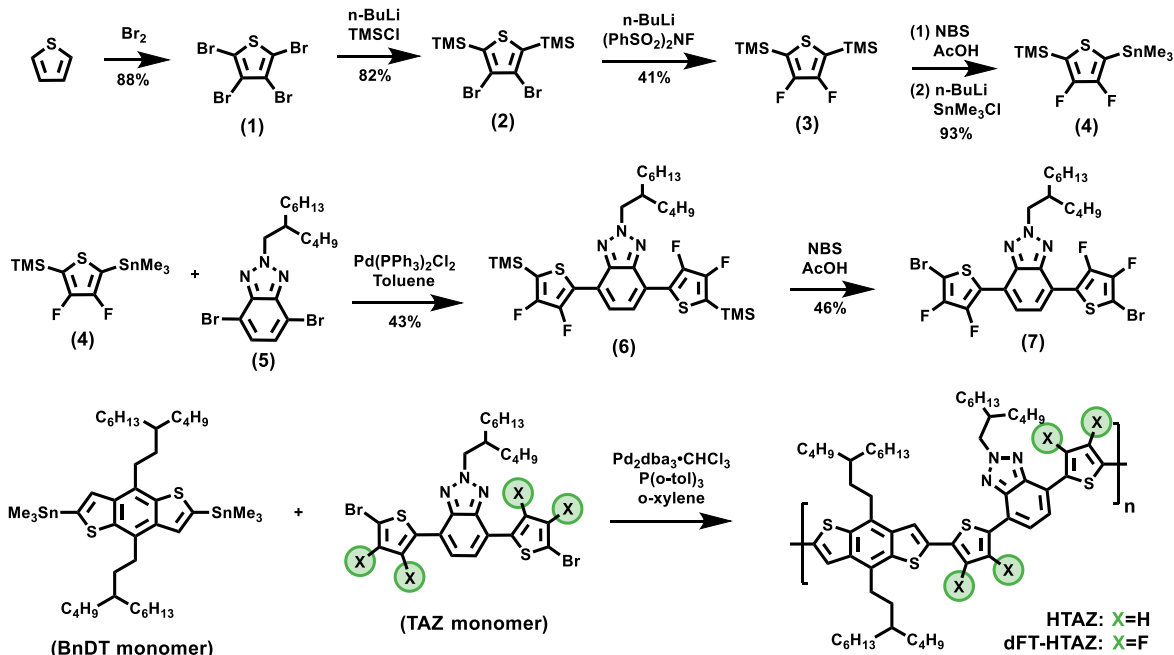
Scheme 4.1: Synthesis of the fluorinated thiophene units, monomers, and Stille-coupling based polymerization to make HTAZ and dFT-HTAZ polymers

Full details for each reaction, nuclear magnetic resonance (NMR) characterization, and polymerization conditions are described in the Section 4.4 Experimental Details. The number average molar mass (M_n) and dispersities ($Đ$), reported in **Table 4.1**, were acquired through high temperature gel permeation chromatography with (HT-GPC) at 150 °C with 1,2,4-trichlorobenzene (TCB) (stabilized with 125 ppm BHT) as the eluent. Both polymers have M_n values appropriate for high current density while remaining soluble; the dispersity values are also appropriate for such step growth polymerization methods.

Table 4.1 – Molar Mass, Optical Properties, Band Gaps, and Measured Energy Levels for both HTAZ and dFT-HTAZ polymers

Polymer	M_n[a] (kg/mol)	$Đ$ (M_w/M_n)	$\lambda_{max,sol}$[b] (nm)	$\lambda_{max,film}$[c] (nm)	$E_{g,opt}$[d] (eV)	HOMO[e] (eV)	LUMO[f] (ev)
HTAZ	44.1	3.0	535/570	537/580	2.01	− 5.44	− 3.43
dFT-HTAZ	59.2	2.1	534	530	2.01	− 5.78	− 3.77

[a]Measured by high temperature gel permeation chromatography. [b]Absorption maximum in chloroform solution. [c]Absorption maximum in thin film. [d]Optical band gap is found by dividing 1240 by the absorption onset (618 nm for both polymers). [e]Measured by cyclic voltammetry. [f]Calculated by electrochemical HOMO and optical band gap: LUMO = HOMO + $E_{g,opt}$.

In order to understand the impact of the dFT units, we first looked at variations in the optical and electrochemical properties of the resulting polymers. First, the optical properties of the polymers HTAZ and dFT-HTAZ were compared with solution UV-Vis absorption of the polymer dissolved in chloroform in **Figure 4.1a**. Both polymers absorb in the same range and have an absorption onset at 618 nm, which equates to an optical band gap of 2.01 eV. While the HTAZ polymer shows a slightly stronger aggregation shoulder around 580 nm, both polymers have a similar λ_{max} around 535 nm. When thin films of polymers are deposited via spin-coating, similar results are seen in the absorption when comparing HTAZ and dFT-HTAZ (**Figure 4.1b**). In short, with the exception of a slight difference in aggregation strength, both polymers have very similar optical properties.
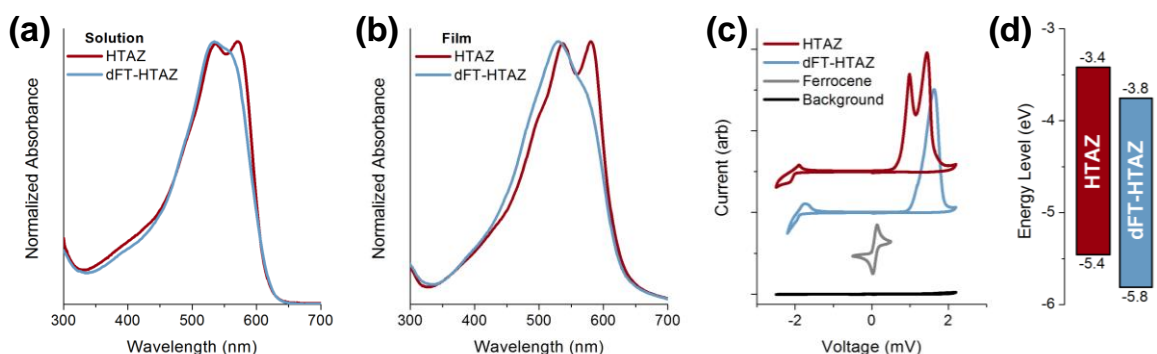
Figure 4.1 – Normalized UV-Vis spectra of the HTAZ and dFT-HTAZ polymers (a) in chloroform solution and (b) as thin films cast from chlorobenzene. (c) Cyclic voltammogram of each polymer as a thin film, with a scan rate of 0.1 V s^{-1}. (d) Energy levels of both polymers calculated from cyclic voltammetry.

Next we estimated the highest occupied molecular orbital (HOMO) and lowest unoccupied molecular orbital (LUMO) energy levels by cyclic voltammetry (CV) of a thin polymer film for both polymers (**Figure 4.1c** showing the voltammograms). Full details for the CV setup can be found in the section 4.4.2. Key optical and electrochemical data is

summarized in **Table 4.1**. Unlike the optical properties, there are large differences when comparing the electrochemical properties of the two polymers. First, the conversion of oxidation onset (E_{OX}) to HOMO energy level is done through the ferrocene standard (E_{FC}) using the equation $HOMO = -(4.8eV + e(E_{OX} - E_{Fc/Fc+}))$. The HTAZ polymer has an oxidation onset of 0.72 V, which corresponds to a HOMO energy level of – 5.44 eV, while the dFT-HTAZ polymer is shifted to an oxidation onset of 1.11 V, corresponding to a HOMO energy level of – 5.78 eV. The LUMO was estimated through the optical band gap, and using the information learned from the optical and electrochemical properties, an approximate energy level diagram for the devices can be constructed, as shown in **Figure 4.1d.** In comparison, it is clear that the addition of the electron withdrawing fluorine substituents to the thiophene linkers lowers the HOMO energy levels by ~ 0.4 eV. The deeper HOMO energy level is advantageous as the V_{OC} is linked to the energy level difference between the HOMO and LUMO levels of the donor and acceptor materials. Lowering the HOMO level of HTAZ by additional 0.4 eV would indicate that the dFT-HTAZ based photovoltaic devices should have a much larger V_{oc} than that of HTAZ based ones.

4.2.3 Photovoltaic properties

To determine the efficacy of the fluorinated thiophene units as a means to improve device efficiency, the photovoltaic properties were next investigated in a bulk heterojunction (BHJ) solar cell with a normal device configuration: ITO/CuSCN/dFT-HTAZ:PCBM/Ca/Al and ITO/PEDOT:PSS/HTAZ:PCBM/Ca/Al. The polymer:PCBM ratio was 1:2, and the active layer thickness was ~ 250 nm for both types of devices. The solar cell characteristics

are shown in **Table 4.2** and a representative *J-V* curve is found in **Figure 4.2a**, with different optimization conditions summarized in **Table 4.3**.
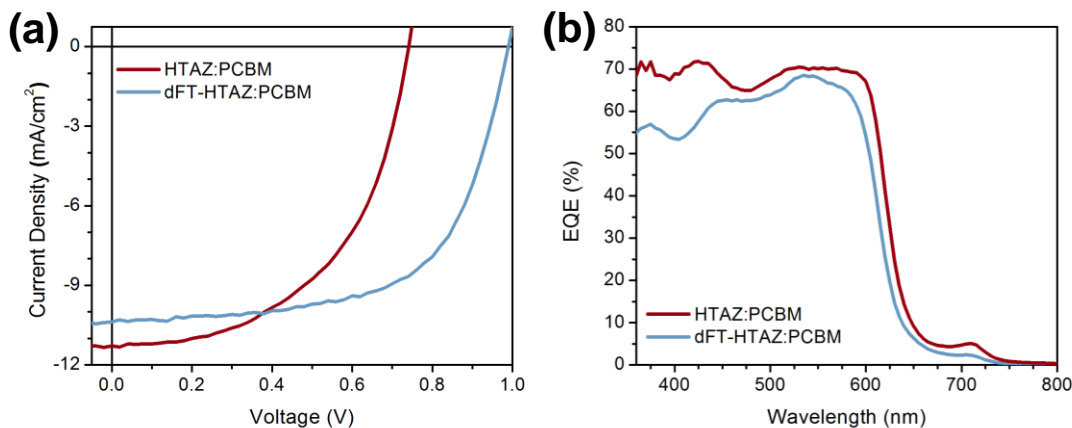
Figure 4.2 – (a) Representative *J-V* curve for HTAZ:PCBM and dFT-HTAZ:PCBM devices with (b) corresponding EQE responses

Table 4.2 – Photovoltaic Parameters of Organic Solar Cells for each polymer (HTAZ and dFT-HTAZ) paired with various acceptors (PCBM, ITIC, and ITIC-Th1)

Donor	Acceptor	J_{SC} (mA/cm^2)	V_{OC} (V)	*FF* (%)	PCE (%)	PCE$_{max}$ (%)
	PCBM	11.10 ± 0.25	0.741 ± 0.001	53.3 ± 1.3	4.39 ± 0.17	**4.40**
HTAZ	ITIC[46]	12.54 ± 0.49	0.851 ± 0.001	39.9 ± 0.9	4.26 ± 0.24	--
	ITIC-Th1	11.77 ± 0.72	0.749 ± 0.010	35.8 ± 1.2	3.16 ± 0.29	**3.54**
	PCBM	9.74 ± 0.33	0.990 ± 0.002	61.9 ± 1.4	5.97 ± 0.28	**6.41**
dFT-HTAZ	ITIC	6.39 ± 0.35	0.973 ± 0.008	42.7 ± 1.1	2.66 ± 0.20	**2.92**
	ITIC-Th1	16.12 ± 0.97	0.991 ± 0.002	57.1 ± 0.6	9.12 ± 0.49	**9.76**

Table 4.3 – Optimization of dFT-HTAZ:PCBM blends with different conditions

Solvent (+ Additives)	Hole Transport Layer	J_{SC} (mA/cm^2)	V_{OC} (V)	*FF* (%)	PCE (%)
CB + 3% DIO	**CuSCN**	9.74 ± 0.33	0.989 ± 0.002	61.9 ± 1.4	5.97 ± 0.28
CB + 3% DPE	**CuSCN**	8.30 ± 0.35	0.983 ± 0.002	67.3 ± 0.7	5.49 ± 0.23
CB + 3% CN	**CuSCN**	7.95 ± 0.38	0.986 ± 0.001	60.9 ± 0.9	4.77 ± 0.21
TCB	**CuSCN**	6.93 ± 0.56	0.978 ± 0.002	66.5 ± 0.6	4.51 ± 0.34
CB + 3% DIO	**PEDOT:PSS**	8.84 ± 0.17	0.951 ± 0.011	41.7 ± 2.1	3.51 ± 0.26
TCB	**PEDOT:PSS**	4.18 ± 1.46	0.931 ± 0.019	28.7 ± 1.2	1.12 ± 0.40

Please note that we used two different hole transport layers (HTLs): PEDOT:PSS and CuSCN. Given the low HOMO energy level of the dFT-HTAZ polymer, CuSCN, which has more appropriate work function (5.5 eV),[269] was chosen as the HTL for dFT-HTAZ based devices. The HTAZ polymer blend used PEDOT:PSS at the HTL, as it had a more appropriate work function (5.1 eV). To illustrate the impact of the HTL, the dFT-HTAZ polymer was also tested with PEDOT:PSS and the results are shown in **Figure 4.3**. While similar V_{OC} and J_{SC} are obtained, there is a drastic difference in the FF (41.7 % vs 62.9 %), which is attributed to the energy level misalignment with the PEDOT:PSS interlayer.
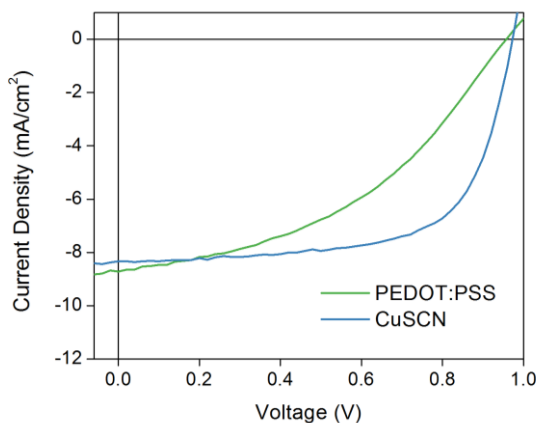
Figure 4.3 – Representative J-V curves of dFT:HTAZ-PCBM blends with different hole transport layers of PEDOT:PSS and CuSCN

Consistent with the prediction above, the V_{OC} value for the dFT-HTAZ blend is significantly improved when compared to the HTAZ devices as the HOMO energy level of dFT-HTAZ is deepened upon addition of the fluorine substituents. Specifically, the V_{OC} of HTAZ is 0.741 ± 0.001 V while dFT-HTAZ has a V_{OC} of 0.990 ± 0.002 V. A strong increase in V_{OC} is often seen upon fluorination, and this increase of 0.25 V in V_{OC} shows the same trends continue to hold when the fluorination occurs on the thiophene linker. It is important to note that the energy levels measured by CV would suggest a 0.4 V change in the V_{OC} value, meaning there is ~ 0.15 V additional energy loss exists in the dFT-HTAZ:PCBM

blend. This energy loss is likely from either a change in the CT state energy, which can be attributed to a change of at the donor/acceptor interfacial morphology or a change in charge recombination loss. Regardless, while the V_{OC} loss appear to be ~ 0.1 V higher for the dFT-HTAZ blends, the larger increase in V_{OC} results in a net improvement in the performance of the dFT-HTAZ blends. Next, the J_{SC} is often related to the absorption spectra of the polymers, which as highlighted previously, are nearly identical for HTAZ and dFT-HTAZ. Yet, the HTAZ polymer has a slightly higher J_{SC} (11.10 ± 0.25 mA/cm^2) than dFT-HTAZ (9.74 ± 0.33 mA/cm^2). Finally, the FF is increased, from 53.3 ± 1.3 % for HTAZ to 61.9 ± 1.4 % for dFT-HTAZ. Our previous work has shown that the increasing of hole mobility through fluorination strongly influences the FF,[125,145,270] which can be attributed to the more planar backbone. To confirm the difference in backbone planarity, we performed density functional theory (DFT) calculations at the DFT B3LYP/6-311+G(d) level of theory on one repeat unit for both HTAZ and dFT-HTAZ, the results of which are shown in **Figure 4.4**. The fluorination of the thiophene linker has a large impact on the most stable conformation and the dihedral angle between units. The dFT-HTAZ polymer has a conformation that is very planar, with the largest dihedral angle of 0.2°, while the HTAZ polymer has a significantly larger dihedral angle of 11.6° between the BnDT donor moiety and the thiophene linker. This change in the backbone planarity can be facilitated through non-covalent inter- and intra-molecular interactions, such as F···H, F···S, and F···π; the fluorinated thiophene units can impart the same interactions, thus explaining the increase in FF from 53.3 to 61.9 %. The impact on mobility is also directly measured through space charge limited current (SCLC) measurements (**Figure 4.5** and **Table 4.4**). The hole mobility value for the dFT-HTAZ:PCBM blend (15.5×10^{-4} cm^2/V·s) is nearly a magnitude higher

than the HTAZ:PCBM blend (1.70×10^{-4} cm^2/V·s), which is attributed to the more planar

backbone from the dFT units as demonstrated above. In summary, when paired with PCBM,

the HTAZ blends can reach a PCE of 4.40 % while dFT-HTAZ can achieve a higher value

over 6.41 %, a very large 46 % increase in efficiency, mainly due to much improved V_{OC} and

FF.
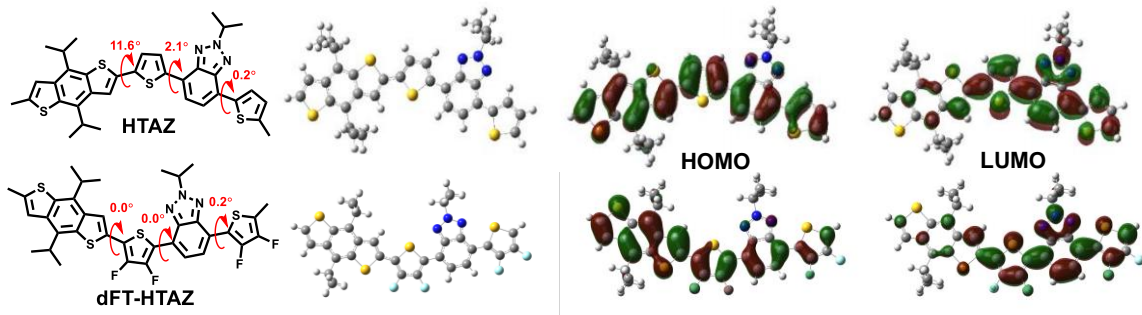
Figure 4.4 – Chemical structures of HTAZ and dFT-HTAZ with optimized conformation per repeat unit with calculated dihedral angles shown on the structures. Also HOMO and LUMO distributions structures for each polymer are shown.
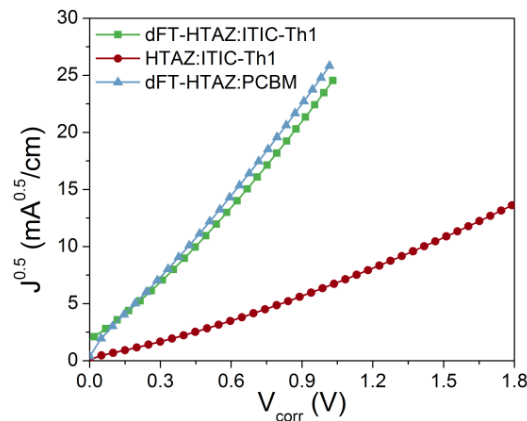
Figure 4.5 – SCLC hole mobility curves for various active layers

Table 4.4 – Mobility Values for key blends

Active Layer	Thickness (nm)	Hole Mobility (x10^{-4} cm^2/Vs)
HTAZ:PCBM [135]	249	1.7
dFT-HTAZ:PCBM	191	15.5 ± 5.3
HTAZ:ITIC-Th1	162	6.27 ± 0.59
dFT-HTAZ:ITIC-Th1	153	1.09 ±0.22

While these device results show an optimistic outlook for fluorinated thiophene units, fullerene electron acceptors, such as PCBM, have been rapidly replaced by the new non-fullerene acceptors (NFAs). Compared to PCBM, these new NFAs, such as ITIC and ITIC-Th1 shown in **Chart 4.1**, have superior light absorption in the visible and near infrared range and high levels of tunability in optoelectronic properties.[31,63,64,143] More importantly, these advantages have pushed OSC performance surpassing 16 %.[57] Because of the rapid growth and use of NFAs, we next paired the polymers with common high performance acceptors ITIC and ITIC-Th1 to see if the same improvements are found when comparing the different thiophene linkers.
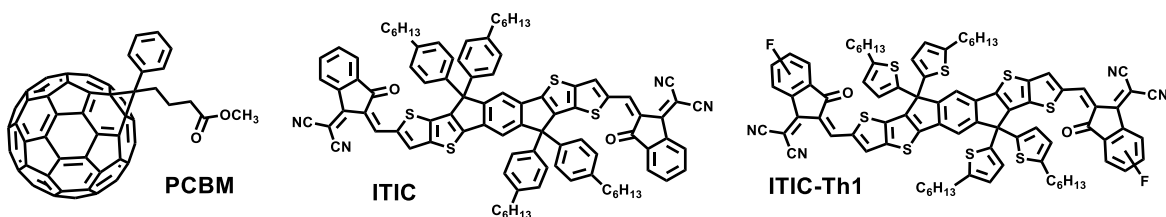
Chart 4.1 – Chemical structures for the three electron acceptors used in the publication: PCBM, ITIC, and ITIC-Th1
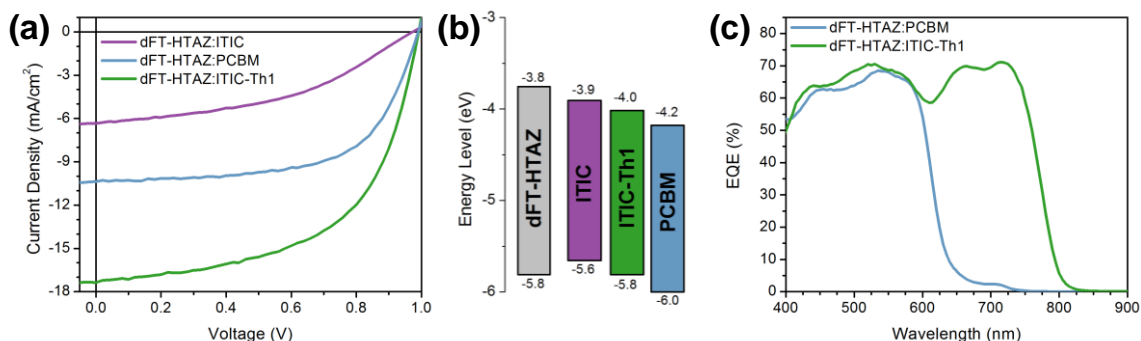
Figure 4.6 – (a) Representative *J-V* curves for dFT-HTAZ:acceptor blends, (b) HOMO/LUMO energy levels as measured through CV, and (c) EQE response for various blends

The effectiveness of the fluorinated thiophene units in NFA blends is next explored. First, the photovoltaic properties were investigated with inverted configuration solar cell:

ITO/ZnO/dFT-HTAZ:acceptor/MoO₃/Al. For the NFA-based devices, the polymer:acceptor ratio was changed to 1:1, and active layer thickness where between 75 – 100 nm. As shown in the representative *J-V* curve in **Figure 4.6a**, the high V_{OC} value of ~ 1 V is maintained for all three blends, but there are very large differences in the J_{SC} and *FF*. Interestingly, the dFT-HTAZ:ITIC blend has very poor performance compared to the dFT-HTAZ:PCBM blend, suffering from very low J_{SC} and *FF*. While this seems unexpected, as ITIC has shown great performance with many other BHJ blends, the energy levels of each component (shown in **Figure 4.6b**) illustrates an important issue – dFT-HTAZ:ITIC forms a type I heterojunction instead of the conventional type II heterojunction. The HOMO energy level of the ITIC molecule (– 5.6 eV) is higher than the HOMO energy level of the dFT-HTAZ polymer (– 5.8 eV), which can lead to the formation of traps and thus erode the performance. Just as the CuSCN HTL was needed instead of the more common PEDOT:PSS HTL in the conventional architecture when paired with PCBM, the dFT-HTAZ polymer has such a deep HOMO energy level from the fluorine substituents that the other components (e.g., the pairing NFA) need to be carefully considered in order to obtain an ideal energetic landscape.

In order to realize the benefits of the dFT units, an acceptor with a deeper HOMO energy level needs to be used. Therefore, using the same fluorination theme, a fluorinated derivative of ITIC called ITIC-Th1 was next explored.[38,62] Compared to ITIC, the ITIC-Th1 acceptor has thienyl instead of phenyl side chains and a fluorinated end group; these changes can decrease the HOMO energy level to match that of dFT-HTAZ and form an effective type II heterojunction. When comparing the dFT-HTAZ:PCBM and dFT-HTAZ:ITIC-Th1 blends, there is a very large increase in the J_{SC} from 9.74 ± 0.33 mA/cm² to 16.12 ± 0.97 mA/cm², respectively. This large 66% increase in the J_{SC} is attributed to the extra complimentary

absorbance of the ITIC-Th1 acceptor, which is best illustrated in the EQE response on

Figure 4.6c. In the wavelengths of 400 ~ 650 nm, the response is primarily from the dFT-

HTAZ polymer, which remains unchanged in the different blends; however, the ITIC-Th1

has strong absorbance in the visible and near infrared range, and contributes to the

absorbance values out to ~ 800 nm. This extra ~ 150 nm worth of harvestable photons helps

increase the J_{SC} compared to the PCBM acceptor, which primarily absorbs higher energy UV

light. When comparing the *FF* of the dFT-HTAZ:PCBM (61.9 ± 1.4 %) blend with dFT-

HTAZ:ITIC-Th1 (57.1 ± 0.6 %), there is a slight decrease in value. While the overall PCE is

much higher (9.76 % vs 6.41 %), driven by the much improved J_{SC}, we studied the

morphology of the active layer to better understand the BHJ blend films and the decrease in

FF for the dFT-HTAZ:ITIC-Th1 blend.

4.2.4 Morphology

We began our study on morphology with measuring the texture and molecular

packing of the materials through synchrotron radiation-based grazing incidence wide angle

X-ray scattering (GIWAXS).[126] The 2D GIWAXS patterns for neat dFT-HTAZ films cast

from chlorobenzene with 3% 1,8-diiodooctane additive (CB+DIO) and toluene (TOL)

solvents are shown in **Figure 4.7a** and **Figure 4.7b**. Neat films of ITIC-Th1 cast from

toluene can also be found in **Figure 4.8**. Also, the blend films of dFT-HTAZ with both

PCBM and ITIC-Th1 are shown in the 2D GIWAXS patterns in **Figure 4.7c** and **Figure

4.7d**. The corresponding in-plane (dotted lines) and out-of-plane (solid lines) profile for each

pattern is shown in **Figure 4.7e**. When comparing the neat dFT-HTAZ films with different

solvents, the dFT-HTAZ cast from CB+DIO shows higher order lamellar (*h*00) including:

(100) at $q = 0.32$ Å^{-1}, (200) at $q = 0.66$ Å^{-1}, (300) at $q = 0.99$ Å^{-1}, and another set of peak with

the first order peak $q = 0.46$ Å^{-1}, and the second order peak at $q = 0.92$ Å^{-1}. There is also a

strong out-of-profile (010) π-π stacking peak at $q = 1.73$ Å^{-1}, which corresponds to a real-

space packing distance of 3.63 Å. Comparatively, when dFT-HTAZ was cast from toluene,

while having a favorable face-on packing, the resulting neat film has lower order, only being

able to resolve peaks of (100) at $q = 0.32$ Å^{-1} and (200) at $q = 0.65$ Å^{-1}. Additionally, the

(010) π-π stacking peak shifts to $q = 1.67$ Å^{-1}, which corresponds to a larger distance of 3.76

Å. This suggests that dFT-HTAZ has higher molecular ordering when cast from the CB+DIO

solvent compared to toluene.
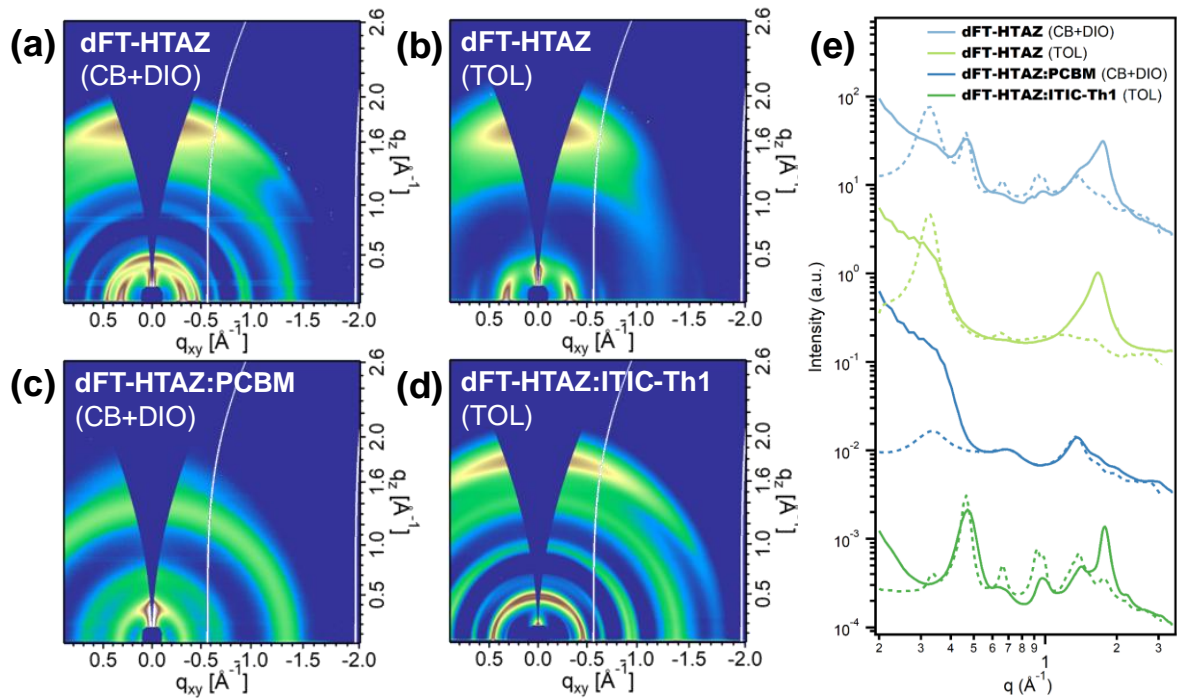
Figure 4.7 – 2D GIWAXS patterns for (a) neat dFT-HTAZ cast from chlorobenzene (CB) with 3% 1,8-diiodooctane (DIO) additive, (b) neat dFT-HTAZ cast from toluene, (c) blend film of dFT-HTAZ:PCBM cast from CB+DIO, (d) blend film of dFT-HTAZ:ITIC-Th1 cast from toluene, and (e) corresponding linecuts for each. The 1D profiles have both in-plane q_{xy} (dotted lines) and out-of-plane q_z (solid lines) directions shown.

104
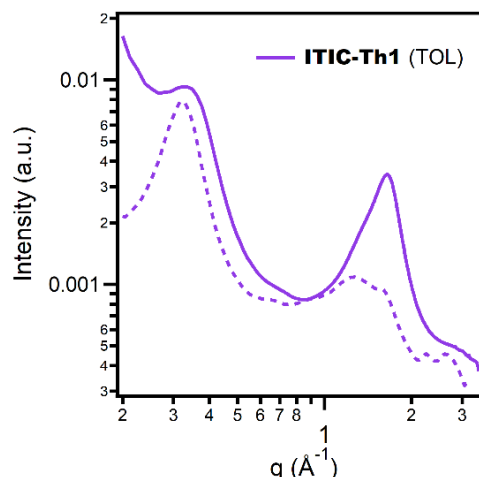
Figure 4.8 – 1D GIWAXS profile for neat ITIC-Th1; 1D profile has both in-plane q_{xy} (dotted line) and out-of-plane q_z (solid line) directions shown.

Interestingly, when blended with the appropriate electron acceptor, the dFT-HTAZ:PCBM blend, which was cast from CB+DIO, shows reduced molecular ordering than the neat film, and the dFT-HTAZ:ITIC-Th1 blend, which was cast from toluene, shows much improved molecular packing than the neat film. The more crystalline dFT-HTAZ:ITIC-Th1 film shows higher order (h00) peaks: (100) at $q = 0.33$ Å^{-1}, (200) at $q = 0.66$ Å^{-1}, (300) at $q = 0.99$ Å^{-1}, and one more set of peaks with first order peak at $q = 0.46$ Å^{-1}, and second order peak at $q = 0.92$ Å^{-1}. This suggests that PCBM suppresses the packing of dFT-HTAZ in the blend while ITIC-Th1 can improve it, which is important as the higher ordering of dFT-HTAZ in the dFT-HTAZ:ITIC-Th1 blend is beneficial for the charge transport in the polymer-rich domains. Another difference comes from the (010) peak position when blended with the electron acceptor. For dFT-HTAZ:ITIC-Th1, there is a strong (010) π-π stacking peak at $q = 1.78$ Å^{-1}, which corresponds to a real-space packing distance of 3.53 Å. The dFT-HTAZ:PCBM blend has a much larger (010) π-π stacking peak which corresponds to a real space packing distance of 3.76 Å. Through the full width at half maximum of the (010) peaks, found through fitting with pseudo-Voigt functions and shown in **Figure 4.9**, the

105

coherence length can be calculated, and the dFT-HTAZ:PCBM blend has a much smaller

coherence length of 9.1 Å compared to the 35.3 Å value for the dFT-HTAZ:ITIC-Th1 blend.

Blends of dFT-HTAZ:ITIC-Th1 has both a smaller π-π stacking distance and much longer

coherence length (nearly 4× longer), both of which is beneficial for charge transport and help

contribute to the much higher J_{SC} compared to the PCBM blend.
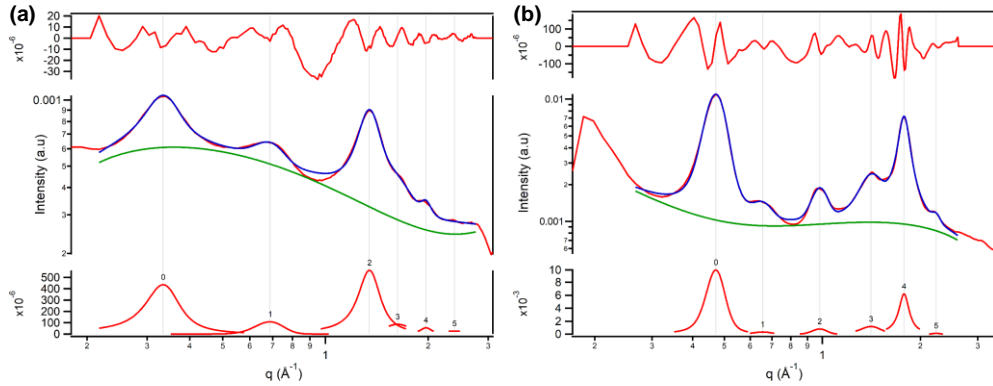
Figure 4.9 – Diffraction profiles cut along the ~q_z axis of the 2D GIWAXS images for (a) dFT-HTAZ:PCBM and (b) dFT-HTAZ:ITIC-Th1 blend films (blue line), their fits (red line) fitted to pseudo-Voigt functions
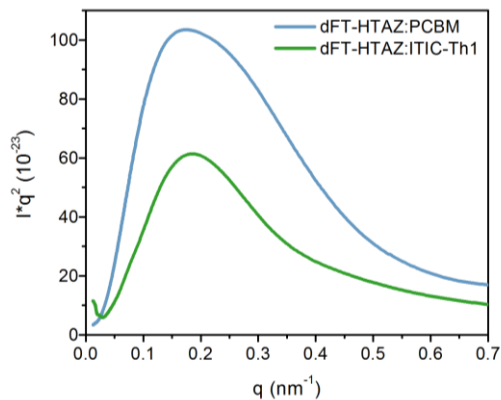
Figure 4.10 – Lorentz-corrected RSoXS profiles of dFT-HTAZ:PCBM and dFT-HTAZ:ITIC-Th1 blend films

We next applied resonant soft X-ray scattering (RSoXS)[271] to compare the domain

purity and spacing for the two blends (dFT-HTAZ:PCBM and dFT-HTAZ:ITIC-Th1). The

thickness normalized and Lorentz-corrected RSoXS profiles are shown in **Figure 4.10**, and

the real-space domain spacing (referred to as long period) and relative root-mean square

composition variation (referring to previous reported average domain purity) resolved from

RSoXS are shown in **Table 4.5**. The analysis procedures and meaning of these

morphological parameters were well discussed in our recent publication.[272] Both blends

have a very similar peak position at $q \sim 0.18$ nm^{-1} (0.181 nm^{-1} for PCBM blend and 0.175

nm^{-1} for ITIC-Th1 blend) which correspond to a similar long period of ~ 35 nm. The relative

root-mean square (RMS) composition, related to domain purities, are 1 and 0.73 for dFT-

HTAZ:PCBM and dFT-HTAZ:ITIC-Th1, respectively. The higher RMS composition of

dFT-HTAZ:PCBM can help explain the higher *FF* compared to the dFT-HTAZ:ITIC-Th1

blend, as impure domains can lead to increased bimolecular recombination and thus reduce

the *FF*.[273] We have previously published the morphology of HTAZ with both fullerene and

non-fullerene acceptors, and generally amorphous packing is observed with both.[46,270,274]

Both the (100) and (010) peaks are broad peaks, thus shorter coherence lengths and a higher

degree of disorder, compared to dFT-HTAZ. Furthermore, the long period for non-fullerene

blends, such as HTAZ:ITIC, show larger domain spacing values of ~ 60 nm.[46] Additionally,

HTAZ blends have generally shown lower relative domain purity compared to the fluorinated

alternatives, which can help explain the lower *FF* values which are seen when comparing

HTAZ and dFT-HTAZ blends.

Table 4.5 – Summary of morphology results: peak distances and corresponding coherence
length from GIWAXS, along with long period and average phase purity from RSoXS

	Processing Solvent	dFT-HTAZ (010) peak (Å^{-1})	π-π stacking distance (Å)	(010) peak coherence length (Å)	Long Period (nm)	σ^a
dFT-HTAZ	**CB + DIO**	1.73	3.63	23.4	--	--
dFT-HTAZ	**TOL**	1.67	3.76	22.4	--	--
dFT-HTAZ:PCBM	**CB + DIO**	1.66	3.78	27.3	34.7	1.00
dFT-HTAZ:ITIC-Th1	**TOL**	1.78	3.53	35.3	35.9	0.73

[a]Root-mean-square composition variation, which represents the average domain purity

Finally, we want to draw attention to an important comparison: the HTAZ:ITIC-Th1 and dFT-HTAZ:ITIC-Th1 solar cells. Much like with the PCBM acceptor based devices as we discussed earlier, when ITIC-Th1 was used as the acceptor, the dFT-HTAZ blend has a much higher V_{OC} (0.991 ± 0.002 V) compared to HTAZ (0.749 ± 0.010 V) – a 32 % increase. The *FF* was also 60 % higher in the dFT-HTAZ (57.1 ± 0.6 %) compared to HTAZ (35.8 ± 1.2 %) blend. The increase in V_{OC} and *FF* can be explained using the same reasoning when comparing the HTAZ:PCBM and dFT-HTAZ:PCBM blends (*vide supra*). The deeper HOMO energy level of dFT-HTAZ can allow for the higher V_{OC}, and the improved planarity from the fluorine interactions can boost the *FF* and mobility values nearly six times higher (dFT-HTAZ:ITIC-Th1 with 6.27×10^{-4} cm^2/V·s while HTAZ:ITIC-Th1 has 1.09×10^{-4} cm^2/V·s). Interestingly, when paired with ITIC-Th1, the HTAZ blend doesn't show the same level of improvement in terms of J_{SC} as the dFT-HTAZ blend does. This is likely due to the fact that the HTAZ had lower mobility values, saturated photocurrent, and charge collection probability when paired with NFAs, as we previously explored.[46] Because of HTAZ has worse charge transport and extraction, the J_{sc} values for the HTAZ:ITIC-Th1 blend (11.77 ± 0.72 mA/cm^2) are much lower than dFT-HTAZ (16.12 ± 0.97 mA/cm^2). As the dFT-HTAZ showed improved V_{oc}, J_{sc}, and *FF* values compared to HTAZ, the overall efficiency is significantly higher. In fact, the champion dFT-HTAZ:ITIC-Th1 solar cell device had an efficiency of 9.76 %, an astounding 176% increase compared to the champion HTAZ:ITIC-Th1 device of only 3.54 %. This nearly 3× better performance from the dFT units demonstrates the effectiveness of this design strategy.

4.3 Conclusion

A new conjugated polymer, dFT-HTAZ, was synthesized and characterized in order to better understand the impact that difluorinated thiophene units have on the performance of conjugated polymers based organic solar cells. Using HTAZ and dFT-HTAZ as model conjugated polymers, we demonstrate that fluorination of the thiophene linkers used to connect the donor and acceptor moieties in typical conjugated copolymers can lead to a nearly 3× improvement in device performance in our particular system. The observed increase in V_{OC} upon fluorination – in PCBM, ITIC, and ITIC-Th1 based devices – can be attributed to the deeper HOMO level introduced by the difluorinated thiophene linkers (dFT). Furthermore, when comparing the ITIC-Th1 based devices, dFT-HTAZ has substantially improved FF (60% higher) and J_{SC} (37% higher), which is explained through the increased planarity and mobility values offered by the dFT unit. One important caveat with using the dFT units is the significant deepening of energy levels, which makes pairing with acceptors and transport layers necessary. The results of this study demonstrate that the dFT units are a viable method to further increase efficiency of organic solar cells, and dFT units can be especially useful for polymers that do not have locations for fluorination on the acceptor moiety.

4.4 Experimental Details

4.4.1 Synthesis of dFT-HTAZ
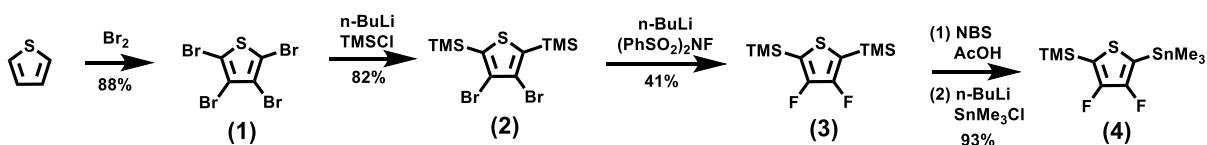
Scheme 4.2 – Synthesis of difluorinated thiophene linker

Synthesis of *2,3,4,5-Tetrabromothiophene* (**1**): First a solution of chloroform (20 mL) and thiophene (5.0 g, 0.06 mol, 1 eq.) was prepared and cooled to 0 °C with an ice/water bath. Then,

via addition funnel, a solution of chloroform (10 mL) and liquid bromine (5.4 mL, 0.21 mol, 3.5 eq.) was added dropwise slowly over the course of 4 hours. After that time period, the reaction mixture was allowed to warm to room temperature by removal the ice/water bath. An additional aliquot of liquid bromine (1.1 mL, 0.042 mol, 0.7 eq.) was added, and the reaction mixture was subsequently stirred under reflux for 4 hours. To remove any excess liquid bromine, a saturated aqueous solution of NaOH was added to quench the mixture. The reaction mixture continued to stir under reflux for one additional hour. To workup the reaction, the mixture was first extracted with dichloromethane (x3) and the combined organic portions were dried over magnesium sulfate. After filtration, the organic solution was concentrated under reduced pressure/rotovap. Finally, the crude solid was recrystallized from a 1:1 solution (by volume) of chloroform:ethanol to provide pure (1) as long colorless needlelike crystals (21.11 g, 88% yield).

Synthesis of *3,4-Dibromo-2,5-bis(trimethylsilyl)thiophene* (2): 2,3,4,5-Tetrabromothiophene (1) (15 g, 37.5 mmol, 1 eq.) was added to a 250 mL three-necked flask which was sequentially evacuated and refilled with argon three times. The starting material was then dissolved in anhydrous THF (80 mL) which was distilled over sodium and benzophenone (via THF still) under the protection of argon. The solution was cooled to -78 °C with dry ice/acetone bath. After cooling for 30 minutes, a solution of *n*-BuLi (2.5 M in hexanes, 15 mL, 37.5 mmol, 1 eq.) was slowly added in a dropwise fashion over the course of 15 minutes. After the final drops of *n*-BuLi were added, the mixture was stirred for 30 minutes. While the reaction flask was still at -78 °C, a solution of chlorotrimethylsilane (4.76 mL, 37.5 mmol, 1 eq.) was then added in one portion and stirring was maintained for 90 minutes. An additional 1 equivalent of *n*-BuLi (2.5 M in hexanes, 15 mL, 37.5 mmol, 1 eq.) was added dropwise to the reaction mixture, and after the solution was stirred for a further 30

minutes, a second portion of chlorotrimethylsilane (4.76 mL, 37.5 mmol, 1 eq.) was added.

The reaction mixture was then stirred for 30 minutes at -78 °C. After this time, the reaction

mixture was allowed to slowly warm to room temperature and left to stir overnight. To

workup the reaction mixture, first a saturated ammonium chloride solution (100 mL) was

prepared. The reaction mixture was quenched with water, opened to air, and then poured into

the ammonium chloride solution. The organic components of the mixture were extracted with

dichloromethane (x3), and the combined organic phases were washed with water (x3). After

being dried over MgSO$_4$, the organic phase was filtered and the resulting filtrate was

concentrated under reduced pressure/rotovap. The resulting colorless oil was purified by

vacuum distillation to give (**2**) (11.84 g, 82%). ^{1}H (400 MHz, CDCl$_3$): δ 0.39 (18H, s).

Synthesis of *3,4-Difluoro-2,5-bis(trimethylsilyl)thiophene* (**3**): 3,4-Dibromo-2,5-

bis(trimethylsilyl)thiophene (**2**) (10.9 g, 28.22 mmol, 1 eq.) was added to a multineck round

bottom flask, which was then evacuated and refilled with an argon atmosphere three times.

The starting material was dissolved in 150 mL dry tetrahydrofuran (from still) and cooled to -

78 °C in a dry ice/acetone bath. Then n-BuLi (2.5 M in hexane) and N-fluoro-N-

(phenylsulfonyl)benzenesulfonamide (herein abbreviated NFSI), which was dissolved in dry

THF, were added at -78 °C alternately in the following portions:

> i) n-BuLi (11.74 mL, 29.35 mmol, 1.04 eq.), stir for 30 min, then NFSI (9.25 g,
>   29.35 mmol, 1.04 eq.) dissolved in 50 mL THF, stir for an additional 30 min.
> ii) n-BuLi (5.87 mL, 14.67 mmol, 0.52 eq.), stir for 30 min, then NFSI (4.63 g,
>   14.67 mmol, 0.52 eq.) dissolved in 20 mL THF, stir for an additional 30 min.
> iii) n-BuLi (2.94 mL, 7.34 mmol, 0.26 eq.), stir for 30 min, then NFSI (2.31 g, 7.34
>   mmol, 0.26 eq.) dissolved in 15 mL THF, stir for an additional 30 min.
> iv) n-BuLi (1.47 mL, 3.67 mmol, 0.13 eq.), stir for 30 min, then NFSI (1.16 g, 3.67
>   mmol, 0.13 eq.) dissolved in 10 mL THF, stir for an additional 30 min.
> v) n-BuLi (1.47 mL, 3.67 mmol, 0.13 eq.), stir for 30 min, then NFSI (1.78 g, 5.64
>   mmol, 0.20 eq.) dissolved in 20 mL THF, stir for an additional 30 min.

The dry ice/acetone bath was removed and the mixture was stirred at room temperature overnight. To workup the reaction mixture, first the flask was quenched with water. This was followed with 200 mL of 1 M HCl being added to the suspension. The organic layer was separated, washed with brine (x3), and dried over magnesium sulfate. After filtration, the solution was concentrated under reduced pressure/rotovap and run through a silica gel plug using hexane as eluent. After removing the hexane under reduced pressure/rotovap, the resulting oil was purified via vacuum distillation and yielded (3) (3.06 g, 41%) as a colorless oil. ^{19}F (376 MHz, CDCl$_3$): δ -130.5 (s, 2F). ^{1}H (400 MHz, CDCl$_3$): δ 0.32 (s, 18H).

Alternatively, we have also tried a different approach where the order of addition for n-BuLi and NFSI was changed: First, 3,4-Dibromo-2,5-bis(trimethylsilyl)thiophene (2) (24.60 g, 63.7 mmol, 1 eq.) and NFSI (36.15 g, 114.6 mmol, 1.8 eq.) were added to a multineck round bottom flask which was evacuated and refilled with argon three times. The starting material and NFSI where then dissolved in dry tetrahydrofuran (from still) and cooled to -78 °C in a dry ice/acetone bath. Then n-BuLi (2.5 M in hexane) and NFSI were added at -78 °C in the following portions:

i) n-BuLi (17.8 mL, 44.60 mmol, 0.7 eq.), stir for 1 h,
ii) n-BuLi (17.8 mL, 44.60 mmol, 0.7 eq.), stir for 1 h,
iii) n-BuLi (17.8 mL, 44.60 mmol, 0.7 eq.), stir for 1 h,
iv) NFSI (24.10 g, 76.4 mmol, 1.2 eq.) dissolved in dry THF, stir for 30 min,
v) n-BuLi (30.6 mL, 76.4 mmol, 1.2 eq.), stir for 1 h,
vi) NFSI (20.08 g, 63.7 mmol, 1 eq.) dissolved in dry THF, stir for 30 min,
vii) n-BuLi (25.5 mL, 63.7 mmol, 1 eq.), stir for 1 h,

The dry ice/acetone bath was then removed and the mixture was stirred at room temperature overnight. The mixture was quenched with water, and the workup began with extracting the organic layer with ethyl acetate. After being washed with brine (x2) and water

(x2), and dried over magnesium sulfate, the organic phase was filtered and the resulting solution was concentrated under reduced pressure and run through a silica gel plug using hexane as eluent. After removing the hexane under reduced pressure/rotovap, vacuum distillation yielded (3) (6.74 g, 40%) as a colorless oil. Interestingly, both procedures produced nearly identical yields. In previous reports, when synthesizing a mono-fluorinated thiophene unit, the yields for the different protocols varied largely.

Synthesis of *3,4-Difluoro-2-trimethylsilyl-5-(trimethylstannyl)thiophene* **(4)**:A mixture of 3,4-Difluoro-2,5-bis(trimethylsilyl)thiophene **(3)** (6.4 g, 24.2 mmol, 1 eq.) and NBS (*N*-bromosuccinimide) (4.73 g, 26.6 mmol, 1.1 eq.) in acetic acid was stirred at 80 °C overnight. The reaction mixture was wrapped in aluminum foil to minimize light exposure, and the reaction proceeded under a normal air atmosphere. The resulting mixture was purified using the following protocol: first, the reaction mixture was poured into water and extracted with ethyl acetate. The resulting organic layer was washed with 1 M NaOH, brine, and water (x1 each), then dried with magnesium sulfate. After filtration, the filtrate was concentrated under reduced pressure/rotovap. The resulting residue was purified through silica gel column (hexanes eluent), to yield the intermediate (3.64 g, 56%). Warning, the intermediate is very low boiling point and can be pulled off at low temperatures on the rotovap. ^{19}F (376 MHz, CDCl$_3$): δ -125.4 (d, J=14.4 Hz, 1F), -134.5 (d, J=14.1 Hz, 1F). ^{1}H (400 MHz, CDCl$_3$): δ 0.32 (s, 9H).

The resulting brominated material (2.98 g, 10.99 mmol, 1 eq.) was added to a flask which was then evacuated and refilled with argon three times. The oil was solubilized in dry THF (30 mL) from the still, and the mixture was cooled with a dry ice/acetone bath. Next, 2.5 M n-BuLi in hexanes (4.6 mL, 11.54 mmol, 1.05 eq.) was added to the flask, still at -78

113

°C and under argon. The mixture was stirred at -78 °C for 30 minutes. A 1 M solution of

Me$_3$SnCl in hexanes (12.1 mL, 12.09 mmol, 1.1 eq.) was added dropwise, and the resulting

solution was stirred at -78 °C for 1 hour. The reaction mixture was allowed to warm to room

temperature for 45 minutes and was then quenched with water. After extraction with

hexanes, the organic layer was washed with brine (x3), dried with magnesium sulfate,

filtered, and concentrated under reduced pressure/rotovap to give **(4)** as a faint yellow oil

(3.63 g, 93%). Note: there were trace impurities on the ^{19}F NMR spectra, but the ^{1}H NMR

spectra was clean. ^{19}F (376 MHz, CDCl$_3$): δ -131.1 (d, J=16.6 Hz, 1F), -131.8 (d, J=16.8 Hz,

1F). ^{1}H (400 MHz, CDCl$_3$): δ 0.40 (s, 9H), 0.31 (s, 9H).
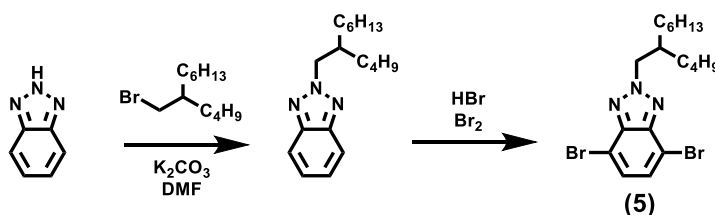
Scheme 4.3 – Synthesis of benzotriazole core

Synthesis of *4,7-dibromo-2-(2-butyloctyl)-2H-benzo[d][1,2,3]triazole* **(5)**:4,7-

dibromo-2-(2-butyloctyl)-2H-benzo[d][1,2,3]triazole **(5)** was synthesized according to

previously literature reports. (doi.org/10.1021/cm802937x)
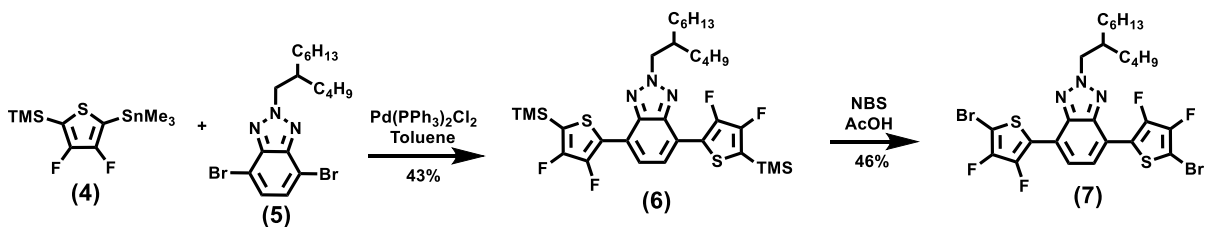
Scheme 4.4 – Synthesis of dFT-HTAZ monomer

Synthesis of *2-(2-butyloctyl)-4,7-bis(3,4-difluoro-5-(trimethylsilyl)thiophen-2-yl)-2H-*

benzo[d][1,2,3]triazole **(6)**: Both **(4)** (3.6 g, 10.2 mmol, 2.5 eq.) and **(5)** (1.8 g, 4.05 mmol, 1.0

eq.) were added to a multineck round bottom flask fitted with a condensing column. The

114

flask was evacuated and refilled with an argon atmosphere three times. The starting materials

where dissolved by the addition of anhydrous toluene. Finally,

bis(triphenylphosphine)palladium (II) dichloride (86 mg, 0.12 mmol, 0.03 eq.) was added

under argon stream. The reaction mixture was purged with argon for 30 minutes, which was

then refluxed for 50 hours. Toluene was removed under reduced pressure/rotovap, and the

reaction mixture was purified through silica gel column (9:1 hexanes:dichloromethane

eluent), to yield (**6**) as a yellow oil (1.15 g, 43%). ^{19}F (376 MHz, CDCl$_3$): δ -128.4 (d, J=15.6

Hz, 2F), -133.8 (d, J=15.3 Hz, 2F). ^{1}H (400 MHz, CDCl$_3$): δ 7.89 (s, 2H), 4.79 (d, J=4.24 Hz,

2H), 2.28 (m, 1H), 1.19-1.49 (m, 16H), 0.80-0.94 (m, 6H), 0.32 (s, 18H).

Synthesis of *4,7-bis(5-bromo-3,4-difluorothiophen-2-yl)- 2-(2-butyloctyl)-2H-benzo[d][1,2,3]triazole* (**7**):The starting material (**6**) (1.15 g, 1.71 mmol, 1.0 eq.) was added to

a flask which was then evacuated and refilled with argon three times. The starting material

was then dissolved in a mixture of dichloromethane:acetic acid = 10:1 (33 mL) which was

purged with argon gas for 1 hour. NBS (630 mg, 3.54 mmol, 2.05 eq.) was then added under

a stream of argon, and the reaction mixture was stirred in dark at ambient temperatures

(under argon) for 75 hours. To workup the reaction, the reaction mixture was first poured

into a mixture of water and ethyl acetate (1:1). The organic layer was extracted with ethyl

acetate (x2), and the combined organic layer was washed with water and brine (x2). The

organic solution was dried over magnesium sulfate, filtered, and concentrated under reduced

pressure/rotovap. The crude product was purified through silica gel column (20:1

hexanes:dichloromethane elutent), and (**7**) was further recrystallized in ethanol multiple

times. The resulting yellow crystalline powder was the product (520 mg, 46%). Overall

reaction scheme yield: 2.5%. ^{19}F (376 MHz, CDCl$_3$): δ -130.7 (d, J=12.9 Hz, 2F), -134.1 (d,

J=12.9 Hz, 2F). ^{1}H (400 MHz, CDCl$_3$): δ 7.92 (s, 2H), 4.75 (d, J=6.34 Hz, 2H), 2.26 (m, 1H),

1.28-1.51 (m, 16H), 0.92 (t, J=7.22 Hz, 3H), 0.87 (t, J=6.63 Hz, 3H).
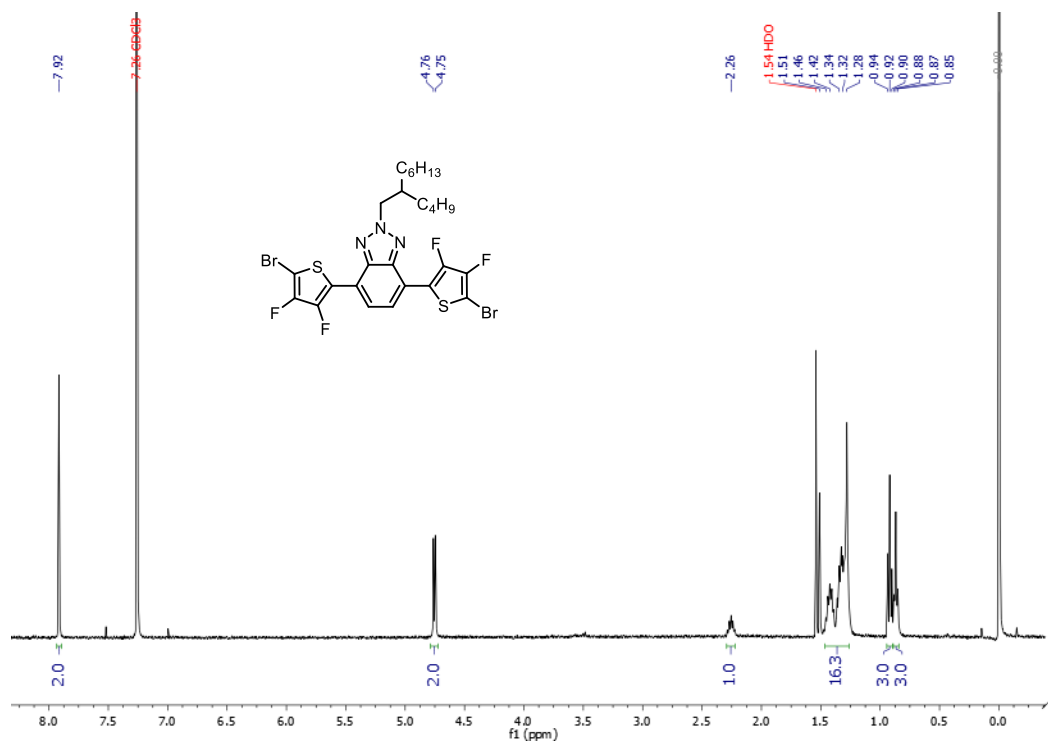
Figure 4.11 – ^{1}H NMR for dFT-HTAZ monomer
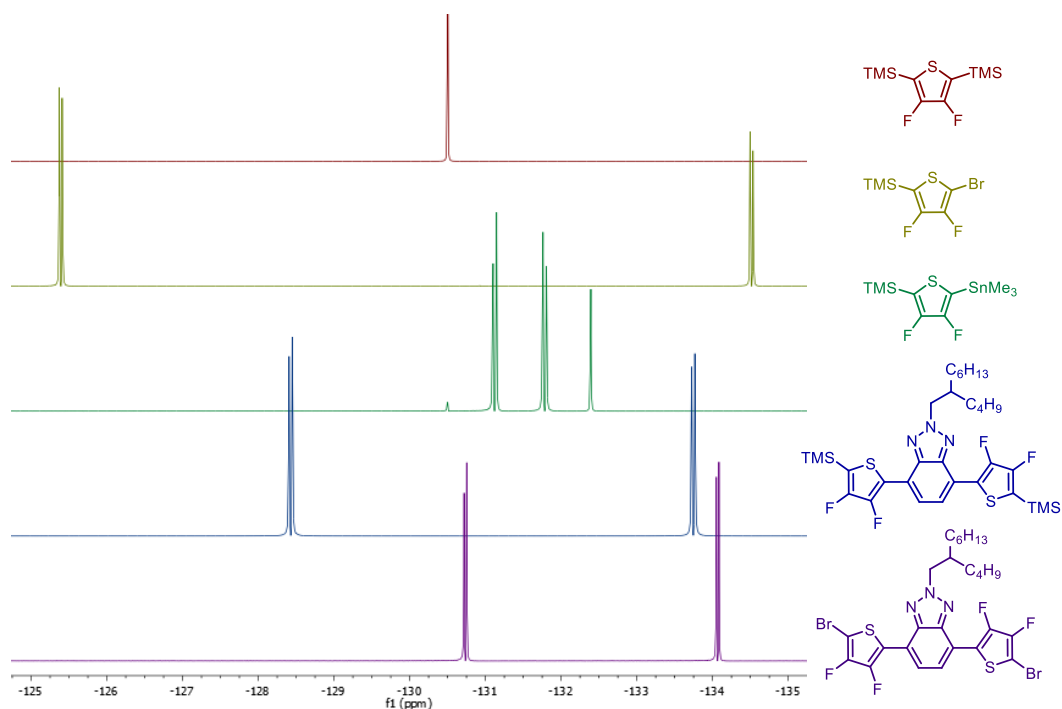
Figure 4.12 – ^{19}F NMR for dFT-HTAZ monomer and various precursors
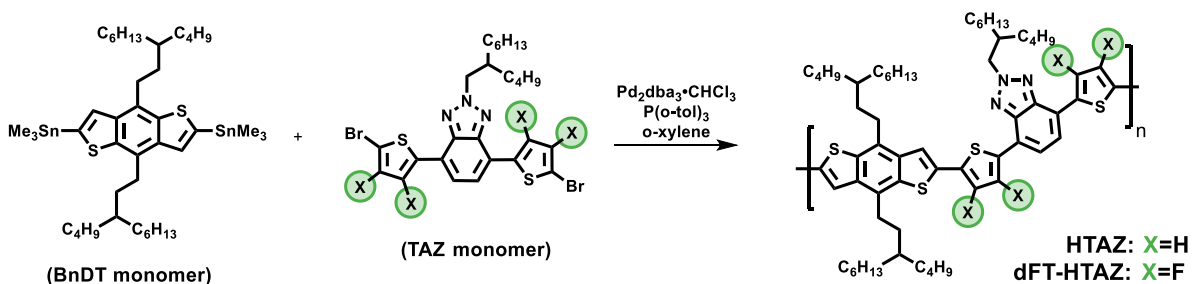
Scheme 4.5 – Polymerization of HTAZ and dFT-HTAZ

Polymerization of HTAZ and dFT-HTAZ: BnDT monomer (0.100 mmol, 1 eq.), TAZ

monomer (0.100 mmol, 1 eq.), $Pd_2(dba)_3 \cdot CHCl_3$ (0.002 mmol, 0.02 eq.) and P(o-tol)$_3$ (0.016

mmol, 0.16 eq.) were charged into a 10 mL vial designed for microwave reactor. The mixture

was evacuated and refilled with argon for three cycles before addition of anhydrous o-xylene

under an argon stream. The reaction was heated up to 200 °C and held at that temperature for

10 min in a CEM microwave reactor. After the polymerization, the crude polymer was

dissolved in hot chlorobenzene and precipitated into stirring methanol. The collected polymer

was extracted via a Soxhlet extractor with ethyl acetate, hexanes, and chloroform. The

polymer solution in chloroform was concentrated under reduced pressure/rotavap, and the

polymer was redissolved into a minimal amount of hot chlorobenzene and precipitated into

methanol. The polymer was then collected via vacuum filtration and formed a thin metallic

golden colored film, which was then dried under vacuum. Note: the molecular weight of the

polymer can be controlled by tuning the ratio of the BnDT and TAZ monomers.

4.4.2 Characterization Details

^{1}H and ^{19}F nuclear magnetic resonance (NMR) measurements were recorded with

Bruker DRX spectrometer (400 MHz). UV-Visible absorption spectra were obtained with a

Shimadzu UV-2600 spectrophotometer. CV measurements were carried out on thin films

using a Bioanalytical Systems Epsilon potentiostat with a standard three-electrode

configuration. A three electrode cell of a glassy carbon working electrode, Ag/Ag$^+$ reference

electrode, and Pt counter electrode were used. Films of the FREAs were drop-cast onto the glassy carbon electrode from hot chloroform solution (2 mg/mL, with tetrabutylammonium hexafluorophosphate added at 100 wt%) and dried using a heat gun. 0.1 M solution of tetrabutylammonium hexafluorophosphate in anhydrous acetonitrile was used as a supporting electrolyte. Scans were carried out under argon atmosphere at a scan rate of 100 mV/s. The reference electrode was calibrated using a ferrocene/ferrocenium redox couple. Solar cell devices were tested under AM 1.5G irradiation calibrated with an NREL certified standard silicon solar cell. Current density-voltage curves were measured via a Keithley 2400 digital source meter. GIWAXS measurements were performed at beamline 7.3.3 (DOI: 10.1088/1742-6596/247/1/012007) at the ALS. The 10 KeV X-ray beam was incident at a grazing angle of 0.13 degree. The scattered X-rays were detected using a 2D area detector (Pilatus 1M). All measurements were conducted under He atmosphere to reduce air scattering.

SCLC mobility was acquired through the hole-only devices with a configuration of ITO/PEDOT:PSS/active layer/MoO_3/Al. The experimental dark current densities J were measured by Keithley 2400. The applied voltage V was corrected from the voltage drop V_{rs} dur to the series resistance and contact resistance, which were found from a reference device without the active layer, and the build-in potential, which are estimated from the V_{OC} of corresponding hole-only devices under 1 sun condition. From the plots of $J^{0.5}$ vs V, hole mobilities of polymers were deduced from the Mott-Gurneys law:

$$J = \frac{9}{8} \varepsilon_r \varepsilon_o \mu_h \frac{V^2}{L^3}$$

where ε_0 is the permittivity of free space, ε_r is the dielectric constant of the polymer which is assumed to be around 3, μ_h is the hole mobility, V is the voltage drop across the device, and L is the film thickness of the active layer.

4.4.3. Device Fabrication

Glass substrates coated with patterned indium doped tin oxide (ITO) were purchased from Thin Film Devices, Inc. About 150 nm sputtered ITO pattern had a resistivity of 20 Ω/sq. Prior to use, the substrates were ultrasonicated in deionized water, acetone, and then 2-proponal for 15 min each. The substrates were dried under a stream of nitrogen gas and subjected to the treatment of UV−ozone for 15 min. The devices were made by the following methods: (1) Polymer:PCBM blends with device stack: ITO/HTL/polymer:PCBM/Ca/Al.

For devices with PEDOT:PSS as the hole transport layer, a filtered dispersion of PEDOT:PSS in water (Clevios PH500 from Heraeus) was then spun cast onto cleaned ITO substrates at 4000 rpm for 60 s and then baked at 130 °C for 15 min in air to give a thin film with a thickness of about 40 nm. For devices with CuSCN as the hole transport layer, the CuSCN was dissolved in diethylsulfide with the concentration 22.7 mg/mL under stirring for 1 h. Then the CuSCN solution was filtered by 0.2 μm poly(tetrafluoroethylene) (PTFE) filter and spun-cast on the cleaned ITO substrates at 7000 rpm for 60 s and then baked at 100 °C for 10 min in air to give a thin film with a thickness of about 40 nm. Then blends of polymer:PC$_{61}$BM (1:2 w/w) were dissolved in chlorobenzene and 3% 1,8-diiodooctane with heating at 130 °C for 6 h. All the solutions were filtered through a 5.0 μm PTFE filter and spun-cast at an optimized rpm for 60 s onto the PEDOT:PSS or CuSCN layer. The devices were finished for measurement after thermal deposition of a 30 nm film of calcium and a 70

nm aluminum film as the cathode for a conventional structure at a base pressure of 2×10^{-6} mbar. There are 8 devices per substrate, with an active area of 13 mm^2 per device.

(2) Polymer:ITIC/ITIC-Th1 blends with device stack: ITO/ZnO/polymer:acceptor/MoO$_3$/Al.

The ZnO precursor solution was prepared by dissolving 1 g zinc acetate dihydrate and 0.28 g ethanolamine in 10 mL of 2-methoxyethanol. The solution was stirred overnight, then spun cast onto the cleaned ITO slides at 4,000 rpm for 30 s and baked for 30 min at 150 °C in air. The substrates were then transferred to a nitrogen filled glovebox for active layer deposition. For polymer:ITIC and polymer:ITIC-Th1 devices, the polymers:acceptor (1:1 w/w) were dissolved in tolune with heating at 80 °C for 6 h. The active layer solutions were then spun-cast atop the ZnO layer at an optimized RPM for 60 s, followed by thermal annealing at 150 °C for 15 min. The devices were finished by evaporation of 10 nm of MoO$_3$ and 70 nm of aluminum. These blends also have 8 devices per substrate, with an active area of 13 mm^2 per device.

CHAPTER 5: Effect of Cyano Substitution on Conjugated Polymers for Bulk Heterojunction Solar Cells [14]

5.1 Introduction

As shown in the previous chapter, the most widely-studied electron-withdrawing substituent is fluorine, which can effectively tune energy levels, charge transport properties, and morphology of active layer of OSCs and to correspondingly improve efficiency of OSCs.[275–277] However, some limitations are associated with fluorine substitution: due to the resonance donating properties of fluorine, the decrease of energy levels of polymers induced by fluorine substitution is limited, which consequently limits the enhancement of the open circuit voltage (V_{OC}); moreover, the effect of fluorine on the band gap and absorption of conjugated polymers are usually minor, which hinders the improvement of the short circuit current density (J_{SC}) by absorption of fluorinated polymers.[275–277] To provide an example, we recently found that putting fluorine substituents on appropriate positions of thiophene linker units can extend the absorption of polymers by planarizing the polymer backbones;[135] however, the red-shift induced by fluorinating thiophene units only occurred when substituted to certain locations. As a result, J_{SC} values of corresponding devices were only marginally improved.

---

[14] Parts of this chapter previously appeared as an article in *ACS Applied Polymer Materials*. Reprinted with permission from © 2021 American Chemical Society. The original citation is as follows: Qianqian Zhang, **Jeromy James Rech**, Liang Yan, Quanbin Liang, Zhengxing Peng, Harald Ade, Hongbin Wu, and Wei You. "Effect of Cyano Substitution on Conjugated Polymers for Bulk Heterojunction Solar Cells." *ACS Applied Polymer Materials*, **2019**, 1 (12), 3313-3322.

Compared to the widely-studied fluorine substitution, the cyano functional group is a stronger electron withdrawing functional group due to the inductive and resonance effects, thus, adding cyano substituent to conjugated polymer backbones can decrease the highest occupied molecular orbital (HOMO) energy level of the polymer by a larger degree and shift the absorption of the polymers to long wavelength, which benefits the V_{OC} and J_{SC} of the solar cells respectively.[147,278] Currently, cyano units are widely used in non-fullerene acceptors end groups; however, cyano-substituted polymers with high performance have not been widely reported.[141,279–282] In our previous study, Li *et al*. developed a benzotriazole (TAZ) acceptor moiety based polymer with two cyano units on the TAZ unit (CNTAZ, renamed diCNTAZ herein for clarity)[141] and achieved an efficiency of 6.0 %. While a high V_{OC} was obtained with deeply-lying HOMO level, the J_{SC} was low despite of the large red-shift of absorption, which together with the low fill factor (*FF*), limited the improvement of efficiency to a higher value. However, by adding single cyano unit to pyridine-fused-triazole (PyTAZ) unit (PyCNTAZ), Li *et al*. were able to achieve a high efficiency of 8.4% with PCBM as electron acceptor material with much improved V_{OC}, J_{SC} and *FF*. While this result shows great promise, the source of the distinct device performance of diCNTAZ and PyCNTAZ was unclear because of the structural differences: which of the different chemical structure (PyTAZ unit vs. TAZ unit) or the amount of cyano unit (one vs. two per repeating unit) played the most important role?

In order to get a comprehensive understanding of the effect of the cyano substitution on polymers, in this study, we synthesized a series of polymer with varying amounts of cyano group on the TAZ unit: HTAZ (0), monoCNTAZ[147] (1), and diCNTAZ (2). Along with understanding the optical, electrochemical, and photovoltaic characteristics, we also

explored changes in morphology, charge transfer state energy, charge carrier density and lifetime, and non-geminate recombination rate as the number of cyano substituents change. Interestingly, the monoCNTAZ polymer outperformed both the HTAZ and diCNTAZ when these polymers were employed in OSCs. With just one cyano substituent per repeating unit, monoCNTAZ blends achieved a high V_{OC} value close to that of diCNTAZ. In addition, the red-shifted absorption of monoCNTAZ effectively resulted in a high J_{SC} of its solar cells. Also, noticeably improved hole mobility of monoCNTAZ blends improved the *FF*; thus, a high efficiency of 8.6% (average) is achieved by monoCNTAZ:PCBM blends. Our results demonstrate both the benefits that cyano functionalization can offer and the limitations of this approach.

5.2 Results and Discussion

5.2.1 Synthesis
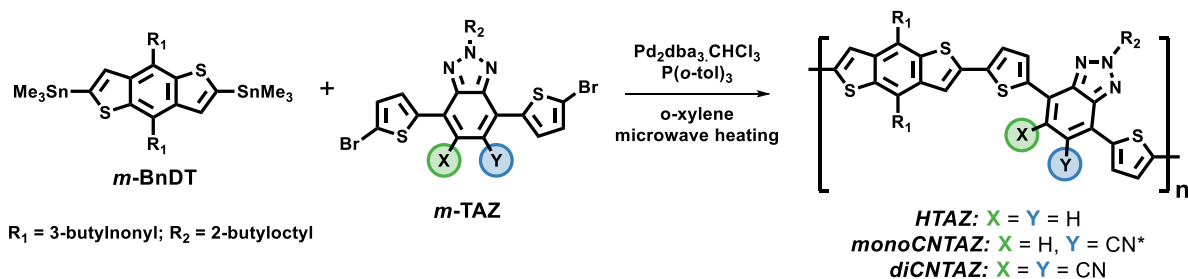
Scheme 5.1 – Microwave-assisted Stille-polycondensation approach to synthesis three polymers: HTAZ, monoCNTAZ, and diCNTAZ. *Note, the cyano group of monoCNTAZ can be in either the X or Y position, so both X=H, Y=CN and X=CN, Y=H represent the monoCNTAZ polymer.

The conjugated polymers are made via step growth polymerization between the benzodithiophene monomer (*m*-BnDT) and functionalized benzotriazole monomer (*m*-TAZ), as shown in **Scheme 5.1**. For clarity, we will use HTAZ, monoCNTAZ and diCNTAZ to represent the polymers and use *m*-HTAZ, *m*-monoCNTAZ and *m*-diCNTAZ to represent the corresponding *m*-TAZ based monomers in the following discussion.

123

Scheme 5.2 – Synthesis of monoCNTAZ and diCNTAZ monomers
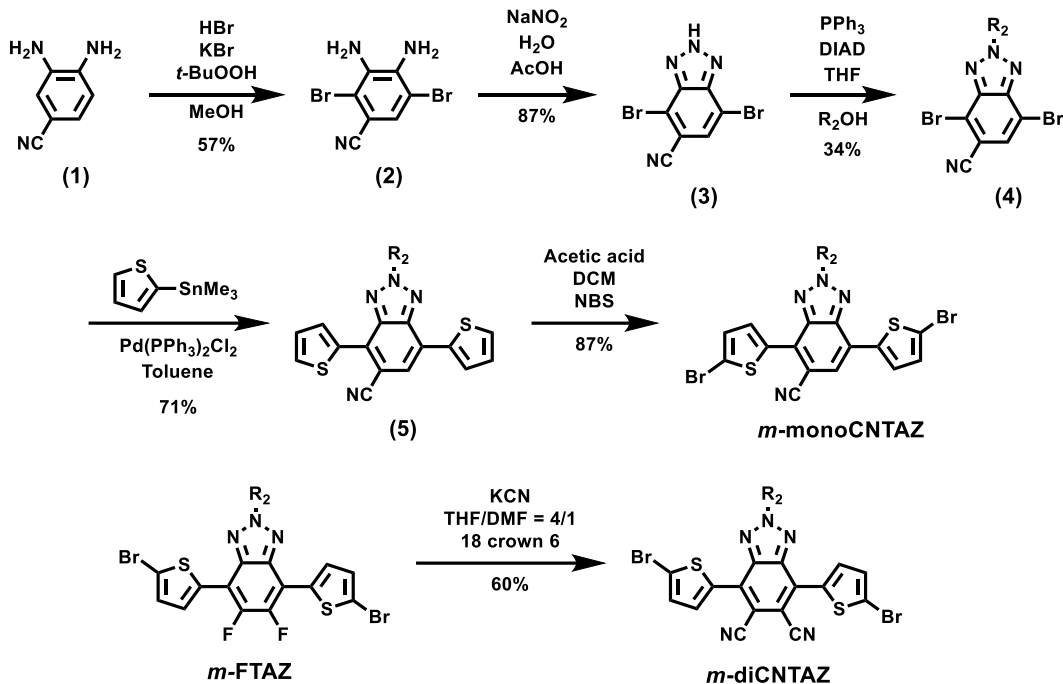
The synthesis of *m*-BnDT and *m*-HTAZ follows literature procedures[125,135] and the reaction schemes for *m*-monoCNTAZ and *m*-diCNTAZ are shown in **Scheme 5.2**. The starting material for the *m*-monoCNTAZ is 3,4-diaminobenzonitrile (compound **1**). Compound **1** underwent oxidative bromination with potassium bromide, hydrogen bromide acid and *tert*-butyl hydroperoxide to achieve compound **2**.[283] Following purification, compound **2** was cyclized to obtain the triazole structure of compound **3**. After alkylation of N-2 position of compound **3**, compound **4** was then subjected to Stille coupling reaction with a stannylated thiophene linker to achieve compound **5**. Afterwards, compound **5** was subsequently brominated by excessive *N*-bromosuccinimide (NBS) to obtain the *m*-monoCNTAZ. Please note that the substitution of one CN group on the TAZ unit significantly reduces the reactivity of compound **5**, so excessive NBS together with an extended time (7 days) was needed. Even through these reaction conditions are unfavorable,

124

the resulting monomer was made with appropriate yields and after recrystallization, had very high purity appropriate for polymerization.

PATHWAY A **2.8 % overall yield**

PATHWAY B **7.2 % overall yield**
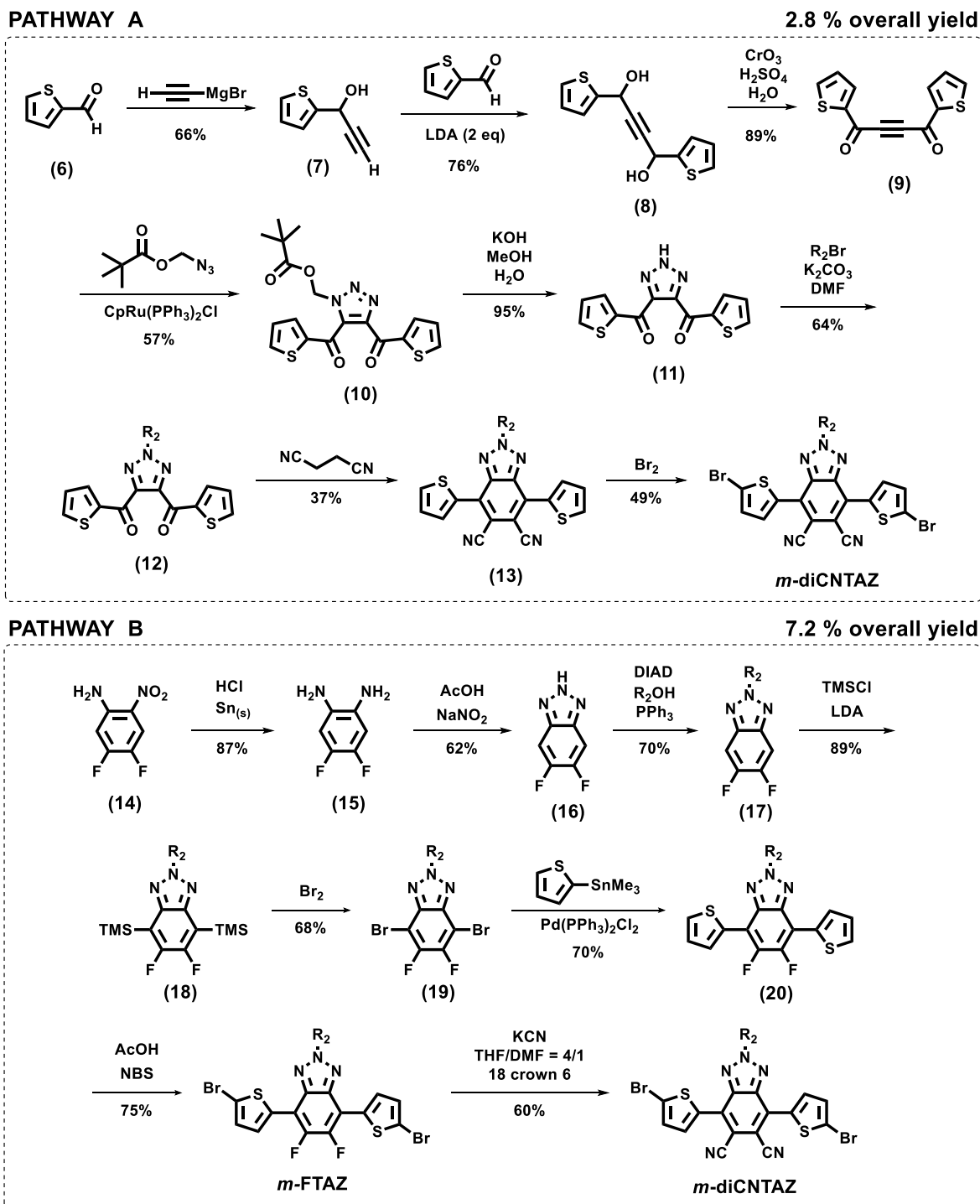
Scheme 5.3 – Two pathways to synthesize the diCNTAZ monomer, where Pathway A was previously reported in literature and Pathway B is newly developed.

125

We have previously reported the synthesis of *m*-diCNTAZ based on a general methodology, which is shown as Pathway A in the **Scheme 5.3**.[141] In this study, a new synthetic approach, Pathway B (**Scheme 5.3**), was developed to get *m*-diCNTAZ from fluorinated TAZ monomer (*m*-FTAZ) via nucleophilic aromatic cyanation (shown in **Scheme 5.2**), as *m*-FTAZ can be readily prepared with higher yields. After we succeeded to prepare *m*-diCNTAZ through the new reaction approach, Casey *et al*. reported a similar synthetic approach through nucleophilic aromatic cyanation on an FTAZ compound but without bromo-unit and brominated the cyano- substituted-TAZ compound to obtain the final monomer, which thus also suffered from the low yield in the bromination step due to the decreased reactivity with strong electron withdrawing cyano unit.[282] Comparing the two different pathways (**Scheme 5.3**), each have the same number of reaction steps and the yields for most steps are similar, with the key exception of the last two steps. In Pathway A, the condensation of compound **12** and succinonitrile suffers from a low yield of 37 %. This is nearly half the yield of the new approach (Pathway B) to add the cyano substituents (60%). Also in Pathway A, NBS was unable to brominate the monomer because of the highly electron deficient backbone. Instead of NBS, molecular bromine was required to make the final monomers. Along with lower yields, molecular bromine can more easily lead to overbromination. Using the new approach of Pathway B, the bromination of the fluorinated benzotriazole can be done in higher yields with the milder NBS reagent. Therefore, when comparing the overall yield of both synthetic approaches, the newly developed Pathway B offers a higher overall yield of 7.2 %, which is 2.5× higher than the 2.8 % yield from the originally reported Pathway A. This new pathway is also advantageous, as many current

126

fluorinated monomers can be converted to cyano functionalized polymers in a single

reaction, allowing for many new types of conjugated polymers to be made.

Finally, the polymers (HTAZ, monoCNTAZ, and diCNTAZ) were synthesized

through microwave-assisted Stille-coupling based polymerization methodology.[158] The

number average molar mass (M_n) of each polymer, ranging from 44 to 52 kg/mol, was

optimized by adjusting the monomer ratios. The molar mass for each polymer was measured

through high temperature gel permeation chromatography (HT-GPC), and the resulting traces

are shown in **Figure 5.1**. The polymers all exhibited high thermal stability, with

decomposition temperature (T_d, 5% weight loss temperature) around 400 °C, as measured by

thermogravimetric analysis (TGA) and no thermal transitions in the processing window, as

measured by differential scanning calorimetry (DSC) (**Figure 5.2**). All three polymers can be

dissolved in common solvent used in OSCs, such as chloroform and chlorobenzene at

elevated temperature. While the solubility of monoCNTAZ is significantly reduced when

compared to HTAZ and diCNTAZ, it is still appropriate for device fabrication.
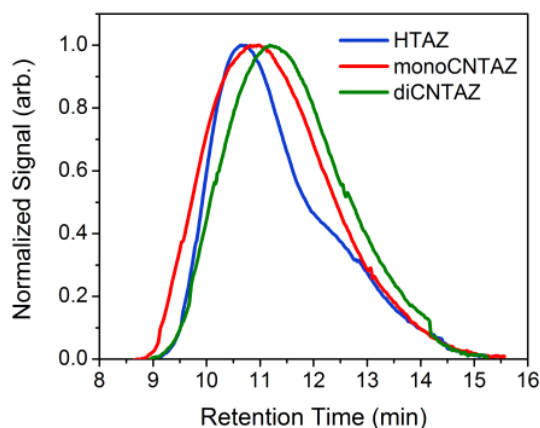
Figure 5.1. HT-GPC curves of HTAZ, monoCNTAZ, and diCNTAZ polymers at 160°C
with 1,2,4-trichlorobenzene as eluent.
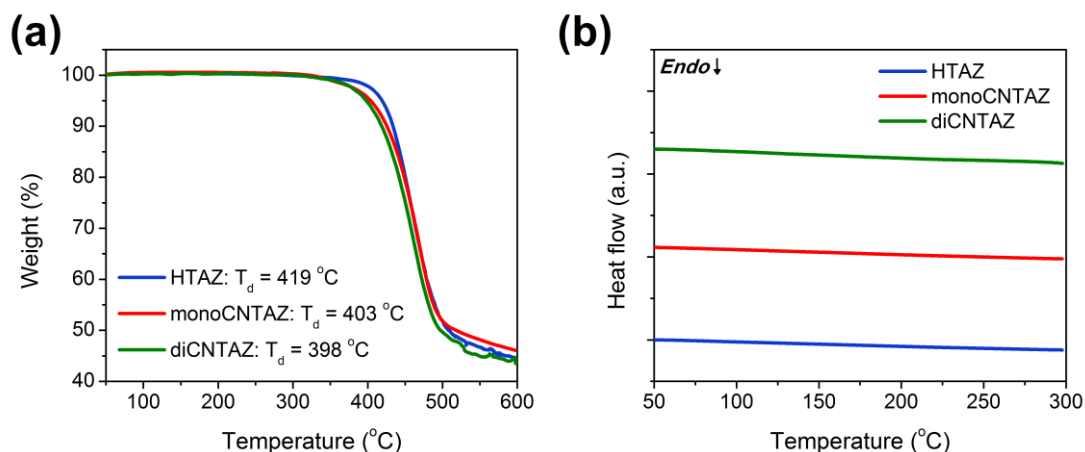
Figure 5.2. (a) TGA scan for all three polymers, including T_d (decomposition temperature, i.e. where 5% weight loss occurs), at ramp rate of 10 °C/min, and (b) second heat DSC scans of all three polymers at 10 °C/min.

5.2.2 Optical and Electrochemical Properties

Once the polymers where synthesized, the next characterization approach was to look at the optical and electrochemical properties for each. To begin with, the optical properties of the polymers were investigated with UV-Vis absorption of the polymer solution in 1,2-dichlorobenzene (*o*-DCB) (**Figure 5.3a**) and polymer thin films (**Figure 5.3b**). By comparison, a gradual bathochromic shift of the UV-Vis absorption induced by cyano substituents was observed: for each cyano substituent, the absorption edge shows a red-shift by 30 – 40 nm, and the optical band gap decreases by ~ 0.1 eV. Additionally, the UV-Vis absorption spectra of the polymers in solution at room temperature are almost the same with that of thin films, which means the polymer chains already aggregate in the solution at ambient conditions. Finally, the thickness normalized absorption coefficient is both high (~ 10^5 cm^{-1}) and similar for each of the polymers, suggesting the key impact of the cyano substituent is the red shift of absorbance.
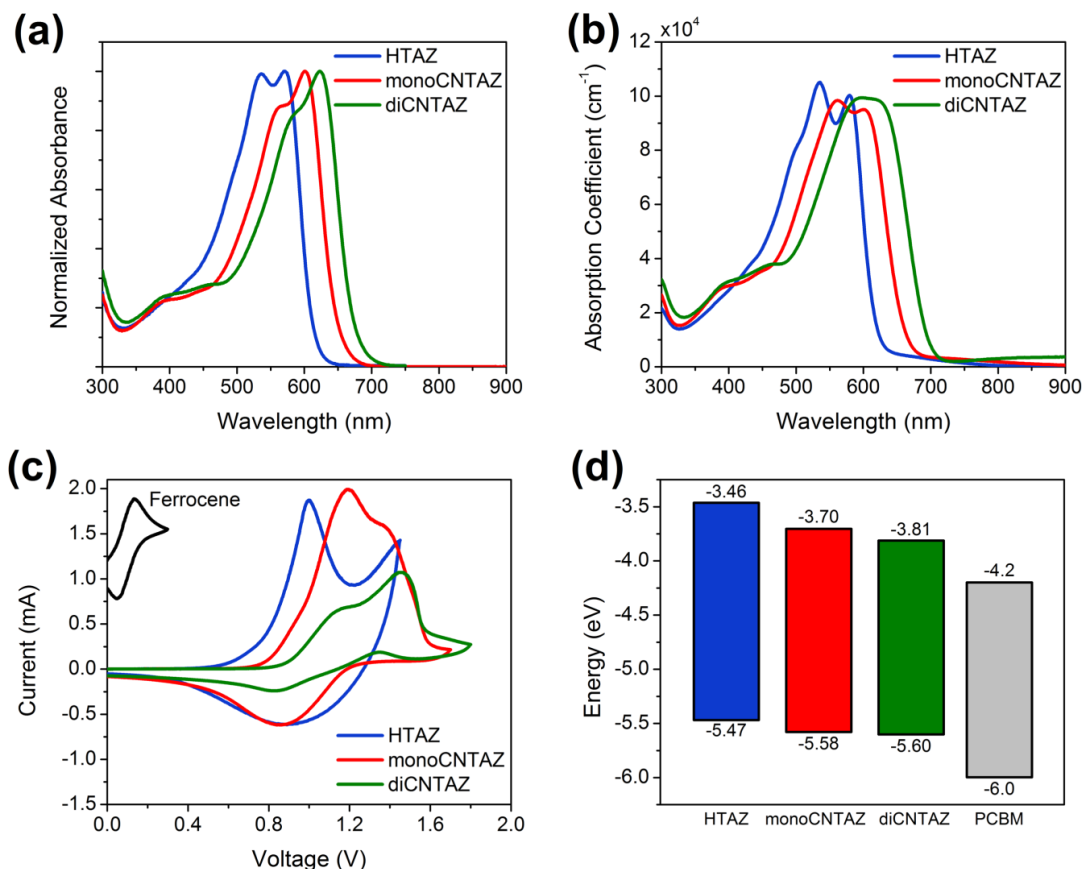
Figure 5.3 – (a) Solution UV-Vis for HTAZ, monoCNTAZ, and diCNTAZ in 1,2-dichlorobenzene, (b) thickness-normalized absorption coefficient of thin polymer films measured through UV-Vis, (c) cyclic voltammetry of polymer thin films to determine HOMO energy level using a three electrode set up of glassy carbon working electrode, Ag/Ag$^+$ reference electrode and Pt counter electrode, and (d) resulting HOMO/LUMO energy level diagram for each polymer and PCBM in this study.

Next, the electrochemical properties of each polymer were measured through cyclic voltammetry (CV). The HOMO energy levels of the polymers were measured by the onset of the oxidation peaks, shown in **Figure 5.3c**. Using the ferrocene/ferrocenium reference peak, the HOMO levels are estimated to be – 5.48, – 5.58, and – 5.60 eV for HTAZ, monoCNTAZ, and diCNTAZ, respectively (more details available in section 5.4). This follows as the strong electron withdrawing nature of the cyano substituent should pull down the energy levels of the conjugated polymer. Interestingly, the degree of the HOMO level decrease induced by

the second cyano unit is smaller than by the first cyano unit, indicating that further addition of the cyano substituent to already electron-deficient aromatics only offer a diminished return. Similar behavior has been observed in our previous report where the PBnDT-FTAZ polymer (with difluorinated benzotriazole) only has negligible decrease of the HOMO energy level when compared with the HOMO of the monofluorinated version.[145] The energy levels for each polymer and PCBM is shown in **Figure 5.3d**. The lowest occupied molecular orbital (LUMO) energy level is estimated through using the HOMO energy level found via CV and the optical band gap measured from the absorption onset of the UV-Vis spectra. A summary of the optical and electrochemical properties can be found in **Table 5.1**.

Table 5.1 – Molar mass, optical, and electrochemical properties of the three polymers

Polymer	M_n (kg/mol)	Đ (M_w/M_n)	Absorbance Onset (nm)	HOMO[a] (eV)	LUMO[b] (ev)	Optical Band Gap[c] (eV)
HTAZ	44.1	3.0	616	– 5.47	– 3.46	2.01
monoCNTAZ	52.0	3.5	658	– 5.58	– 3.70	1.88
diCNTAZ	50.6	3.3	693	– 5.60	– 3.81	1.79

[a]HOMO levels were estimated by cyclic voltammetry; [b] LUMO = HOMO + optical band gap; [c]Optical band gap was estimated from the onset of absorption of polymer films

5.2.3 Photovoltaic Properties

The photovoltaic properties of the three polymers were investigated in the bulk heterojunction (BHJ) solar cells with a conventional device configuration: indium doped tin oxide (ITO)/copper(I) thiocyanate (CuSCN)/polymer:PCBM/Ca/Al. The weight ratio of the polymer:PCBM was 1:2 for all the three polymer blends, and because of the deep HOMO energy levels of the polymers, CuSCN was selected as the hole transporting layer.[269] The *J-V* curves and EQE curves of thick (~ 300 nm) solar cell devices are presented in **Figure 5.4**,

respectively, with the related device characteristics summarized in **Table 5.2**. The photovoltaic properties of the solar cell devices at different thickness can be found in **Table 5.3**, and slightly higher efficiency can be obtained at lower thickness for HTAZ and diCNTAZ. In addition to the above device architecture, a second set of devices were fabricated with a slightly modified structure of ITO/PEDOT:PSS/polymer:PCBM/PFN (5nm)/Al (80nm), where PFN is poly[(9,9-bis(3′-(N,N-dimethylamino)propyl)-2,7-fluorene)-alt-2,7-(9,9–dioctylfluorene)].[284] This device structure was used for transient photocurrent (TPC) and transient photovoltage (TPV) measurements (*vide infra*). The efficiency of the devices used for TPC and TPV are also shown in **Table 5.2.** Both device architectures produce similar photovoltaic characteristics. We note that the devices with PFN interlayer shows relatively higher *FF* regardless of active layer, indicating PFN plays an role in facilitating charge transport and extraction.[285] On the other side, the J_{SC} values of corresponding devices with PFN interlayer were smaller, which can be ascribed to (a) unfavorable nanoscale morphology of the active layer when PFN was used and (b) thinner films of the devices with the PFN interlayer . Nevertheless, these devices show similar trends in V_{OC} and J_{SC}, thus enable us to probe charge carrier recombination dynamics in freshly made devices.
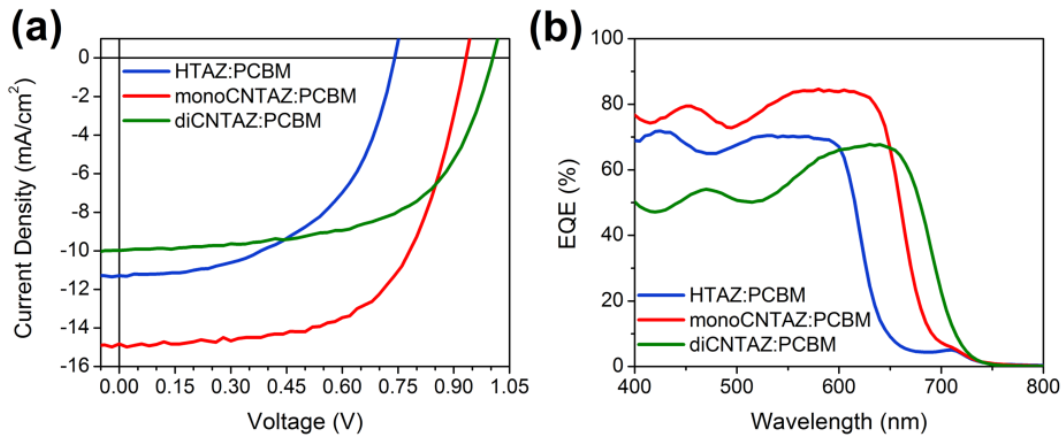
Figure 5.4 – (a) Representative *J-V* curve and (b) EQE curves of each OSC device

Table 5.2 – Photovoltaic properties of the various polymer solar cells

Polymer	Stack[a]	Thickness (nm)	J_{SC} (mA/cm2)	V_{OC} (V)	FF (%)	PCE (%)
HTAZ	A	249	11.10 ± 0.25	0.741 ± 0.001	53.3 ± 1.3	4.39 ± 0.17
	B	153	10.11 ± 0.17	0.757 ± 0.002	58.5 ± 1.8	4.48 ± 0.19
monoCNTAZ	A	333	14.97 ± 0.40	0.932 ± 0.001	61.6 ± 1.1	8.60 ± 0.27
	B	270	13.28 ± 0.28	0.921 ± 0.003	62.8 ± 1.3	7.68 ± 0.29
diCNTAZ	A	282	11.30 ± 0.33	0.998 ± 0.008	49.6 ± 1.5	5.59 ± 0.28
	B	112	8.81 ± 0.44	1.043 ± 0.002	63.6 ± 0.9	5.85 ± 0.26

Table 5.3: Photovoltaic performance at different thickness

Polymer	Stack[a]	Thickness (nm)	J_{SC} (mA/cm2)	V_{OC} (V)	FF (%)	PCE (%)
HTAZ	A	153	10.11 ± 0.17	0.757 ± 0.002	58.5 ± 1.8	4.48 ± 0.19
		205	10.55 ± 0.21	0.752 ± 0.001	56.9 ± 1.1	4.52 ± 0.18
		249	11.10 ± 0.25	0.741 ± 0.001	53.3 ± 1.3	4.39 ± 0.17
	B	153	8.13 ± 0.65	0.731 ± 0.002	62.3 ± 1.6	3.70 ± 0.30
		156	10.11 ± 0.17	0.757 ± 0.002	58.5 ± 1.8	4.48 ± 0.19
		205	10.55 ± 0.21	0.752 ± 0.001	56.9 ± 1.1	4.52 ± 0.18
monoCNTAZ	A	231	13.14 ± 0.47	0.935 ± 0.002	65.0 ± 1.2	7.98 ± 0.22
		262	13.67 ± 0.31	0.930 ± 0.001	63.3 ± 1.7	8.04 ± 0.23
		324	14.38 ± 0.33	0.917 ± 0.001	63.3 ± 1.3	8.34 ± 0.11
	B	270	13.28 ± 0.28	0.921 ± 0.003	62.8 ± 1.3	7.68 ± 0.29
		310	13.05 ± 0.91	0.922 ± 0.002	59.6 ± 1.8	7.17 ± 0.49
		474	13.28 ± 0.86	0.931 ± 0.002	51.6 ± 1.7	6.38 ± 0.38
diCNTAZ	A	106	8.75 ± 0.31	1.007 ± 0.005	63.1 ± 0.7	5.56 ± 0.21
		123	8.76 ± 0.37	1.010 ± 0.006	60.1 ± 2.5	5.32 ± 0.32
		172	10.12 ± 0.37	1.001 ± 0.007	58.6 ± 1.5	5.94 ± 0.32
	B	112	8.81 ± 0.44	1.043 ± 0.002	63.6 ± 0.9	5.85 ± 0.26
		139	8.53 ± 0.67	1.033 ± 0.002	60.9 ± 2.5	5.37 ± 0.52
		197	8.99 ± 0.99	1.018 ± 0.002	54.5 ± 3.8	4.97 ± 0.50

[a]There are two different device architectures used: A = ITO/CuSCN/polymer:PCBM/Ca/Al and B =ITO/PEDOT:PSS/polymer:PCBM/PFN/Al

In terms of the impact of the cyano groups on photovoltaic properties, the first clear

trend is with the V_{OC}. Much like the HOMO energy level differences, cyano functionalization

increased the V_{OC}, but the addition of the second cyano had diminished returns. With the

second device architecture (where PFN was used as the interlayer), the *FF* also increases

with cyano content; however, the large decrease in J_{SC} erodes the values of this *FF* increase.

Out of the three polymers, the highest average efficiency of 8.6 % is achieved by

monoCNTAZ:PCBM, nearly double that of HTAZ:PCBM based devices with 4.4 %. For

diCNTAZ:PCBM, with the addition of the second cyano group, a significant drop of J_{SC}

leads to a significant decrease in *PCE* to 5.6 %. While cyano substitution effectively red-

shifts the absorption of the polymer, as shown in **Figure 5.4b**, EQE values of diCNTAZ

based devices are significantly lower than HTAZ. In contrast, the EQE values of

monoCNTAZ based devices are higher over the whole absorption range than HTAZ and

diCTAZ, so are the J_{SC} of the monoCNTAZ. To better understanding the negative effect of

the second cyano addition, further characterization is required, and in the next sections, we

will gain a deeper understanding the differences in the photovoltaic parameters (V_{OC}, J_{SC}, and

FF) by investigating the morphology, charge recombination dynamics, and CT state of the

three polymers.

5.2.4 Morphology and Fill Factor

To further understand the effect of cyano substitution on molecular ordering of

polymers and the morphology of the active layer of BHJ devices, we utilized synchrotron

radiation based grazing incidence wide angle X-ray scattering (GIWAXS)[126] to investigate

the texture and packing of the polymers in neat films and blends with PCBM (**Figure 5.5,

Figure 5.6**). In the neat polymer films (**Figure 5.5a-c**), there are some interesting effects of

the cyano substituents. In the case of HTAZ, there is no preferred orientation, as the (010) π-π stacking peak and (h00) lamella peak are both in the out-of-plane (OOP) direction. With the addition of the first cyano group, i.e., monoCNTAZ, the polymer has a slightly stronger preference towards the face-on orientation, as the (100) and (200) contribution to the in-plane (IP) direction is increased. Similarly, the addition of the second cyano group, i.e., diCNTAZ, has an even stronger preference towards face-on orientation, as the contribution of the (h00) lamella peaks are increased further. This trend of an increase in cyano substitution leading to an increase in face-on preferential ordering would suggest that the diCNTAZ would have the best performance, as face-on is beneficial for charge transport.[100,104,286–289] However, when the polymers are blended with PCBM, the fine difference between polymers quickly vanishes, as all three BHJ blends have a general isotropic ordering. There is, however, a trend with the π-π stacking distances of the polymers in blends, determined through the OOP (010) peak, getting smaller: 3.98 Å, 3.92 Å and 3.85 Å for HTAZ, monoCNTAZ and diCNTAZ blends respectively. This observation indicates that cyano units on the polymer backbone might strengthen the π-π stacking within the system. Nevertheless, the coherence length of the (010) peaks of the three polymers in BHJ blends is similar to each other (~ 3 nm), as shown in **Table 5.4**, meaning the difference in the polymer crystallinity is minimal.
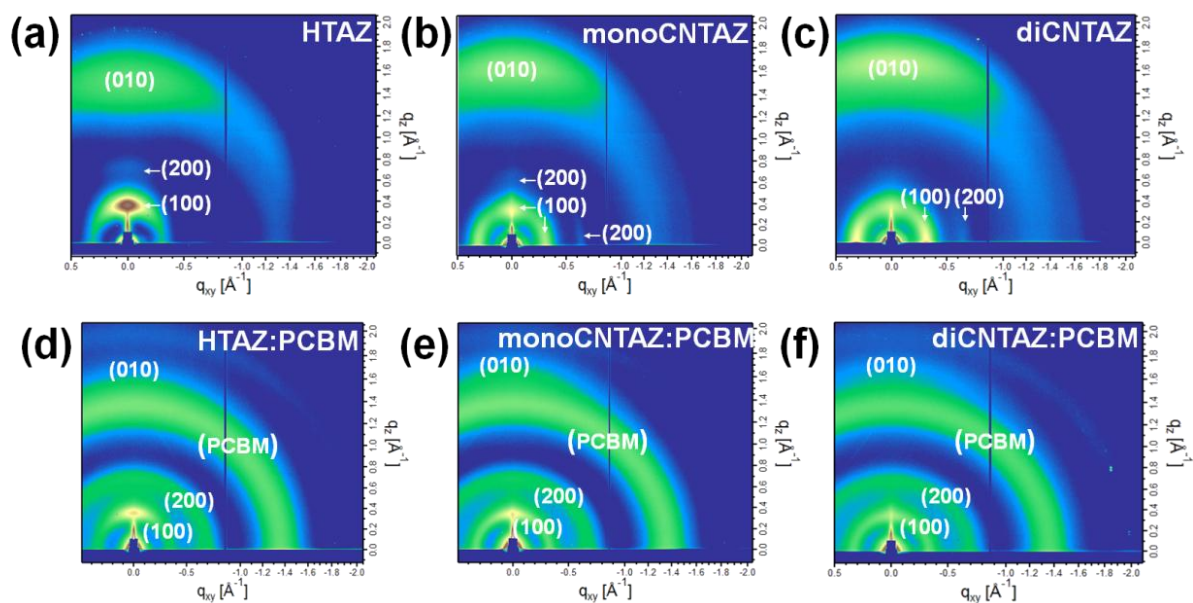
Figure 5.5 – 2D GIWAXS patterns of neat films of (a) HTAZ, (b) monoCNTAZ, (c) diCNTAZ, and blend films of (d) HTAZ:PCBM, (e) monoCNTAZ:PCBM and (f) diCNTAZ:PCBM.
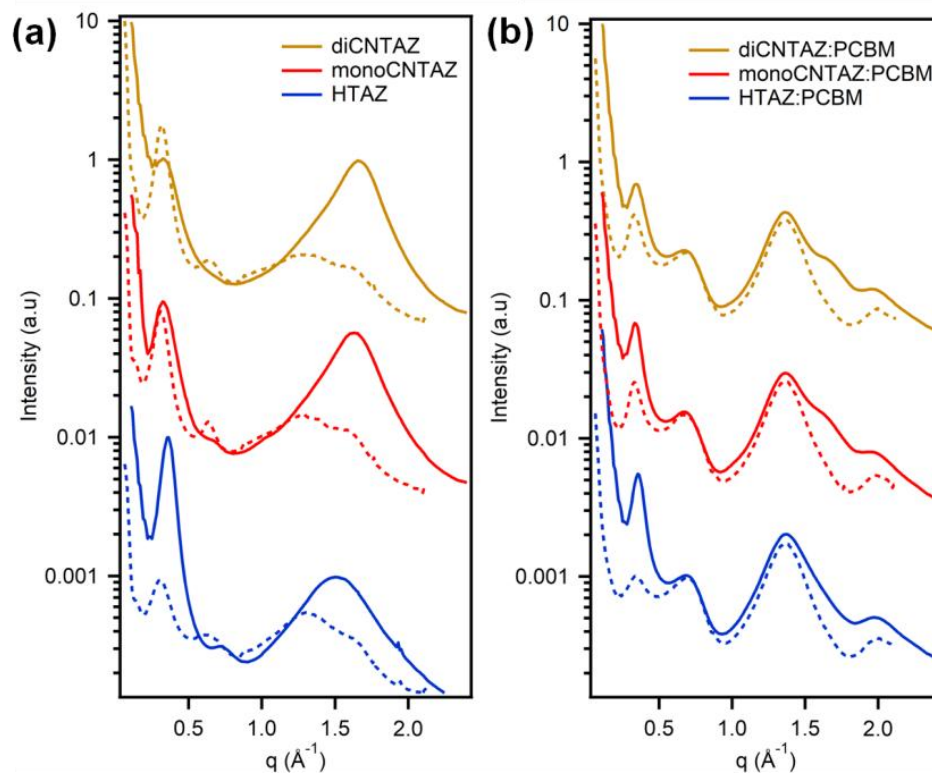
Figure 5.6. GIWAXS linecuts for both (a) neat HTAZ, monoCNTAZ, and diCNTAZ polymer films and (b) HTAZ:PCBM, monoCNTAZ:PCBM, and diCNTAZ blend films. These 1D profiles have both in-plane q_{xy} (dotted lines) and out-of-plane q_z (solid lines) directions shown.

135

Table 5.4 – Mobility and morphological features of polymer:PCBM blends

Blend	π-π stacking distance (Å)	(010) peak coherence length (Å)	Long Period (nm)	Relative domain purity	Hole mobility (cm² V⁻¹ s⁻¹)
HTAZ:PCBM	3.98	31.2	45.7	0.73	0.18×10^{-3}
monoCNTAZ:PCBM	3.92	27.8	36.6	1.00	1.08×10^{-3}
diCNTAZ:PCBM	3.85	27.8	48.2	0.88	0.07×10^{-3}

Since GIWAXS detects only the crystalline part of the samples, we utilized resonant soft X-ray scattering (RSoXS) to inspect the domain information in the polymer:PCBM blends (**Figure 5.7**).[290] The long period (related to domain spacing) of the three polymer:PCBM blends is generally similar; specifically, monoCNTAZ blend has smaller domain spacing of ~ 36 nm than the other two polymer:PCBM blends (~ 46 nm). However, since the weight ratio of the polymers to PCBM is 1:2 for all samples, the domain sizes of the polymers phase are estimated to be 12 and 15 nm, which are all in the range of the exciton diffusion distance. While this difference might have some effect on the J_{SC} and EQE, we do not believe this is the dominant cause for the photovoltaic characteristics, as the morphological differences are minor. Conversely, the domain purity (**Table 5.4**) of the monoCNTAZ:PCBM blends is the highest among the three polymer:PCBM blends. The mean-square composition variation, as defined by the integral of the scattering profiles over the length scale probed, is a widely used indicator related to the average domain purity of the OPV blend. The more pure domains of monoCNTAZ:PCBM can help minimize the amount of bimolecular recombination and improve the *FF*.
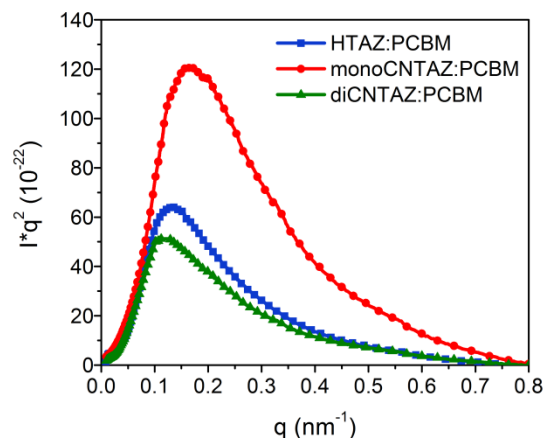
Figure 5.7. Lorentz-corrected RSoXS profile of HTAZ:PCBM, monoCNTAZ:PCBM, and diCNTAZ blend films

Overall, the morphology of all three polymer:PCBM blends are similar, which indicates that cyano substituents on the TAZ units would not strongly affect the overall morphology of the blends. The lower *FF* of diCNTAZ based devices stems from a more impure domain, while the higher purity domain of monoCNTAZ based devices result in the highest *FF*. Additionally, hole mobilities of the polymer:PCBM blends were also measured and demonstrate a similar trend (**Figure 5.8b** and **Table 5.5**). Hole mobility, measured through space-charge limited current (SCLC), of monoCNTAZ:PCBM blend is highest with a value of 1.08×10^{-3} cm^2/(V·s), which is much higher than HTAZ:PCBM blend (0.18×10^{-3} cm^2/(V·s)) and diCNTAZ:PCBM blend (0.07×10^{-3} cm^2/(V·s)). These values match the same trend found in the neat polymer blends (**Figure 5.8a** and **Table 5.5**). In our previous study, we found that hole mobility strongly influences the *FF* of TAZ based polymers.[135,270] For the cyano-substituted polymers, the noticeably enhanced hole mobility of monoCNTAZ above the threshold ($\sim 1 \times 10^{-3}$ cm^2/(V·s)) induces high *FF* of thick solar cell devices compared to HTAZ and diCTNAZ. Therefore, both the low hole mobility and lower domain

137

purity of diCNTAZ based devices contributes to the lower J_{SC} and FF. This begins to describe why the second cyano substituent causes a decrease in performance.
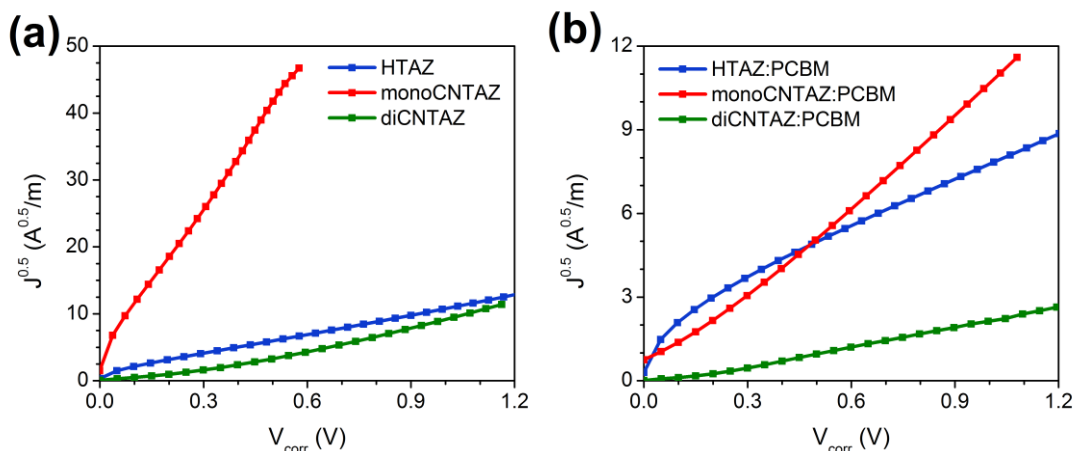
Figure 5.8. SCLC hole mobility curves for (a) neat polymer and (b) polymer:PCBM blend systems

Table 5.5: Mobility Data

Polymer	Neat Polymer Mobility		Polymer:PCBM Blend Mobility	
	Thickness (nm)	Hole Mobility (10^{-4} cm²/V·s)	Thickness (nm)	Hole Mobility (10^{-4} cm²/V·s)
HTAZ	160	1.70 ± 0.27	251	1.75 ± 0.23
monoCNTAZ	117	31.2 ± 10.4	303	10.8 ± 3.6
diCNTAZ	140	0.94 ± 0.20	283	0.65 ± 0.36

5.2.5 CT State and V_{OC} Loss

V_{OC} values are expected to be enhanced by cyano substitution as the HOMO energy levels of the polymers is effectively decreased, as demonstrated by the CV data (*vide supra*). Noticeably enhanced V_{OC} values were achieved by monoCNTAZ and diCNTAZ compared to the non-functionalized HTAZ polymer. Moreover, the increase of V_{OC} values from HTAZ to monoCNTAZ (0.19 V) is near three times of that from monoCNTAZ to diCNTAZ (0.07 V). The trend of increase of V_{OC} matches the decrease of HOMO energy levels of the polymers and indicates that the second cyano unit has much less impact than the first cyano unit does,

which was also observed by Casey *et al.*[281] Although the deeper HOMO levels of monoCNTAZ and diCNTAZ explain well the higher V_{OC} values, the V_{OC} is more directly related with the CT state energy (E_{CT}). The CT states more directly affects V_{OC} of solar cells as illustrated in **Equation 5.1**,[191] where k is Boltzmann's constant, q is the elementary charge, J_{ph} is photogenerated current density, J_o is dark current density, λ is the reorganization energy associated with the CT absorption process, and EQE_{EL} is the electroluminescence external quantum efficiency. We measured the energy of CT states with high sensitivity of EQE (**Figure 5.9**) and fitted the spectra to **Equation 5.2**,[191] where E is the photon energy and EQE_{PV} is the photovoltaic EQE. Total energy loss ($E_{opt} - eV_{OC}$) in the device is divided into two parts: (1) from minimum of the optical band gap of the components of the devices to CT state: ($E_{opt} - E_{CT}$), which acts as the driving force for the exciton splitting; and (2) from the CT state to V_{OC}: ($E_{CT} - eV_{OC}$), which originates from the non-geminate recombination. [291]

$$V_{oc} = \frac{kT}{q} ln\left(\frac{J_{ph}}{J_0} + 1\right) = \frac{E_{CT}}{q} + \frac{kT}{q} ln\left(\frac{J_{sc}h^3c^2}{fq2\pi(E_{CT} - \lambda)}\right) + \frac{kT}{q} ln(EQE_{EL}) \quad \textbf{(Eq 5.1)}$$

$$EQE_{PV}(E) = \frac{f}{E\sqrt{4\pi\lambda kT}} \exp\left(\frac{-(E_{CT} + \lambda - E)^2}{4\lambda kT}\right) \quad \textbf{(Eq 5.2)}$$

The energy of the CT state and the V_{OC} loss of devices are summarized in **Table 5.6**. The loss from the CT state to the V_{OC} (~ 0.62 eV) is similar for all the three polymer-based devices, indicating the non-geminate recombination caused V_{OC} loss is similar for the three polymers. However, there is a noticeable difference in the loss from the minimum band gap to the CT state: the driving force for the exciton splitting gets reduced with the cyano substitution. For the diCNTAZ, CT state energy is close to the minimum band gap, and the driving force is extremely low. Though this high lying CT state is beneficial for the high V_{OC} obtained, the low driving force in the diCNTAZ based devices may harm the exciton splitting

and hole transport from the PCBM to diCNTAZ, especially if there is energy transfer from

diCNTAZ to PCBM, which will increase the geminate recombination in the device and

decrease J_{SC} of diCNTAZ based devices.[142,292]
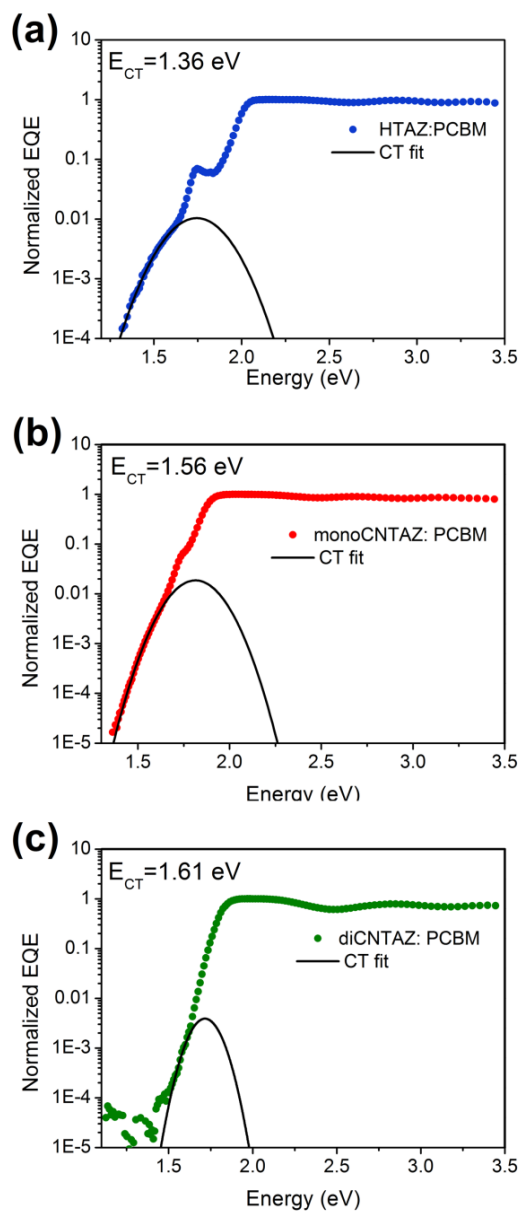
Figure 5.9. CT state fit of polymer:PCBM blend based on high sensitivity EQE.

Table 5.6 – CT state energy and the V_{oc} loss the devices

Polymer	V_{OC} (V)	E_{opt}[a] (eV)	E_{CT} (eV)	$E_{CT} - eV_{OC}$ (eV)	$E_{opt} - E_{CT}$ (eV)	Total Loss (eV)
HTAZ	0.74	1.66	1.36	0.62	0.30	0.92
monoCNTAZ	0.93	1.66	1.56	0.63	0.10	0.73
diCNTAZ	1.00	1.66	1.61	0.61	0.05	0.66

[a]smaller optical bandgap (E_{opt}) of the two components, which is PCBM in these cases.

While we have already demonstrated the negative effect on hole mobility with the addition of the second cyano group, exciton splitting was explored next. To further understand the reasons of different J_{SC} of monoCNTAZ and diCNTAZ, quenching of excitons in polymer:PCBM blend was investigated by photoluminescence (PL) (**Figure 5.10**). Comparably high PL quenching efficiency were observed in both cases for diCNTAZ:PCBM (96 %) and monoCNTAZ:PCBM (98 %), which suggests that excitons are effectively split; however, this high PL quench does not rule out geminate recombination, as mentioned above, because energy transfer from diCNTAZ to PCBM is possible. Therefore, while the addition of further cyano groups can allow for a high V_{OC} and decrease V_{OC} loss, the decrease in exciton driving force and decreased hole mobility results in a lower J_{SC}. As the improvement in V_{OC} is minor with the addition of the second cyano group, the optimized functionalization of a single cyano group (i.e., monoCNTAZ) demonstrates the ideal balance between improvements of photovoltaic parameters.
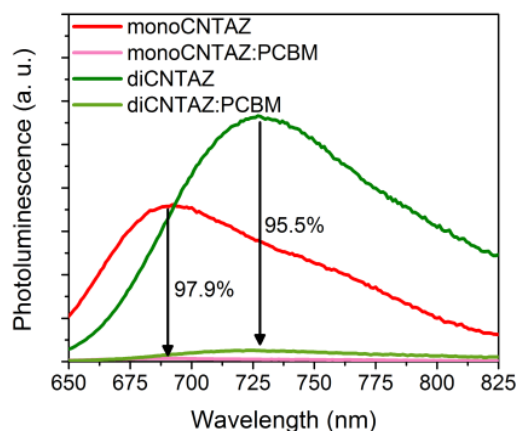
Figure 5.10. Photoluminescence of polymer and polymer:PCBM blend.

5.2.6 Charge Recombination Dynamics

To further investigate the influence of cyano substitutions on device characteristics, transient photocurrent (TPC) and transient photovoltage (TPV) measurements were undertaken to determine the lifetime, density, and recombination dynamics in the active layer,[284,293,294] using fresh devices with the ITO/PEDOT:PSS/polymer:PCBM/PFN/Al device architecture. First, we measured charge carrier density as a function of V_{OC} for the devices (**Figure 5.11a**). Variations of V_{OC} between 0.60 – 0.76 V for HTAZ:PCBM device, 0.69 – 0.93 V for monoCNTAZ:PCBM and 0.76 – 1.03 V for diCNTAZ:PCBM device were achieved by adjusting the intensity light between 2 – 100 mW/cm^2, a method previously outlined in literature.[295] The $n(V_{OC})$ characteristics visualizes the bulk quasi-Fermi level splitting in the photoactive layer at different illumination intensities, thus representing how far away the active layer is from equilibrium under operation conditions.[296,297] At representative charge density range of $1 – 2 \times 10^{-16}$ cm^{-3}, the quasi-Fermi level splitting is the largest for the diCNTAZ:PCBM device, consistent with the largest measured open-circuit voltage. It is worthy to note that the measured charge density in all devices increases exponentially as a function of V_{OC}, following a relationship $n = n_0 e^{\gamma V_{OC}}$, where n$_0$ is the

142

charge density in the dark and γ is the slope of the $ln(n) \sim V_{OC}$ curves (**Figure 5.11a**). A clear trend in the slope is observed with the three polymers: as the amount of cyano groups on the polymer increases, the slope decreases. While diCNTAZ has the lowest slope (γ), the highest $n(V_{OC})$ value results in an increase in the J_{Loss}, as described in **Equation 5.3**. This can also help describe the lower J_{SC} value of diCNTAZ compared to monoCNTAZ.
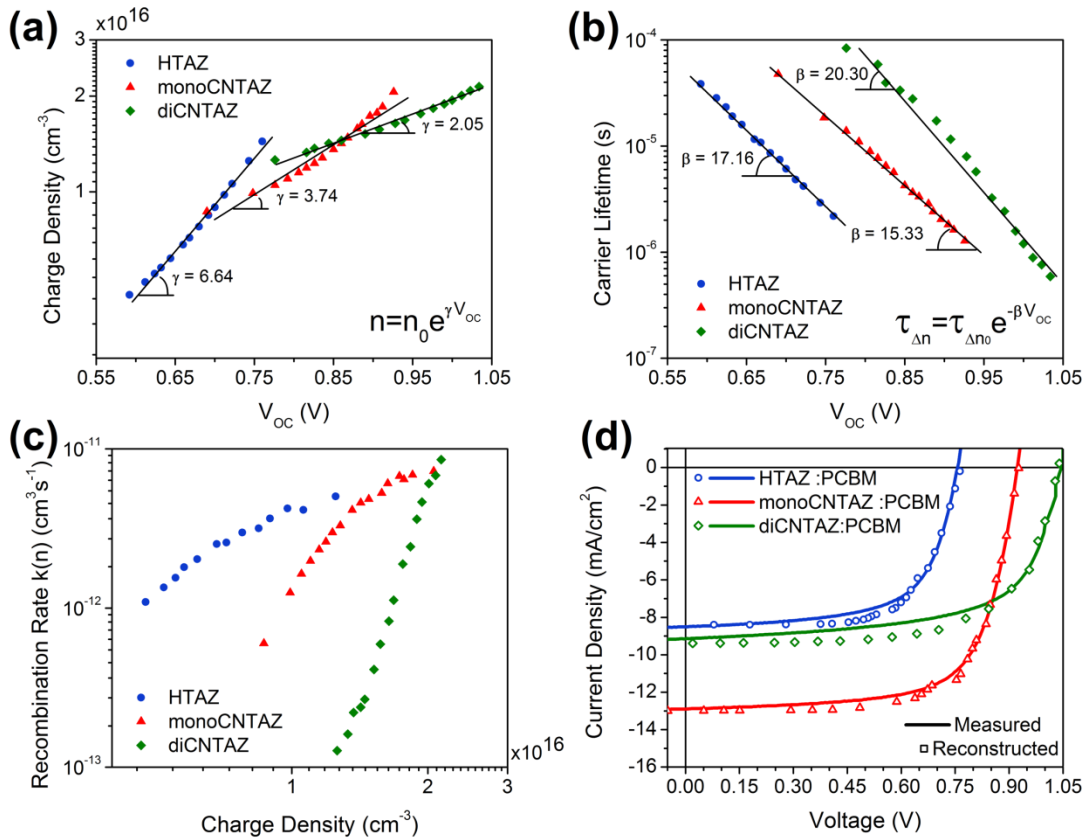
Figure 5.11 – (a) The measured charge carrier density (n) as a function of V_{OC}, (b) measured charge carrier lifetime as a function of V_{OC}. Solid lines represent the fit to each equation (shown on the graph), with the slopes shown next to each fit. (c) The calculated non-geminate recombination rate coefficient as a function of charge carrier density. (d) Reconstructed J-V characteristics (open symbols) vs. measured J-V characteristics (solid line), assuming only non-geminate recombination contributes to losses.

Next, the measured charge carrier lifetime in the devices as a function of V_{OC} is depicted in **Figure 5.11b**. For all of the devices, the lifetime decreases exponentially as a

function of V_{OC} via $\tau_{\Delta n} = \tau_{\Delta n_0} e^{-\beta V_{OC}}$, where $\tau_{\Delta n_0}$ is the carrier lifetime in the dark and β is

the decay constant. Because the devices show a decreasing lifetime as the charge carrier

density increases, following a power law dependence with charge density, this indicated that

non-geminate recombination is the dominant recombination pathway for loss in the device.

Therefore, the loss current can be quantified via **Equation 5.3**,[284] where *k(n)* is the non-

geminate recombination rate coefficient and is given by **Equation 5.4**, where *e* the

elementary charge, *d* the photoactive layer thickness, and *n(V$_{OC}$)* is the measured charge

carrier density (shown in **Figure 5.11a**) and $\tau(V_{OC})$ the measured carrier lifetime (shown in

Figure 5.11b) obtained under different illumination intensity.

$$J_{Loss} = edk(n)n^2 = ed \frac{n(V_{OC})}{\tau(V_{OC})} \quad \textbf{(Eq 5.3)}$$

$$k(n) = \frac{1}{(1+\frac{\beta}{\gamma})n\tau_{\Delta n}} \quad \textbf{(Eq 5.4)}$$

The measured *k(n)* for all devices is depicted in **Figure 5.11c**. While it is clear that

the diCNTAZ:PCBM device shows the lowest *k(n)* at most charge carrier densities, the

dependence on carrier density is larger (i.e., larger slope – small changes in charge carrier

density results in higher recombination rate coefficients). While monoCNTAZ:PCBM device

also shows reduced non-geminate recombination rate coefficient compared to the

HTAZ:PCBM device, it is only at higher charge carrier densities that monoCNTAZ has a

lower recombination rate coefficient that diCNTAZ. As a result of reduced non-geminate

recombination losses, the diCNTAZ:PCBM device and monoCNTAZ:PCBM device can

afford higher charge accumulation and therefore leading to a larger quasi-Fermi level

splitting versus HTAZ:PCBM device. However, as the charge carrier density increases,

diCNTAZ:PCBM devices have a recombination rate that surpasses those rates of the other two blends, which can result in detrimental device performance. The $\tau_{\Delta n_0}$, charge carrier lifetime in the dark, for diCNTAZ (904 s) is substantially larger than monoCNTAZ (2 s) and HTAZ (1 s), which can result in the larger accumulation of charges, and while this boosts V_{OC}, the diCNTAZ has an increasingly higher recombination rate coefficient with charge carrier density. This is also consistent the significantly lower mobility values measured for the diCNTAZ:PCBM blend. Therefore, while the addition of the second cyano group allows for higher charge carrier density and lifetimes, this results in increased recombination and lower J_{SC}. In the case of monoCNTAZ, the balance between charge carrier density and lifetime results in the improved performance and less recombination.

To demonstrate the validity of this approach, the current density can be predicted at the various V values and a J-V curve can be simulated.[298] As shown in **Figure 5.11d**, the reconstructed and the measured J-V curves coincide well with each other, verifying non-geminate recombination is in fact the dominating loss pathway for these devices.[299] Furthermore, in case that non-geminate recombination of charge carriers is negligible at short-circuit conditions, the open-circuit voltage under one sun illumination can be calculated, and thus enables a quantitative assessment of impact of changes in energetic and recombination rate on V_{OC}. The open-circuit voltages under AM 1.5G illumination predicted by **Equation 5.5** are 0.796 V for the HTAZ:PCBM device, 0.932 V for the monoCNTAZ:PCBM device and 1.060 V for the diCNTAZ:PCBM device respectively, in excellent agreement with the measured values (0.75 V, 0.92 V and 1.05 V, respectively), confirming the validity of transient optoelectronic analyses.

$$V_{OC} = \frac{1}{\beta + \gamma} \ln \left(\frac{J_{SC} \tau_{\Delta n_0} (1 + \frac{\beta}{\gamma})}{edn_0} \right) \quad \textbf{(Eq 5.5)}$$

These results and analyses showed that the cyano groups play a very important role in the charge recombination dynamics. Adding cyano substituents boosted the V_{OC} from the increase in charge carrier density and lifetime; however, in the case of diCNTAZ, this also results in larger dependence of charge carrier density on recombination rate coefficients. The best device of monoCNTAZ:PCBM showed the higher J_{SC} and FF mainly due to its higher charge mobilities and the balanced between recombination kinetics and charge extraction in the devices.[300]

5.3. Conclusion

In this study, we gradually increased the amount of cyano substituent on conjugated polymers and systematically studied the effect of cyano substitution on properties of polymers. The strong electron-withdrawing cyano unit can effectively tune the energy levels and band gaps, with deepened energy levels, the cyano-substituted polymers achieve high V_{OC}. Cyano substituent also proves efficient in decreasing optical band gaps and shifting the absorption of polymers to long wavelength, which benefits the J_{SC} of solar cells. Moreover, cyano unit also increases the π-π stacking distance and increases the charge transport properties of monoCNTAZ. With all the three parameters (V_{OC}, J_{SC} and FF) been improved, monoCNTAZ achieved a high PCE of 8.6% with PCBM as electron acceptor. However, further addition of cyano groups shows degradation in the device performance, driven by a decrease in the mobility and purity of domains, along with an increase in recombination kinetics. This study proves the benefit of incorporating cyano unit in conjugated polymers to improve properties of polymers and provides guidelines to optimize structure of polymers.

5.4 Experimental Details

5.4.1 Synthesis of Cyano containing Polymers

All chemicals were purchased from commercial sources and were utilized as received except when specified. For reactions that was ran under argon, the flask was evacuated and refilled with argon before reactants were charged.
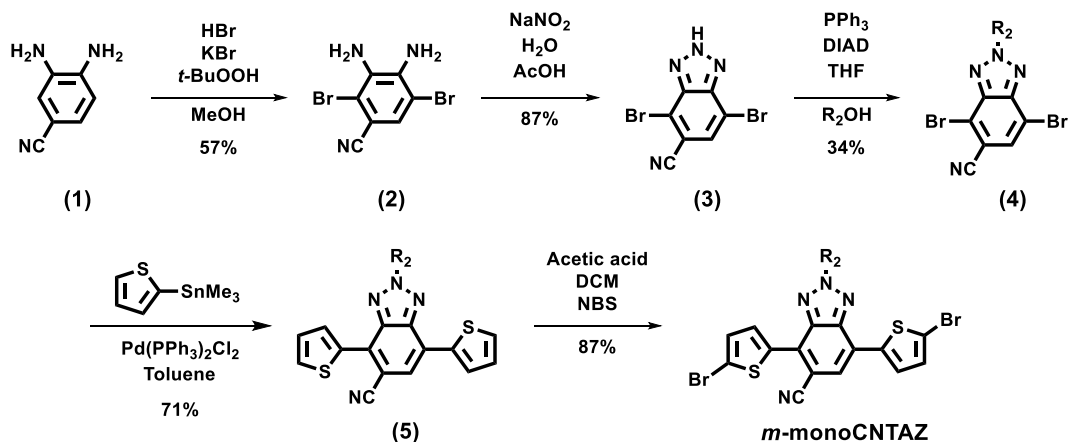
Scheme 5.4 – Synthesis of monoCNTAZ monomer

3,4-diamino-2,5-dibromobenzonitrile (**Compound 2**) (under argon) The solution of 3,4-diaminobenzonitrile (**Compound 1**, 2.66 g, 20.0 mmol) and potassium bromide (31.65 g, 266 mmol) in 300 mL methanol was purged with argon for 20 min. 62% hydrogen bromide solution (3.54 mL) was added at 0 °C slowly. 70% *tert*-butylhydroperoxide solution (1.74 mL) was added and stirred at room temperature for 6 hr. Then a second portion of 70% *tert*-butylhydroperoxide solution (1.74 mL) was added and stirred for 6 hr before the third portion of 70% *tert*-butylhydroperoxide solution (1.74 mL) was added and stirred overnight. The reaction mixture poured into water and filtered. The red solid was washed with water and dried over phosphorus pentoxide under low pressure. Yield, 3.31 g, 56.9%. ^{1}H NMR (600 MHz, MeOD) δ 7.22 (1H).
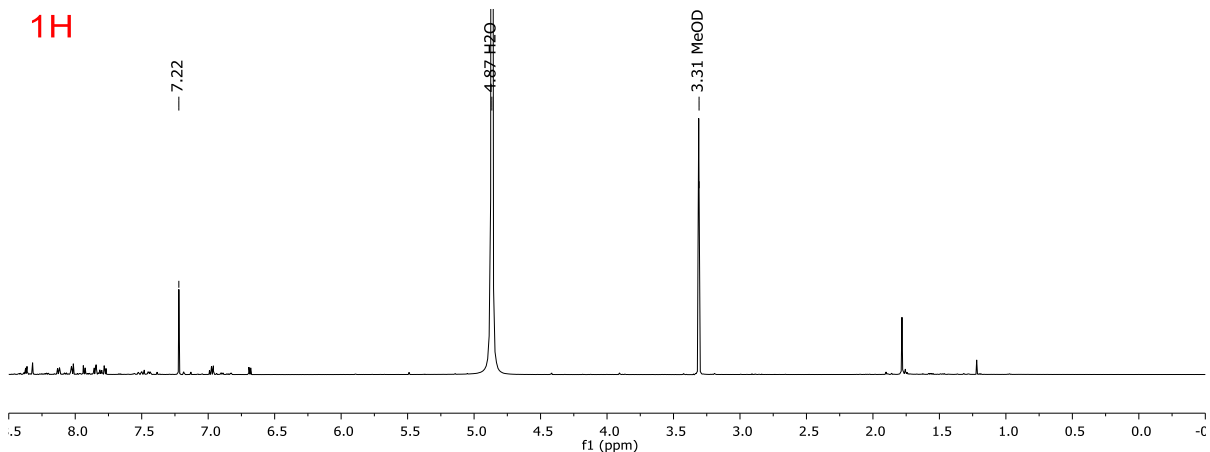
Figure 5.12 – ¹H NMR of compound 2

*4,7-dibromo-2H-benzo[d][1,2,3]triazole-5-carbonitrile (**Compound 3**)* To the solution of **2** (2.33 g, 8.0 mmol) in 18 mL acetic acid, sodium nitrite (0.91 g, 13.2 mmol) in 14 mL water was added at 0 °C. The reaction was stirred at room temperature for 1.5 hr before being poured into water. The product was extracted with ethyl acetate three times, and the combined organic solution was washed with water for two times and brine. The organic solution was then dried over magnesium sulfate, filtered, and the solvent was removed with rotovap. Yield, dark red solid, 2.1 g, 86.9%. ¹H NMR (600 MHz, MeOD) δ 7.98.
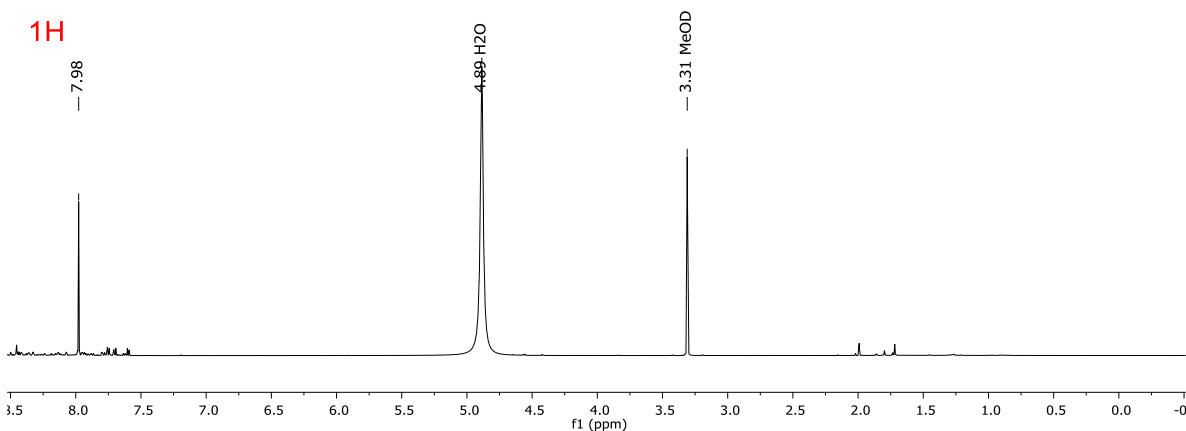
Figure 5.13 – ¹H NMR of compound 3

148

*4,7-dibromo-2-(2-butyloctyl)-2H-benzo[d][1,2,3]triazole-5-carbonitrile (**Compound 4**)* (under argon) To the solution of **Compound 3** (2.1 g, 6.95 mmol) and triphenylphosphine (2.73 g, 10.43 mmol) in anhydrous THF, 2-butyl-1-octanol (1.94 g, 10.43 mmol) was added at 0 °C, and then di*iso*propyl azodicarboxylate (DIAD) (2.67 g, 13.20 mmol) was added at 0 °C. The reaction was slowly warmed to room temperature and stirred overnight. Then the reaction mixture was poured into water, and the product was extracted with ethyl acetate for three times. The combined organic solution was washed with water for two times and brine for one time. The organic solution was dried over magnesium sulfate and filtered. The solvent was removed with rotovap, and the crude product was purified through silica gel column chromatography with hexanes:ethyl acetate = 15:1 as eluent. Yield, colorless oil, 1.11 g, 34.0%. ^{1}H NMR (600 MHz, Chloroform-*d*) δ 7.72 (s, 1H), 4.72 (d, *J* = 7.1 Hz, 2H), 2.33 (m, 1H), 1.40 – 1.15 (m, 16H), 0.87 (m, 6H). ^{13}C NMR (151 MHz, Chloroform-*d*) δ 144.69, 143.27, 130.78, 117.59, 116.36, 113.74, 111.34, 61.72, 39.27, 31.79, 31.24, 30.96, 29.53, 28.33, 26.09, 22.95, 22.73, 14.22, 14.10.
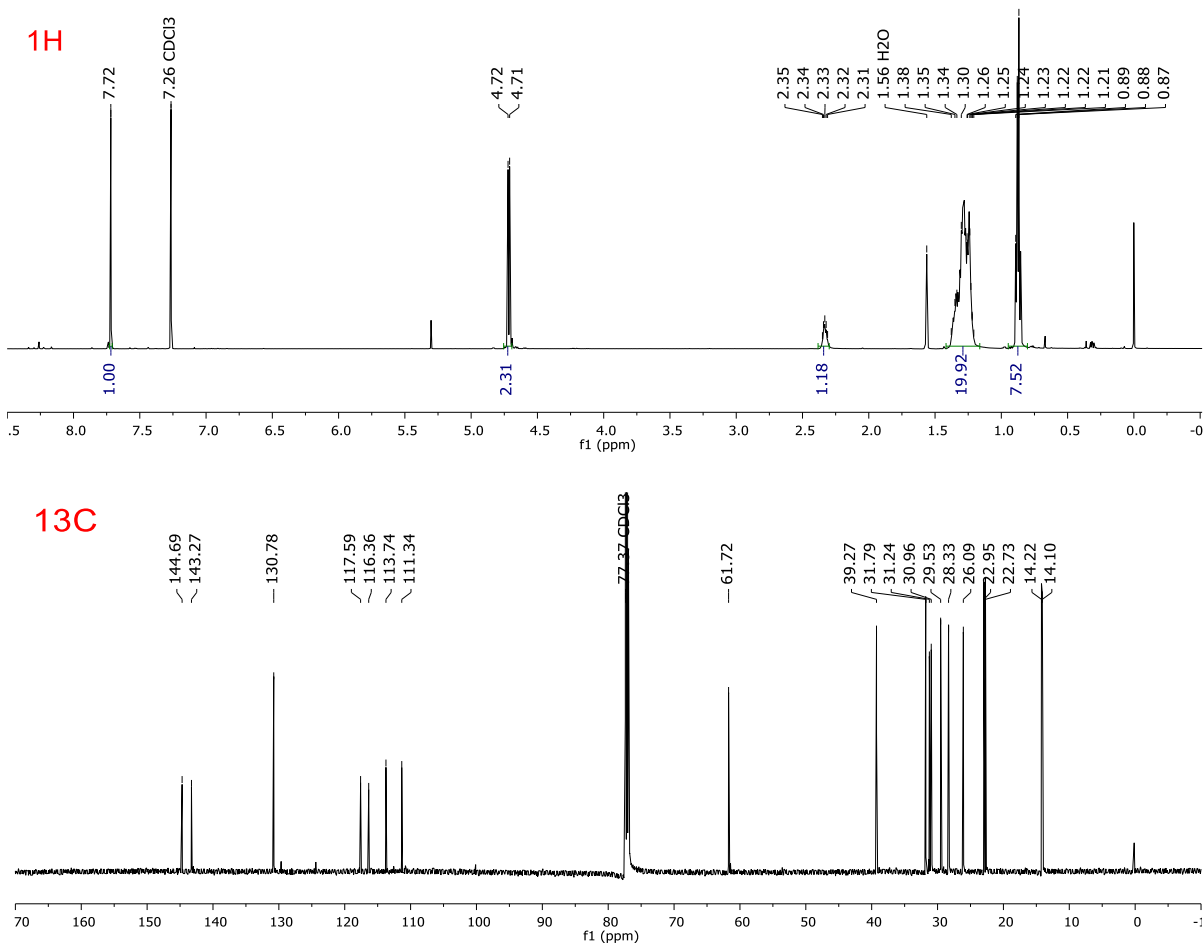
Figure 5.14 – ^{1}H and ^{13}C NMR of compound 4

2-(2-butyloctyl)-4,7-di(thiophen-2-yl)-2H-benzo[d][1,2,3]triazole-5-carbonitrile

(Compound 5) (under argon) To the solution of **Compound 4** (1.30 g, 2.76 mmol) and

trimethyl(thiophen-2-yl)stannane (1.70 g, 6.91 mmol) in anhydrous toluene, Pd(PPh$_3$)$_2$Cl$_2$

(0.058 g, 0.083 mmol) was added under argon stream, and the solution was purged with

argon for 20 min. The reaction was refluxed for 48 hr. The solvent was removed via rotovap.

And the product was purified via silica column chromatography with

hexanes:dichloromethane = 10:1 to 4:1 as eluent. Yield, yellow oil, 0.93 g, 70.7%. ^{1}H NMR

(600 MHz, Chloroform-*d*) δ 8.21 (dd, *J* = 3.8, 1.1 Hz, 1H), 8.12 (dd, *J* = 3.7, 1.1 Hz, 1H),

7.83 (s, 1H), 7.63 (dd, *J* = 5.1, 1.1 Hz, 1H), 7.47 (dd, *J* = 5.1, 1.1 Hz, 1H), 7.26 (m, 1H),

7.21 (dd, *J* = 5.1, 3.7 Hz, 1H), 4.77 (d, *J* = 6.6 Hz, 2H), 2.31 (h, *J* = 6.4 Hz, 1H), 1.47 – 1.15 (m, 16H), 0.88 (m, 6H). ^{13}C NMR (151 MHz, Chloroform-*d*) δ 142.69, 142.40, 137.78, 134.86, 130.44, 129.54, 128.90, 123.30, 128.21, 127.64, 127.09, 125.31, 124.55, 119.68, 105.59, 60.48, 39.15, 31.79, 31.39, 31.13, 29.52, 28.44, 26.18, 22.92, 22.64, 14.09, 14.05.
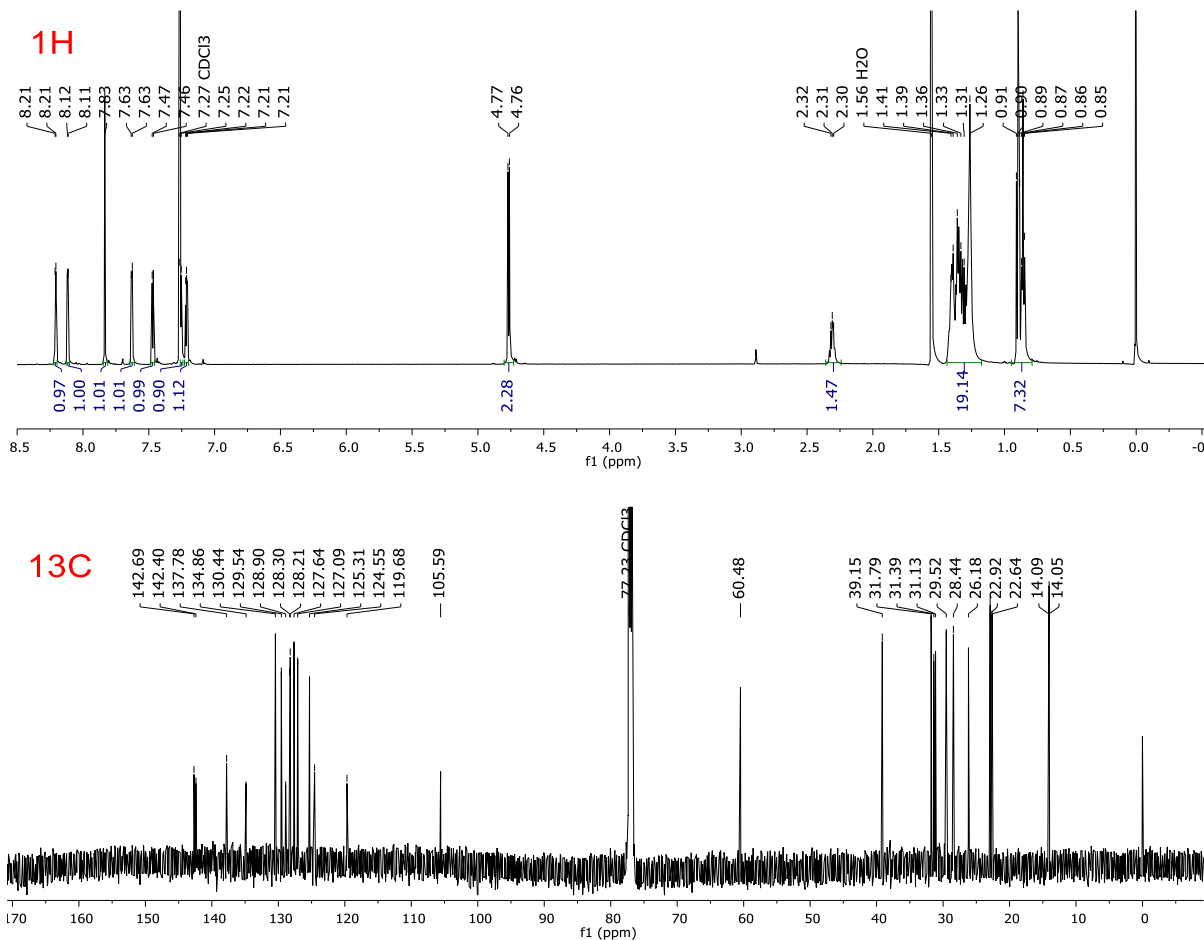
Figure 5.15 – ^{1}H and ^{13}C NMR of compound 5

*4,7-bis(5-bromothiophen-2-yl)-2-(2-butyloctyl)-2H-benzo[d][1,2,3]triazole-5-carbonitrile (**m-monoCNTAZ**)* (under argon) To the solution of **Compound 4** (0.92 g, 1.93 mmol) in 50 mL dichloromethane and 18 mL acetic acid, NBS (0.72 g, 4.05 mmol) was added in dark. The reaction was stirred in dark at room temperature for 40 hr. The second portion of NBS (0.12 g, 0.68 mmol) was added and stirred in dark at room temperature for 50

hr. The third portion of NBS (0.21 g, 1.16 mmol) was added and stirred overnight. Then the fourth portion of NBS (0.16 g, 0.79 mmol) was added and stirred overnight. The fifth portion of NBS (0.18 g, 1.0 mmol) was added and stirred overnight. The sixth portion of NBS (0.05 g, 0.28 mmol) was added and stirred overnight. The reaction was tracked with ^{1}H NMR until the dibromination was complete. The reaction was then poured into water, and the product was extracted with dichloromethane for three times. The combined organic solution was washed with water for two times and brine for one time. The organic solution was dried over magnesium sulfate and filtered. The solvent was removed via rotovap. And the product was purified with silica column chromatography with hexanes:dichloromethane = 4:1 as eluent and was then recrystallized in ethanol. Yield, yellow solid, 0.96 g, 78.4%. ^{1}H NMR (600 MHz, Chloroform-d) δ 8.01 (d, J = 4.1 Hz, 1H), 7.79 (d, J = 4.0 Hz, 1H), 7.71 (s, 1H), 7.21 (d, J = 4.1 Hz, 1H), 7.16 (d, J = 4.0 Hz, 1H), 4.77 (d, J = 6.5 Hz, 2H), 2.28 (p, J = 6.3 Hz, 1H), 1.47 – 1.21 (m, 16H), 0.89 (m, 6H). ^{13}C NMR (151 MHz, chloroform-d) δ 142.43, 142.11, 139.11, 136.50, 131.23, 130.71, 130.68, 128.21, 127.96, 125.00, 123.93, 119.46, 118.04, 115.27, 105.22, 60.60, 39.36, 31.96, 31.54, 31.31, 29.70, 28.60, 26.32, 23.10, 22.81, 14.25, 14.23. [M+H]$^+$ (ESI) calculated 633.035135, measured 633.03567.
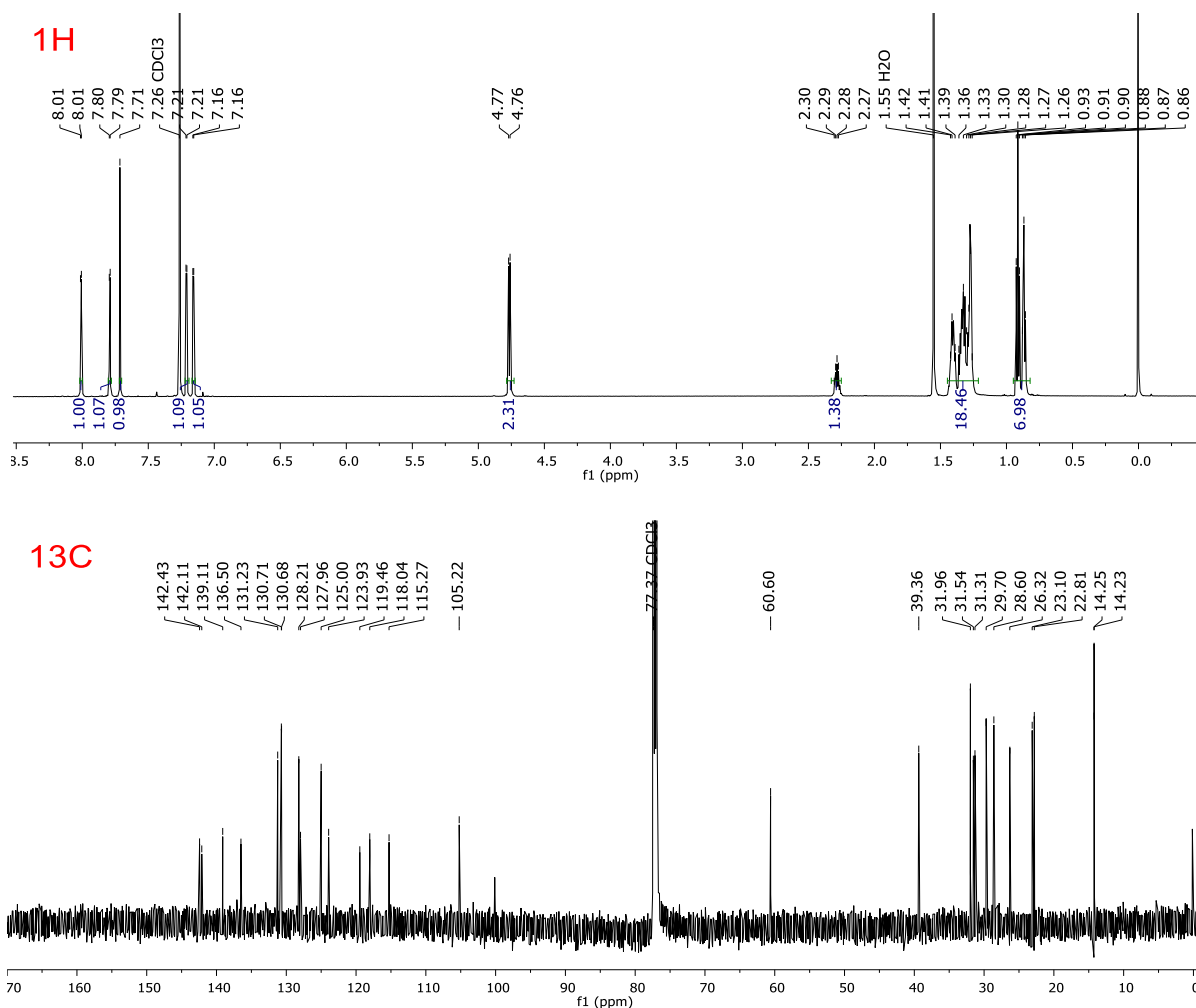
Figure 5.16 – ^{1}H and ^{13}C NMR of monoCNTAZ monomer
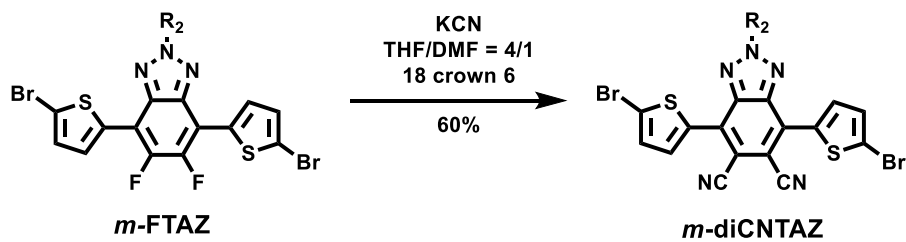
Scheme 5.5– Synthesis of diCNTAZ monomer

4,7-bis(5-bromothiophen-2-yl)-2-(2-butyloctyl)-2H-benzo[d][1,2,3]triazole-5,6-

*dicarbonitrile (**m-diCNTAZ**)* (under argon) The solution of 4,7-bis(5-bromothiophen-2-yl)-2-

(2-butyloctyl)-5,6-difluoro-2H-benzo[d][1,2,3]triazole (*m*-**FTAZ**) (0.97 g, 1.5 mmol),

potassium cyanide (0.59 g, 9.0 mmol) and 18-crown-6 ether (0.221 g, 0.9 mmol) in 65 mL

THF and 11 mL DMF was purged with argon for 20 min. The reaction was refluxed for 48

hr. The reaction mixture was poured into water. The product was extracted with ethyl acetate

for three times, and the combined organic solution was washed with water for two times and

brine for one time. The aqueous solution was treated with excessive sodium hypochlorite

solution to oxidize the residue potassium cyanide before being poured into waste container.

The organic solution was dried over magnesium sulfate and filtered. The solvent was

removed via rotovap. The product was purified via silica column chromatography with

hexanes:dichloromethane = 3:2 as eluent and was recrystallized in ethanol for further

purification. Yield, yellow solid, 0.66 g, 66.0%. ^{1}H NMR (600 MHz, Chloroform-d) δ 8.07

(d, *J* = 4.1 Hz, 2H), 7.24 (d, *J* = 4.1 Hz, 2H), 4.80 (d, *J* = 6.4 Hz, 2H), 2.27 (p, *J* = 6.3 Hz,

1H), 1.49 – 1.21 (m, 16H), 0.90 (m, 6H). ^{13}C NMR (151 MHz, chloroform-d) δ 142.51,

134.81, 132.15, 130.98, 129.91, 119.78, 116.77, 107.54, 61.04, 39.46, 31.95, 31.50, 31.27,

29.68, 28.56, 26.29, 23.09, 22.80, 14.24, 14.23. [M]$^{+}$ (ESI), calculated 657.023107, measured

657.02739.
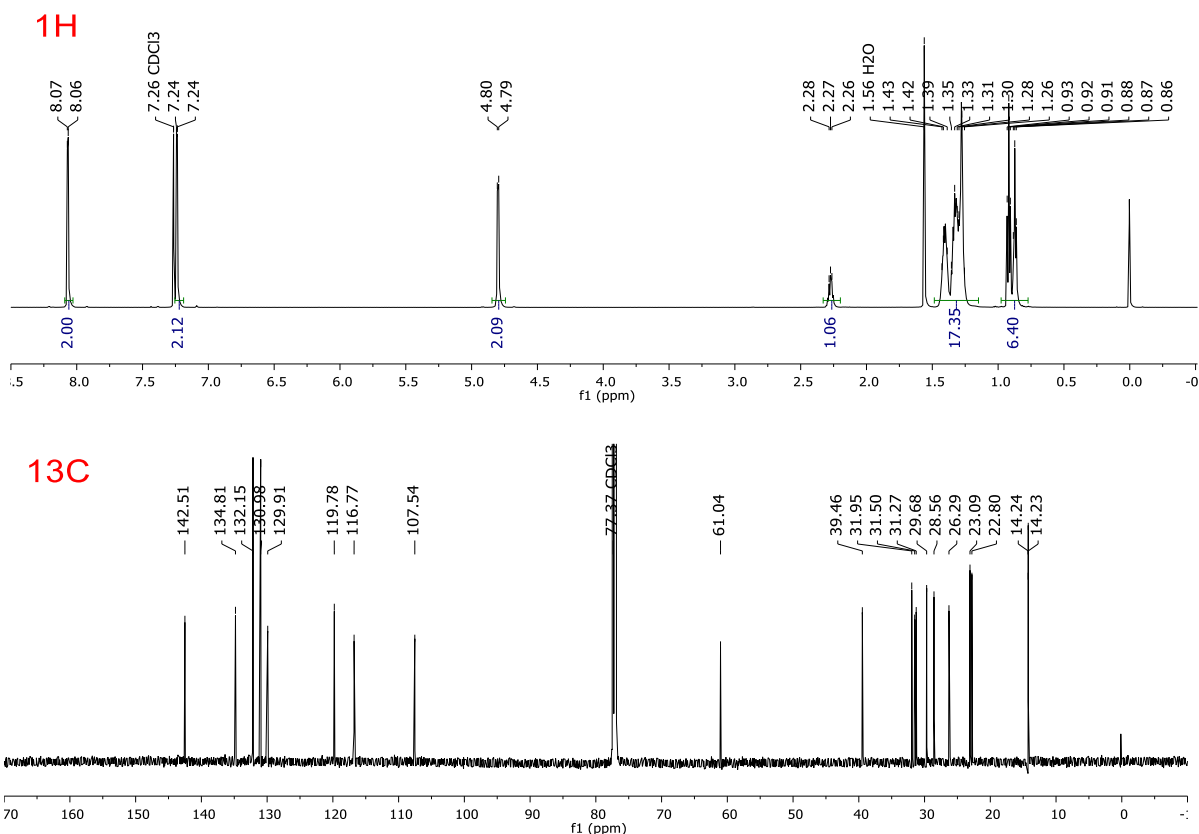
Figure 5.17 – ^{1}H and ^{13}C NMR of diCNTAZ monomer
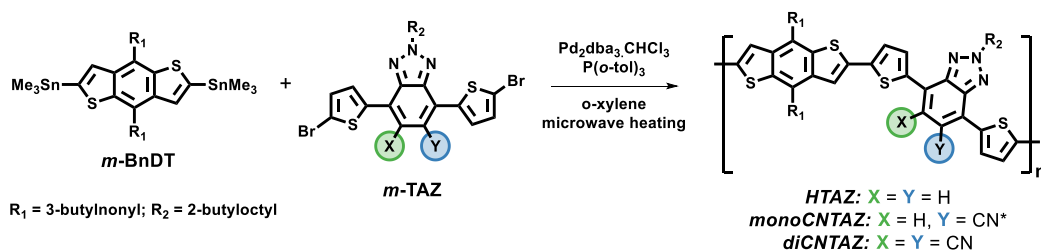
Scheme 5.6 – Polymerization of HTAZ, CNTAZ, and diCNTAZ

BnDT monomer (1.030 eq for *m*-HTAZ, 1.020 eq for *m*-monoCNTAZ and 1.015 eq for *m*-diCNTAZ), TAZ monomers (1.000eq), Pd$_2$(dba)$_3$·CHCl$_3$ (0.02 eq) and P(o-tol)$_3$ (0.16 eq) were charged into a 10 mL vial designed for microwave reactor. The mixture was evacuated and refilled with argon for three cycles before addition of anhydrous o-xylene under argon stream. The reaction was heated up to 200 °C and held in a CEM Discover

Benchmate microwave reactor for 10 min. After the polymerization, the crude polymer was dissolved in hot chlorobenzene (use 1,2-dichlorobenzene for monoCNTAZ polymer) and precipitated into stirring methanol. The collected polymer was extracted via a Soxhlet extractor with ethyl acetate, hexanes, and chloroform. The polymer solution in chloroform was concentrated via rotovap. The collected polymer was re-dissolved into hot chlorobenzene and precipitated into methanol. The polymer was then collected via filtration and dried under vacuum. For the Soxhlet extraction of monoCNTAZ, after chloroform, chlorobenzene was used. Some insoluble polymer solid floated in chlorobenzene was transferred into the chlorobenzene solution carefully with pipet. The chlorobenzene fraction was combined with the chloroform fraction. The solvent was removed, and the polymer was redissolved in dichlorobenzene, precipitated into methanol, filtered and dried under vacuum.

5.4.2 Characterization Details

Thermogravimetric analysis (TGA) measurements were taken on a TA instrument TGA-5500, with nitrogen at 25 mL/min, and ~1.5 mg of each polymer in platinum pans. The ramp rate was 10 °C per minute til 600 °C. Differential scanning calorimetry (DSC) measurements where also run on a TA instrument DSC-2500. The polymer samples, ~4 mg, where sealed in a Tzero pan, and the second heat (10 °C/min) was reported out after cycle of a first heat (10 °C/min) and cool (100 °C/min), under nitrogen. High temperature gel permeation chromatography (HT-GPC) measurements were performed on a Agilent PL220 instrument with TCB as the eluent (stabilized with 250 ppm BHT) at 160 °C. The obtained molar mass is relative to the polystyrene standard. ^{1}H and ^{13}C nuclear magnetic resonance (NMR) measurements were recorded with Bruker DRX spectrometers (400 MHz, 500 MHz or 600 MHz). Mass Spectrometry was run on a Q Exactive Orbitrap (ThermoFisher, Bremen,

Germany) mass spectrometer and analyzed via Xcalibur (ThermoFisher, Breman, Germany). UV-visible absorption spectra were obtained with a Shimadzu UV-2600 spectrophotometer. The film thicknesses were recorded by a profilometer (Alpha-Step 200, Tencor Instruments).

CV measurements were carried out on solid films using a Bioanalytical Systems (BAS) Epsilon potentiostat with a standard three-electrode configuration. A three electrode cell of a glassy carbon working electrode, Ag/Ag^+ reference electrode and Pt counter electrode were used. Films were drop-cast onto the glassy carbon electrode from hot chloroform solution (2 mg/mL, with tetrabutylammonium hexafluorophosphate added at 100% wt% relative to polymers) and dried using a heat gun. 0.1 M solution of tetrabutylammonium hexafluorophosphate in anhydrous acetonitrile was used as a supporting electrolyte. Scans were carried out under argon atmosphere at a scan rate of 100 mV/s. The reference electrode was calibrated using a ferrocene/ferrocenium redox couple. The HOMO in electron volts was calculated from the onset of the oxidation potential (E_{ox}) according to the following equation:

$$HOMO = -[4.8eV + e(E_{ox} - E_{Fc/Fc^+})]$$

Mobility values were acquired through hole-only devices with a configuration of ITO/CuSCN/active layer/MoO$_3$/Al. The experimental dark current densities (J) were measured by Keithley 2400. The applied voltage (V) was corrected from the voltage drop (V_{rs}) due to the series resistance and contact resistance, which were found from a reference device without the active layer. From the plots of $J^{0.5}$ vs V, hole mobilities (μ_h) of polymers were deduced from the Mott-Gurneys law: $J = \frac{9}{8} \varepsilon_r \varepsilon_0 \mu_h \frac{V^2}{L^3}$, where ε_0 is the permittivity of free space, ε_r is the dielectric constant of the polymer, which is assumed to be around 3, and L is the film thickness of the active layer.

GIWAXS was measured at beamline 7.3.3 of Advanced Light Source (ALS) at Lawrence Berkeley National Laboratory. The 10 keV X-ray beam was incident at a grazing angle of 0.13°, which maximized the scattering intensity from the samples and minimized the scattering intensity from the substrate. The scattered intensity was detected with a Dectris Pilatus 1M photon counting detector.

R-SoXS was measured at beamline 11.0.1.2 of the ALS on blend films. Data were acquired at the photon energy of 283.6 eV where the contrast between polymer and fullerene is relatively high enough for these materials, yet does not lead to beam damage or background fluorescence.

The high sensitive EQE measurement was conducted using a similar in-house setup except that a monochromatic illumination (OrielCornerstone 260 1/4 m monochromator equipped with Oriel 70613NS QTH lamp), a monocrystalline silicon diode (Model No.: Newport 71580) for calibration, and a 665 nm long-pass filters (Thorlabs FGL665S) was used accordingly and the signal was recorded by SR830 DSP lock-in amplifier in current mode without using the Keithley 428 current amplifier.

TPV and TPC measurements were carried out following a well-established experimental setup [*Appl. Phys. Lett.* **92**, 093311 (2008)]. Charge carriers were generated by a laser pulse excitation at 532 nm, with a pulse width of 8 ns at a frequency of 20 Hz from an Nd:YAG solid nanosecond pulse laser (Q-smart 100 of Quantel). For TPV measurement, the signal was recorded by a Tektronix DPO4014 oscilloscope with 1MΩ input impedance under open-circuit condition. The V_{OC} of the devices were tuned by adjusting the illumination intensity of a 100 W bromine tungsten lamp through the use of neutral density filters, producing steady-state illumination intensity between 10 and 100 mW cm^{-2} (approximately

corresponding to 0.1–1.0 sun). The power of the pulsed laser was attenuated by a set of neutral density filter so that the amplitude of TPV (ΔV) is much smaller (<5%) as compared to the V_{OC} of that under standard 1 sun illumination. With these conditions, the TPV data can be described by a mono-exponential decay course, following $\Delta V = V_p \exp(-t/\Delta\tau)$. Thus the perturbation carrier decay lifetime ($\Delta\tau$) can be determined through an exponential fitting. For the TPC measurement, the signal was collected by recording the transient photovoltage across a 50Ω load resistor through a Tektronix DPO4014 oscilloscope. The transient photovoltage in TPC measurement was generated at the same pulse intensity as TPV measurement, and was converted to current according to the Ohm's law. All of transient data were obtained by averaging 32 measurements in the oscilloscope. The TPV measurement was performed at open circuit condition, in which all of the excess charge carriers are forced to recombine inside the device and therefore no charge carriers are collected by the electrodes. In contrast, TPC measurement was carried out at short circuit condition, which enables the collection of nearly all the free charge carriers. With both the TPV and TPC data, the total charge density (n) and their lifetime ($\Delta\tau$) in a device at open voltage under varied light intensity can be deduced.

5.4.3 Device Fabrication

Glass substrates coated with patterned indium doped tin oxide (ITO) were purchased from Thin Film Devices, Inc. About 150 nm sputtered ITO pattern had a resistivity of 20Ω/□. Prior to use, the substrates were ultrasonicated in deionized water, acetone, and then 2-proponal for 15 minutes each. The substrates were dried under a stream of nitrogen gas and subjected to the treatment of UV-Ozone for 15 min. For device with CuSCN as the hole transport layer, the CuSCN was dissolved in diethylsulfide with the concentration 23 mg/mL

under stirring for 1 h. Then the CuSCN solution was filtered by 0.2 µm poly(tetrafluoroethylene) (PTFE) filter and spun-cast on the cleaned ITO substrates at 6000 rpm for 60 s and then baked at 100 °C for 10 min in air to give a thin film with a thickness of about 40 nm. For device with PEDOT:PSS (CLEVIOS™ P VP AI 4083) as hole transfer layer, the PEDOT:PSS was filtered by 0.45 µm poly(vinylidene fluoride) (PVDF) filter and spun-cast on the cleaned ITO substrates at 4000 rpm for 60 s and then baked at 130 °C for 15 min in air to give a thin film with a thickness of about 40 nm. Blends of polymer:PCBM (1:2 w/w) were dissolved in 1,2,4-trichlorobenzene with heating at 130 °C for 6h. All the solutions were filtered through a 5.0 µm PTFE filter and spun-cast at an optimized rpm for 60 seconds onto the HTL layer. The substrates were transferred into vacuum chamber immediately after spin-coating and then dried at 30 mmHg below atmosphere for 30 mins. For device with PFN as electron transfer layer, the PFN was dissovled in methanol with 0.3% ethyl acid (0.2mg/ml) and spun-cast on the active layer at 1800 rpm for 30 s. The devices were finished for measurement after thermal deposition of a 30 nm film of calcium and a 70 nm aluminum film for device without PFN or a 70 nm aluminum film for device with PFN as the cathode at base pressure of 2×10^{-6} mbar. The concentrations of the polymer and PCBM solution in 1,2,4-trichlorobenzene are as follows: 10 mg/mL for HTAZ, 6 – 7 mg/mL for monoCNTAZ and 7 – 8 mg/mL for diCNTAZ. There were 8 devices per substrate, with an active area of 13 mm^2 per device. Device characterization was carried out under AM 1.5G irradiation with the intensity of 100 mW/cm^2 (Oriel 91160, 300 W) calibrated by an NREL certified standard silicon cell. Current density versus voltage (J-V) curves was recorded with a Keithley 2400 digital source meter. EQE was detected under monochromatic illumination (OrielCornerstone 260 1/4 m monochromator equipped with Oriel 70613NS QTH lamp), and

the calibration of the incident light was performed with a monocrystalline silicon diode (Model No.: Newport 71580). All fabrication steps after adding the PEDOT:PSS or CuSCN layer onto ITO substrate, and characterizations were performed in gloveboxes under nitrogen atmosphere.

CHAPTER 6: Functionalization of Benzotriazole-Based Conjugated Polymers for Solar Cells: Heteroatom vs Substituents [15]

6.1 Introduction

The research community has devoted tremendous amount of efforts towards the structure-property relationship to make organic solar cells commercially viable by design.[28,31,301–304] These relationships include the impact of chemical structure on both the performance and long-term stability of the solar cell.[305–309] Our research lab, along with various others across the world, have worked on the synthesis of a large library of organic semiconducting polymers over the past decade;[44,45,310–312] however, many of these are missing key polymers to truly distill a complete ensemble of the structure-property relationships. From our current database of TAZ-based polymers, there are a series of unanswered questions which we intend to address in this work.

In the previous chapter, we demonstrated a series of TAZ based polymers with varying amounts cyano functionalization (zero – HTAZ, one – CNTAZ, and two – diCNTAZ).[14] Unlike the trends we see with FTAZ, the addition of a second cyano group (diCNTAZ) results in a large decrease in the performance. In that work, we found that this degradation in performance upon addition of the second cyano group was driven by a

---

[15] Parts of this chapter previously appeared as an article in *ACS Applied Polymer Materials*. Reprinted with permission from © 2021 American Chemical Society. The original citation is as follows: **Jeromy James Rech**, Liang Yan, Zhen Wang, Qianqian Zhang, Spencer Bradshaw, Harald Ade, and Wei You. "Functionalization of Benzotriazole based Conjugated Polymers for Solar Cells: Heteroatoms vs. Substituents" *ACS Applied Polymer Materials*, **2021**, 3 (1), 30-41.

decrease in the hole mobility and purity of domains, along with an increase in the recombination kinetics. This leads to our first set of questions: *Is this decrease in performance upon further functionalization of cyano-functionalized polymers unique to only the cyano group? Or is a single cyano group the optimal amount of functionalization for the TAZ series?*

Furthermore, while we have done a large variety of work with fluorination, the use of nitrogen heteroatoms was rather limited. In 2015 our group reported a pyridazine based polymer (PrzTAZ); however, the efficiency was low (4.8%) primarily because of poor hole mobility and fill factor.[141] Interestingly, we also reported a pyridine-based polymer with an additional cyano substituent (PyCNTAZ) which demonstrated significantly higher efficiency (7.5%).[141] This brings up the next set of questions: *How does the performance of a pyridine-based TAZ core compare to the benzene and pyridazine-based polymers? How does the method of nitrogen incorporation (i.e., nitrogen heteroatom vs cyano functional group) impact the polymer properties? Does the PrzTAZ polymer suffer from the same overfunctionalization issues as diCNTAZ?*

And finally, we reported isomers of PBnDT-FTAZ in which the fluorine substituents are moved from the TAZ acceptor moiety to the thiophene linkers connecting the BnDT and TAZ components (3FT-HTAZ and 4FT-HTAZ).[135] These publications have shown promise of fluorinated thiophene as structural units but there are limited numbers of polymers which they have been included on. This leads to the final question: *Can the incorporation of fluorine substituents on the thiophene linker result in improved solar cell performance for these new nitrogen-based functionalized acceptor moieties?*

Each of these questions can be answered with a specific new series of conjugated polymers which are shown in **Chart 6.1**. These include the pyridine-based polymers of PyTAZ and 4FT-PyTAZ and the cyano functionalized CNTAZ and 4FT-CNTAZ polymers. This series can offer further insight into the structure-property relationships of TAZ-based polymers, a deeper understanding to systems with various different types of functional groups, and help design new materials in the future.
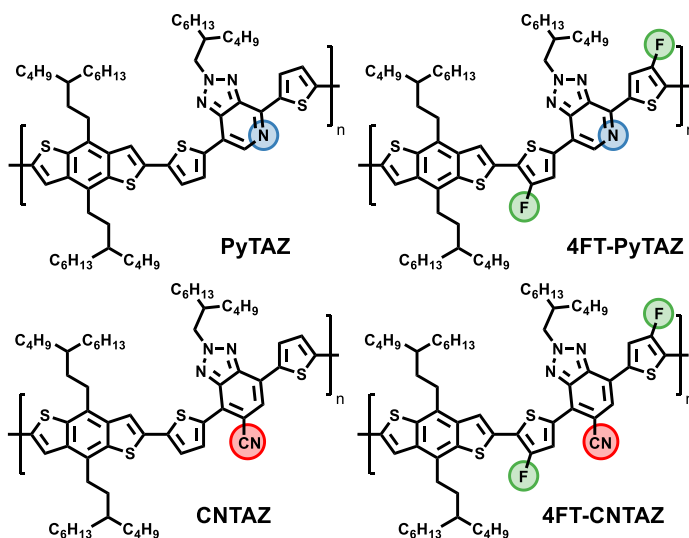
Chart 6.1 – Chemical Structures for the four polymers used in this study: PyTAZ, 4FT-PyTAZ, CNTAZ, and 4FT-CNTAZ

To create a detailed structure-property relationship, we investigated the optical, electrochemical, and photovoltaic properties of these polymers, and in order to understand the solar cell device results, we also explored the changes in morphology, charge transfer state energy, and charge recombination dynamics. The PyTAZ polymer has an improved efficiency when paired with PCBM compared to HTAZ and PrzTAZ; however, trap-assisted recombination driven by low mobility, large domain size, and excessively pure domain purity holds back the efficiency. The addition of the fluorine substituent (4FT-PyTAZ) results in a red-shifted UV-vis absorption and improved mobility. These changes are driven by the non-

covalent intramolecular interactions which results in a more planar backbone and closer π-π

spacing. For the cyano-based polymers (CNTAZ and 4FT-CNTAZ), the stronger electron

withdrawing strength of the cyano group results in a red shift and deeper HOMO energy

levels. Furthermore, the cyano modification produced an improved voltage and current

compared to the pyridine-based polymers. The 4FT-CNTAZ polymer has a decrease in

efficiency compared to CNTAZ, but the magnitude of decrease is much smaller compared to

diCNTAZ. The 4FT-CNTAZ is able to maintain a high open circuit voltage and hole

mobility value, but a decrease in the domain purity and increased in charge carrier

recombination – geminate recombination from low exciton splitting driving force – result in

a loss of short circuit current density and fill factor. Overall, this work highlights the key

structure-property relationships with regards to nitrogen heteroatoms, cyano-, and fluorine

functional groups on TAZ-based semiconducting polymers used in organic solar cells.

6.2 Results and Discussion

6.2.1 Synthesis

      We began with the synthesis of the acceptor moiety core for both the PyTAZ and

CNTAZ, shown in **Scheme 6.1a**. There are three fundamental steps which include (1)

bromination of the aromatic core, (2) ring closure to form the triazole, and (3) addition of the

solubilizing side chain. Normally a different order is used when synthesizing TAZ-based

monomers in which bromination is the final step. For the PyTAZ and CNTAZ cores

however, it is important to brominate prior to forming the triazole, as the electron

withdrawing nature of the triazole in addition to the new functional groups significantly

increased the difficulty of the bromination. Specifically, after the triazole is formed (for both

PyTAZ and CNTAZ), we tried a variety of brominating conditions, including very harsh

conditions like refluxing for an entire week, and there was no appreciable amount of product

formed.
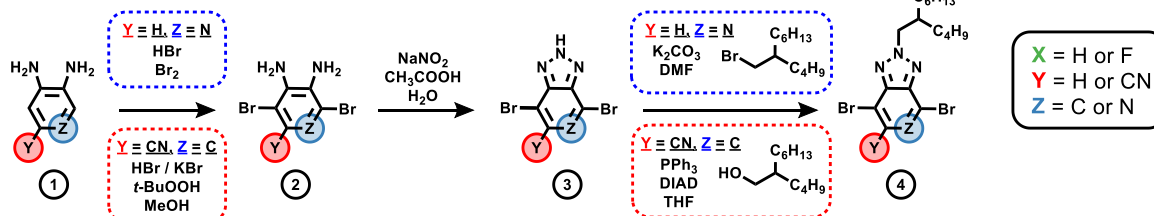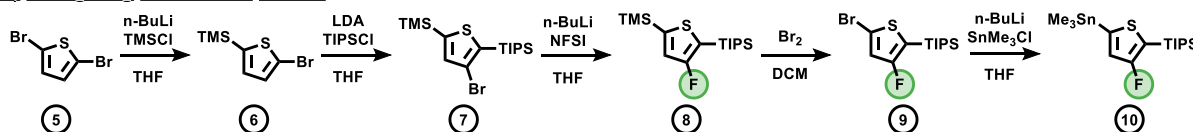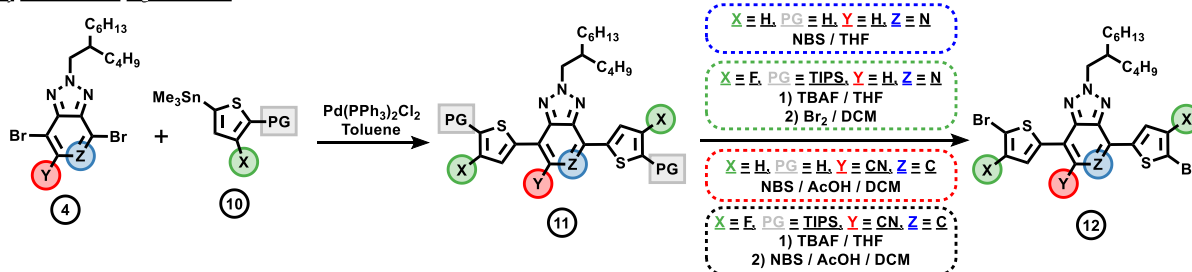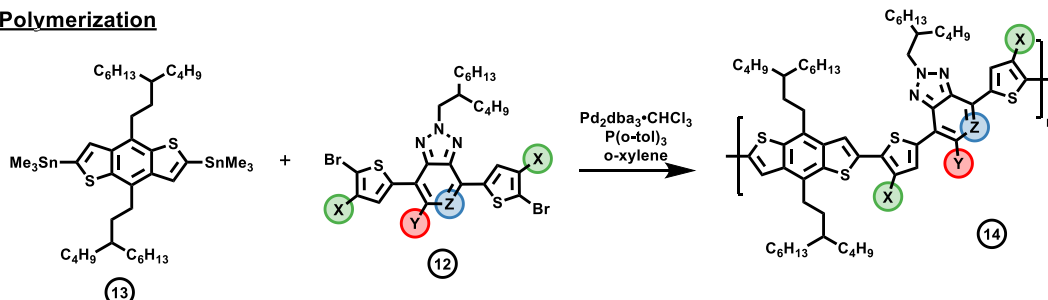
Scheme 6.1 – Reaction Scheme for the Synthesis of the (a) Pyridine and Cyano-based Acceptor Moieties, (b) Fluorinated Linker, (c) Final Monomers, and (d) Polymerization. Note: Some reaction arrows include various reaction conditions, denoted by the dashed boxes, based on the chemical identity of the starting material.

Therefore, to circumvent this issue, we used 3,4-diaminopyridine and 3,4-

diaminobenzonitrile (compound **1**) as the starting materials for PyTAZ and CNTAZ

respectfully. The pyridine-based substrate can undergo a straightforward bromination with

hydrobromic acid and liquid bromine. However, for the cyano-substituted starting material, a

more aggressive oxidative bromination with potassium bromide, hydrobromic acid, and *tert-*

butyl hydroperoxide is needed to achieve compound **2**. This bromination protocol has been previously published by us and others.[14,283] Following purification, compound **2** can be cyclized through conventional triazole chemistry to form compound **3**. In the case of the PyTAZ core, the solubilizing side chain can be added through a standard alkylation reaction between the triazole and the brominated side chain; however, this same chemistry resulted in very poor yields on the CNTAZ substrate. Therefore, in order to synthesize compound **4** where Y=CN and Z=C, a Mitsunobu-type reaction was explored. In this reaction, the alcohol variant of the side chain is added with the assistance of triphenyl phosphine and diisopropyl azodicarboxylate (DIAD).

Next is the synthesis of the functional thiophene linker (4FT) for 4FT-PyTAZ and 4FT-CNTAZ. We have previously published a reaction scheme to a mono-fluorinated thiophene linker; however, that chemistry involved extra synthetic steps including a series of protection and deprotection reactions for the final compound to be fluorinated at the four position and stannylated at the two position. Furthermore, the starting material must be brominated on the 4 position, which increases the cost of the starting material by almost double. Here we report a different synthetic route (**Scheme 6.1b**) to the same product that avoids these aforementioned issues. Starting with 2,5-dibromothiophene (compound **5**), the first two reactions involve protection of the 2 and 5 position of the thiophene linker. After one equivalence of *n*-butyl lithium (*n*-BuLi) followed with chlorotrimethylsilane, the two position is protected with the TMS group. The next step utilizes a halogen dance rearrangement to protect the five position while simultaneously moving the bromine to the four position.[313] The choice of lithium diisopropylamide (LDA) as the nucleophile is important as it will lithiate the four position rather than removing the bromine, which is what

167

n-BuLi would do. As the stability of the four position and five position of the thiophene differ, the halogen (bromine) and lithium would undergo a rearrangement to relocate the anion to the five position, so upon addition of the electrophile/protecting group of chlorotriisopropylsilane, compound **7** is formed. Compound **8** is formed via electrophilic fluorination with N-fluorobenzenesulfonimide (NFSI). In order to increase the yield of this reaction, *n*-BuLi and NFSI were added in specific amounts over time; more details can be found in section 6.4. Finally, the two position, which is protected by TMS, can be selectively brominated and subsequently stannylated to form compound **10**.

The stannylated thiophene linker and the brominated triazole core then undergo a Stille coupling reaction to form compound **11**, which is the protected form of the final monomer. For PyTAZ and CNTAZ, there is no protecting group (i.e., PG=H), and the compound can be directly brominated. For 4FT-PyTAZ and 4FT-CNTAZ, the TIPS protecting group needs to first be removed with tetra-*n*-butylammonium fluoride (TBAF). The brominating conditions slightly vary for each of the substrates. PyTAZ can be brominated with *N*-bromosuccinimide (NBS), while a harsher reaction with liquid bromine is needed for 4FT-PyTAZ. Both of the CNTAZ-based compounds can undergo similar NBS bromination with the assistance of catalytic amounts of acetic acid. After compound **12** is made, the monomer is recrystallized multiple times to increase the purity to a level appropriate for polymerization. The BnDT monomer (compound **13**) is synthesized according to previous reports.[125]

The conjugated polymers (PyTAZ, 4FT-PyTAZ, CNTAZ, and 4FT-CNTAZ) are made through a microwave-assisted, step growth, Stille polycondensation polymerization,[158] shown in **Scheme 6.1d**. The ratio of compound **12** and compound **13** is varied to control the

168

molar mass of the polymer through the Carothers' equation. The number average molar mass (M_n) and dispersity ($Đ$) of each polymer was measured through high-temperature gel permeation chromatography (HT-GPC), and the results are included in **Table 6.1**. All four of the resulting polymers can be dissolved in common solvents used in OSCs, such as chloroform and chlorobenzene at elevated temperatures.

Table 6.1 – Molar mass, optical, and electrochemical properties of the polymers

Polymer	Mn (kg/mol)	Đ	$\lambda_{max, sol}$ (nm)	$\lambda_{max, film}$ (nm)	λ_{onset} (nm)	HOMO [a] (eV)	LUMO [b] (eV)	Optical E_{gap} [c] (eV)
PyTAZ	34.3	2.6	550 591	549 594	639	-5.48	-3.54	1.94
4FT-PyTAZ	26.6	2.5	563 606	559 607	666	-5.64	-3.78	1.86
CNTAZ	44.7	2.4	564 603	565 605	664	-5.60	-3.72	1.87
4FT-CNTAZ	39.2	2.0	583 623	583 625	693	-5.66	-3.87	1.79

[a]HOMO levels were estimated by cyclic voltammetry; [b] LUMO = HOMO + optical band gap; [c]Optical band gap was estimated from the onset of absorption of polymer films

6.2.2 Optical and Electrochemical Properties

To investigate the impact of the structural changes on the optical and electrochemical properties, we first investigated the UV-vis absorption of the polymers in a solution of 1,2,4-trichlorobenzene (**Figure 6.1a**). The attenuation coefficient was also measured for thin films of each polymer and is depicted in **Figure 6.1b**; all of the polymers exhibit strong absorption in the visible region with similar attenuation coefficients slightly less than 1×10^5 cm^{-1}. The most notable differences between the four polymers optical properties occur at the longer wavelength region which corresponds to the intramolecular charge transfer (ICT) formation of the polymer backbones. Comparatively, the cyano substituted polymers are red shifted to

the corresponding pyridine containing polymers (CNTAZ vs. PyTAZ, 4FT-CNTAZ vs. 4FT-PyTAZ), and this shift is attributed to the stronger ICT formation due to the higher electron-withdrawing ability of the cyano group. The maximum absorption wavelengths and the absorption onset values for each polymer are included in **Table 6.1**.
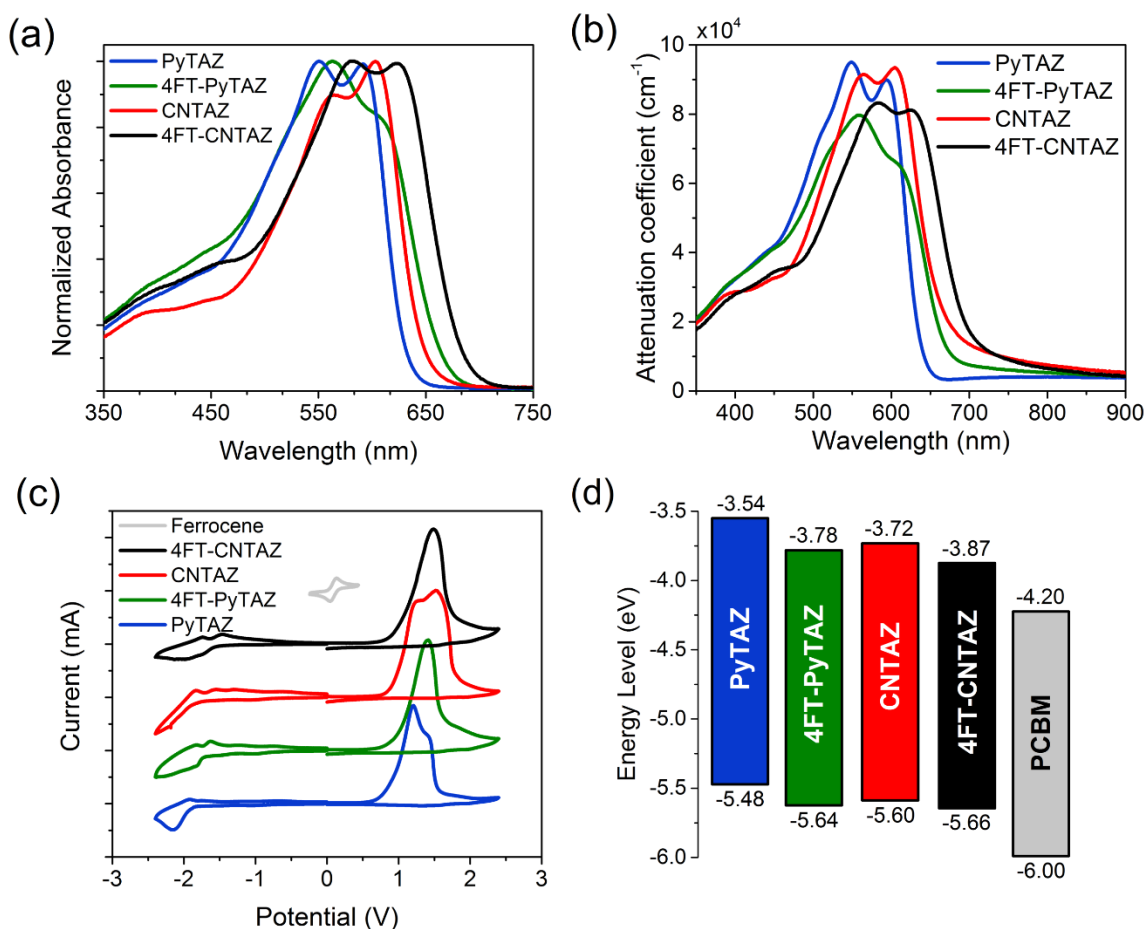
Figure 6.1 – (a) Solution UV-vis for PyTAZ, 4FT-PyTAZ, CNTAZ, and 4FT-CNTAZ in trichlorobenzene, (b) thickness-normalized attenuation coefficient of thin polymer films measured via UV-vis, (c) cyclic Voltammetry of polymer think films, and (d) resulting HOMO/LUMO energy level diagram for each polymer and PCBM.

Also, the addition of the fluorine on the thiophene linker results in a bathochromic shift of the UV-vis absorption by ~30 nm for both polymer types (CNTAZ vs. 4FT-CTAZ, PyTAZ vs.4FT-PyTAZ). The fluorine induced red-shift is likely caused by the electron withdrawing nature of fluorine coupled with non-covalent intramolecular interactions

between the linker and neighboring core, which lead to a more planar backbone. There are a variety of reports demonstrating S···F interactions along the conjugated polymer backbones,[226,229,314] but we also confirmed this through computational modeling. We performed density functional theory (DFT) calculations at the DFT B3LYP/6-311+G(d) level of theory on one repeat unit for all four polymers, with the side chains reduced to an ethyl unit to reduce the complexity of the model. The results are included in **Figure 6.2** along with energy level distributions (*vide infra*). In the non-fluorinated polymers (PyTAZ and CNTAZ), the dihedral angle between the BnDT unit and the thiophene linker is ~ 12˚; upon addition of the fluorine that same dihedral angle is drastically reduced towards zero. There are additional non-covalent planarizing interactions present in the PyTAZ series in the form of N···S interaction between the pyridine and neighboring thiophene. When Z=C (i.e., benzene core), the dihedral angle between the TAZ core and thiophene linker is around 2–3˚, and when the carbon is replaced with a nitrogen to form the pyridine core, that same angle is reduced to 0˚. A final note with the modeling involves the impact of the cyano substituent; while the cyano group is a very strong electron withdrawing group, it is also bulkier than fluorine and increases the twisting of the backbone. The dihedral angle of the CNTAZ and 4FT-CNTAZ polymers about the cyano group increases from 2–3˚ to ~ 30˚ for both polymers. Fortunately, this steric impact does not negatively affect the mobility of the polymer which is measured directly through space charge limited current (SCLC) measurements (**Table 6.2**).
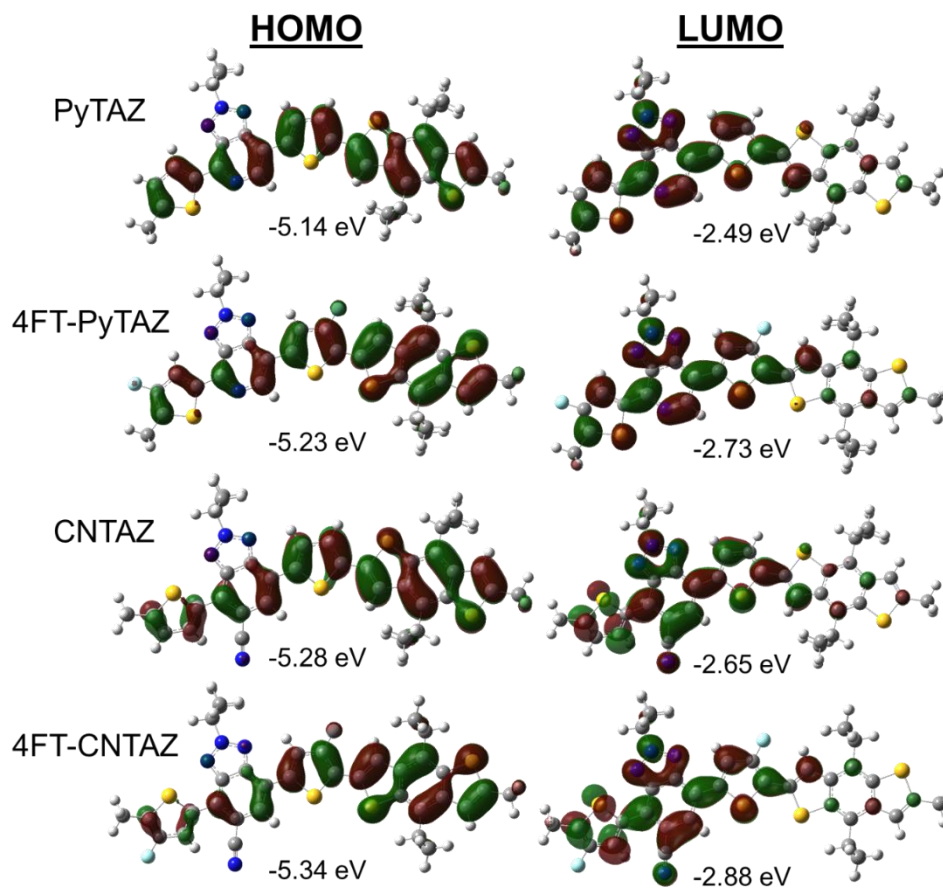
Figure 6.2 – Chemical structure of PyTAZ, 4FT-PyTAZ, CNTAZ, and 4FT-CNTAZ with HOMO and LUMO orbitals and corresponding energy levels as calculated through DFT

Additionally, the UV-vis absorption spectra of the polymers in solution at room temperature are nearly identical to those of the thin film, which suggests that the polymer chains are already aggregated in the solution. The aggregation behavior of the polymers was also measured through temperature dependent UV-vis absorption spectra in 1,2,4-trichlorobenzene between 20 and 120 °C (**Figure 6.3**). The most notable difference between the spectra of the four polymers is the change in aggregation strength upon fluorination. While PyTAZ (**Figure 6.3a**) and CNTAZ (**Figure 6.3c**) exhibit a complete loss of the far wavelength shoulder at elevated temperatures, 4FT-CNTAZ (**Figure 6.3d**) still includes the

aggregation shoulder. This aligns with the modeling results, as the more planar backbones

will have stronger interactions and thus aggregate.
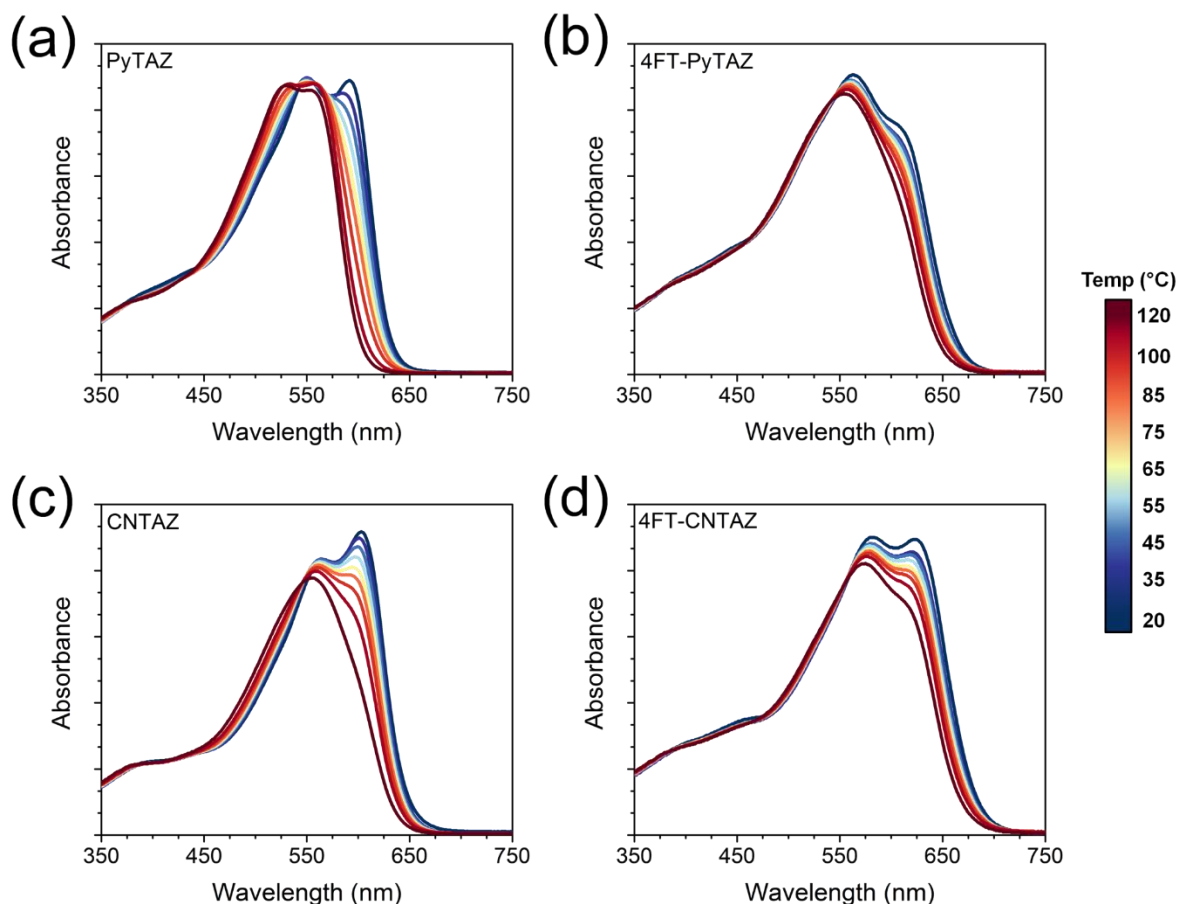
Figure 6.3 – Temperature dependent solution UV-Vis for each polymer. The color of the curve corresponds to the heat bar legend. (a) PyTAZ, (b) 4FT-PyTAZ, (c) CNTAZ, and (d) 4FT-CNTAZ

Finally, the electrochemical properties of the four polymers were measured through

cyclic voltammetry (CV). A thin polymer film was deposited onto a glassy carbon working

electrode, and the CV measurements were taken through a three-electrode configuration with

the aforementioned working electrode, a Ag/Ag^+ reference electrode, and a platinum counter

electrode. The oxidation and reduction peaks for the three polymers are depicted in **Figure**

6.1c. The HOMO levels are estimated from the oxidation onset peak, in reference to a

ferrocene/ferrocenium peak. The LUMO energy levels are estimated for each polymer

through the optical band gap measured from the absorption onset of the UV-vis spectra and the HOMO. The DFT calculations also produce a value for the HOMO and LUMO energy values, which are included in **Figure 6.2**. Compared with the experimentally determined values, the values of energy levels from the calculations are all systematically shifted based on the assumptions made in the modeling; however, the same trends are seen among all four of the polymers. The corresponding highest occupied molecular orbital (HOMO) and lowest unoccupied molecular orbital (LUMO) energy levels for each polymer is shown in **Figure 6.1d**.

The CNTAZ HOMO energy level is 0.12 eV deeper than PyTAZ because the cyano group is a stronger electron withdrawing group, which is also consistence with the UV-vis results. This is advantageous as the open circuit voltage (V_{OC}) is generally related to the energy difference between the LUMO of the acceptor (i.e., PCBM) and the HOMO of the donor polymer. Therefore, the CNTAZ based polymers should exhibit an improved V_{OC} compared to the PyTAZ series. Next, when fluorine substituents are added to the polymer, the HOMO energy is also lowered from the electron withdrawing nature of fluorine; however, the impact on the 4FT-PyTAZ polymer is different than on 4FT-CNTAZ. Between PyTAZ and 4FT-PyTAZ, there is a 0.16 eV decrease in the HOMO energy level upon fluorination; but on the cyano series, this change in only 0.06 eV. This trend is consistent with our previous report where we investigated cyano substitution; the addition of a second cyano group to form diCNTAZ only lowers the HOMO energy level by 0.02 eV.[14] This diminishing return upon further functionalization occurs because the while the substituent is electron withdrawing, the acceptor moiety is already heavily electron-deficient and the net impact of further functionalization is minimal.

6.2.3 Photovoltaic Properties

Next, these newly synthesized polymers were incorporated into bulk heterojunction (BHJ) solar cells with a conventional configuration of indium doped tin oxide (ITO)/copper(I) thiocyanate (CuSCN)/polymer:PCBM/PFN/aluminum, where PFN stands for Poly[(9,9-bis(3'-(N,N-dimethylamino)propyl)-2,7-fluorene)-alt-2,7-(9,9–dioctylfluorene)].[284] The active layer consisted of a 1:2 weight ratio of polymer:PCBM, and the thickness was kept to ~260 nm for all devices reported herein. The hole transport layer of CuSCN was selected because of the deep HOMO energy levels of the cyano-functionalized polymers.[269] A representative current density (J) *vs.* voltage (V) response for each solar cell is presented in **Figure 6.4a**. Similarly, the device characteristics of short circuit current density (J_{SC}), open circuit voltage (V_{OC}), fill factor (FF), and power conversation efficiency (PCE) are summarized in **Table 6.2**, where each entry is the average of at least 8 solar cells.
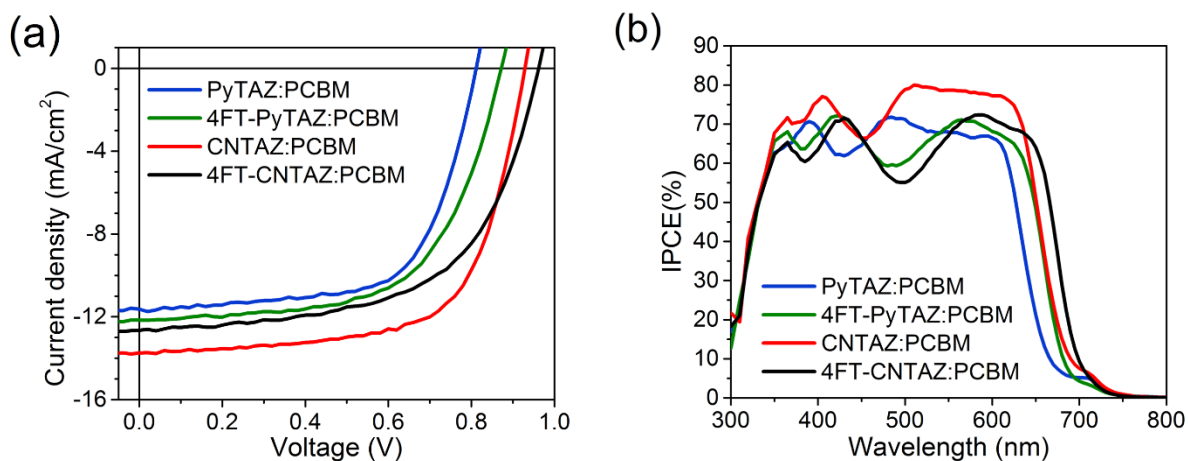
Figure 6.4 – (a) Representative *J-V* curve and (b) IPCE curves of each OSC device

Table 6.2 – Photovoltaic properties of the various polymer:PCBM solar cells

Polymer	J_{SC} (mA/cm^2)	V_{OC} (V)	*FF* (%)	PCE (%)	Hole mobility ($\times 10^{-3}$ cm^2/V·s)
PyTAZ	11.36 ± 0.49	0.809 ± 0.002	65.0 ± 0.8	5.98 ± 0.30	0.39
4FT-PyTAZ	11.85 ± 0.32	0.872 ± 0.001	62.4 ± 1.3	6.44 ± 0.23	0.56
CNTAZ	13.82 ± 0.32	0.926 ± 0.004	66.2 ± 1.0	8.48 ± 0.32	1.04
4FT-CNTAZ	12.63 ± 0.63	0.961 ± 0.001	57.4 ± 2.5	6.96 ± 0.18	1.08

With regards to structure-property relationship, the first clear trend is with V_{OC}. Comparing the V_{OC} values for PyTAZ (0.809 V) and CNTAZ (0.926 V) polymers, the stronger electron withdrawing strength from the cyano group results in a deeper HOMO energy level and thus higher V_{OC}. Similarly, with the fluorine impact, the V_{OC} increases between PyTAZ and 4FT-PyTAZ (0.809 V to 0.872 V) and from CNTAZ to 4FT-CNTAZ (0.926 V to 0.961 V). This is also consistent with the electrochemical properties highlighted previously, including the diminishing returns of further fluorination on flanking thiophenes (4FT) on the CNTAZ substrate compared to PyTAZ (0.06 V increase in the case of PyTAZ compared to 0.03 V for CNTAZ). While the electrochemical and photovoltaic properties present an overview, a more detailed investigation including measurements of the charge transfer (CT) state and V_{OC} loss of each blend was conducted (*vide infra*, section 6.2.5).

Comparatively, the trends with J_{SC} are not as obvious. The addition of fluorine substituent in the form of 4FT to the PyTAZ core increases the current density (11.36 mA/cm^2 to 11.85 mA/cm^2 for 4FT-PyTAZ) which is a trend previously demonstrated with fluorination.[135] This increase in J_{SC} can be explained by the red shift in absorption allowing for a wider range of photon harvesting coupled with the increase in hole mobility offered from the more planar backbone. The red shift is also clear on the incident photon to charge carrier efficiency (IPCE) plot in **Figure 6.4b**. The CNTAZ exhibits the largest J_{SC} value of

13.82 mA/cm^2; however, upon addition of the fluorine substituent, although the absorption red shifts and the hole mobility is maintained, the 4FT-CNTAZ has a lower J_{SC} of only 12.63 mA/cm^2. This result dictates a further investigation to understand the loss mechanism for the current density in the 4FT-CNTAZ. Based on our previous results with diCNTAZ (benzotriazole core functionalized with two cyano groups), the addition of the second cyano group resulted in a degradation in device performance compared to CNTAZ, which was driven by a decrease in hole mobility, poor domain purity, and an increase in recombination kinetics.[14] Interestingly, the hole mobility of 4FT-CNTAZ is actually marginally improved compared to that of CNTAZ. Therefore, the investigation was first be directed to morphology (*vide infra*, section 6.2.4) and then to the charge recombination dynamics (*vide infra*, section 6.2.6).

As mentioned previously, the inclusion of two cyano group in diCNTAZ resulted in poor domain purity compared to CNTAZ, and this unfavorable morphology resulted in a lower *FF*.[14] Similarly, further functionalization of CNTAZ with fluorinated thiophene linkers (4FT) also decreases the *FF* from 66.2% for CNTAZ to 57.4% for 4FT-CNTAZ. When looking at the *FF* for the PyTAZ series, a similar effect, with less magnitude, is observed when comparing PyTAZ (65.0%) and 4FT-PyTAZ (62.4%). To confirm that the decrease in *FF* is from a morphological change, the morphology of each blend was explored (*vide infra*, section 6.2.4).

Altogether, the combination of the V_{OC}, J_{SC}, and *FF* make up the PCE of the solar cell. Of the four polymers reported here, the PyTAZ exhibits the lowest efficiency of 5.98%. However, compared to the unfunctionalized HTAZ (X=Y=H and Z=C) polymer which has an efficiency of 4.39%,[13,125] the inclusion of the nitrogen heteroatom notably improved the

efficiency. This increase in efficiency is driven by an increase in V_{OC}, J_{SC}, and FF, which highlights the value of the nitrogen heteroatom. Further functionalization of PyTAZ with fluorinated thiophene units (4FT) improved the J_{SC} and V_{OC}, and while there was a loss in FF, the overall efficiency of 4FT-PYTAZ is improved to 6.44%. Instead of incorporating the nitrogen group as a heteroatom, the stronger electron withdrawing cyano group can achieve an even larger efficiency; with an average efficiency of 8.48% for CNTAZ. Further functionalization beyond one cyano group results in a degradation of performance. While 4FT-CNTAZ has an improved V_{OC}, the loss in J_{SC} and FF results in a net lowering of the efficiency to 6.96%. As mentioned previously, to gain a more in-depth understanding of the structure-property relationship for this series of polymers, the morphology, charge transfer energy, and charge recombination dynamics need to be explored.

6.2.4 Morphology and Fill Factor

The morphology of the active layer can be probed via synchrotron-radiation-based grazing incident wide-angle X-ray scattering (GIWAXS)[126] and resonant soft X-ray scattering (RSoXS).[315] We first utilized GIWAXS to investigate the texture and packing of the polymers in both neat films (**Figure 6.5**) and blends with PCBM (**Figure 6.6**). Firstly, all four neat polymers have some degree of preferential orientation. While all polymers exhibit a (010) π-π stacking peaks in the out-of-plane (OOP) direction, the strength of the (100) lamellar peaks in the in-plane (IP) direction varies. A quantitative analysis would require pole-figure analysis taking the Ewald sphere correction into account. Qualitatively, 4FT-PyTAZ and 4FT-CNTAZ have the strongest face-on orientation, likely driven by the fluorine substituents. CNTAZ has both face-on and edge-on population, with a larger population of face-on orientation. Finally, PyTAZ is the most weakly oriented. Face-on morphological

arrangement is often beneficial to charge transport in OSCs,[100,286,287] which is also consistent with the higher mobility upon fluorination. There is also a trend in the π-π spacing upon fluorination; the 4FT-PyTAZ and 4FT-CNTAZ have (010) peaks in the OOP direction at higher q values than PyTAZ and CNTAZ. The larger reciprocal space values result in a smaller real space distances, thus the fluorine substituent (i.e., 4FT) decreases the π-π stacking for both PyTAZ (3.85 to 3.70 Å) and CNTAZ (3.80 to 3.66 Å) series. This trend is also in good agreement with the computational and UV-vis results that suggest the fluorine can help planarize the backbone and allow for closer and stronger interactions between polymers. However, none of the polymers are semi-crystalline (as processed) as the coherence lengths of the (010) peaks of the polymers, estimated from the Scherrer's equation, are similar and small (~2 nm) and the paracrystalline disorder parameter (g) is consistently high (~17%) for all polymers, above the g-value of 12% of amorphous silicon.[316–318]
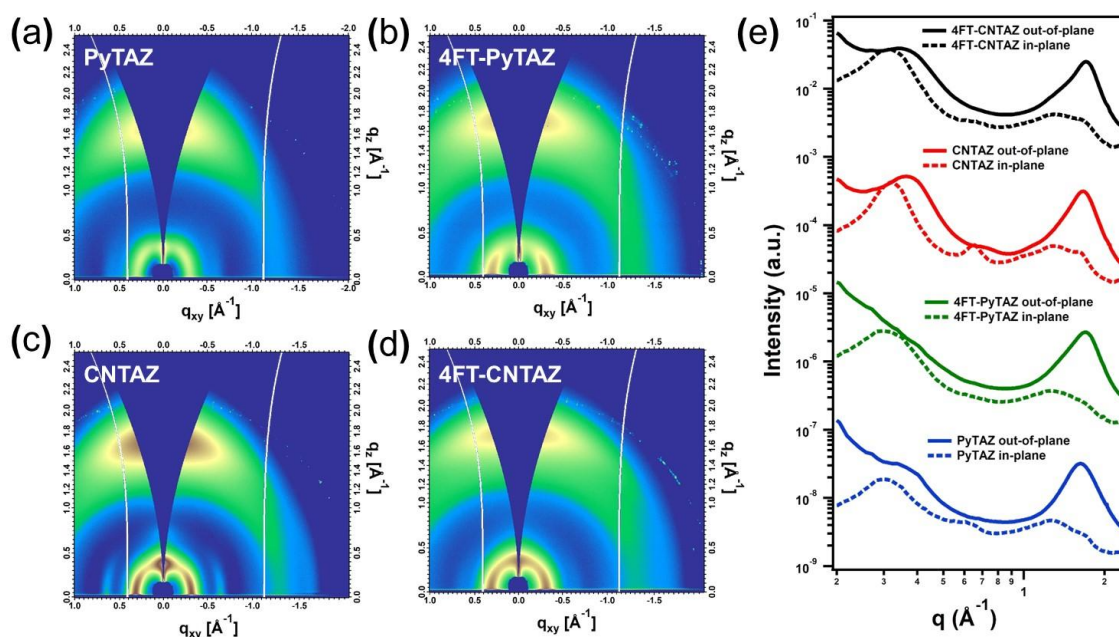
Figure 6.5 – 2D GIWAXS patterns of neat films of (a) PyTAZ, (b) 4FT-PyTAZ, (c) CNTAZ, and (d) 4FT-CNTAZ. (e) 1D profiles for both in-plane (dashed) and out-of-plane (solid) directions.

179

When the various polymers were blended with PCBM to form the BHJ morphology, some of the differences are lost and characteristics are altered. The GIWAXS patterns (**Figure 6.6**) for the blend films show relative diffuse halos of both the PCBM and polymer diffraction features that cover both the OOP and IP direction which represents a completely amorphous morphology. This is particularly the case for 4F-PyTAZ and 4F-CNTAZ with strong rings for (100) and (010), indicating a three dimensional isotropic amorphous material. In contrast, PyTAZ and CNTAZ have simultaneously enhanced intensities for the (010) and (100) peaks, indicating a two dimensional isotropic powder ("rolling log") with the polymer backbone preferentially in-plane but no other preferred orientation. The g value of ~13% for each polymer also supports the disordered morphology. GIWAXS detects only the molecular packing of the samples, and if the neat films have poor packing, blending with a second component (i.e., PCBM) would normally worsen the packing. Therefore, RSoXS is used to better probe the blend film morphology (**Figure 6.7**).[315,319] The long period (related to domain spacing) of the polymer:PCBM blends are generally similar for both CNTAZ and 4FT-CNTAZ (27.2 and 29.5 nm, respectfully). The 4FT-PyTAZ:PCBM has two peaks which correspond to the pure acceptor phase and the mixed polymer phase (83.7 and 25 nm). Finally, the PyTAZ has a much larger domain with the long period of 49.8 nm, which can cause issues with charge separation.
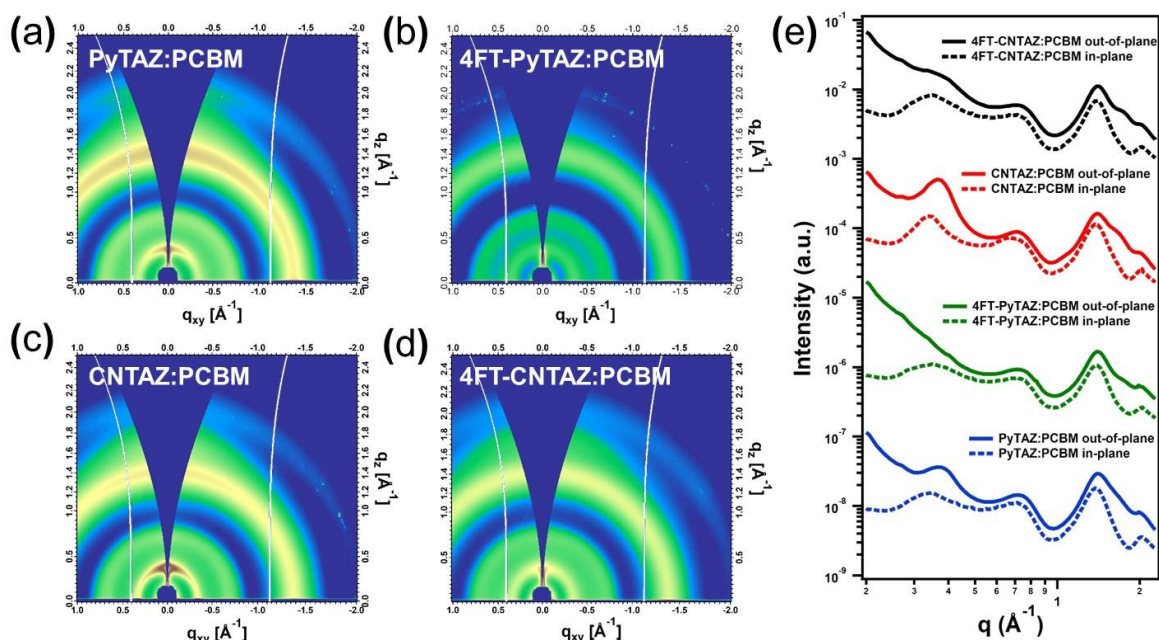
Figure 6.6 – 2D GIWAXS patterns of blend films of (a) PyTAZ:PCBM, (b) 4FT-PyTAZ:PCBM, (c) CNTAZ:PCBM, and (d) 4FT-CNTAZ:PCBM. (e) 1D profiles for both in-plane (dashed) and out-of-plane (solid) directions.
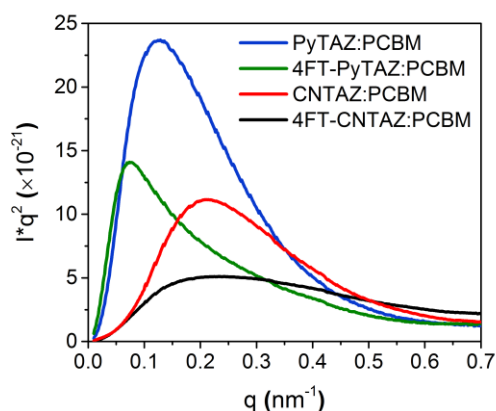
Figure 6.7 – Lorentz-corrected RSoXS profiles of each polymer:PCBM blend film

The relative root-mean-square (RMS) variation of the composition is proportional to the integral of the scattering profiles over the length scale probed, is a widely used indicator related to the average domain purity of the OPV blends.[272,319] Domain purity is typically reflected in the *FF* value; impure domains lead to bimolecular recombination and excessively pure domains can lead to isolated charge traps.[117,179–181,273] Of the four polymer blends

181

measured here, PyTAZ:PCBM has the purest domain. The combination of the large domain

size and excessively pure domain results in reduced efficiency of exciton harvesting, which

explains why PyTAZ:PCBM has the lowest J_{SC}. The mechanism for this loss is presumably

due to isolated charge traps based on the morphology; this will be further explored in the

charge recombination dynamics section (*vide infra*, section 6.2.6). Also, the 4FT-

CNTAZ:PCBM blend has the most impure domain which can explain the *FF* loss in the case

of 4F-CNTAZ when comparing CNTAZ and 4FT-CNTAZ. The molecular packing and

morphological data from GIWAXS and RSoXS are summarized in **Table 6.3**.

Table 6.3 – Morphological features of polymer films and polymer:PCBM blends

Polymer	(010) peak location [a] ($Å^{-1}$)	π-π stacking distance [a] ($Å$)	(010) peak coherence length [a] ($Å$)	Long Period [b] (nm)	Relative RMS Composition Variation [c]
PyTAZ	1.63 / 1.68	3.85 / 3.74	14.7 / 45.2	49.8	1.00
4FT-PyTAZ	1.70 / 1.65	3.70 / 3.81	27.0 / 30.9	83.7 / 25.0	0.76
CNTAZ	1.65 / 1.62	3.80 / 3.87	17.0 / 34.2	27.2	0.77
4FT-CNTAZ	1.72 / 1.66	3.66 / 3.79	17.4 / 31.9	29.5	0.62

[a]In the format of neat polymer/blend film; [b]Approximately equal to the spacing of like-domains and roughly twice the domain size; [c]Formerly referred to as "relative domain purity"; an imprecise notation.

6.2.5 CT State and V_{OC} Loss

While V_{OC} trends can be predicted by the difference in the HOMO energy level of the

polymers, it is generally accepted that the V_{OC} is primarily determined by the energy of the

interfacial charge-transfer (CT) state of the donor and the acceptor materials.[320–322]

Vandewal and coworkers demonstrated that the CT state has a more direct relationship with

V_{OC} through **Equation 6.1**.[191] Based on that same work, though less rigorous, the CT state

(E_{CT}) can be estimated by fitting high sensitivity EQE measurements with **Equation 6.2**.[191]

High sensitivity EQE measurements and curve fittings for all four polymers can be found in

Figure 6.8.

$$V_{oc} = \frac{kT}{q} ln\left(\frac{J_{ph}}{J_0} + 1\right) = \frac{E_{CT}}{q} + \frac{kT}{q} ln\left(\frac{J_{sc}h^3c^2}{fq2\pi(E_{CT} - \lambda)}\right) + \frac{kT}{q} ln(EQE_{EL}) \quad \textbf{(Eq 6.1)}$$

$$EQE_{PV}(E) = \frac{f}{E\sqrt{4\pi\lambda kT}} \exp\left(\frac{-(E_{CT}+\lambda-E)^2}{4\lambda kT}\right) \quad \textbf{(Eq 6.2)}$$
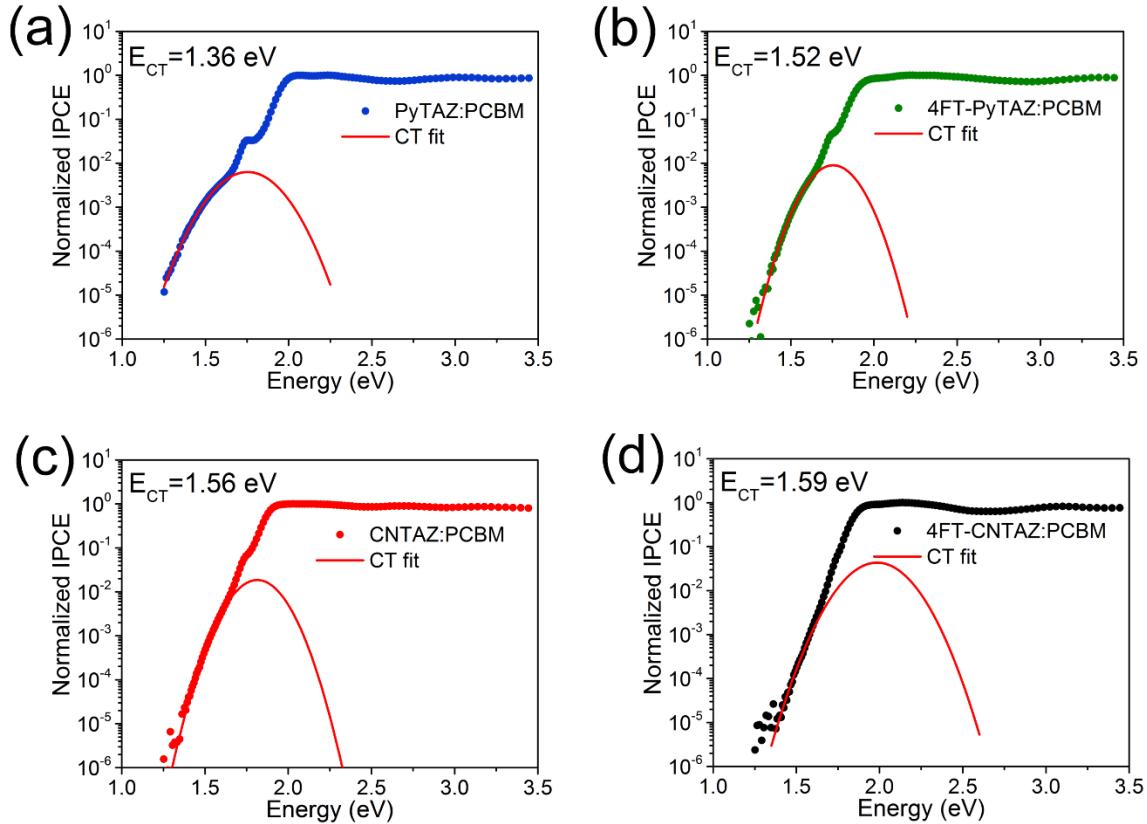
Figure 6.8 – CT state fit of polymer:PCBM blend based on high sensitivity EQE. (a) PyTAZ:PCBM, (b) 4FT-PyTAZ:PCBM, (c) CNTAZ:PCBM, and (d) 4FT-CNTAZ:PCBM

Once the CT state is known, the mechanism for the V_{OC} can also be narrowed down.

For example, the loss from nongeminate recombination can be found by finding the

difference between the CT state energy and the V_{OC} (i.e., $E_{CT} - eV_{OC}$).[291] Furthermore,

another significant loss mechanism comes from the exciton splitting energy (also referred to

as the charge separation energy), which is described as the difference between the optical

183

band gap (PCBM in this case) and the charge transfer state ($E_{opt} - E_{CT}$).[291] **Table 6.4** highlights these calculations detailing each of these loss mechanisms.

Similar to the claims made previously with regards to the HOMO energy levels, the cyano groups have a stronger electron withdrawing strength and therefore lowers the HOMO energy of the resulting polymer. The lower HOMO energy level results in a CT state higher than the PyTAZ-based polymers. The addition of the fluorine to the thiophene linker also raises the CT state energy; however, the impact on the PyTAZ polymer backbone is much larger than CNTAZ (0.16 eV vs 0.03 eV), which again shows the diminishing returns on further functionalizing the CNTAZ polymer backbone.

Typical organic solar cells have similar nongeminate recombination values with loss values in the 0.5–0.7 eV range, which also holds true for the four polymers reported here. Furthermore, all of the blends have a V_{OC} loss to nongeminate recombination ($E_{CT} - eV_{OC}$) of ~ 0.65 eV except for PyTAZ:PCBM which is 0.1 eV lower. On the other hand, the required energy to split the exciton was estimated using ($E_{opt} - E_{CT}$). The cyano and fluorine substituents of 4FT-CNTAZ resulted in a polymer with a very low driving force for exciton splitting. While there have been recent reports with polymer blends that have both low exciton splitting energy and high exciton splitting efficiency, the lower driving force can result in increased geminate recombination and cause the decrease in J_{SC}.[142,292] This is likely the case for the J_{SC} loss in 4FT-CNTAZ, which is also consistent with the trends seen in CNTAZ vs diCNTAZ.

Table 6.4 – CT state energy and the V_{oc} loss the devices

Polymer	V_{OC} (V)	E_{opt} [a] (eV)	E_{CT} (eV)	$E_{CT} - eV_{OC}$ (eV)	$E_{opt} - E_{CT}$ (eV)	Total Loss (eV)
PyTAZ	0.81	1.66	1.36	0.55	0.30	0.85
4FT-PyTAZ	0.87	1.66	1.52	0.65	0.14	0.79
CNTAZ	0.93	1.66	1.56	0.63	0.10	0.73
4FT-CNTAZ	0.96	1.66	1.59	0.63	0.07	0.70

[a]smaller optical band gap (E_{opt}) of the two components, which is PCBM, is used.

6.2.6 Charge Recombination Dynamics

Finally, the mechanism for charge recombination was investigated through measuring *J-V* characteristics as a function of incident light intensity. It has been previously found that the slope of the log-log plot of J_{SC} vs light intensity can indicate the strength of bimolecular recombination under short-circuit conditions because of the power law dependence of J_{SC} on light intensity.[185,186,188] As shown in **Figure 6.9a**, the slopes (α) for all four polymer blends are similar and close to one. While the J_{SC} dependence doesn't yield any differences, the polymers blends have a very different response from the V_{OC} dependence.
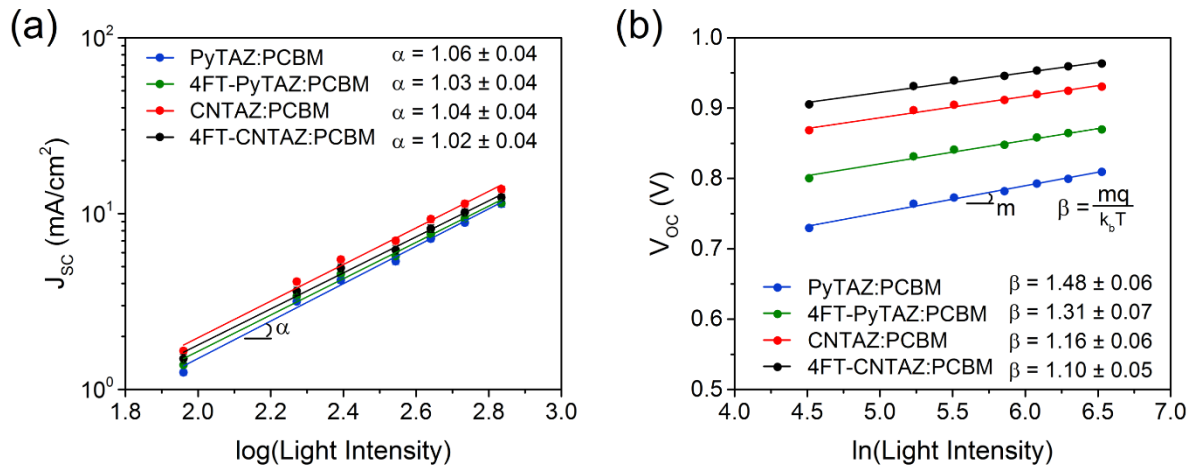
Figure 6.9 – Light intensity measurements for (a) log-log fitting of J_{SC} vs light intensity and (b) semi-log fitting of V_{OC} vs light intensity.

In a semi-log plot of V_{OC} vs light intensity (**Figure 6.9b**), the value of the slope (factored into β with k_bT/q) can provide what type of recombination is the major loss mechanism under open-circuit conditions. A β=2 indicates that trap-assisted recombination is the dominant recombination mechanism, while β<1 signify that surface recombination is prevalent.[132,189] PyTAZ:PCBM has the largest value (β=1.48) which indicates an increase of trap-assisted recombination. This is consistent with the morphological data which showed the PyTAZ:PCBM blends have the large and excessively pure domains, which can lead to isolated traps.[318] The addition of the fluorinated thiophene linker can help reduce the amount of trap-assisted recombination through a combination of higher mobility, smaller domain size, and more appropriate domain purity. On the other hand, with β values close to 1, the cyano-functionalized polymers of CNTAZ and 4FT-CNTAZ do not appear to suffer from trap-assisted recombination, which results in the higher PCE.

6.3. Conclusion

In this study, we systematically explored various functionalization approaches on TAZ-based conjugated polymers that are used for organic solar cells. These approaches included the addition of nitrogen heteroatoms, fluorine substituents, and cyano groups along the polymer backbone. The PyTAZ:PCBM blend had the worst performance of the four blends presented here. The weaker electronic effects of the nitrogen heteroatom limited the V_{OC}, and trap-assisted recombination led to the lower J_{SC}. The cause for the trap-assisted recombination originated from a lower hole mobility and a morphology of large and excessively pure domains. Including a fluorine substituent on the thiophene linkers of PyTAZ was able to mitigate some of these issues and increase the solar cell efficiency. More specifically, the electron withdrawing nature of the fluorine atom can tune the energy levels

and result in a higher V_{OC}; furthermore, with a more planer backbone, 4FT-PyTAZ has a red shift in absorption and higher mobility which can boost the J_{SC}.

As an alternative approach to incorporate nitrogen into the TAZ-based polymers, a cyano substituent can also be utilized. CNTAZ had the highest performance driven by the impact of the strong cyano electron withdrawing group. In a hope to further improve the efficiency of the cyano-based polymers, the same fluorine approach was also explored to make 4FT-CNTAZ. While the V_{OC} showed improvements, our data show that the combination of two fluorines and one cyano per polymer repeat unit results in over-functionalization of the polymer. Specifically, the 4FT-CNTAZ polymer has the lowest driving force for exciton splitting which can result in geminate recombination; furthermore, the 4FT-CNTAZ:PCBM blends have impure domains which result in FF loss. It is likely that one CN substituent is close to the optimal functionalization for TAZ based polymers, since adding one additional CN was also detrimental to the device performance as previously reported by us with the diCNTAZ polymer. However, the field of cyano-based conjugated polymers is its infancy compared to other functional groups like fluorine. Furthermore, there are even fewer reports which explore cyano-functionalized polymers with non-fullerene acceptors, and as non-fullerene acceptors have recently demonstrated remarkable efficiencies, a natural transition towards future improvement of these polymers involves pairing with appropriate non-fullerene acceptors. We anticipate that cyano substituted polymers might offer excellent efficiencies when paired with non-fullerene acceptors and continue to push polymer solar cells towards commercialization.

Overall, this work contributes to the larger understanding of the structure-properties relationships on TAZ-based polymers and also demonstrates the thresholds for

functionalization. While using electron withdrawing groups can offer great improvements in the solar cell efficiency, thresholds exist which can result in over-functionalization and degradation in performance. Finally, non-fullerene acceptor blends which include cyano-functionalized polymers may offer a promising future direction of exploration of new high efficiency organic solar cells.

6.4 Experimental Details

6.4.1 Synthesis of Various TAZ-polymers

All chemicals were purchased from commercial source (Sigma-Aldrich, Fisher, Acros, etc.) and were used as received except when specified. Anhydrous THF was prepared via distillation over sodium and benzophenone before use. For reactions under argon, the reaction flask was evacuated and refilled with argon for three times.
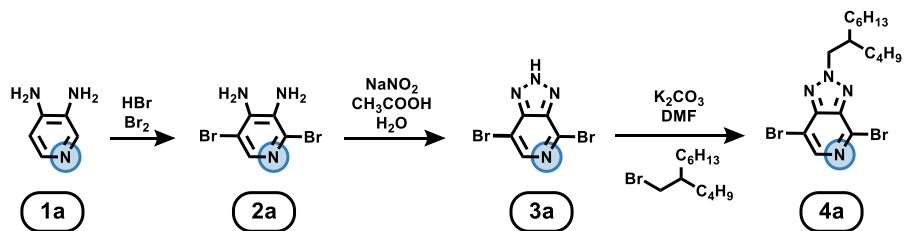
Scheme 6.2 – Synthesis of PyTAZ core

3,4-diaminopyridine (**1a**) was purchased from Matrix Scientific (No 011183, 98%) and used without further purification.

2,5-dibromopyridine-3,4-diamine (**2a**) was synthesized as follows: In a 250 mL round bottom flask, **1a** (10.9 g, 1 eq, 100 mmol) was dispersed in 48% hydrobromic acid (HBr, 100 mL). The reaction flask was cooled to 0 ˚C with an ice/water bath. Liquid bromine (Br$_2$, 43.0 g, 13.8 mL, 2.7 eq, 270 mmol) was slowly added dropwise. The solution was heated to 110 ˚C and refluxed for five hours. The reaction flask was then cooled to 0 ˚C with an ice/water bath. The solid was collected via vacuum filtration and slowly washed with saturated

bicarbonate solution (NaHCO$_3$, 500 mL) – warning, there is a large amount of acid which needs to be neutralized and caution should be taken. The remaining solid is dissolved in ethyl acetate (EtOAc, 500 mL) and washed with brine (saturated NaCl solution) twice. The organic phase was dried with magnesium sulfate (MgSO$_4$), filtered, and concentrated via rotary evaporation. Yield: Light brown solid, 10.68 g, 40%. ^{1}H NMR (400 MHz, d6-DMSO) δ 7.53 (s, 1H), 5.99 (s, 2H), 5.05 (s, 2H).

4,7-dibromo-2H-[1,2,3]triazolo[4,5-c]pyridine (**3a**) was synthesized as follows: In a 250 mL round bottom flask, **2a** (4.9 g, 1 eq, 18.4 mmol) was mixed with glacial acetic acid (CH$_3$COOH, 50 mL). In a separate scintillation vial, sodium nitrite (NaNO$_2$, 1.33 g, 1.05 eq, 19.3 mmol) was dissolved in water (H$_2$O, 20 mL). The sodium nitrite solution is added dropwise to the first mixture, and the reaction mixture is allowed to stir (open air) for four hours. The reaction flask was then cooled to 0 ˚C with an ice/water bath. The solid was collected via vacuum filtration and dried in the oven overnight. By NMR, there was a small amount (2.6%) of acetic acid still stuck in the crystal. Yield: yellow-brown solid, 4.42 g, 86%. ^{1}H NMR (400 MHz, d6-DMSO) δ 8.50 (s, 1H).

4,7-dibromo-2-(2-butyloctyl)-2H-[1,2,3]triazolo[4,5-c]pyridine (**4a**) was synthesized as follows: In a dry, 2 neck, 100 mL round bottom flask with an attached condensing column, **3a** (4.22 g, 1 eq, 15.2 mmol) and potassium carbonate (K$_2$CO$_3$, 4.19 g, 2.0 eq, 30.4 mmol) were added. The reaction flask was seal, evacuated and refilled with argon three times. Anhydrous dimethylformamide (DMF, 60 mL) was added and the reaction mixture was heated to 70 ˚C. After 30 minutes, 5-(bromomethyl)undecane (4.16 g, 1.1 eq, 16.7 mmol) was added and the reaction continued to stir at 70 ˚C overnight. The reaction mixture was quenched with saturated ammonium chloride (NH$_4$Cl, 100 mL); the product was extracted

with dichloromethane (DCM) and washed with H_2O three times. After drying the organic

phase with $MgSO_4$ and filtering the mixture, the mixture was concentrated via rotary

evaporation. The product was purified through silica gel column chromatography – first, a

byproduct was removed with a 10:1 hexanes:DCM solvent system. Afterwards, the solvent

system was gradually changed to a 2:1 hexanes:DCM mixture which was used to collect the

product. Yield: pale yellow oil, 2.81 g, 42%. ^{1}H NMR (400 MHz, CDCl$_3$) δ 8.36 (s, 1H),

4.71 (d, J = 7.1 Hz, 2H), 2.34 (m, 1H), 1.39 – 1.19 (m, 16H), 0.87 (m, 6H).
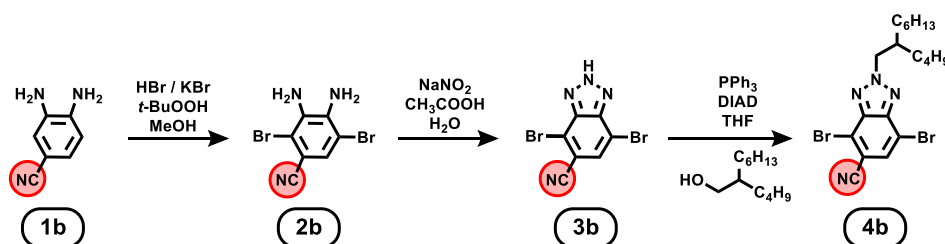
Scheme 6.3 – Synthesis of CNTAZ core

3,4-diaminobenzonitrile (**1b**) was purchased from Alfa Aesar (No H6695414, 97%)

and used without further purification.

3,4-diamino-2,5-dibromobenzonitrile (**2b**) was synthesized as follows: A solution of

1b (2.66 g, 1 eq, 20.0 mmol) and potassium bromide (KBr, 31.65 g, 13.3 eq, 266 mmol) in

300 mL methanol was purged with argon for 20 min. To that solution, 62% hydrogen

bromide solution (3.54 mL) was added at 0 °C slowly. 70% tert-butylhydroperoxide solution

(*t*-BuOOH, 1.74 mL) was added and stirred at room temperature for 6 hr. Then a second

portion of 70% tert-butylhydroperoxide solution (1.74 mL) was added and stirred for 6 hours

before the third portion of 70% tert-butylhydroperoxide solution (1.74 mL) was added and

stirred overnight. The reaction mixture poured into water and filtered. The product was

washed with water and dried over phosphorus pentoxide under low pressure. Yield: red solid,

3.31 g, 57%. ^{1}H NMR (600 MHz, MeOD) δ 7.22 (s, 1H).

4,7-dibromo-2H-benzo[d][1,2,3]triazole-5-carbonitrile (**3b**) was synthesized as follows: To the solution of **2b** (2.33 g, 1 eq, 8.0 mmol) in 18 mL acetic acid, sodium nitrite (0.91 g, 1.6 eq, 13.2 mmol) in 14 mL water was added at 0 °C. The reaction was stirred at room temperature for 90 minutes before being poured into water. The product was extracted with ethyl acetate and washed with water for two times and brine once. The organic solution was then dried over magnesium sulfate, filtered, and the solvent was removed with rotary evaporation. Yield: dark red solid, 2.1 g, 87%. ^{1}H NMR (600 MHz, MeOD) δ 7.98 (s, 1H).

4,7-dibromo-2-(2-butyloctyl)-2H-benzo[d][1,2,3]triazole-5-carbonitrile (**4b**) was synthesized as follows: **3b** (2.1 g, 1 eq, 7.0 mmol) and triphenylphosphine (2.73 g, 1.5 eq, 10.5 mmol) where added to a 250 mL round bottom flask which was then evacuated and refilled with argon three times. Anhydrous THF (125 mL) was added to make a solution of the starting materials. 2-butyl-1-octanol (1.94 g, 1.5 eq, 10.5 mmol) was added at 0 °C, and then di*iso*propyl azodicarboxylate (DIAD) (2.67 g, 1.9 eq, 13.2 mmol) was added at 0 °C. The reaction was slowly warmed to room temperature and stirred overnight. Then the reaction mixture was poured into water, and the product was extracted with ethyl acetate. The organic solution was washed with water for two times and brine for one time. The organic solution was dried over magnesium sulfate and filtered. The solvent was removed with rotary evaporation, and the crude product was purified through silica gel column chromatography with hexanes:ethyl acetate = 15:1 as eluent. Yield: colorless oil, 1.11 g, 34%. ^{1}H NMR (600 MHz, CDCl$_3$) δ 7.72 (s, 1H), 4.72 (d, J = 7.1 Hz, 2H), 2.33 (m, 1H), 1.40 – 1.15 (m, 16H), 0.87 (m, 6H).
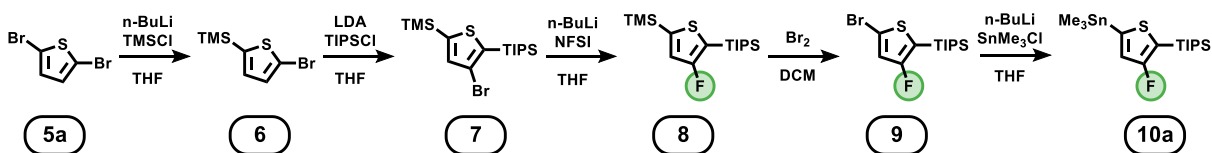
Scheme 6.4 – Synthesis of 4FT linker

2,5-dibromothiophene **(5a)** was purchased from Acros Organics (No 148681000, 95%) and used without further purification.

(5-bromothiophen-2-yl)trimethylsilane **(6)** was synthesized as follows: **5a** (24.2 g, 1 eq, 100 mmol) was added to a 500 mL multineck round bottom flask which was subsequently evacuated and refilled three times with argon. Anhydrous tetrahydrofuran (THF, 200 mL) was added and the reaction flask was cooled to -78 ˚C with a dry ice/acetone bath. *n*-butyl lithium (*n*-BuLi, 2.5 M, 20 mL, 0.5 eq, 50 mmol) was added slowly and the reaction remained stirring in the dry ice/acetone bath. 30 minutes later, chlorotrimethylsilane (TMSCl, 6.3 mL, 0.5 eq, 50 mmol) was added. The reaction continued to stir at -78 ˚C for an additional 90 minutes. An additional amount of *n*-BuLi (22 mL, 0.55 eq, 55 mmol) was added. After an hour, a final amount of TMSCl (7.6 mL, 0.6 eq, 60 mmol) was added. The reaction was allowed to slowly warm to room temperature overnight. Afterwards, the reaction was quenched with 20 mL of H_2O and poured into 200 mL of saturated NH_4Cl. The product was extracted with DCM and washed with water three times. The organic phase was dried over magnesium sulfate and filtered. The solvent was removed with rotary evaporation. The crude product was purified through silica gel column chromatography with hexanes as eluent. Note, there is an impurity (yellow band) which can make this column trickier. Yield: 21.05 g, 90%. ^{1}H NMR (400 MHz, CDCl$_3$) δ 7.08 (d, *J* = 3.45 Hz, 1H), 6.98 (d, *J* = 3.45 Hz, 1H), 0.31 (s, 9H)

(4-bromo-5-(triisopropylsilyl)thiophen-2-yl)trimethylsilane (**7**) was synthesized as follows: **6** (20.72 g, 1 eq, 88 mmol) was added to a 500mL multineck round bottom flask which was subsequently evacuated and refilled three times with argon. Anhydrous tetrahydrofuran (THF, 300 mL) was added and the reaction flask was cooled to -78 ˚C with a dry ice/acetone bath. Lithium diisopropylamine (LDA, 2M in THF/heptanesethylbenzene, 52.9 mL, 1.2 eq, 106 mmol) was added dropwise slowly in four portions over the course of one hour. After the final portion of LDA was added, the reaction mixture was stirred at -78 ˚C for 30 minutes. Chlorotriisopropylsilane (TIPSCl, 22.08 g, 24.5 mL, 1.3 eq, 114.5 mmol) was added in one portion and the reaction was allowed to stir for 30 minutes. The reaction was warmed to room temperature and then poured into H_2O (200 mL, 30 minutes after removal from bath). The product was extracted with hexanes and washed with water three times. The organic layer was dried with magnesium sulfate, filtered, and concentrated via rotary evaporation. Yield: 33.03 g, 96%. ^{1}H NMR (400 MHz, CDCl$_3$) δ 7.19 (s, 1H), 1.59 (hept, *J* = 7.42 Hz, 3H), 1.13 (d, *J* = 7.49 Hz, 18H), 0.31 (s, 9H).

(4-fluoro-5-(triisopropylsilyl)thiophen-2-yl)trimethylsilane (**8**) was synthesized as follows: First, **7** (32.42 g, 1 eq, 83 mmol) and N-fluorobenzenesulfonimide (NFSI, 31.33 g, 1.2 eq, 99.3 mmol) were added to a multineck round bottom flask which was evacuated and refilled with argon three times. The starting material and NFSI where then dissolved in dry tetrahydrofuran (from still) and cooled to -78 °C in a dry ice/acetone bath. Then *n*-BuLi (2.5 M in hexane) and NFSI were added at -78 °C in the following portions:

i) n-BuLi (16.56 mL, 0.5 eq, 41.4 mmol), stir for 1 h,
ii) n-BuLi (16.56 mL, 0.5 eq, 41.4 mmol), stir for 1 h,
iii) n-BuLi (16.56 mL, 0.5 eq, 41.4 mmol), stir for 1 h,
iv) NFSI (20.88 g, 0.8 eq, 66.2 mmol) dissolved in dry THF, stir for 30 min,
v) n-BuLi (26.5 mL, 0.8 eq, 66.2 mmol), stir for 1 h,

The dry ice/acetone bath was then removed and the mixture was stirred at room temperature overnight. The mixture was quenched with water, and the workup began with extracting the organic layer with ethyl acetate. After being washed with brine (x2) and water (x2), and dried over magnesium sulfate, the organic phase was filtered and the resulting solution was concentrated under reduced pressure and run through a silica gel plug using hexane as eluent. After removing the hexane via rotary evaporation, vacuum distillation yielded the product. Yield: 11.14 g, 41%. ^{1}H NMR (400 MHz, CDCl$_3$) δ 6.97 (d, J = 1.8 Hz, 1H), 1.38 (hept, J = 7.45 Hz, 3H), 1.10 (d, J = 7.52 Hz, 18H), 0.30 (s, 9H).

(5-bromo-3-fluorothiophen-2-yl)triisopropylsilane (**9**) was synthesized as follows: A mixture of **8** (10.86 g, 32.8 mmol, 1 eq.) and liquid bromine (Br$_2$, 5.75 g, 36.1 mmol, 1.1 eq.) in dichloromethane was stirred at 80 °C for two hours. The reaction mixture was wrapped in aluminum foil to minimize light exposure, and the reaction proceeded under a normal air atmosphere. After naturally cooling to room temperature, the reaction mixture was quenched with saturated sodium sulfite (Na$_2$SO$_3$, 100 mL). The product was extracted with dichloromethane. The resulting organic layer was washed with water twice, then dried with magnesium sulfate. After filtration, the filtrate was concentrated via rotary evaporation. The resulting residue was purified through silica gel column (hexanes eluent), to yield the product. Yield: 9.87 g, 89%. ^{1}H NMR (400 MHz, CDCl$_3$) δ 6.89 (d, J = 1.7 Hz, 1H), 1.34 (m, 3H), 1.09 (d, J = 7.52 Hz, 18H).

(3-fluoro-5-(trimethylstannyl)thiophen-2-yl)triisopropylsilane (**10a**) was synthesized as follows: **9** (9.02 g, 26.7 mmol, 1 eq.) was added to a flask which was then evacuated and refilled with argon three times. The oil was solubilized in dry THF (30 mL) from the still, and the mixture was cooled with a dry ice/acetone bath. Next, 2.5 M *n*-BuLi in hexanes (11.2

mL, 28.1 mmol, 1.05 eq.) was added to the flask, still at -78 °C and under argon. The mixture was stirred at -78 °C for 30 minutes. A 1 M solution of trimeythltin chloride (Me$_3$SnCl in hexanes, 29.4 mL, 29.4 mmol, 1.1 eq.) was added dropwise, and the resulting solution was stirred at -78 °C for 1 hour. The reaction mixture was allowed to warm to room temperature for 45 minutes and was then quenched with water. After extraction with hexanes, the organic layer was washed with brine (x3), dried with magnesium sulfate, filtered, and concentrated under reduced pressure/rotovap to give the product as a faint yellow oil. Yield: 9.64 g, 86%. ^{1}H NMR (400 MHz, CDCl$_3$) δ 6.85 (d, J = 1.8 Hz, 1H), 1.44 (m, 3H), 0.98 (d, J = 7.5 Hz, 18H), 0.27 (s, 9H).
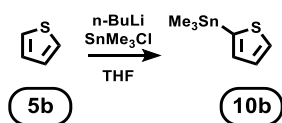
Scheme 6.5 – Synthesis of thiophene linker

Thiophene (**5b**) was purchased from TCI America (No T0223500ML, 98%) and used without further purification.

Trimethyl(thiophen-2-yl)stannane (**10b**) was synthesized as follows: To a dry 250 mL multineck flask which was evacuated and refilled with argon three times, anhydrous THF (100 mL) and 5b (4.21 g, 1 eq, 50 mmol) where added. The reaction flask was cooled to -78 °C in a dry ice/acetone bath. *n*-BuLi (2.5 M, 21 mL, 1.05 eq, 52.5 mmol) was added dropwise and the reaction stirred in the dry ice/acetone bath for 1 hour. Afterwards, trimethyltin chloride (SnMe3Cl, 1M, 55 mL, 1.1 eq, 55 mmol) was added dropwise. The reaction was allowed to slowly warm to room temperature and stir overnight. The reaction mixture was quenched with 20 mL saturated NH$_4$Cl. The organic phase was extracted with ether and washed with brine twice. After drying with magnesium sulfate and filtering, the organic phase was concentrated with rotary evaporation. The product was vacuum distilled to

purify. Yield: colorless oil, 11.24 g, 91%. ^{1}H NMR (400 MHz, CDCl$_3$) δ 7.58 (d, 1H), 7.20 (d, 1H), 7.16 (t, 1H), 0.36 (s, 9H).
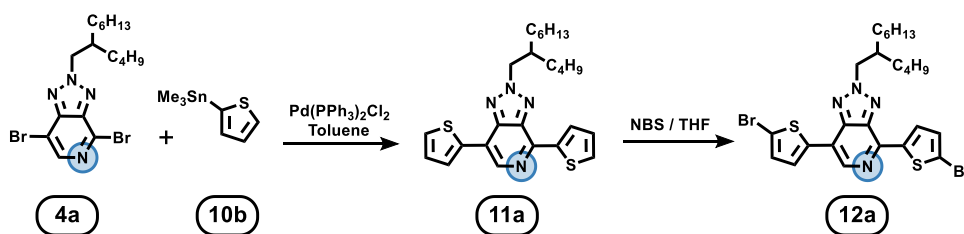
Scheme 6.6 – Synthesis of PyTAZ monomer

2-(2-butyloctyl)-4,7-di(thiophen-2-yl)-2H-[1,2,3]triazolo[4,5-c]pyridine **(11a)** was synthesized as follows: Both **4a** (1.26 g, 1 eq, 2.82 mmol) and **10b** (1.74 g, 2.5 eq, 7.06 mmol) where added to a multineck round bottom flask with condensing column, which was subsequently evacuated and refilled with argon three times. A solution was made by dissolving the starting materials in anhydrous toluene. Afterwards, Pd(PPh$_3$)$_2$Cl$_2$ (59 mg, 0.03 eq, 0.0846 mmol) was added under argon stream, and the solution was purged with argon for 20 min. The reaction was heated to reflux for 48 hours. After cooling, the solvent was removed via rotary evaporation. And the product was purified via silica column chromatography with hexanes:dichloromethane at 9:1 as the eluent. By NMR, a few minor impurities remain, a gradient column might remove these. Yield: yellow oil, 0.98 g, 77%.

4,7-bis(5-bromothiophen-2-yl)-2-(2-butyloctyl)-2H-[1,2,3]triazolo[4,5-c]pyridine **(12a)** was synthesized as follows: In a dry round bottom flask, **11a** (1.36 g, 1 eq, 3 mmol) and N-Bromosuccinimide (NBS, 1.11 g, 2.1 eq, 6.2 mmol) was dissolved in anhydrous THF (35 mL). The flask was wrapped in aluminum foil and stirred in darkness overnight. The reaction mixture was poured into saturated bicarbonate solution (100 mL) and the product was extracted with dicholomethane. The organic phase was washed with a saturated bicarbonate solution twice. Afterwards, the organic phase was dried with magnesium sulfate,

196

filtered, and concentrated via rotary evaporation. The product was purified through silica gel

column chromatography with a 9:1 mixture of hexanes:dichloromethane as the eluent.

Afterwards, the monomer was recrystallized from isopropyl alcohol twice. Yield: yellow

solid, 1.65 g, 82%. ^{1}H NMR (400 MHz, CDCl$_3$) δ 8.54 (s, 1H), 8.20 (d, J = 4.0 Hz, 1H), 7.76

(d, J = 3.9 Hz, 1H), 7.18 (d, J = 3.9 Hz, 1H), 7.14 (d, J = 3.9 Hz, 1H), 4.77 (d, J = 6.7 Hz,

2H), 2.31 (hept, J = 6.5 Hz, 1H), 1.47 – 1.21 (m, 16H), 0.90 (t, J = 7.2 Hz, 3H), 0.86 (t, J =

7.0 Hz, 3H). Mass Spectroscopy: [M+H]$^+$ C$_{25}$H$_{31}$N$_4$S$_2$Br$_2$; m/z = 609.03529 ; mass error =

0.3 ppm

Figure 6.10 – ^{1}H NMR of PyTAZ monomer

Figure 6.11 – Mass Spectra of PyTAZ monomer
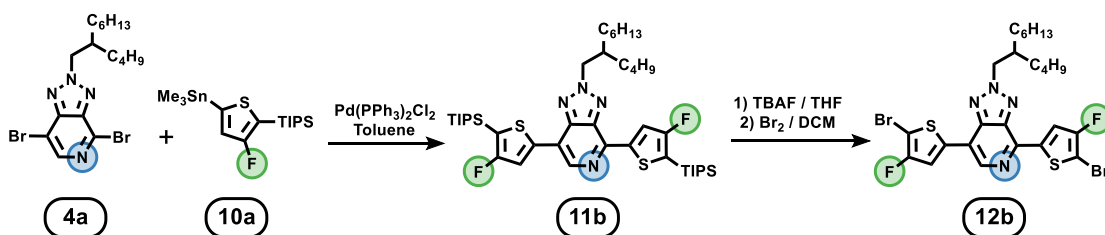
Scheme 6.7 – Synthesis of 4FT-PyTAZ monomer

2-(2-butyloctyl)-4,7-bis(4-fluoro-5-(triisopropylsilyl)thiophen-2-yl)-2H-

[1,2,3]triazolo[4,5-c]pyridine (**11b**) was synthesized as follows: Both **4a** (1.00 g, 1 eq, 2.24

mmol) and **10b** (2.36 g, 2.5 eq, 5.60 mmol) where added to a multineck round bottom flask

with condensing column, which was subsequently evacuated and refilled with argon three

times. A solution was made by dissolving the starting materials in anhydrous toluene.

Afterwards, Pd(PPh$_3$)$_2$Cl$_2$ (47 mg, 0.03 eq, 0.067 mmol) was added under argon stream, and

the solution was purged with argon for 20 min. The reaction was heated to reflux for 48

hours. After cooling, the solvent was removed via rotary evaporation. And the product was

purified via silica column chromatography with hexanes:dichloromethane at 12:1 as the

198

eluent. By NMR, a few minor impurities remain, a gradient column might remove these.

Yield: yellow oil, 0.78 g, 43%.

4,7-bis(5-bromo-4-fluorothiophen-2-yl)-2-(2-butyloctyl)-2H-[1,2,3]triazolo[4,5-c]pyridine (**12b**) was synthesized as follows: **11b** (0.5 g, 1 eq, 0.79 mmol) is added to a dry multineck round bottom flask which is subsequently evacuated and refilled three times with argon. Anhydrous THF (~100 mL) is added to the flask and the reaction stirred for ten minutes. Afterwards, tetrabutylammonium fluoride (TBAF, 1 M in THF, 2.4 mL, 3 eq, 2.4 mmol) was added via syringe and the reaction mixture stirred for six hours at room temperature. The reaction mixture was concentrated via rotary evaporation to produce a brown sludge. Ethanol (100 mL) was added and the solution was stirred. A yellow precipitate formed and was filtered and washed with ethanol. Further purifications are required to isolate the pure product, but we opted to proceed with the next reaction. In a round bottom flask, the yellow solid and NBS (0.35 g, 2.5 eq, 2.0 mmol) was dissolved in DCM (18 mL) and acetic acid (8 mL) mixture. The flask was wrapped in aluminum foil and stirred in darkness overnight. More acetic acid (3 mL) was added and the reaction was stirred in the darkness for another 36 hours. The reaction mixture was poured into saturated bicarbonate solution (50 mL) and the product was extracted with dicholomethane. The organic phase was washed with a saturated bicarbonate solution twice. Afterwards, the organic phase was dried with magnesium sulfate, filtered, and concentrated via rotary evaporation. The product was purified through silica gel column chromatography with a 6:1 mixture of hexanes:dichloromethane which was slowly increased to 4:1 as the eluent. Afterwards, the monomer was recrystallized from ethanol twice. Yield: yellow solid, 384 mg, 75%. ^{1}H NMR (400 MHz, CDCl$_3$) δ 8.52 (s, 1H), 8.11 (s, 1H), 7.70 (s, 1H), 4.78 (d, *J* = 6.7 Hz, 2H), 2.31

(hept, J = 6.4 Hz, 1H), 1.47 – 1.21 (m, 16H), 0.90 (t, J = 7.1 Hz, 3H), 0.86 (t, J = 6.7 Hz,

3H). Mass Spectroscopy: [M+H]$^+$ $C_{25}H_{29}N_4S_2Br_2F_2$; m/z = 645.01630 ; mass error = 0.1

ppm

Figure 6.12 – ^{1}H NMR of 4FT-PyTAZ monomer
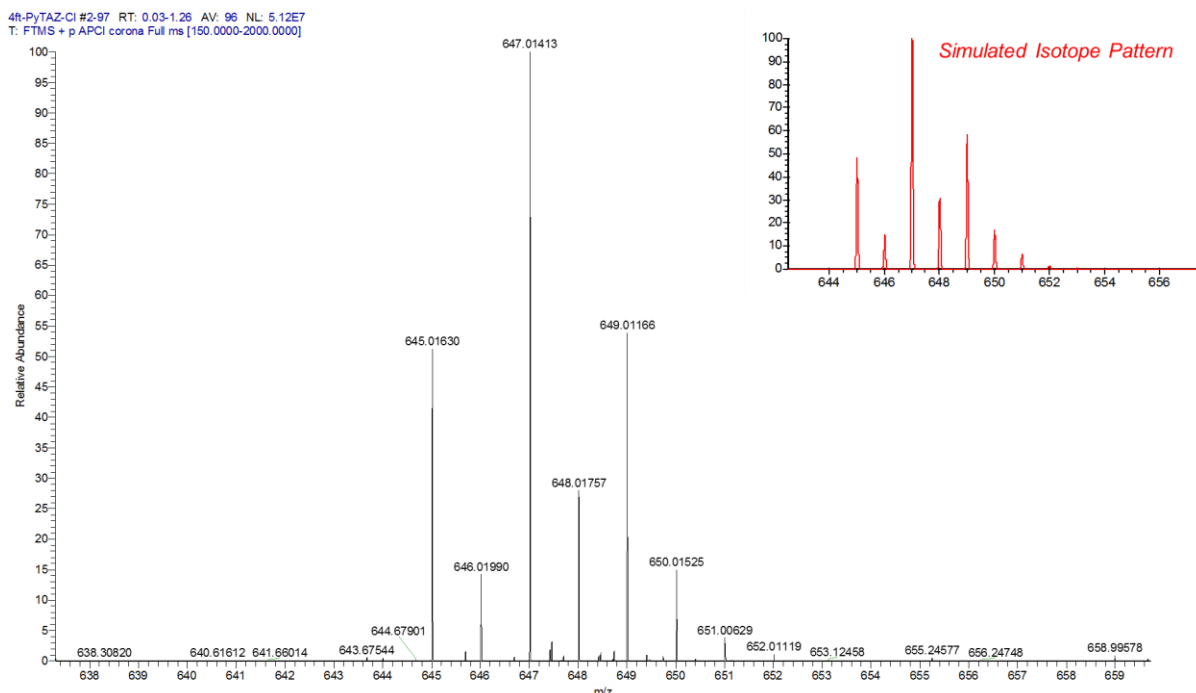
Figure 6.13 – Mass Spectra of 4FT-PyTAZ monomer
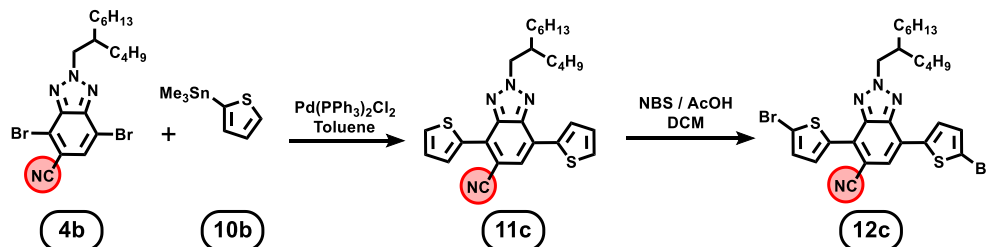
Scheme 6.8 – Synthesis of CNTAZ monomer

2-(2-butyloctyl)-4,7-di(thiophen-2-yl)-2H-benzo[d][1,2,3]triazole-5-carbonitrile

(11c) was synthesized as follows: Both **4b** (1.30 g, 1 eq, 2.76 mmol) and **10b** (1.70 g, 2.5 eq, 6.91 mmol) where added to a multineck round bottom flask with condensing column, which was subsequently evacuated and refilled with argon three times. A solution was made by dissolving the starting materials in anhydrous toluene. Afterwards, Pd(PPh$_3$)$_2$Cl$_2$ (58 mg, 0.03 eq, 0.083 mmol) was added under argon stream, and the solution was purged with argon for 20 min. The reaction was heated to reflux for 48 hours. After cooling, the solvent was removed via rotary evaporation. And the product was purified via silica column

201

chromatography with hexanes:dichloromethane at 9:1 as the eluent. By NMR, a few minor impurities remain, a gradient column might remove these. Yield: yellow oil, 0.93 g, 71%.

4,7-bis(5-bromothiophen-2-yl)-2-(2-butyloctyl)-2H-benzo[d][1,2,3]triazole-5-carbonitrile (**12c**) was synthesized as follows: **11c** (0.92 g, 1 eq, 1.93 mmol) was dissolved in 50 mL dichloromethane and 18 mL acetic acid in a multineck round bottom flask which was wrapped in aluminum foil. NBS (0.72 g, 2.1 eq, 4.05 mmol) was added in dark. The reaction was stirred in dark at room temperature for 40 hr. The second portion of NBS (0.12 g, 0.35 eq, 0.68 mmol) was added and stirred in dark at room temperature for 50 hr. The third portion of NBS (0.21 g, 0.60 eq, 1.16 mmol) was added and stirred overnight. Then the fourth portion of NBS (0.16 g, 0.40 eq, 0.79 mmol) was added and stirred overnight. The fifth portion of NBS (0.18 g, 0.52 eq, 1.0 mmol) was added and stirred overnight. The sixth portion of NBS (0.05 g, 0.15 eq, 0.28 mmol) was added and stirred overnight. The reaction was tracked with ^{1}H NMR until the dibromination was complete. The reaction was then poured into water, and the product was extracted with dichloromethane for three times. The combined organic solution was washed with water for two times and brine for one time. The organic solution was dried over magnesium sulfate and filtered. The solvent was removed via rotary evaporation. And the product was purified with silica column chromatography with hexanes:dichloromethane = 4:1 as eluent and was then recrystallized in ethanol. Yield: yellow-orange solid, 0.96 g, 78%. ^{1}H NMR (600 MHz, CDCl$_3$) δ 8.01 (d, J = 4.1 Hz, 1H), 7.79 (d, J = 4.0 Hz, 1H), 7.71 (s, 1H), 7.21 (d, J = 4.1 Hz, 1H), 7.16 (d, J = 4.0 Hz, 1H), 4.77 (d, J = 6.5 Hz, 2H), 2.28 (hept, J = 6.3 Hz, 1H), 1.47 – 1.21 (m, 16H), 0.89 (m, 6H). Mass Spectroscopy: [M+H]$^+$ C$_{27}$H$_{31}$N$_4$S$_2$Br$_2$; m/z = 633.03540 ; mass error = 0.4 ppm
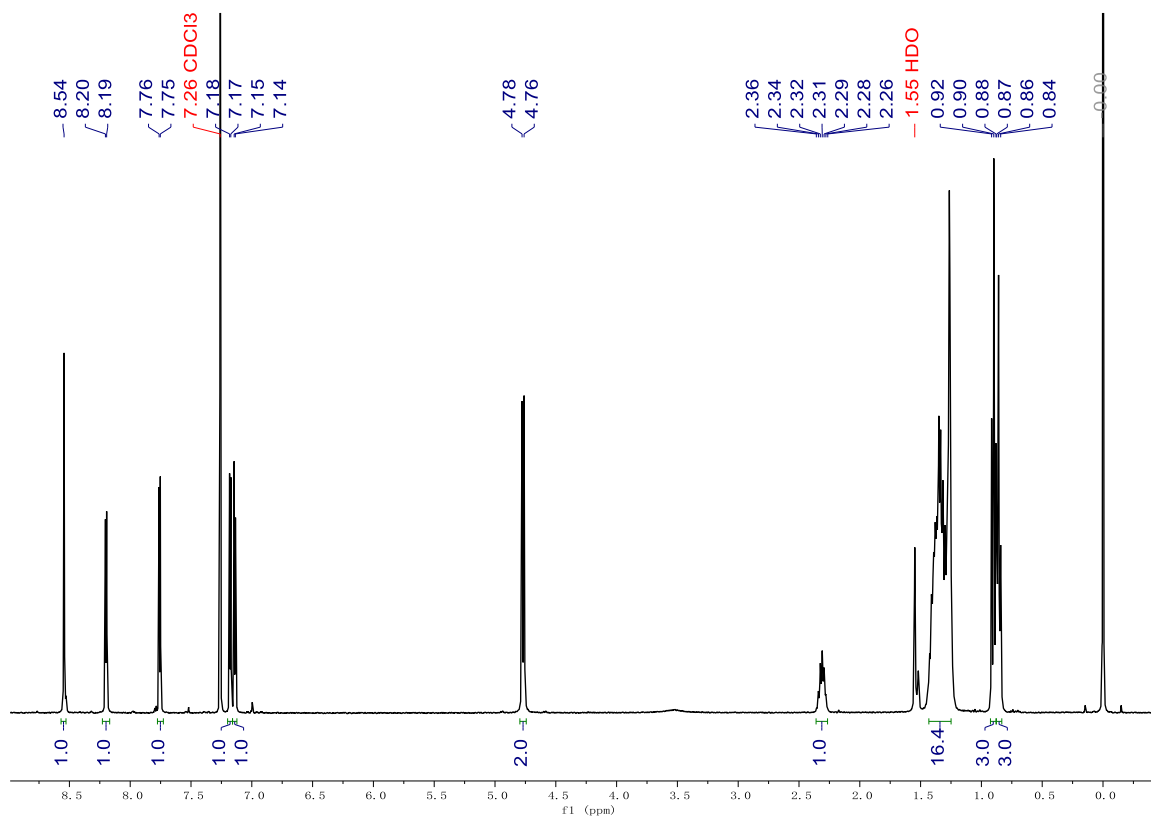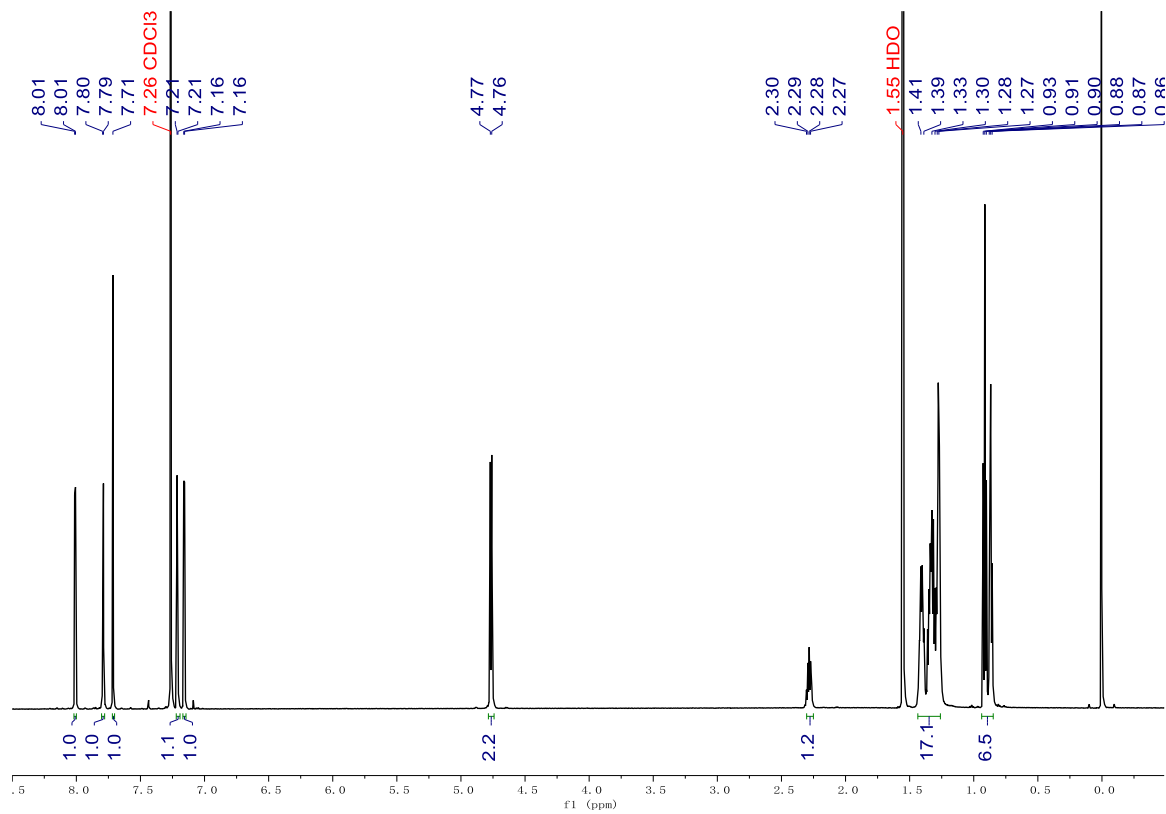
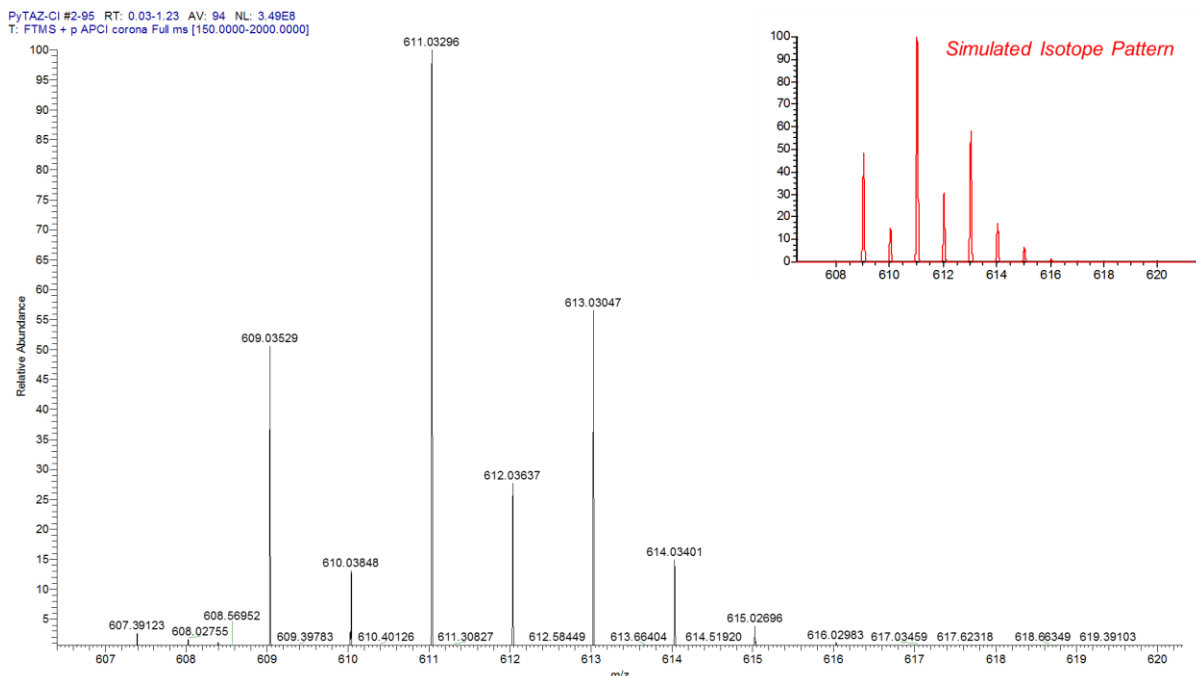**Figure 6.14** – ^{1}H NMR of CNTAZ monomer
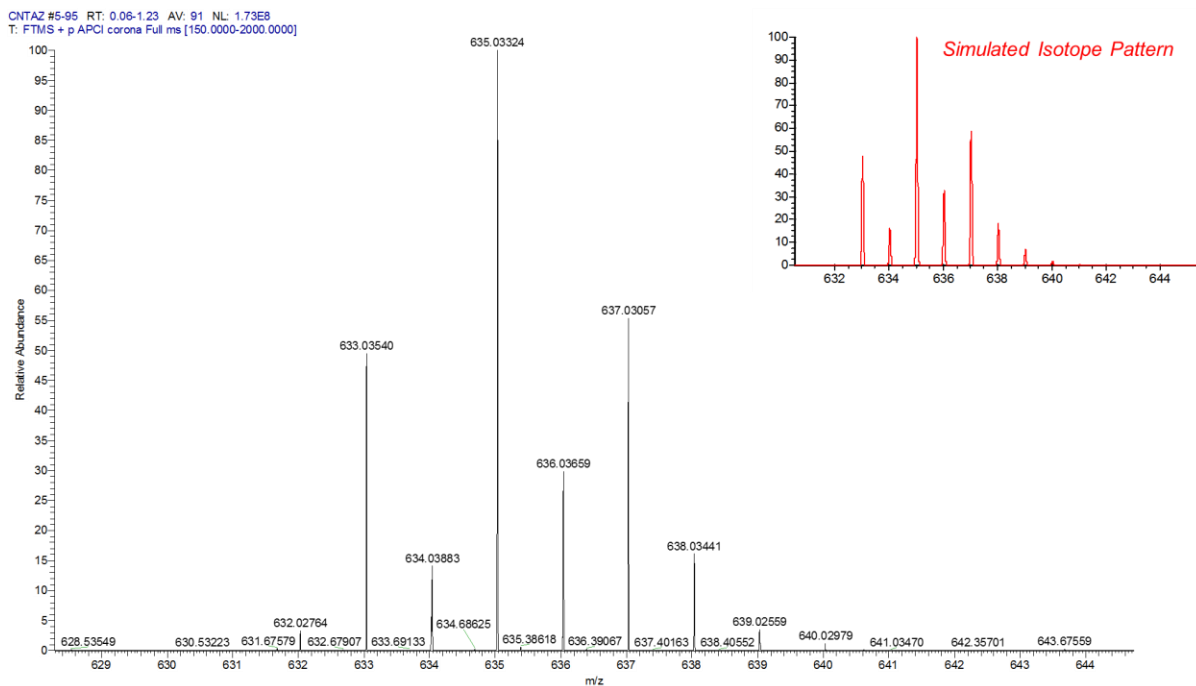
Figure 6.15 – Mass Spectra of CNTAZ monomer
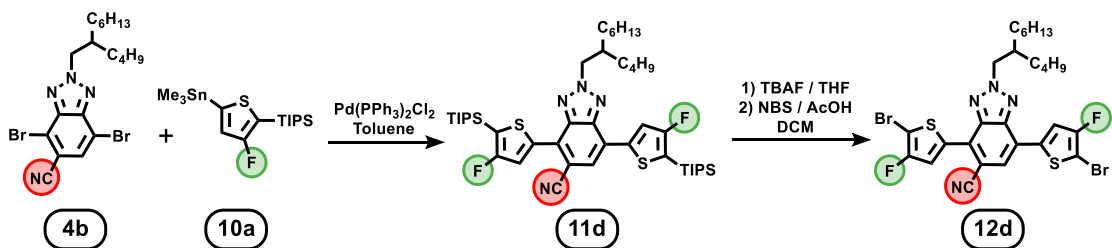
Scheme 6.9 – Synthesis of 4FT-CNTAZ monomer

2-(2-butyloctyl)-4,7-bis(4-fluoro-5-(triisopropylsilyl)thiophen-2-yl)-2H-benzo[d][1,2,3]triazole-5-carbonitrile (**11d**) was synthesized as follows: Both **4a** (0.96 g, 1 eq, 2.0 mmol) and **10b** (2.0 g, 2.5 eq, 5.0 mmol) where added to a multineck round bottom flask with condensing column, which was subsequently evacuated and refilled with argon three times. A solution was made by dissolving the starting materials in anhydrous toluene. Afterwards, Pd(PPh$_3$)$_2$Cl$_2$ (0.042 g, 0.03 eq, 0.06 mmol) was added under argon stream, and the solution was purged with argon for 20 min. The reaction was heated to reflux for 48 hours. After cooling, the solvent was removed via rotary evaporation. And the product was purified via silica column chromatography with hexanes:dichloromethane at 30:1 as the eluent. By NMR, a few minor impurities remain, a gradient column might remove these. Yield: yellow oil, 0.79 g, 50%.

4,7-bis(5-bromo-4-fluorothiophen-2-yl)-2-(2-butyloctyl)-2H-benzo[d][1,2,3]triazole-5-carbonitrile (**12d**) was synthesized as follows: **11d** (0.65 g, 1 eq, 0.79 mmol) is added to a dry multineck round bottom flask which is subsequently evacuated and refilled three times with argon. Anhydrous THF (~100 mL) is added to the flask and the reaction stirred for ten minutes. Afterwards, tetrabutylammonium fluoride (TBAF, 1 M in THF, 2.4 mL, 3 eq, 2.4 mmol) was added via syringe and the reaction mixture stirred for six hours at room temperature. The reaction mixture was concentrated via rotary evaporation to produce a brown sludge. Ethanol (100 mL) was added and the solution was stirred. A yellow-orange

precipitate formed and was filtered and washed with ethanol. Further purifications are required to isolate the pure product, but we opted to proceed with the next reaction. In a round bottom flask, the yellow-orange solid and NBS (0.27 g, 2.1 eq, 1.51 mmol) was dissolved in DCM (17 mL) and acetic acid (12 mL) mixture. Note, reaction was done in inert atmosphere. The flask was wrapped in aluminum foil and stirred in darkness for 48 hours. More acetic acid (3 mL) was added and the reaction was stirred in the darkness for another 48 hours. The reaction mixture was poured into saturated bicarbonate solution (50 mL) and the product was extracted with dicholomethane. The organic phase was washed with a saturated bicarbonate solution twice. Afterwards, the organic phase was dried with magnesium sulfate, filtered, and concentrated via rotary evaporation. The product was purified through silica gel column chromatography with a 8:1 mixture of hexanes:dichloromethane as the eluent. Afterwards, the monomer was recrystallized from ethanol twice. Yield: orange solid, 359 mg, 68%. ^{1}H NMR (400 MHz, CDCl$_3$) δ 7.98 (s, 1H), 7.75 (s, 1H), 7.69 (s, 1H), 4.78 (d, J = 6.5 Hz, 2H), 2.27 (hept, J = 6.3 Hz, 1H), 1.45 – 1.25 (m, 16H), 0.91 (t, J = 7.2 Hz, 3H), 0.86 (t, J = 6.7 Hz, 3H). Mass Spectroscopy: [M+H]$^+$ C$_{27}$H$_{29}$N$_4$S$_2$Br$_2$F$_2$; m/z = 669.01637 ; mass error = 0.1 ppm
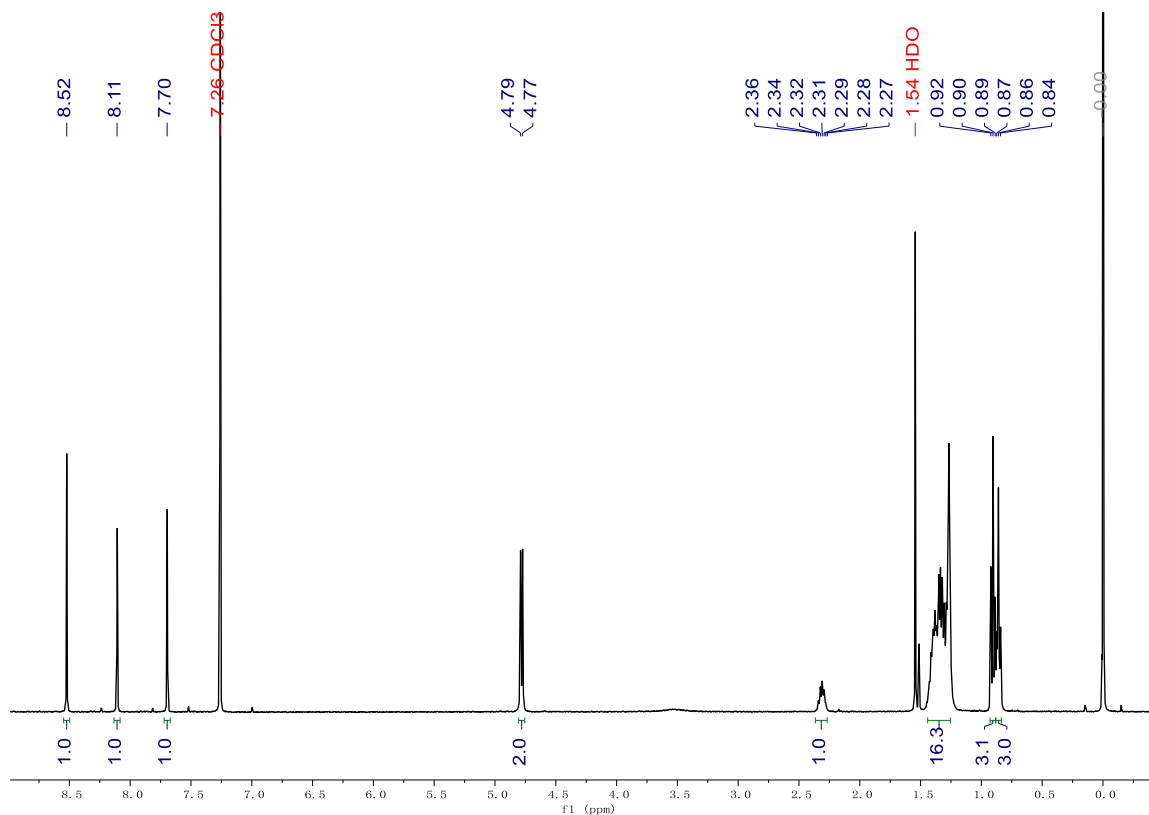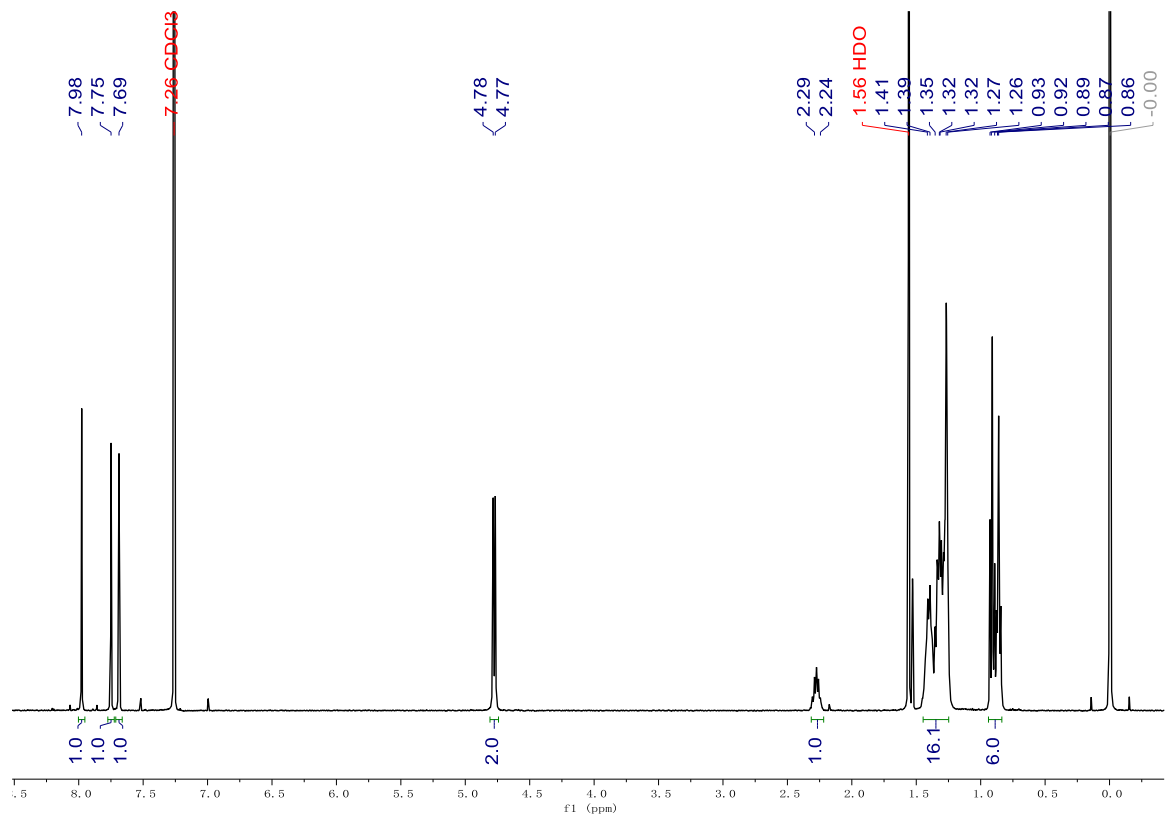
Figure 6.16 – ^{1}H NMR of 4FT-CNTAZ monomer
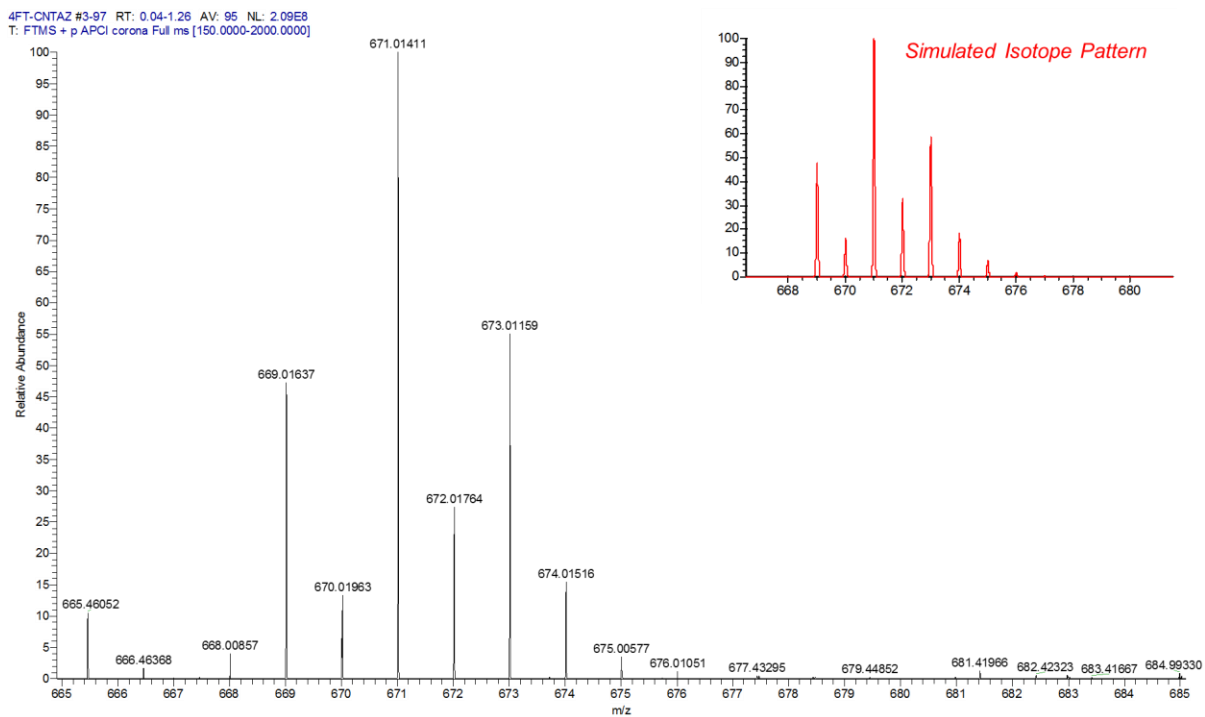
Figure 6.17 – Mass Spectra of 4FT-CNTAZ monomer
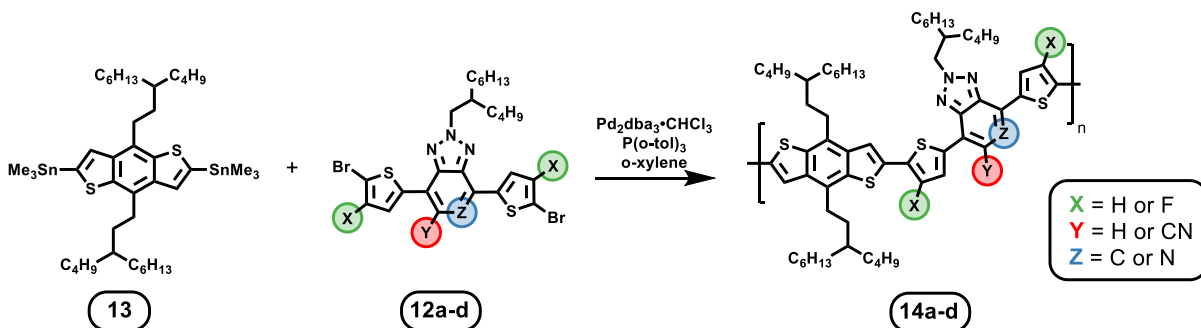
Scheme 6.10 – Polymerization Reaction for All Four Key Polymers

(4,8-bis(3-butylnonyl)benzo[1,2-b:4,5-b']dithiophene-2,6-diyl)bis(trimethylstannane) **(13)** was synthesized according to previous literature reports. (https://doi.org/10.1021/ja1112595)

Poly[7-(5-(4,8-bis(3-butylnonyl)benzo[1,2-b:4,5-b']dithiophen-2-yl)thiophen-2-yl)-2-(2-butyloctyl)-4-(thiophen-2-yl)-2H-[1,2,3]triazolo[4,5-c]pyridine] **(14a – PyTAZ)** was polymerized as follows: **13** (89.1 mg, 1.01 eq, 0.101 mmol), **12a** (61.1 mg, 1 eq, 0.100 mmol), (Pd₂(dba)₃·CHCl₃, 2.0 mg, 0.02 eq, 0.002 mmol), and (P(o-tol)₃, 5.0 mg, 0.16 eq, 0.016 mmol) were charged into a 10 mL vial designed for microwave reactor. The mixture was evacuated and refilled with argon for three cycles before addition of anhydrous o-xylene (0.7 mL) under argon stream. The reaction was heated up to 200 °C and held in a CEM microwave reactor for 10 min. After the polymerization, the crude polymer was dissolved in hot chlorobenzene (<10 mL) and precipitated into stirring methanol (200 mL). The collected polymer was extracted via a Soxhlet extractor with ethyl acetate, hexanes, and chloroform. The polymer solution in chloroform was concentrated and precipitated into methanol. The polymer was then collected via filtration and dried under vacuum. Yield: golden colored film, 102.4 mg, 100%.

Poly[7-(5-(4,8-bis(3-butylnonyl)benzo[1,2-b:4,5-b']dithiophen-2-yl)-4-fluorothiophen-2-yl)-2-(2-butyloctyl)-4-(4-fluorothiophen-2-yl)-2H-[1,2,3]triazolo[4,5-

c]pyridine] **(14b – 4FT-PyTAZ)** was polymerized as follows: **13** (89.0 mg, 1.01 eq, 0.101 mmol), **12b** (64.4 mg, 1 eq, 0.100 mmol), Pd$_2$(dba)$_3$·CHCl$_3$ (2.0 mg, 0.02 eq, 0.002 mmol), and P(o-tol)$_3$ (4.8 mg, 0.16 eq, 0.016 mmol) were charged into a 10 mL vial designed for microwave reactor. The mixture was evacuated and refilled with argon for three cycles before addition of anhydrous o-xylene (0.7 mL) under argon stream. The reaction was heated up to 200 °C and held in a CEM microwave reactor for 30 min. After the polymerization, the crude polymer was dissolved in hot chlorobenzene (<10 mL) and precipitated into stirring methanol (200 mL). The collected polymer was extracted via a Soxhlet extractor with ethyl acetate, hexanes, and chloroform. The polymer solution in chloroform was concentrated and precipitated into methanol. The polymer was then collected via filtration and dried under vacuum. Yield: golden colored film, 82.7 mg, 79%.

Poly[4-(5-(4,8-bis(3-butylnonyl)benzo[1,2-b:4,5-b']dithiophen-2-yl)thiophen-2-yl)-2-(2-butyloctyl)-7-(thiophen-2-yl)-2H-benzo[d][1,2,3]triazole-5-carbonitrile] **(14c - CNTAZ)** was polymerized as follows: **13** (89.0 mg, 1.01 eq, 0.101 mmol), **12c** (63.4 mg, 1 eq, 0.100 mmol), Pd$_2$(dba)$_3$·CHCl$_3$ (2.1 mg, 0.02 eq, 0.002 mmol), and P(o-tol)$_3$ (4.9 mg, 0.16 eq, 0.016 mmol) were charged into a 10 mL vial designed for microwave reactor. The mixture was evacuated and refilled with argon for three cycles before addition of anhydrous o-xylene (0.7 mL) under argon stream. The reaction was heated up to 200 °C and held in a CEM microwave reactor for 10 min. After the polymerization, the crude polymer was dissolved in hot chlorobenzene (<10 mL) and precipitated into stirring methanol (200 mL). The collected polymer was extracted via a Soxhlet extractor with ethyl acetate, hexanes, and chloroform. The polymer solution in chloroform was concentrated and precipitated into methanol. The

polymer was then collected via filtration and dried under vacuum. Yield: golden colored film, 94.8 mg, 91%.

Poly[4-(5-(4,8-bis(3-butylnonyl)benzo[1,2-b:4,5-b']dithiophen-2-yl)-4-fluorothiophen-2-yl)-2-(2-butyloctyl)-7-(4-fluorothiophen-2-yl)-2H-benzo[d][1,2,3]triazole-5-carbonitrile] **(14d – 4FT-CNTAZ)** was polymerized as follows: **13** (88.9 mg, 1.01 eq, 0.101 mmol), **12d** (67.0 mg, 1 eq, 0.100 mmol), Pd$_2$(dba)$_3$·CHCl$_3$ (2.2 mg, 0.02 eq, 0.002 mmol), and P(o-tol)$_3$ (4.7 mg, 0.16 eq, 0.016 mmol) were charged into a 10 mL vial designed for microwave reactor. The mixture was evacuated and refilled with argon for three cycles before addition of anhydrous o-xylene (0.7 mL) under argon stream. The reaction was heated up to 200 °C and held in a CEM microwave reactor for 30 min. After the polymerization, the crude polymer was dissolved in hot chlorobenzene (<10 mL) and precipitated into stirring methanol (200 mL). The collected polymer was extracted via a Soxhlet extractor with ethyl acetate, hexanes, and chloroform. The polymer solution in chloroform was concentrated and precipitated into methanol. The polymer was then collected via filtration and dried under vacuum. Yield: golden colored film, 87.1 mg, 81%.

6.4.2 Characterization Details

Mass Spectroscopy samples were analyzed with a Q Exactive HF-X (ThermoFisher, Bremen, Germany) mass spectrometer. Samples were introduced via an atmospheric pressure chemical ionization (APCI) source at a flow rate of 20 µL/min. One hundred time domain transients were averaged in the mass spectrum. APCI source conditions were set as: nebulizer temperature 350 °C, sheath gas (nitrogen) 20 arb, auxillary gas (nitrogen) 5 arb, sweep gas (nitrogen) 0 arb, capillary temperature 225 °C, RF voltage 35 V, spray voltage 5.0 KV. The mass range was set to 150-2000 m/z. All measurements were recorded at a resolution setting

of 120,000. Solutions were analyzed at 0.1 mg/mL or less based on responsiveness to the

APCI mechanism. Xcalibur (ThermoFisher, Breman, Germany) was used to analyze the data.

Molecular formula assignments were determined with Molecular Formula Calculator (v

1.2.3). All observed species were singly charged, as verified by unit m/z separation between

mass spectral peaks corresponding to the ^{12}C and $^{13}C^{12}C_{c-1}$ isotope for each elemental

composition.

High temperature gel permeation chromatography (HT-GPC) measurements were

performed on a Agilent 1260 HT-GPC instrument with TCB (1,2,4-trichlorobenzene) as the

eluent at 150 °C. The obtained molar mass is relative to the polystyrene standard. ^{1}H and ^{13}C

nuclear magnetic resonance (NMR) measurements were recorded with Bruker DRX

spectrometers (400 MHz or 600 MHz). UV-visible absorption spectra were obtained with a

Shimadzu UV-2600 spectrophotometer. The film thicknesses were recorded by a

profilometer (Alpha-Step 200, Tencor Instruments). CV measurements were carried out on

thin films using a Bioanalytical Systems (BAS) Epsilon potentiostat with a standard three-

electrode configuration. A three electrode cell of a glassy carbon working electrode, Ag/Ag+

reference electrode, and Pt counter electrode were used. Films of the FREAs were drop-cast

onto the glassy carbon electrode from hot chloroform solution (2 mg/mL, with

tetrabutylammonium hexafluorophosphate added at 100 wt%) and dried using a heat gun. 0.1

M solution of tetrabutylammonium hexafluorophosphate in anhydrous acetonitrile was used

as a supporting electrolyte. Scans were carried out under argon atmosphere at a scan rate of

100 mV/s. The reference electrode was calibrated using a ferrocene/ferrocenium redox

couple. Solar cell devices were tested under AM 1.5G irradiation calibrated with an NREL

certified standard silicon solar cell. Current density-voltage curves were measured via a Keithley 2400 digital source meter.

SCLC mobility was acquired through the hole-only devices with a configuration of ITO/PEDOT:PSS/active layer/MoO3/Al. The experimental dark current densities J were measured by Keithley 2400. The applied voltage V was corrected from the voltage drop Vrs due to the series resistance and contact resistance, which were found from a reference device without the active layer, and the build-in potential, which are estimated from the V_{OC} of corresponding hole-only devices under 1 sun condition. From the plots of J 0.5 vs V, hole mobilities of polymers were deduced from the Mott-Gurneys law:

$$J = \frac{9}{8} \varepsilon_r \varepsilon_0 \mu_h \frac{V^2}{L^3}$$

where ε_0 is the permittivity of free space, ε_r is the dielectric constant of the polymer which is assumed to be around 3, μ_h is the hole mobility, V is the voltage drop across the device, and L is the film thickness of the active layer.

GIWAXS measurements were performed at beamline 7.3.3 (DOI: 10.1088/1742-6596/247/1/012007) at the ALS. The 10 KeV X-ray beam was incident at a grazing angle of 0.13 degree. The scattered X-rays were detected using a 2D area detector (Pilatus 1M). All measurements were conducted under He atmosphere to reduce air scattering.

6.4.3 Device Fabrication:

Glass substrates coated with patterned indium doped tin oxide (ITO) were purchased from Thin Film Devices, Inc. About 150 nm sputtered ITO pattern had a resistivity of 20 Ω/sq. Prior to use, the substrates were ultrasonicated in deionized water, acetone, and then 2-proponal for 15 min each. The substrates were dried under a stream of nitrogen gas and subjected to the treatment of UV−ozone for 15 min. The CuSCN was dissolved in

diethylsulfide with the concentration 22.7 mg/mL under stirring for 1 hour. Then the CuSCN

solution was filtered by 0.2 μm poly(tetrafluoroethylene) (PTFE) filter and spun-cast on the

cleaned ITO substrates at 7000 rpm for 60 s and then baked at 100 °C for 15 min in air to

give a thin film with a thickness of about 40 nm. Then blends of polymer:$PC_{61}BM$ (1:2 w/w)

were dissolved in chlorobenzene (with 0.5% diphenyl ether for 4FT-CNTAZ blends) with

heating at 130 °C for 6 hours. All the solutions were filtered through a 5.0 μm PTFE filter

and spun-cast at an optimized rpm for 60 s onto the CuSCN layer for conventional structure.

The substrates were transferred into vacuum chamber immediately after spin-coating and

then dried at 30 mmHg below atmosphere for 30 min. The devices were finished for

measurement after thermal deposition of a 30 nm film of calcium and a 70 nm aluminum film

as the cathode for a conventional structure at a base pressure of 2×10^{-6} mbar. There are 8

devices per substrate, with an active area of 13 mm^2 per device.

CHAPTER 7: Designing Simple Conjugated Polymers for Scalable and Efficient Organic Solar Cells [16]

7.1 Introduction

In the past few chapters, structure-property relationships have been established for various conjugated polymers, and many noteworthy polymers recently emerged which have continued to push the record high efficiency number to new heights, now exceeding 18%.[323] A small selection of record holding polymers throughout the past twenty five years are highlighted in **Figure 7.1**.[21,323–327] The rapid growth in efficiency of OSCs demonstrate that this technology is nearing a commercialize level; however, many of these conjugated polymers have increasingly long and complex synthetic routes. This, in part, comes from the donor-acceptor co-polymer motif which most groups utilize for tunability of various polymer properties.[328–330] For a conjugated polymer to be realized in a commercially viable OSC, it should have (1) solution processability, (2) high efficiency, (3) sufficient stability, and (4) low cost.

There is also an additional consideration: synthetic complexity (SC), which is a measure of how difficult the material is to make, and can be used to assess the scalability of the synthesis of the material.[331,332] We were inspired by the work of Andrea Pellegrino in

---

[16] Parts of this chapter previously appeared as an article in *ChemSusChem*. Reprinted with permission through Copyright Clearance Center and John Wiley and Sons. The original citation is as follows: **Jeromy James Rech**, Justin Neu, Yunpeng Qin, Stephanie Samson, Jordan Shanahan, Richard F. Josey III, Harald Ade, and Wei You. "Designing Simple Conjugated Polymers for Scalable and Efficient Organic Solar Cells." *ChemSusChem*, **2021**, Early View, https://doi.org/10.1002/cssc.202100910

which they explored the synthetic complexity of various conjugated polymers for OSCs.[333,334] They identified five major parameters to assess the synthetic accessibility, including (1) the number of reaction steps, (2) the reaction yields, (3) the number of isolation/purification steps, (4) the number of column chromatographic purifications needed, and (5) the number of hazardous chemicals used. Further details can be found in Section 7.4 on how these parameters are converted into the final synthetic complexity value. The synthetic complexity, which ranges between 0-100, is also included in **Figure 7.1**.
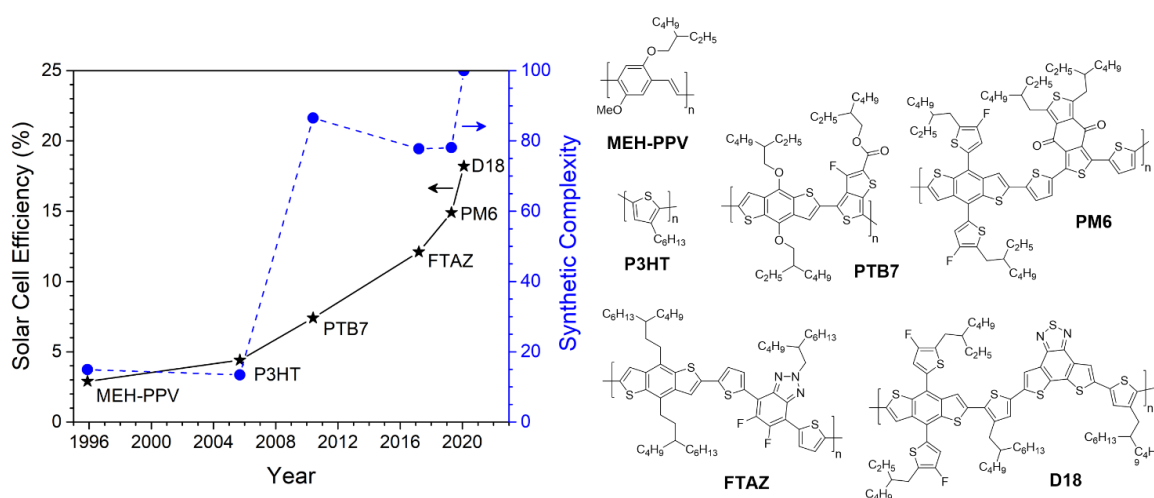
Figure 7.1 – A historical perspective on how the efficiency (black stars, solid line) and complexity (blue circles, dotted line) of conjugated polymers used in organic solar cells have evolved over time. The chemical structure of each polymer is also shown

Materials with a high synthetic complexity (SC approaching 100), which happened to encompass most of the current state-of-the-art conjugated polymers, would have a very difficult road for production on a kilogram/industrial scale. The final value of SC can be used to qualitatively compare many additional themes outside of the various inputs provided, such as waste generation and sustainability for example. While SC does not provide a specific value for these terms, both scale with the SC number (i.e., a synthetic route with a high SC is likely to have a larger amount of waste generated). For example, when comparing to a

different metric such as process mass intensity (PMI), which looks at the sustainability of a synthetic route via the amount of waste generated,[335–337] the same trends follow. Additionally, PMI is calculated for select polymers Section 7.4. **Figure 7.1** clearly demonstrates that while the efficiency of OSC polymers has grown tremendously compared to the original conjugated polymers such as poly(3-hexylthiophene) (P3HT), so has the synthetic complexity.

In a similar vein, Frederik Krebs and coworkers have done significant amount of work in exploring the scale up of materials to manufacture OSCs on a commercial level, and the cost analysis from their various works have identified a few milestones to achieve in order to realize a viable and competitive product.[338–341] The cost of inorganic photovoltaics is often calculated in $/$W_p$ (dollars per Watt peak), and a strong argument for scale-up and industrialization of OSCs can be made with a 10% efficiency module which costs less than $0.18/$W_p$ (i.e., matching inorganic performance). Based on cost analysis from Krebs, considering the cost for the entire organic solar cell module, the polymer donor would need to have a cost less than $12/g to match the competitive target (i.e., $0.18/$W_p$).[341] Based on our cost analysis data (see Section 7.4), PTB7 ($160.94/g), FTAZ ($132.71), PM6 ($184.20/g), and D18 ($179.76/g) are significantly higher than that threshold. This creates a dilemma as the current high efficiency blends use polymers with notably higher cost.

Considering that the current high-performance polymers exhibit both high cost and synthetic complexity, we began to look for conjugated polymers which had both simply synthesis and high efficiency. The PTQ10 polymer, designed in Yongfang Li's lab, has been able to achieve high performance with various acceptors: 12% with IDIC[342] and over 16% with Y6.[343] Furthermore, the synthetic complexity of PTQ10, estimated from the reported

synthetic route, is only 10.0, placing it on the level of polymers like MEH-PPV and P3HT. This material struck our interest as a perfect candidate for further exploration; however, while the PTQ10 polymer has low synthetic complexity, a cost analysis reveals that the reported synthetic approaches is very prohibitive at $214.18/g. Therefore, we set our goal to re-design the synthesis of PTQ10 to drastically cut the cost of synthesis, while maintaining a low synthetic complexity and high performance. Herein we report our new synthetic pathway to make the same PTQ10 polymer, which has a significantly reduced cost of $30.29/g – 1/7th the original cost. This work identifies a candidate conjugated polymer for further investigation for scale up and commercialization of OSCs.

7.2 Results and Discussion

The alternating copolymer of PTQ10 consists of a thiophene unit and a fluorinated quinoxaline with solubilizing side chains. Compared to many current polymers, the molecular weight of the repeat unit is much lower, driven by the move away from common 'donor-*linker*-acceptor-*linker*' architecture.[13,135] This change in polymer design helps to realize the low synthetic complexity of the PTQ10 polymer. The original synthesis is detailed in **Scheme 7.1**.[342] Beginning with 3,6-dibromo-4,5-difluorobenzene-1,2-diamine (**1**), the quinoxaline (**2**) can be formed with high yield through a condensation reaction with glyoxylic acid, aided by heat. The resulting product can then undergo a S_N2 chemistry protocol to add a solubilizing side chain to form the final monomer (**3**). The PTQ10 polymer can then be made through a Stille cross-coupling polymerization approach using a bis-stannylated thiophene unit (**4**). Each of these reaction steps have impressively high yields and the entire scheme (3 steps) is notably different from other materials such as PTB7 (15 steps),

216

FTAZ and PM6 (16 steps), and D18 (22 steps). This combination of high yields and few reaction steps drive down the synthetic complexity.
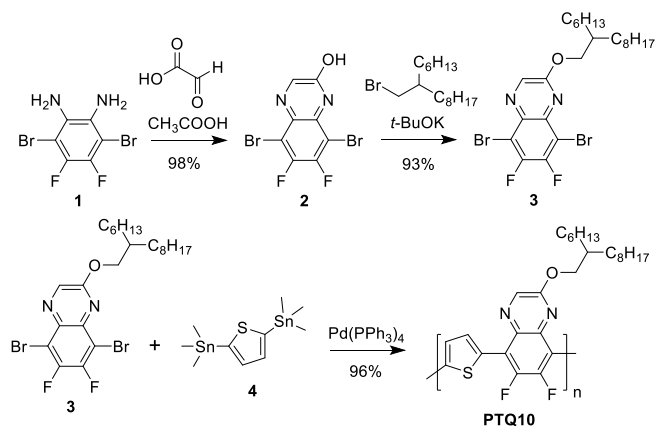
Scheme 7.1 – Previously reported synthetic pathway for PTQ10

However, while PTQ10 has a very low synthetic complexity, this does not translate into a low cost. A thorough cost analysis reveals that PTQ10, synthesized via the original approach, is one of the most expensive materials. A closer look into where the cost comes from highlights a few problems. Firstly, the starting material (**1**) is only commercially available from a few specialized vendors and thus the cost is very high. Next, the polymerization approach uses a Stille coupling which requires the use of a stannylated monomer. Tin reagents have both high cost and a variety of safety and environmental hazards associated with them.[344–346] Other shortcomings of this approach include the tunability to make derivative monomers and polymers. For example, the forming of the quinoxaline had poor yields when switching the substrates to nitrogen containing monomers (*vide infra*). This can indicate a limited substrate scope which can utilize this chemistry and thus limit the tunability of other PTQ-analogs. Additionally, the S_N2 chemistry to attach the side chain will require additional synthetic steps if switching to oligo(ethylene glycol) side chains, which are commonly used to add solubility in green processing solvents.[146,347–349]

For these reasons, we wanted to systematically explore and modify the reaction scheme to realize both low synthetic complexity and low cost – making PTQ10 a great candidate for scaling up of organic solar cells.

To begin with, we focused our attention on the starting material (**1**). The prohibitive cost of the fully functionalized substrate justifies additional reaction steps, which will certainly increase the synthetic complexity but could reduce the overall cost. To explore possible synthetic routes, we applied retrosynthetic analysis of the starting material to find possible alternatives, shown in **Scheme 7.2**. By removing one functional group (F, Br, or NH$_2$), there are then three possibilities to explore: (a) fluorination of 3,6-dibromobenzene-1,2,-diamine (**5**), (b) bromination of 1,2-diamino-4,5-difluorobenzene (**6**), and (c) amination of 1,4-dibromo-2,3-difluorobenzene (**7**). The cost of each different starting material also varies: \$220.00/g for 3,6-dibromo-4,5-difluorobenzene-1,2-diamine (**1**), \$97.90/g for 3,6-dibromobenzene-1,2,-diamine (**5**), \$11.00/g for 1,2-diamino-4,5-difluorobenzene (**6**), and \$9.90/g for 1,4-dibromo-2,3-difluorobenzene (**7**). Based on our previous chemistry,[125,248] we also explored 4,5-difluoro-2-nitroaniline (**8**), but the cost for this material is too high at \$56.10/g. Note: all prices are taken from Sigma Aldrich and the \$/g was calculated based the largest available package (e.g., 25g).
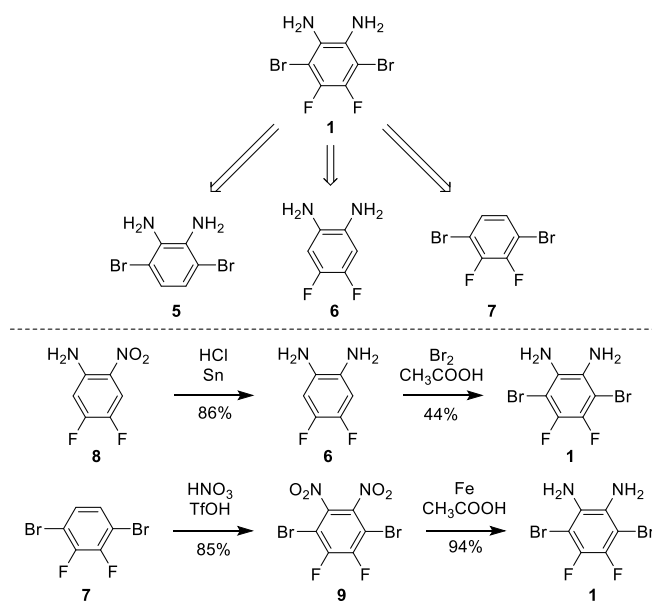
Scheme 7.2 – (top) retrosynthetic analysis for starting material and (bottom) alternative synthetic pathways towards the starting material

The first pathway of fluorination of 3,6-dibromobenzene-1,2,-diamine (**5**) was not explored for a few reasons: (1) the starting material had a cost nearly 10 times of the other potential starting materials, (2) no literature precedent for fluorination of that specific substrate, and (3) fluorination reactions typically result in low yields and have high costs. All these factors make this pathway less desirable for our consideration.

The second pathway of bromination of 1,2-diamino-4,5-difluorobenzene (**6**) can be realized by reacting the starting material (**6**) with liquid bromine in acetic acid and refluxing for a short period of time. The product can be successfully isolated; however, the overall reaction yield was only 44%; such a low yield is not conducive to a low cost. Furthermore, while the isolated product was pure by ^{1}H, ^{13}C, and ^{19}F NMR, the resulting solid still had a reddish-brown color which signified the presence of residual liquid bromine in the product even after purification with column chromatography. Other attempted bromination techniques either failed or had lower yields. Unfortunately, the residual bromine created a

larger issue as the formation of the quinoxaline (**2**) turned out to be very sensitivity of bromine impurities and the reaction yield dropped from the reported 98% to 14% in our hands. Therefore, the combination with lower yields and need for extra purification leaves this synthetic pathway undesirable.

For the third approach, there is not an easy one-step animation process; however, we envisioned that a high yielding nitration followed by a reduction process can suffice. For the nitration, we first tried to react 1,4-dibromo-2,3-difluorobenzene (**7**) with fuming nitric acid and sulfuric acid. This approach was able to successfully yield the product, but there was a large amount of byproduct which needed column chromatography to separate and reaction yield was quite low at 36%. After troubleshooting this reaction, we were able to find an appropriate reaction protocol with nitric acid and triflic acid.[350] This new approach exhibited high yields of 85% and did not need to undergo column chromatography which can help lower the synthetic complexity. After isolation, the nitrated product (**9**) can be effectively reduced with iron to yield the desired product in high yields. Furthermore, this approach avoids bromination and the starting material (**1**) can be formed with high yields (2 step overall yield of 80%).

While the originally reported quinoxaline formation reaction to make (**2**) works well for the non-functionalized (H-variant) and fluorinated PTQ10 version, we noticed that this same chemistry did not work effectively with other derivatized quinoxaline. In the original approach (**Scheme 7.1**), the starting material (**1**) was dissolved in glacial acetic acid, and the mixture was heated up for a short amount of time, before the product (**2**, quinoxaline) was collected as a precipitate upon cooling. While this reaction has great scalability and low synthetic complexity, we found that the substrate scope is rather limited. For example, when

switching from 3,6-dibromo-4,5-difluorobenzene-1,2-diamine (**1**) to a non-fluorinated

pyridine-based substrate or a mono-cyano functionalized substrate, as shown in **Scheme 7.3**,

the reaction yields for the quinoxaline formation were less than 10%. When troubleshooting

this reaction to extend the scope of substrates, we found that changing the solvent system to a

mixture of ethanol and glacial acetic acid aided in solubility of the starting material (i.e.,

these analogs of (**1**)). Furthermore, extracting the product with dichloromethane and washing

with water prior to recrystallization helped to improve the yield of the corresponding

quinoxaline. Overall, this optimized synthetic protocol retained the high yields for the

original substrates studied but substantially boosted the yields of materials (e.g., the pyridine-

based quinoxaline at over 85% yield).
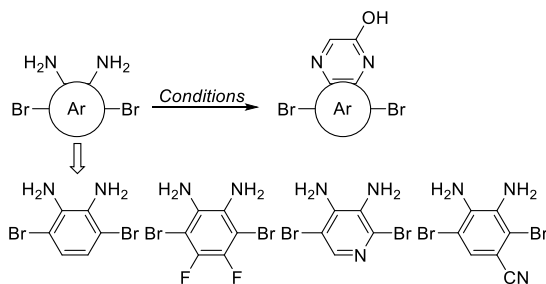
Scheme 7.3 – Quinoxaline formation for various functionalized substrates

Next, a solubilizing side chain needs to be added in order for the final polymer to be

solution processable. The original publication reported a high yielding S_N2 reaction between

the quinoxaline (**2**) and the brominated side chain, aided by potassium *tert*-butoxide as the

base (**Scheme 7.1**). While this approach works well, we wanted to explore a different

approach which uses an alcohol-functionalized side chain instead of a brominated one. As we

will discuss below, this alcohol-based side chain functionalization becomes crucial in

attaching oligio(ethylene glycol) (OEG) side chains to enable green solvent

solubility/processability of the final polymer. Most OSCs reported in literature use

halogenated and/or aromatic solvents such as chlorobenzene, dichlorobenzene, chloroform, toluene, among others. While these solvents can be effective in making an OSC, these solvents have various hazards which are detrimental for large scale up of manufacturing such OSCs. For these reasons, a variety of groups have been attempting to design conjugated polymers which are processable in green solvents (by 'green', we define as non-halogenated and non-aromatic solvents) such as ethanol, methanol, and water.[347,348] One common approach to add green solvent processability to a conjugated polymer is to replace the alkyl side chains with oligio(ethylene glycol) (OEG) variants.[146,347–349] Many OEG side chain variants are commercial available, however, most have end groups as alcohols (R-OH) instead of bromines (R-Br). In fact, the cost of R-OH side chain is significantly less than R-Br in the case of OEG variants. For example, one can purchase 2,000 mL of triethylene glycol monoethyl ether (OH-variant) or 5 mL of 1-(2-bromoethoxy)-2-(2-methoxyethoxy)ethane (Br-variant) with the same cost! For this reason, we aimed to find a different approach to add the solubilizing side chains which could accommodate a wider substrate scope.
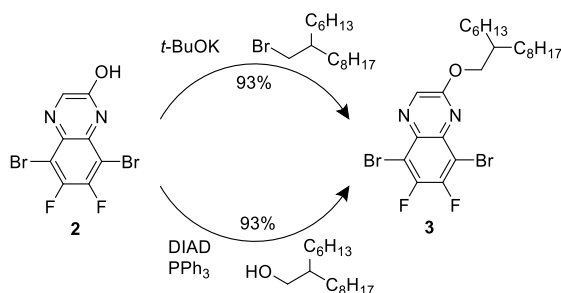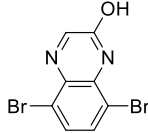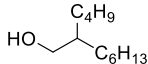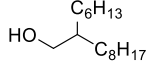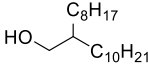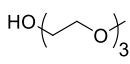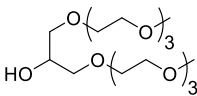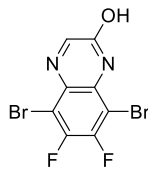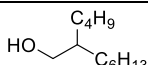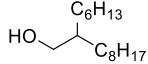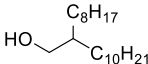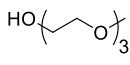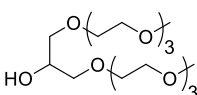
Scheme 7.4 – Two different methods to add solubilizing side chains. (top) SN2 chemistry and (bottom) Mitsunobu reaction

Based upon our previously published work,[14,15] we explored the use of Mitsunobo reaction to add solubilizing side chains to the quinoxaline substrate (**2**). **Scheme 7.4** highlights the differences in reagents needed, including the diisopropyl azodicarboxylate

222

(DIAD) and triphenylphosphine (PPh$_3$). While the Mitsunobu reaction has a complex reaction mechanism and poor atom economy (need full equivalence of all reagents), we are able to achieve the same high yield as the S$_N$2 approach. There is still room for improvement with this reaction, and various groups in literature are exploring methods to run Mitsunobu reaction with catalytic amounts of the azodicaroxylate and triphenyl phosphine by adding oxidants and reductants.[351–353] In addition, Denton and coworkers has demonstrated a new redox free organocatalytic Mitsunobu reaction on various substrates.[354] Exploring these routes in the future and adapting to the synthesis of conjugated materials in organic solar cell arena can provide great benefits to the community.

To demonstrate this Mitsunobu based method of adding solubilizing side chains is robust and can be used with a variety of potential side chains, we have synthesized a variety of different quinoxaline monomers based on a range of substrates. **Table 7.1** summarizes the same approach on various substrates (H and F functionalized) with various length alkyl side chains, as well as both linear and branched OEG side chain. All of these final monomers are able to be synthesized with yields and purities which are appropriate for polymerization. Reaction conditions and ^{1}H NMRs for each are included in the Section 7.4.

Table 7.1 – Demonstrating the versatility of the Mitsunobu reaction

Core	Side Chain	Product	Yield
	HO—C_4H_9/C_6H_{13}	**10**	79%
	HO—C_6H_{13}/C_8H_{17}	**11**	89%
	HO—C_8H_{17}/$C_{10}H_{21}$	**12**	91%
(quinoxaline core: OH, N, N, Br, Br)	HO—(O)$_3$	**13**	88%
	HO—(O—(O)$_3$)$_3$	**14**	55%
	HO—C_4H_9/C_6H_{13}	**15**	94%
	HO—C_6H_{13}/C_8H_{17}	**3**	93%
	HO—C_8H_{17}/$C_{10}H_{21}$	**16**	91%
(quinoxaline core: OH, N, N, Br, Br, F, F)	HO—(O)$_3$	**17**	72%
	HO—(O—(O)$_3$)$_3$	**18**	63%

Finally, the conjugated polymer of PTQ10 was made through a microwave-assisted Stille polymerization with the monomers synthesized following our optimized procedures.[14,355] The ratio of dibrominated quinoxaline monomer and bis-stannylated thiophene monomer can be varied to control the molar mass of the polymer through the

Carothers' equation.[11,12,158] The number average molar mass (M_n) and dispersity ($Đ$) of each

polymer was measured through high-temperature gel permeation chromatography (HT-

GPC). In comparison, commercially available PTQ10 from the company 1-Materilas (Lot

#HW5148CH) had a slightly larger M_n compared to our batch (25 vs 18 kg/mol); however,

further optimization with the polymerization conditions should be able to produce polymers

of higher M_n. These as-synthesized PTQ10 polymers can be dissolved in common solvents

used in OSCs, such as chloroform and chlorobenzene at elevated temperatures.

In order to test the efficiency of our PTQ10 polymer, we fabricated bulk

heterojunction solar cells with a conventional device architecture of indium doped tin oxide

(ITO)/poly(3,4-ethylenedioxythiophene) polystyrene sulfonate (PEDOT:PSS)/

PTQ10:Y6/PFN-Br/aluminum, where PFN-Br is poly(9,9-bis(3'-(N,N-dimethyl)-N-

ethylammoinium-propyl-2,7-fluorene)-alt-2,7-(9,9-dioctylfluorene))dibromide. The active

layer consisted of a 1:1.2 weight ratio of PTQ10:Y6, and the thickness was kept to ∼120 nm

for all devices reported herein. A representative current density (J) vs voltage (V) response

for each solar cell is presented in **Figure 7.2**. Similarly, the device characteristics of short-

circuit current density (J_{SC}), open circuit voltage (V_{OC}), fill factor (FF), and power

conversation efficiency (PCE) are summarized in **Table 7.2**, where each entry is the average

of at least sixteen solar cells.
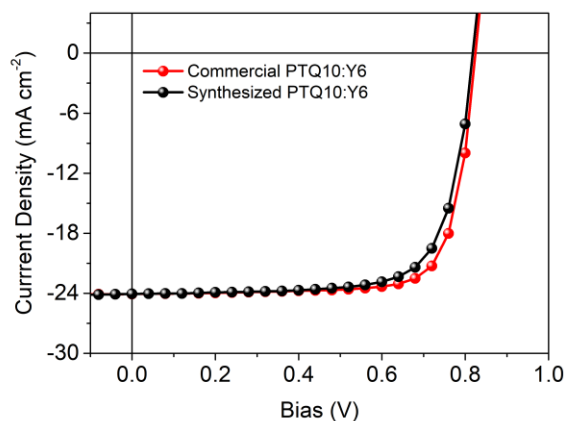
Figure 7.2 – Representative J-V curve for PTQ10:Y6 solar cells.

Table 7.2 – Photovoltaic properties of PTQ10-Y6 solar cells

PTQ10 Source	J_{SC} (mA/cm²)	V_{OC} (V)	FF (%)	PCE (%)
Commercial	24.0 ± 0.1	0.83 ± 0.01	77.0 ± 0.2	15.4 ± 0.2
Synthesized	23.9 ± 0.1	0.82 ± 0.01	73.8 ± 0.1	14.5 ± 0.1

From the solar cell device results, we demonstrate that the new synthetic route also yields high performance PTQ10. The commercial and synthesized batches of PTQ10 yield the same J_{SC} and V_{OC} when blended with Y6. The slightly lower fill factor can be contributed to slightly lower molecular weight of the synthesized PTQ10 batch. Further tuning of the polymerization conditions can increase the molecular weight to match (and possible exceed) the 15.4% efficiency mark.

While this polymerization approach can yield high performing polymers, the use of tin is problematic. Aside from the toxicity, cost analysis reveals that ~40% of the overall cost of PTQ10 through our new synthetic approach comes from the trimethyltin chloride reagent which is used to make the stannylated thiophene monomer. Therefore, finding a polymerization approach which avoids the Stille coupling can be an important area of further

investigation in the future. We have done initial work with attempting both a direct arylation

polymerization (DArP) and a Suzuki polymerization approach, and while both of these have

great promise, only short low molecular weight oligomers could be obtained.
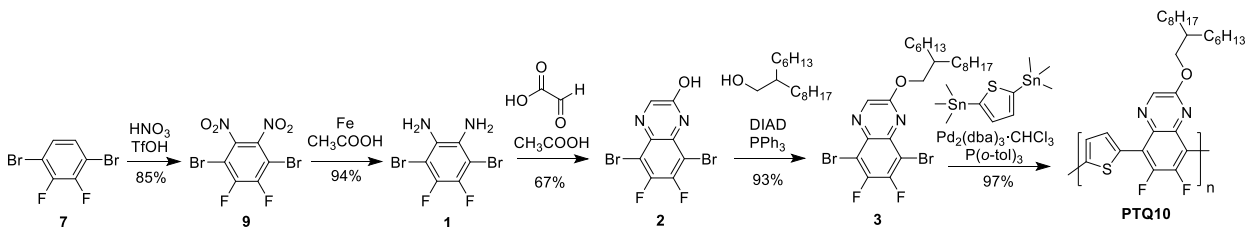
Scheme 7.5 – Updated synthetic route for PTQ10

7.3 Conclusion

With efficiencies of organic solar cells increasingly approaching 20%, the community

needs to focus on addressing the remaining questions required to realize widely accessible

and commercially available organic solar cell. Along with long term stability and green

solvent processability, conjugated polymers should exhibit both low synthetic complexity

and cost. We have taken PTQ10 as one example to show that the cost of this particular

polymer can be reduced from \$214.18/g with the original synthetic route down to \$30.29/g

with the optimized one (summarized in **Scheme 7.5**). This new pathway also has the ability

to accommodate different variations, including the inclusion of oligio(ethylene glycol) side

chains, which can help realize a green solvent processable version of PTQ10. This work also

highlights further areas for investigation, including (1) a catalytic synthesis for the

Mitsunobu reaction to add the solubilizing side chains and (2) a tin-free polymerization

approach such as direct arylation polymerization. Finally, since PTQ10 is a donor polymer,

we suggest that the same approach should be taken for the electron acceptor to realize a blend

with high performance and low synthetic complexity and cost. We hope that this work helps

227

to inspire others to consider the end goal of a scalable organic solar cell when designing their new chemistry.

7.4 Experimental

7.4.1 Synthesis of PTQ10

All chemicals were purchased from commercial source (Sigma-Aldrich, Fisher, Acros, etc.) and were used as received except when specified. For comparison, PTQ10 was purchased from 1-Materilas (Lot #HW5148CH). The electron acceptor, Y6, was purchased from eFlexPV LTD (Lot #200921A). Anhydrous THF was prepared via distillation over sodium and benzophenone before use. For reactions under argon, the reaction flask was evacuated and refilled with argon for three times.

Synthesis of *1,4-dibromo-2,3-difluoro-5,6-dinitrobenzene* (**9**): 2 mL of fuming nitric acid (HNO_3) was slowly added to trifluoromethanesulfonic acid (triflic acid, 50 g, 30 mL, 34 eq, 0.33 mol) in an ice bath and allowed to stir for 1 hour. 1,4-dibromo-2,3-difluorobenzene (2.65 g, 1 eq, 9.74 mmol) was added to the reaction in portions over 30 min and left to react in the ice bath for 1 hour then at room temperature for 2 hours. The reaction was placed back in an ice bath and another 2 mL of fuming HNO_3 was added to the reaction. The reaction was heated at 70 °C for 18 hours, a yellow solid formed. After cooling, the reaction was poured into 250 mL of ice water and left to stir for 15 min. The yellow solid was collected via filtration and dried on high vacuum overnight to remove residual solvent. Yield: 3.01 g, 85%. ^{19}F NMR (376 MHz, $CDCl_3$) δ -113.90.

Synthesis of *3,6-dibromo-4,5-difluoro-1,2-benzenediamine* (**1**): 1,4-dibromo-2,3-difluoro-5,6-dinitrobenzene (6.39 g, 1 eq, 17.69 mmol) and iron powder (13.83 g, 14 eq) were added to a 3-neck round bottom flask and under argon. 200 mL of glacial acetic acid

was added to the reaction then heated to 45 °C for 18 hours. After cooling, the reaction was poured into 400 mL of 10% sodium hydroxide solution which was cooled in an ice bath (Warning: very exothermic!). The solid was filtered and dissolved in ethyl acetate and washed with sodium bicarbonate twice, then dried over magnesium sulfate. The white solid was dried over high vacuum to remove residual solvent. Yield: 5.01 g, 94%. Note: the product will slowly oxidize in air, so use immediately or store under inert atmosphere. ^{1}H NMR (400 MHz, CDCl$_3$) δ 4.10 (s, 4H). ^{13}C NMR (101 MHz, CDCl$_3$) δ 143.03, 142.85, 140.63, 140.45, 129.54, 98.31, 98.20, 98.09.

Synthesis of *5,8-dibromo-6,7-difluoroquinoxalin-2-ol* (**2**): 3,6-dibromo-4,5-difluoro-1,2-benzenediamine (2.54 g, 1 eq, 8.41 mmol) and glyoxylic acid (655 mg, 1.05 eq, 8.8 mmol) were added to a 100 mL 3-neck round bottom flask under argon. Glacial acetic acid (15 mL) and anhydrous ethanol (15 mL) were added to the reaction and heated to reflux for 3 hours. The product was extracted with dichloromethane, and washed with water then dried with magnesium sulfate. The product was recrystallized in ethanol and dried overnight to a light beige crystalline solid. Yield: 1.92 g; 67%. ^{1}H NMR (400 MHz, DMSO) δ 12.75 (s, 1H), 8.45 (s, 1H). ^{13}C NMR (101 MHz, DMSO) δ 156.88, 147.58, 145.46, 145.40, 143.37, 140.58, 104.46, 102.97.

Synthesis of *5,8-dibromo-6,7-difluoro-2-((2-hexyldecyl)oxy)quinoxaline* (**3**): 5,8-dibromo-6,7-difluoroquinoxalin-2-ol (209 mg, 1 eq, 0.61 mmol) and triphenylphosphine (179 mg, 1.11 eq, 0.68 mmol) were added to a 50 mL 2-neck round bottom flask under argon. Anhydrous tetrahydrofuran (20 mL) was added to the reaction vessel via cannula. The reaction was cooled to 0 °C in an ice bath. 2-hexyldecan-1-ol (158 mg, 1.06 eq, 0.65 mmol) was added to the reaction followed by the slow addition of diisopropyl azodicarboxylate

(DIAD) (189 mg, 1.5 eq, 0.94 mmol). The reaction mixture became a clear yellow/orange upon the addition of DIAD. The reaction was removed from the ice bath and heated at reflux for 18 hours. After cooling, the reaction was quenched with distilled water and extracted in dichloromethane. The organic layer was subsequently washed with water and dried over magnesium sulfate and filtered. The filtrate was concentrated and triphenylphosphine oxide was precipitated out by adding dropwise to a large volume of hexanes. The crude product which was then purified by column chromatography (12:1 hexanes:ethyl acetate, rf ~0.8). The product was a pale yellow sticky oil, which could be frozen and then recrystallized in methanol to yield a white crystalline solid. Yield: 322 mg, 93%. ^{1}H NMR (400 MHz, CDCl$_3$) δ 8.52 (s, 1H), 4.49 (d, J = 5.7 Hz, 2H), 1.88 (q, J = 6.0 Hz, 1H), 1.55 – 1.19 (m, 24H), 0.87 (dt, J = 7.1, 3.2 Hz, 6H). ^{13}C NMR (100 MHz, CDCl$_3$): δ 158.69, 151.82, 149.33, 146.88, 140.66, 136.31, 133.26, 109.75, 107.60, 70.50, 37.46, 31.87, 31.36, 29.98, 29.61, 29.31, 26.84, 22.67, 14.09.

Synthesis of *2,5-bis(trimethylstannyl)thiophene* (**4**): A 250 mL 3-neck round bottom flask was evacuated and refilled with argon three times. Anhydrous tetrahydrofuran (100 mL) was added to the reaction vessel via cannula along with thiophene (1.26 g, 1.19 mL, 1 eq, 15 mmol). The vessel was placed in a dry ice/acetone bath and allowed to cool to -78 °C. Once the reaction was cooled, n-butyllithium (12.6 mL, 2.5 M, 2.10 eq, 31.5 mmol) was added dropwise. The reaction was left to stir at -78 °C for 1 hour. Then, trimethyltin chloride (31.5 mL, 1 M, 2.10 eq, 31.5 mmol) was slowly added to the reaction. The reaction was removed from the dry ice/acetone bath and brought to room temperature and allowed to stir for 15 hours. The reaction was quenched with 15 mL of saturated ammonium chloride and then extracted with hexanes and washed with brine and water several times. The organic

layer was dried over magnesium sulfate then filtered and concentrated. The product was recrystallized in methanol to yield long white crystalline needles. Yield: 5.04 g, 82%. ^{1}H NMR (400 MHz, CDCl$_3$) δ 7.38 (s, 2H), 0.37 (s, 18H).

Polymerization of **PTQ10**: 2,5-bis(trimethylstannyl)thiophene (51.5 mg, 1.0 eq, 0.126 mmol), 5,8-dibromo-6,7-difluoro-2-((2-hexyldecyl)oxy)quinoxaline (70.9 mg, 1 eq, 0.126 mmol), Pd$_2$(dba)$_3$·CHCl$_3$ (2.6 mg, 0.02 eq, 0.0025 mmol), and P(o-tol)$_3$ (6.1 mg, 0.16 eq, 0.020 mmol) were charged into a 10 mL vial designed for microwave reactor. The mixture was evacuated and refilled with argon for three cycles before addition of anhydrous toluene (0.9 mL) under argon stream. The reaction was heated up to 200 °C and held in a CEM microwave reactor (300 W) for 10 min. After the polymerization, the crude polymer was dissolved in hot chlorobenzene (<10 mL) and precipitated into stirring methanol (200 mL). The collected polymer was extracted via a Soxhlet extractor with ethyl acetate, hexanes, and chloroform. The polymer solution in chloroform was concentrated and precipitated into methanol. The polymer was then collected via filtration and dried under vacuum as thin golden/metallic flakes. Yield: 69.4 mg, 97%.

7.4.2 Device Fabrication

The OSCs were fabricated with a conventional configuration of indium tin oxide (ITO)/PEDOT:PSS(4083)/active layer/PFN-Br/Al. The ITO substrates were first scrubbed by detergent and then sonicated with deionized water, acetone and isopropanol subsequently. The glass substrates were treated by UV-Ozone for 15 min before use. PEDOT:PSS (4083) was spin-cast onto the ITO substrates at 4000 rpm for 30 s and then dried at 150 °C for 15 min in air. The PTQ10:Y6 blends (1:1.2 weight ratio) were dissolved in chloroform (the total concentration of blend solutions was 19.8 mg/mL), with the addition of 0.5% CN as additive,

and stirred in a nitrogen-filled glove box. The blend solutions were spincast at 2500 rpm for 30s on the top of a PEDOT:PSS layer followed by a thermal annealing step at 100°C for 10min. Then a thin PFN-Br layer (≈5nm) was coated on the active layer. At last the top metal electrode was evaporated at ≈1×10^{-6} Torr and consisted of an Al (100 nm) layer. J–V characteristics were recorded with a Keithley 2400 source meter under 100 mW cm^{-2} AM 1.5G light. The light is provided by a Class 3A Solar Simulator and KG5 silicon reference cell.

7.4.3 Substrate Scope

General Synthetic Details for Quinoxaline Monomers: The quinoxaline core (1 eq) and PPh$_3$ (1.1 eq) were added to a 50 mL 2-neck round bottom flask. The reaction vessel was evacuated and refilled with argon 3 times. Dry tetrahydrofuran (20 mL) was added to the reaction then cooled to 0 °C in an ice bath. The alcohol side chain (1.1 eq) was added followed by the slow addition of DIAD (1.5 eq). The reaction was removed from the ice bath and heated at reflux for 18 hours. The reaction was quenched with DI H$_2$O and extracted in DCM. The organic layer was subsequently washed with DI H$_2$O then dried over MgSO$_4$ then filtered and concentrated. Triphenylphosphine oxide was precipitated out in hexanes and filtered from the crude product which was then purified by column chromatography (hexanes:ethyl acetate = 12:1 v/v%) to the product as a light yellow oil. The oil can be often be frozen freezer and then recrystallized in methanol to yield a white crystalline solid.

Synthesis of Product 10 (HQx with short alkyl side chain): 5,8-dibromo-2-((2-butyloctyl)oxy)quinoxaline synthesized using general procedure above, recrystallized in EtOH producing a white solid (260.5 mg, 79%). ^{1}H NMR (400 MHz, CDCl$_3$) δ 8.53 (s, 1H),

7.84 (d, *J* = 8.3 Hz, 1H), 7.73 (d, *J* = 8.3 Hz, 1H), 4.50 (d, *J* = 5.7 Hz, 2H), 1.89 (q, *J* = 6.0

Hz, 1H), 1.51 – 1.22 (m, 16H), 0.89 (dt, *J* = 12.3, 7.0 Hz, 6H).
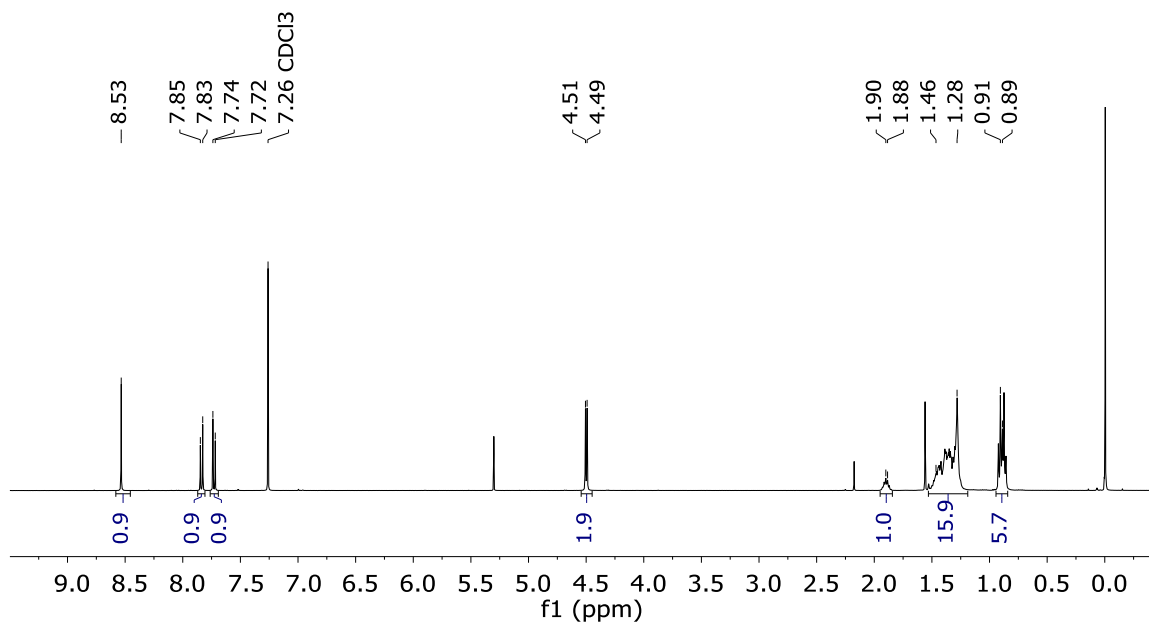
Figure 7.3 – ^{1}H NMR of monomer 10

Synthesis of Product 11 (HQx with medium alkyl side chain): 5,8-dibromo-2-((2-

hexyldecyl)oxy)quinoxaline synthesized using general procedure above producing a yellow

oil (320.1 mg, 89%). ^{1}H NMR (400 MHz, CDCl$_3$) δ 8.53 (s, 1H), 7.84 (d, *J* = 8.2 Hz, 1H),

7.73 (d, *J* = 8.2 Hz, 1H), 4.50 (d, *J* = 5.7 Hz, 2H), 1.90 (dt, *J* = 12.0, 6.3 Hz, 1H), 1.51 – 1.19

(m, 24H), 0.91 – 0.83 (m, 6H).
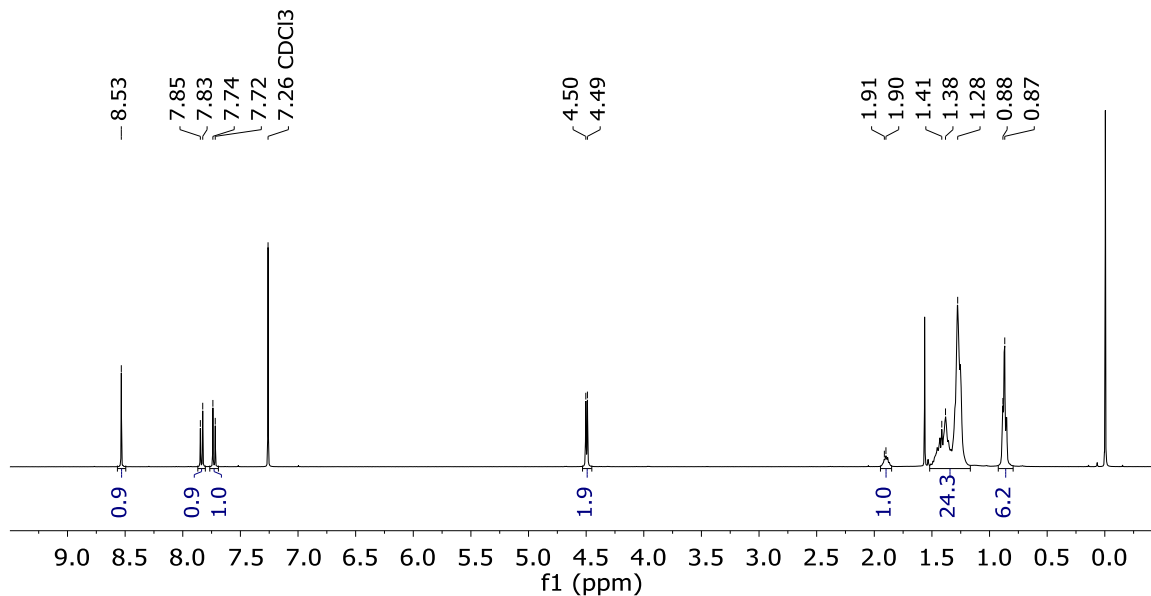
Figure 7.4 – ¹H NMR of monomer 11

*Synthesis of Product 12 (HQx with long alkyl side chain)***:** 5,8-dibromo-2-((2-octyldodecyl)oxy)quinoxaline synthesized using general procedure above producing a yellow oil (362.3 mg, 91%). ¹H NMR (400 MHz, CDCl₃) δ 8.53 (s, 1H), 7.84 (d, J = 8.2 Hz, 1H), 7.73 (d, J = 8.2 Hz, 1H), 4.50 (d, J = 5.7 Hz, 2H), 1.89 (q, J = 6.0 Hz, 1H), 1.55 – 1.14 (m, 32H), 0.87 (t, J = 6.7 Hz, 6H).
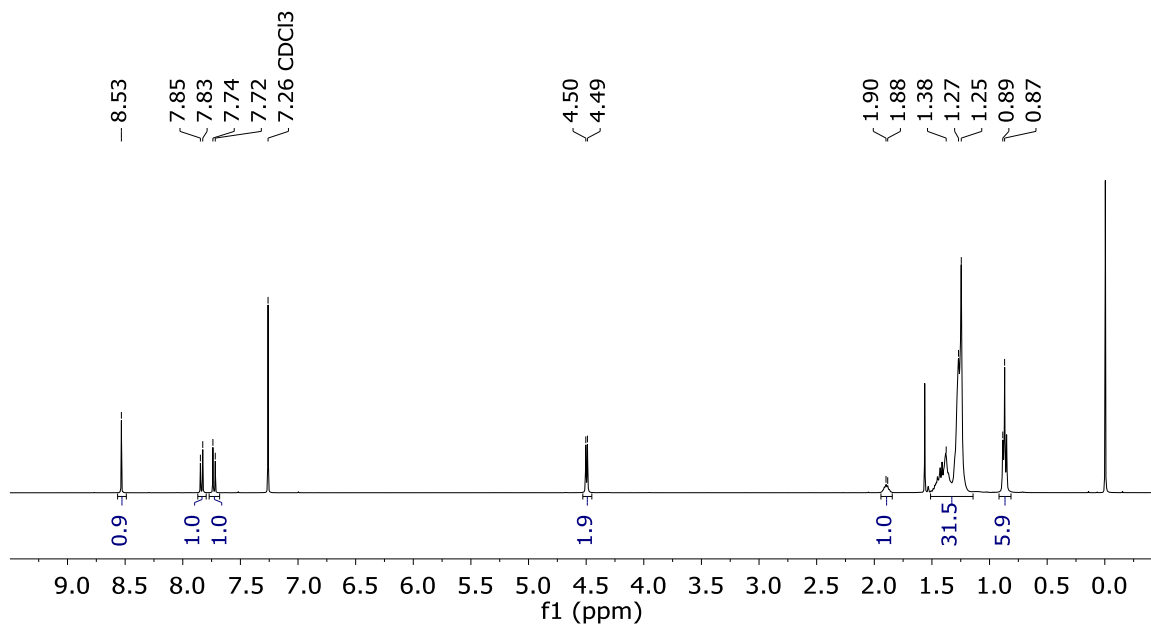
Figure 7.5 – ¹H NMR of monomer 12

Synthesis of Product 13 (HQx with linear OEG side chain): 5,8-dibromo-2-(2-(2-(2-methoxyethoxy)ethoxy)ethoxy)quinoxaline was synthesized using the general procedure above with slight adjustments to the reagent amounts. Increased amounts of PPh$_3$ (1.5 eq), 2-(2-(2-methoxyethoxy)ethoxy)ethan-1-ol (1.5 eq), and DIAD (1.5 eq) were used. The product was purified by column chromatography (EtOAc:hexanes = 1.5:1 v/v%). Recrystallized in MeOH yielding as a white solid (496.4 mg, 88%). ^{1}H NMR (400 MHz, CDCl$_3$) δ 8.61 (s, 1H), 7.84 (d, *J* = 8.2 Hz, 1H), 7.75 (d, *J* = 8.2 Hz, 1H), 4.80 – 4.74 (m, 2H), 4.01 – 3.95 (m, 2H), 3.81 – 3.73 (m, 2H), 3.73 – 3.62 (m, 4H), 3.58 – 3.51 (m, 2H), 3.37 (s, 3H).
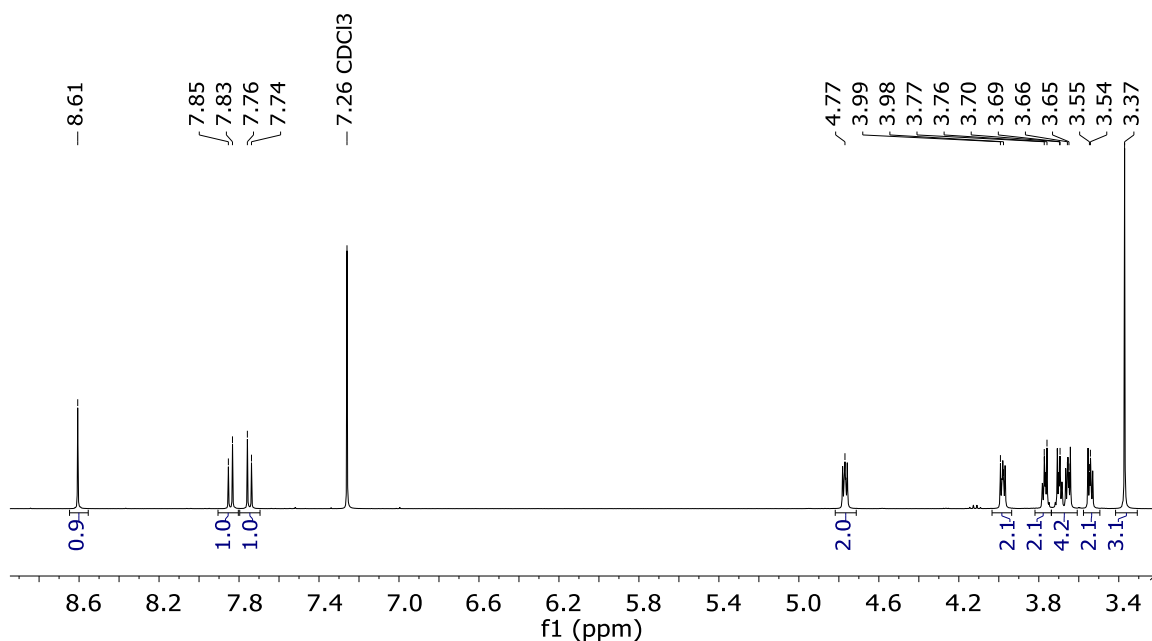
Figure 7.6 – ^{1}H NMR of monomer 13

Synthesis of Product 14 (HQx with branched OEG side chain): 2-((2,5,8,11,15,18,21,24-octaoxapentacosan-13-yl)oxy)-5,8-dibromoquinoxaline synthesized using general procedure above with slight changes to the reagents and workup procedure. Increased amounts of PPh$_3$ (1.5 eq), 2,5,8,11,15,18,21,24-octaoxapentacosan-13-ol (1.2 eq), and DIAD (1.5 eq) were used. After extraction the crude was dissolved in 50 mL of 1:1 v/v%

diethylether:ethanol and zinc(II) chloride (2.4 eq) was added. The solution was brought to a boil to dissolved ZnCl$_2$ then left to cool and precipitate the triphenylphosphine oxide zinc adduct. The product was isolated via column chromatography (ethyl acetate) giving a yellow oil (552.4 mg, 55%). ^{1}H NMR (600 MHz, CDCl$_3$) δ 8.58 (s, 1H), 7.83 (d, J = 8.2 Hz, 1H), 7.74 (d, J = 8.2 Hz, 1H), 5.79 (p, J = 5.0 Hz, 1H), 3.94 – 3.86 (m, 4H), 3.72 (ddd, J = 14.4, 5.7, 4.0 Hz, 4H), 3.67 – 3.57 (m, 16H), 3.57 – 3.49 (m, 4H), 3.36 (s, 6H).
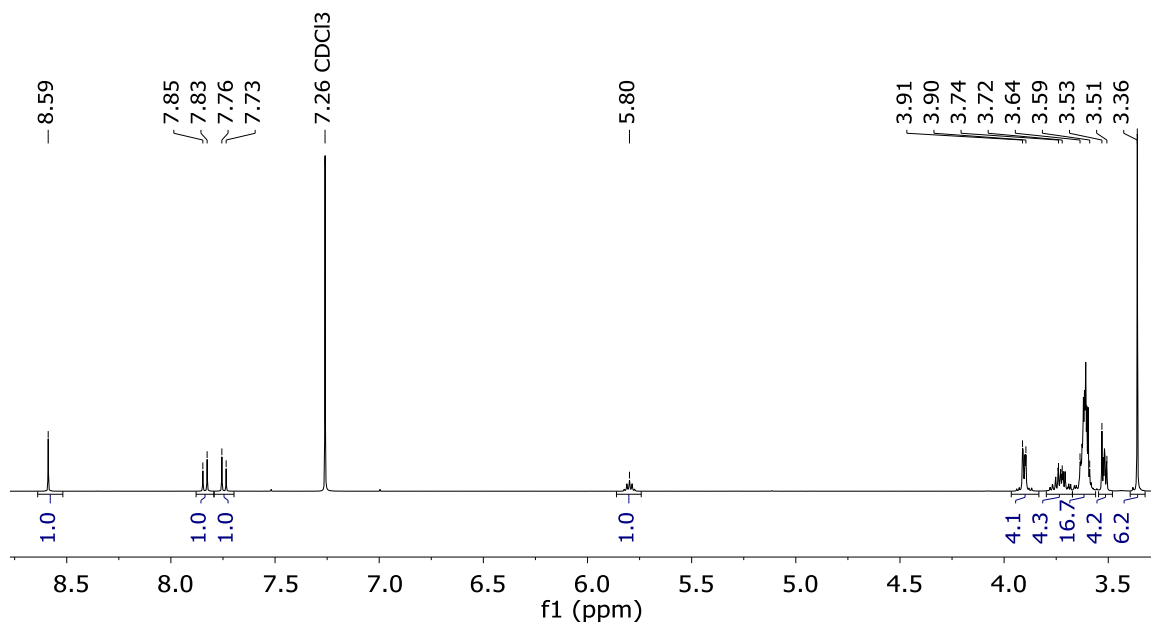
Figure 7.7 – ^{1}H NMR of monomer 14

Synthesis of Product 15 (FQx with short alkyl side chain): 5,8-dibromo-2-((2-butyloctyl)oxy)-6,7-difluoroquinoxaline synthesized using general procedure above, recrystallized in EtOH producing a white solid (2.1144 g, 94%). ^{1}H NMR (400 MHz, CDCl$_3$) δ 8.51 (s, 1H), 4.49 (d, J = 5.7 Hz, 2H), 1.89 (p, J = 6.0 Hz, 1H), 1.52 – 1.23 (m, 16H), 0.89 (dt, J = 11.9, 6.9 Hz, 6H).
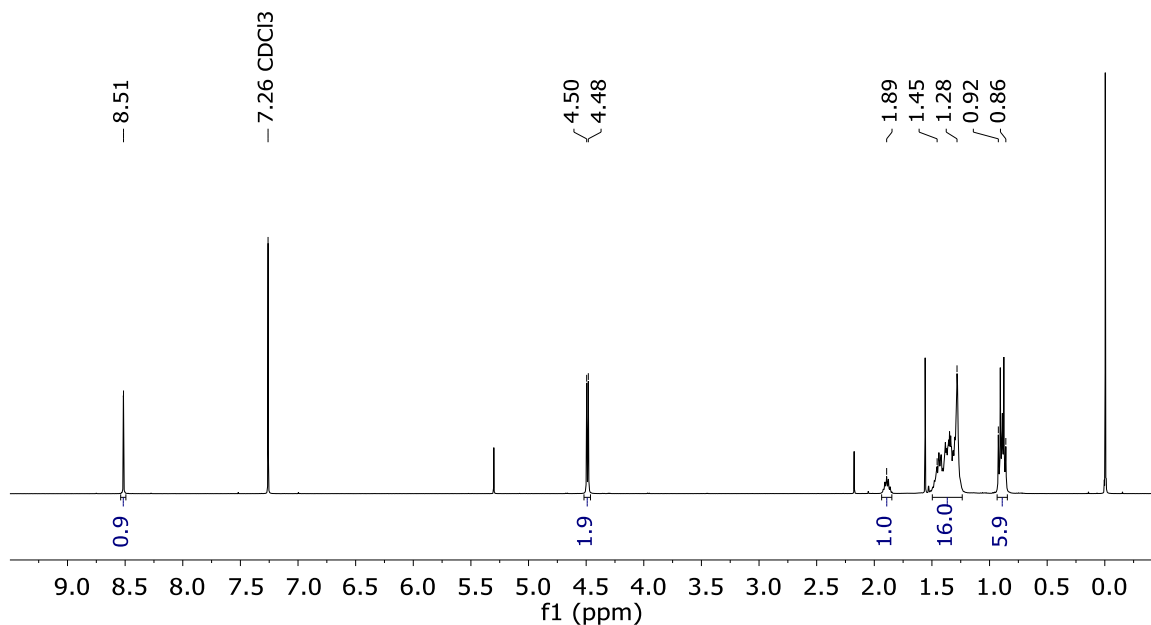
Figure 7.8 – ¹H NMR of monomer 15

Synthesis of Product 3 (FQx with medium alkyl side chain): 5,8-dibromo-6,7-difluoro-2-((2-hexyldecyl)oxy)quinoxaline synthesized using procedure above producing a yellow oil (322.0 mg, 93%). ¹H NMR (400 MHz, CDCl₃) δ 8.52 (s, 1H), 4.49 (d, J = 5.7 Hz, 2H), 1.88 (q, J = 6.0 Hz, 1H), 1.55 – 1.19 (m, 24H), 0.87 (dt, J = 7.1, 3.2 Hz, 6H).
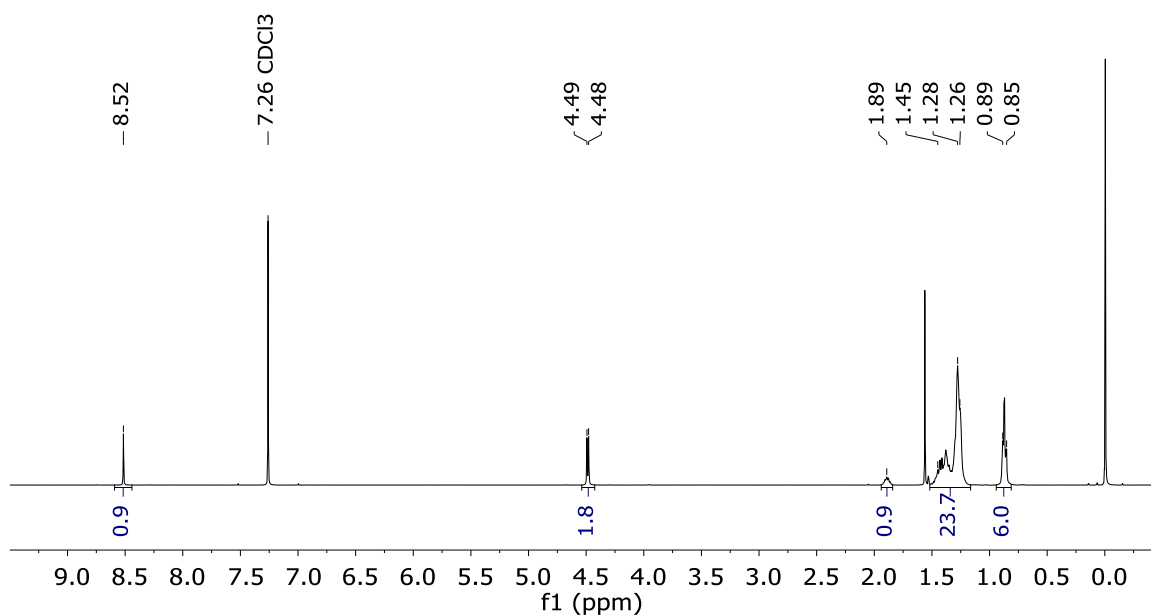
Figure 7.9 – ¹H NMR of monomer 3

237

Synthesis of Product 16 (FQx with long alkyl side chain): 5,8-dibromo-6,7-difluoro-2-((2-octyldodecyl)oxy)quinoxaline synthesized using general procedure above producing a yellow oil (344.5 mg, 91%). ^{1}H NMR (400 MHz, CDCl$_3$) δ 8.51 (s, 1H), 4.49 (d, J = 5.6 Hz, 2H), 1.89 (p, J = 6.1 Hz, 1H), 1.50 – 1.19 (m, 32H), 0.87 (t, J = 6.7 Hz, 6H).
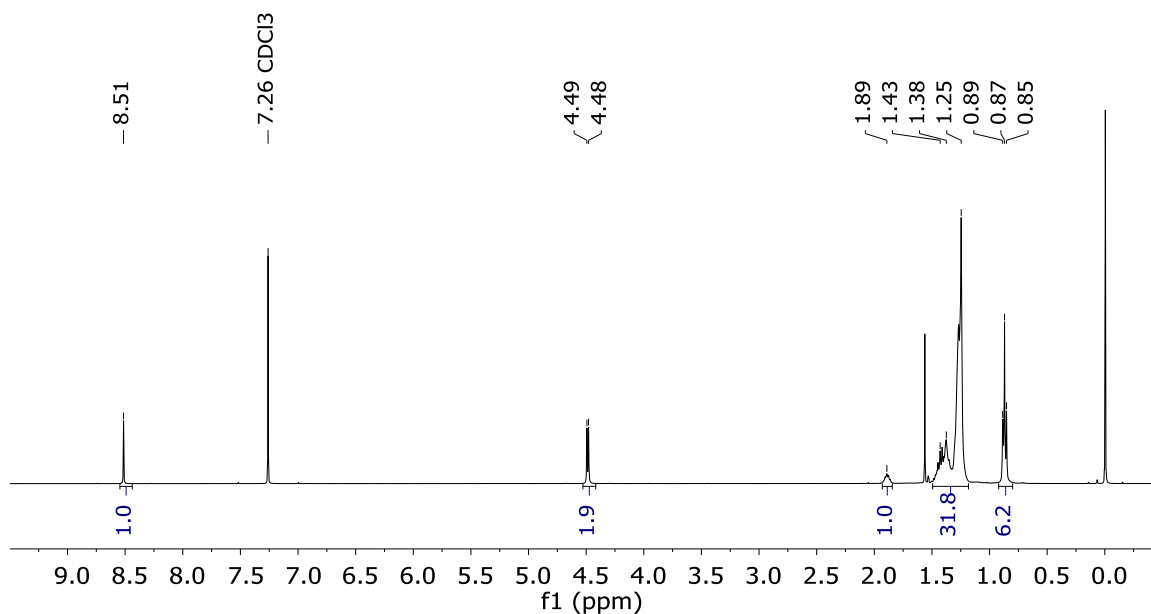
Figure 7.10 – ^{1}H NMR of monomer 16

Synthesis of Product 17 (FQx with linear OEG side chain): 5,8-dibromo-6,7-difluoro-2-(2-(2-(2-methoxyethoxy)ethoxy)ethoxy)quinoxaline was synthesized using the general procedure above with slight adjustments to the reagent amounts. Increased amounts of PPh$_3$ (1.5 eq), 2-(2-(2-methoxyethoxy)ethoxy)ethan-1-ol (1.5 eq), and DIAD (1.5 eq) were used. The product was purified by column chromatography (EtOAc:hexanes = 1.5:1 v/v%). Recrystallized in MeOH yielding as a white solid (327.6 mg, 72%). ^{1}H NMR (400 MHz, CDCl$_3$) δ 8.59 (s, 1H), 4.80 – 4.71 (m, 2H), 4.01 – 3.94 (m, 2H), 3.79 – 3.73 (m, 2H), 3.70 (d, J = 4.9 Hz, 2H), 3.65 (t, J = 4.6 Hz, 2H), 3.58 – 3.51 (m, 2H), 3.37 (s, 3H).
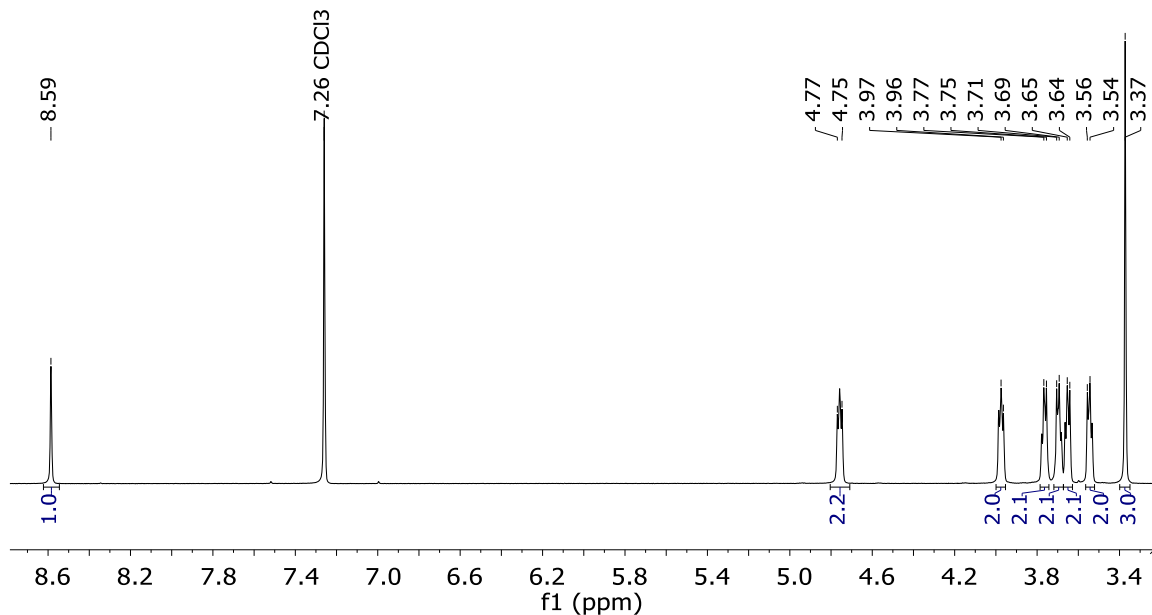
Figure 7.11 – ^{1}H NMR of monomer 17

Synthesis of Product 18 (FQx with branched OEG side chain): 2-((2,5,8,11,15,18,21, 24-octaoxapentacosan-13-yl)oxy)-5,8-dibromo-6,7-difluoroquinoxaline was synthesized using general procedure above with slight changes to the reagents and workup procedure. Increased amounts of PPh$_3$ (1.5 eq), 2,5,8,11,15,18,21,24-octaoxapentacosan-13-ol (1.2 eq), and DIAD (1.5 eq) were used. After extraction the crude was dissolved in 50 mL of 1:1 v/v% diethylether:ethanol and zinc(II) chloride (2.4 eq) was added. The solution was brought to a boil to dissolved ZnCl$_2$ then left to cool and precipitate the triphenylphosphine oxide zinc adduct. The product was isolated via column chromatography (ethyl acetate) giving a yellow oil (798.5 mg, 63%). ^{1}H NMR (600 MHz, CDCl$_3$) δ 8.57 (s, 1H), 5.77 (t, *J* = 5.0 Hz, 1H), 3.90 (dd, *J* = 5.0, 2.4 Hz, 4H), 3.77 – 3.66 (m, 4H), 3.68 – 3.57 (m, 16H), 3.55 – 3.50 (m, 4H), 3.36 (s, 6H).
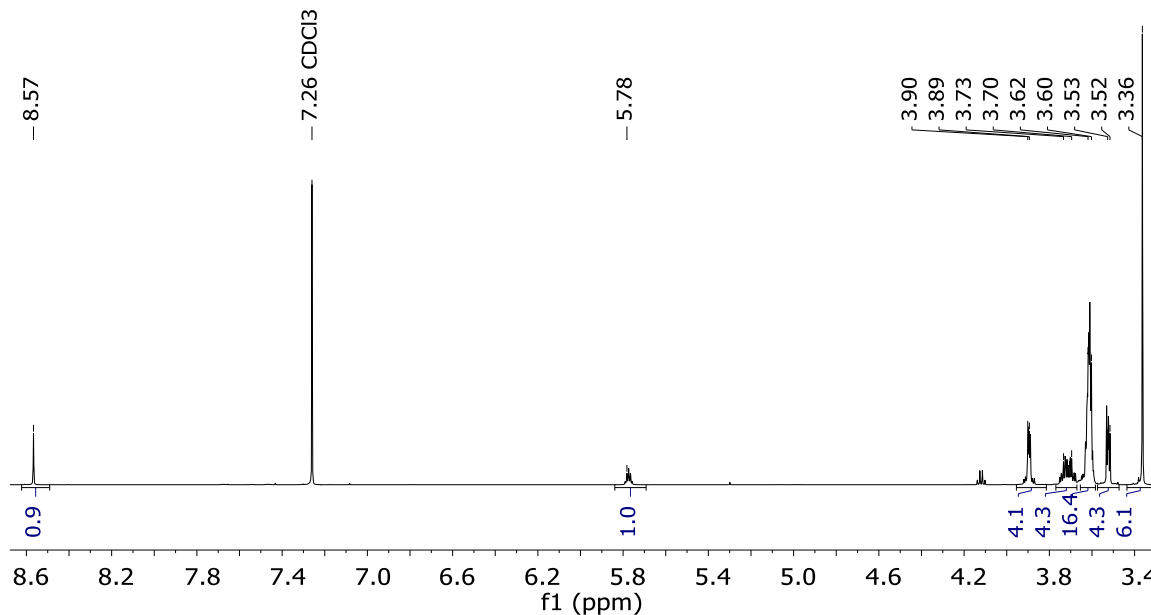
Figure 7.12 – ^{1}H NMR of monomer 18

7.4.4 Synthetic Complexity & Cost Analysis

To begin with, synthetic complexity (SC) is an arbitrary number which is depending on the scaling factors and inputs provided. Often, those who calculate synthetic complexity treat it like a weighted average with values between 0 – 100, where 100 is a very complex material to make. While the exact values might very between various groups, the core goal is to describes how difficult it is to produce a material on an industrial scale. For consistency, we have tried to closely match the most common terms which are found in literature. These can be summarized as below:

$$SC = \Sigma(\bar{\sigma}) + \Gamma(\bar{\gamma}) + \Delta(\bar{\delta}) + X(\bar{\chi}) + \Phi(\bar{\varphi})$$

Each of leading coefficients ($\Sigma, \Gamma, \Delta, X,$ and Φ) are weighting factors which are used to describe the importance of each variable. These numbers can be changed to reflect the specific design of a company's resources, to better reflect the true synthetic complexity for their production line. The only requirement is the coefficients sum to 100.

240

Each of the remaining variables stands for a specific value described herein. The bar atop the variable denotes the parameter has been normalized. For the normalization, we have set arbitrary values for the maximum number of each based on the values we typically see in literature. The normalization value is seen in parathesis next to each; for example, a synthetic route with 12 steps would have a $\bar{\sigma} = 12/25 = 0.48$

$\bar{\sigma}$: Number of synthetic steps (25)
$\bar{\gamma}$: Reaction yield factor (4)
$\bar{\delta}$: Number of purification operators (30)
$\bar{\chi}$: Number of column chromatography purifications (10)
$\bar{\varphi}$: Number of hazardous chemicals (100)

These parameters were chosen as can thoroughly reflect the complexity associated with making each of the target compounds. This equation can always be expanded to include additional parameters is one finds this set is lacking in a certain regard.

The number of synthetic steps ($\bar{\sigma}$) is one of the most important parameters as it inherently contains a ranking which includes labor costs, capital costs, utilities, and maintenance. As the number of steps increase, so do each of these values. Therefore, while we never explicitly address the cost of labor and maintenance, these factors are included in a relative aspect within this factor.

The reaction yield factor ($\bar{\gamma}$) is slightly abnormal to use when looking through literature. A more common factor is the reciprocal yield, which describes the overall yield to make the product; however, only the limiting reagents are taken into account for this value. Because each of these materials includes converging syntheses, the material in excess is ignored. The reaction yield factor takes into account all reactions. By comparing the cost of raw materials (assuming each step has quantitative (i.e., 100%) yield), along with the total

cost of raw materials (scaled to reflect appropriate yields); the reaction yield factor describes the effectiveness in converting the purchased materials to the final product.

The number of purification operators ($\bar{\delta}$) describes the workup steps required between synthetic steps. Each of these increase the labor costs, utilities, etc. A purification operator is described to be one of the following: (1) quenching/neutralization, (2) extraction, (3) column chromatography, (4) recrystallization, and (5) distillation/sublimation. While there are other methods of purification (such as precipitation, filtration, leaching, etc.), we have decided to include on these 5 techniques, as they are the most burdensome in the industrial environment, and often require specialized or additional equipment. In the lab (working at mg – g scale), these processes are very commonplace, but are very important to consider when scaling up. Of these, column chromatography is the most difficult to scale up, and is often avoided if possible, therefore, the number of column chromatography needed are included in a separate category ($\bar{\chi}$), which can be used to serve as an additionally weighting factor for the scalability of the target materials.

Finally, each of these reaction schemes include a large variety of hazardous chemicals. The number of hazardous chemicals used in the process have impact on safety and waste treatment/management, therefore, we have also identified the number of hazardous chemicals used, described by ($\bar{\varphi}$). To help identify hazardous materials used during the synthesis of materials, the Globally Harmonized System of Classification and Labelling of Chemicals (GHS) was used. While a more thorough investigation of hazardous materials (i.e. volume used) can provide more insight into these reactions, we believe that this slightly broader approach will suffice. Any chemicals with the following GHS Hazard Statements have been accounted for:

H200: Unstable explosive; H201: Explosive; mass explosion hazard; H202: Explosive; severe projection hazard; H203: Explosive; fire, blast or projection hazard; H204: Fire or projection hazard; H205: May mass explode in fire; H220: Extremely flammable gas; H222: Extremely flammable aerosol; H224: Extremely flammable liquid and vapour; H240: Heating may cause an explosion; H241: Heating may cause a fire or explosion; H250: Catches fire spontaneously if exposed to air; H271: May cause fire or explosion; strong oxidizer; H290: May be corrosive to metals; H300: Fatal if swallowed; H304: May be fatal if swallowed and enters airways; H310: Fatal in contact with skin; H314: Causes severe skin burns and eye damage; H318: Causes serious eye damage; H330: Fatal if inhaled; H340: May cause genetic defects; H341: Suspected of causing genetic defects; H350: May cause cancer; H351: Suspected of causing cancer; H360: May damage fertility or the unborn child; H361: Suspected of damaging fertility or the unborn child; H370: Causes damage to organs; H372: Causes damage to organs through prolonged or repeated exposure; H400: Very toxic to aquatic life; H410: Very toxic to aquatic life with long-lasting effects; H411: Toxic to aquatic life with long-lasting effects

With each of these terms defined, the following pages include the synthetic pathway for each target molecule and a cost analysis for the raw materials. This information is summarized afterwards in tables. Note, for the cost, it is for the material only. There is no inclusion of equipment, glassware, instrumentation, labor, land, utilities, transportation, etc.
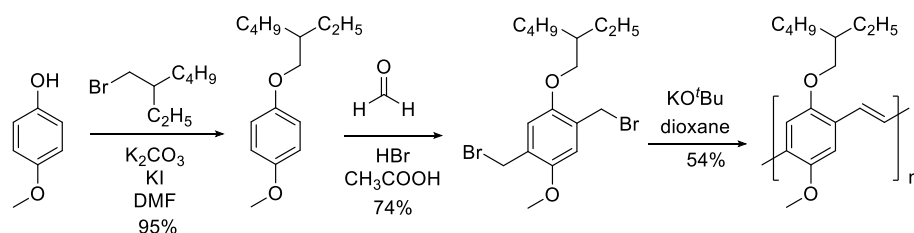
Scheme 7.6 – Synthetic Route for MEH-PPV

Table 7.3 – Cost Analysis of MEH-PPV

Name of Chemical	Hazards	mmol or volume (L)	Cost ($)
4-methoxyphenol	0	2.63	0.01
Dimethylformamide (DMF)	2	0.002 L	0.07
Potassium Carbonate	0	5.27	0.05
Potassium Iodide (KI)	1	0.20	0.00
2-ethylhexyl bromide	0	5.27	0.29
Hydrobromic Acid	2	0.001 L	0.69
Acetic Acid	1	0.001 L	0.03
Paraformaldehyde	3	12.51	0.02
1,4-dioxane (dry)	3	0.123 L	8.18
Potassium t-butoxide (tBuOK)	3	11.3	0.19

Table 7.4 – Summary and Synthetic Complexity for MEH-PPV

Number of Steps	Rxn Yield Factor	No. Work Ups	No. Columns	No. Haz Chem
3	1.915	7	0	15
Cost ($/mmol)	9.53	Cost ($/g)	34.51	Synthetic Complexity	14.9
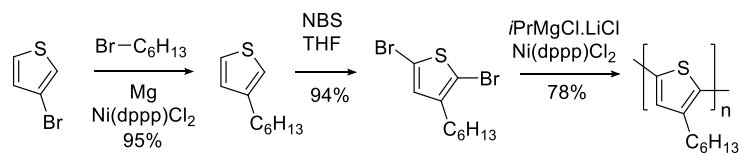
Scheme 7.7 – Synthetic Route for P3HT

Table 7.5 – Cost Analysis of P3HT

Name of Chemical	Hazards	mmol or volume (L)	Cost ($)
3-Bromothiophene	3	1.44	0.42
Diethylether	1	0.005 L	0.05
1-bromohexane	0	2.15	0.03
Magnesium (turnings)	1	2.87	0.06
[1,3-Bis(diphenylphosphino)propane]dichloronickel(II)	1	0.01	0.08
Tetrahydrofuran	1	0.005 L	0.06
N-Bromosuccinimide (NBS)	3	2.86	0.05
Tetrahydrofuran	1	0.006 L	0.07
Isopropylmagnesium chloride lithium chloride complex solution	2	1.28	0.23
[1,3-Bis(diphenylphosphino)propane]dichloronickel(II)	1	0.01	0.07

Table 7.6 – Summary and Synthetic Complexity for P3HT

Number of Steps	Rxn Yield Factor	No. Work Ups	No. Columns	No. Haz Chem
3	1.373	8	1	14
Cost ($/mmol)	1.12	Cost ($/g)	6.65	Synthetic Complexity	13.4
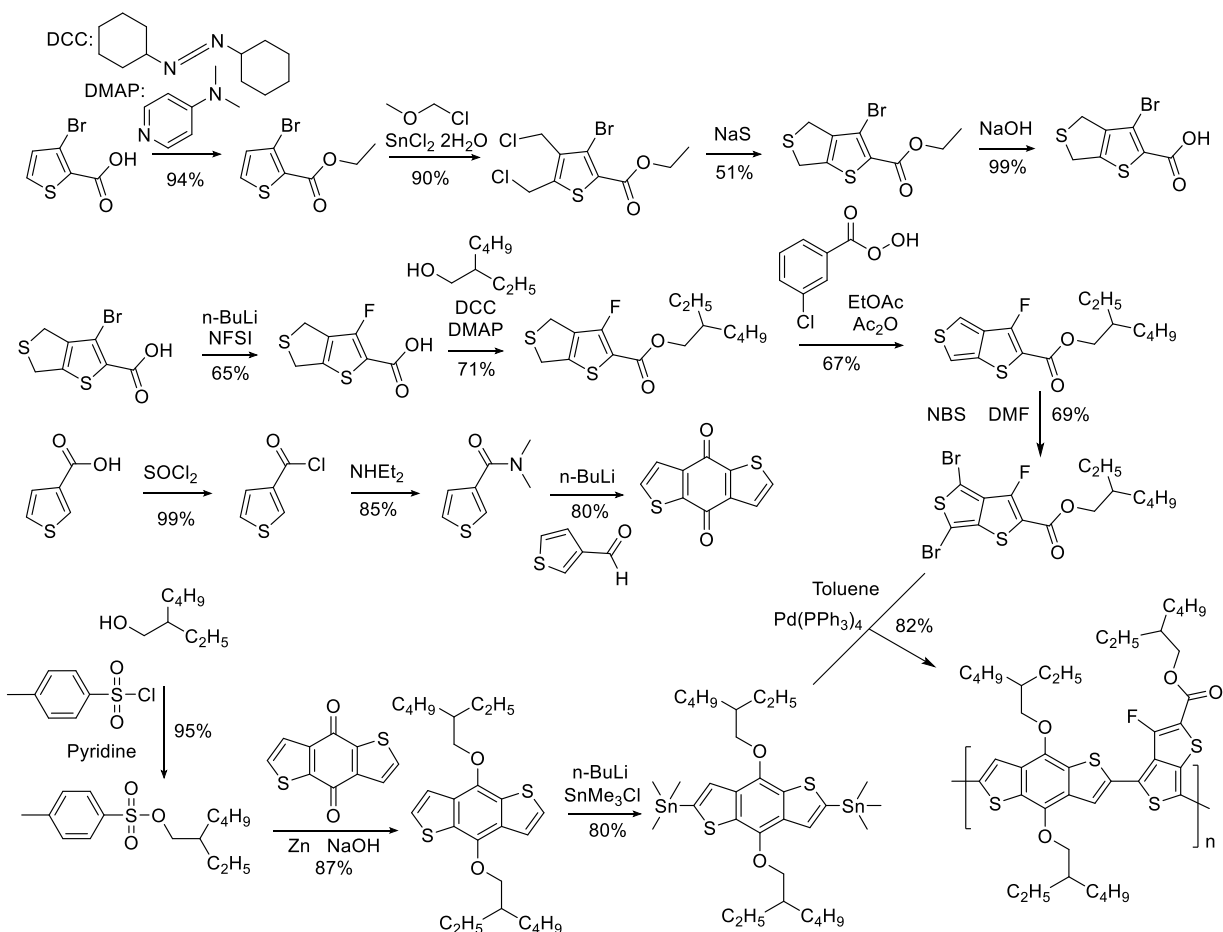
Scheme 7.8 – Synthetic Route for PTB7

Table 7.7 – Cost Analysis of PTB7

Name of Chemical	Hazards	mmol or volume (L)	Cost ($)
3-Thiophenecarboxylic acid	0	13.38	30.49
Methylene Chloride (DCM)	1	0.024 L	0.08
N,N′-Dicyclohexylcarbodiimide (DCC)	1	16.06	0.65
4-(dimethylamino)pyridine (DMAP)	4	4.42	0.09
Ethanol	0	36.13	0.01
Chloromethyl methyl ether (MOM-Cl)	2	98.87	34.31
Tin (II) chloride dihydrate	3	30.19	2.62
Methanol	1	0.057 L	0.13
Sodium Sulfide	3	11.32	9.51
Tetrahydrofuran	1	0.006 L	0.07
Sodium Hydroxide	2	0.003 L	0.00
Tetrahydrofuran	1	0.038 L	0.40
n-butyl lithium (2.5M)	4	12.58	0.47
NFSI (N-Fluorobenzenesulfonimide)	0	7.43	32.48
Methylene Chloride (DCM)	1	0.009 L	0.03
N,N′-Dicyclohexylcarbodiimide (DCC)	1	4.46	0.18
4-(dimethylamino)pyridine (DMAP)	4	1.23	0.03

2-ethyl-1-hexanol	0	37.15	0.13
Ethyl Acetate	0	0.053 L	0.18
Acetic Anhydride	1	0.026 L	0.30
meta-Chloroperoxybenzoic acid (mCPBA)	2	2.64	0.10
Dimethylformamide (DMF)	2	0.006 L	0.21
N-Bromosuccinimide (NBS)	3	4.45	0.08
3-Thiophenecarboxylic acid	0	2.60	5.93
Thionyl Chloride	1	46.85	0.13
Methylene Chloride	1	0.026 L	0.08
Diethylamine	1	5.15	0.01
Tetrahydrofuran	1	0.002 L	0.02
n-butyl lithium (2.5M)	4	4.38	0.16
Pyridine	1	0.006 L	0.00
p-Toluenesulfonyl chloride	2	6.64	0.08
2-ethyl-1-hexanol	0	5.53	0.02
Ethanol	0	0.002 L	0.01
Sodium Hydroxde	2	0.006 L	0.00
Zinc (dust)	2	3.89	0.01
Tetrahydrofuran	1	0.022 L	0.23
n-butyl lithium (2.5M)	4	3.81	0.14
Trimethyltin chloride (1M)	6	4.57	6.91
Dimethylformamide (DMF)	2	0.005 L	0.18
Tetrahydrofuran	1	0.019 L	0.20
Tetrakis(triphenylphosphine) Palladium	0	0.02	0.40

Table 7.8 – Summary and Synthetic Complexity for PTB7

Number of Steps	Rxn Yield Factor	No. Work Ups	No. Columns	No. Haz Chem
15	5.588	15	11	66
Cost ($/mmol)	127.01	Cost ($/g)	160.94	Synthetic Complexity	86.5
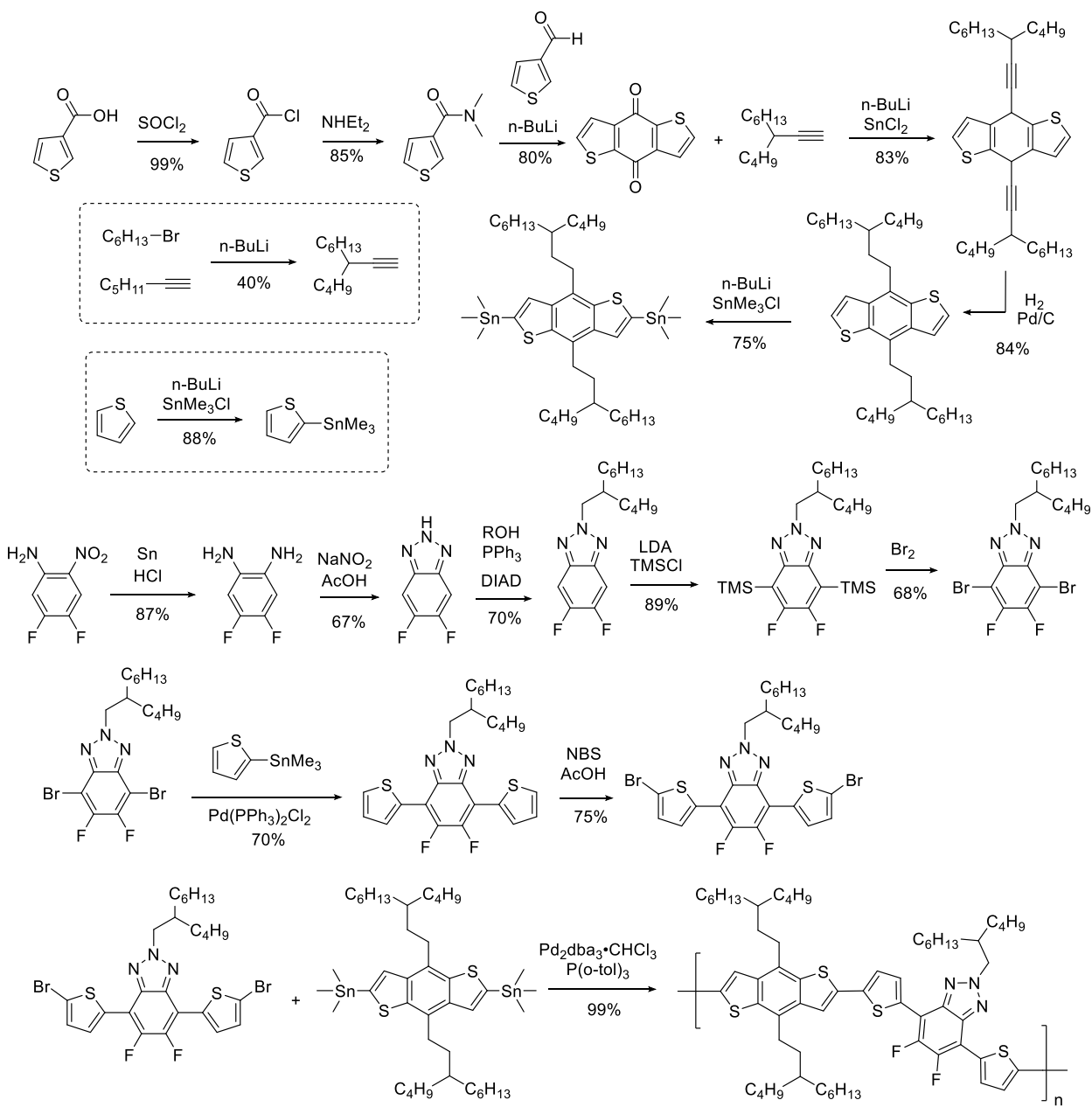
Scheme 7.9 – Synthetic Route for FTAZ

Table 7.9 – Cost Analysis of FTAZ

Name of Chemical	Hazards	mmol or volume (L)	Cost ($)
3-Thiophenecarboxylic acid	0	5.80	13.21
Thionyl Chloride	1	104.33	0.28
Methylene Chloride	1	0.057 L	0.18
Diethylamine	1	11.48	0.01
Tetrahydrofuran	1	0.049 L	0.51
n-butyl lithium (2.5M)	4	4.88	0.18
1-heptyne	1	12.19	3.95
Hexanes	1	0.012 L	0.03

n-butyl lithium (2.5M)	4	26.83	1.01
1-bromohexane	0	12.19	0.17
Tetrahydrofuran	1	0.010 L	0.10
n-butyl lithium (2.5M)	4	4.88	0.18
Tin (II) chloride dihydrate	3	9.76	0.85
Ethyl Acetate	0	0.016 L	0.05
Hydrogen Gas	2	80.97	0.01
10% Palladium on Carbon	0	0.81	1.14
Tetrahydrofuran	1	0.027 L	0.28
n-butyl lithium (2.5M)	4	5.44	0.20
Trimethyltin chloride (1M)	6	6.80	10.27
4,5-difluoro-2-nitroaniline	0	7.69	76.10
Hydrochloric Acid	2	0.031 L	0.86
Tin (powder)	0	58.44	2.00
Acetic Acid	1	0.027 L	0.63
Sodium Sulfide	3	7.12	5.98
Tetrahydrofuran	1	0.014 L	0.15
DIAD (diisopropyl azodicarboxylate)	2	5.45	0.99
Triphenylphosphine	2	5.45	0.13
2-butyl-1-octanol	2	5.45	1.06
Tetrahydrofuran	1	0.011 L	0.11
LDA (2M) (lithium diisopropylamide)	4	6.99	0.91
Trimethylsilyl chloride	2	7.42	2.98
Chloroform	3	0.014 L	0.11
Liquid Bromine	3	8.49	0.92
Thiophene	0	5.25	0.05
Tetrahydrofuran	1	0.010 L	0.11
n-butyl lithium (2.5M)	4	5.51	0.21
Trimethyltin chloride (1M)	6	5.77	8.72
Toluene	2	0.010 L	0.05
Pd(PPh3)2Cl2	0	0.02	0.26
Tetrahydrofuran	1	0.013 L	0.14
N-Bromosuccinimide (NBS)	3	2.83	0.05
o-xylene	1	0.006 L	0.26
Pd2dba3.CHCl3	1	0.02	2.02
P(o-tol)3	0	0.16	0.69

Table 7.10 – Summary and Synthetic Complexity for FTAZ

Number of Steps	Rxn Yield Factor	No. Work Ups	No. Columns	No. Haz Chem
16	3.850	32	9	80
Cost ($/mmol)	138.11	Cost ($/g)	132.71	Synthetic Complexity	77.7
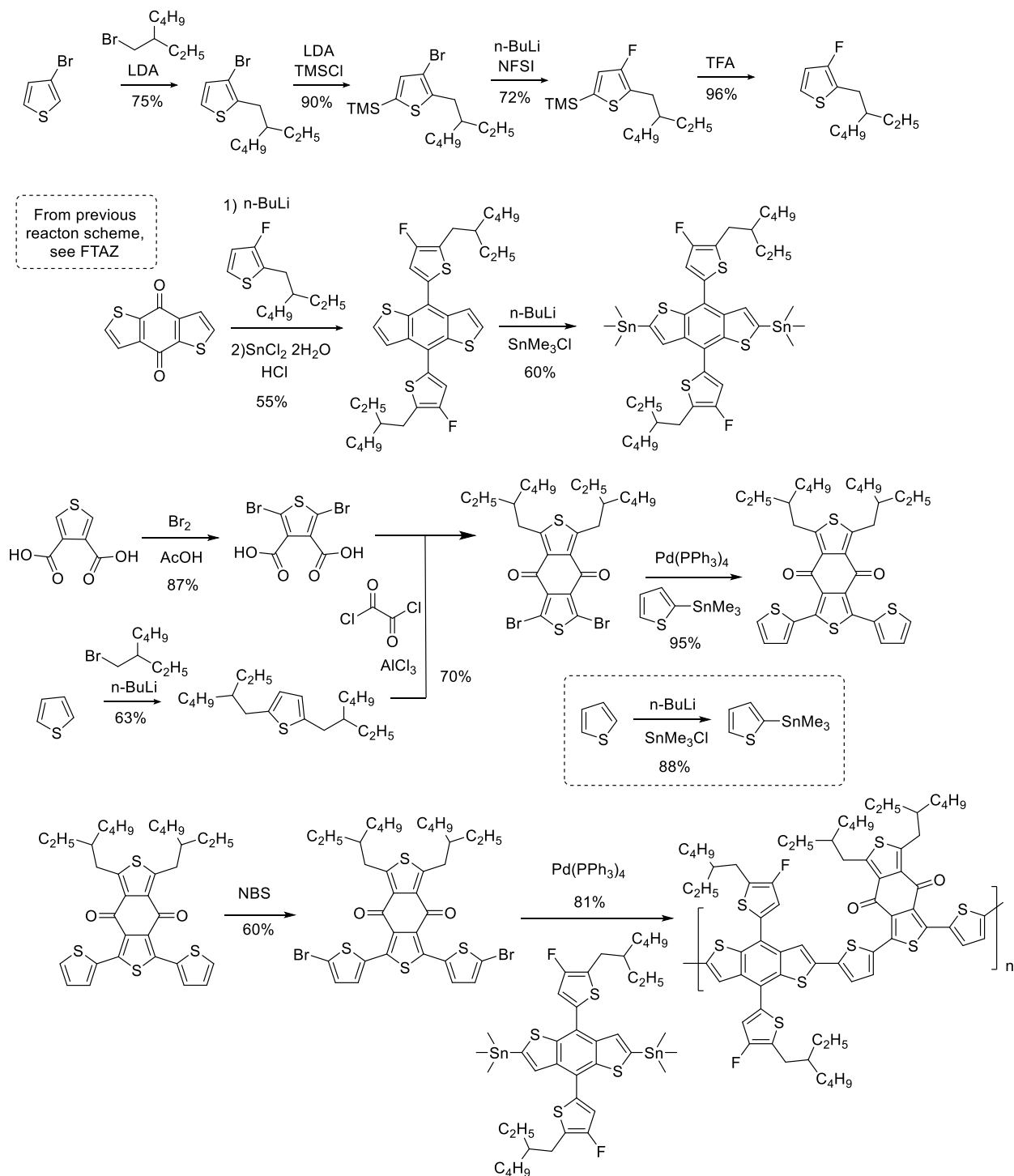
Scheme 7.10 – Synthetic Route for PM6

Table 7.11 – Cost Analysis of PM6

Name of Chemical	Hazards	mmol or volume (L)	Cost ($)
3-Thiophenecarboxylic acid	0	5.56	12.66
Thionyl Chloride	1	100.03	0.27

Methylene Chloride	1	0.060 L	0.17
Diethylamine	1	11.00	0.01
Tetrahydrofuran	1	0.094 L	0.98
n-butyl lithium (2.5M)	4	9.35	0.35
3-Bromothiophene	3	24.06	7.02
Tetrahydrofuran	1	0.024 L	0.25
LDA (2M) (lithium diisopropylamide)	4	28.87	3.77
2-ethylhexyl bromide	0	28.87	1.57
Tetrahydrofuran	1	0.036 L	0.38
LDA (2M) (lithium diisopropylamide)	4	21.65	2.83
Trimethylsilyl chloride	2	25.26	10.15
Tetrahydrofuran	1	0.032 L	0.34
n-butyl lithium (2.5M)	4	24.36	0.91
NFSI (N-Fluorobenzenesulfonimide)	0	29.23	127.74
Methylene Chloride (DCM)	1	0.029	0.09
TBAF (tetra-n-butylammonium fluoride)	1	14.03	4.61
Tetrahydrofuran	1	0.050 L	0.52
n-butyl lithium (2.5M)	4	11.22	0.42
Tin (II) chloride dihydrate	3	24.84	2.15
Tetrahydrofuran	1	0.041 L	0.43
n-butyl lithium (2.5M)	4	4.63	0.17
Trimethyltin chloride (1M)	6	5.14	7.77
3,4-thiophenedicarboxylic acid	0	3.56	19.23
Acetic Acid	1	0.006 L	0.14
Liquid Bromine	3	21.34	2.31
Thiophene	0	4.91	0.05
Tetrahydrofuran	1	0.049 L	0.51
n-butyl lithium (2.5M)	4	14.73	0.55
2-ethylhexyl bromide	0	12.28	0.67
Methylene Chloride (DCM)	1	0.004 L	0.01
1,2-Dichloroethane	1	0.006 L	0.36
Dimethylformamide (DMF)	2	0.03	0.00
Oxalyl Chloride	2	23.98	0.46
Aluminium Chloride (AlCl3)	1	12.38	0.13
Thiophene	0	7.38	0.07
Tetrahydrofuran	1	0.010 L	0.15
n-butyl lithium (2.5M)	4	7.75	0.29
Trimethyltin chloride (1M)	6	8.12	12.26
Toluene	2	0.014 L	0.07
Tetrakis(triphenylphosphine) Palladium	0	0.03	0.45
Dimethylformamide (DMF)	2	0.016 L	0.57
N-Bromosuccinimide (NBS)	3	4.12	0.07
Toluene	2	0.025 L	0.12
Tetrakis(triphenylphosphine) Palladium	0	0.06	1.00

Table 7.12 – Summary and Synthetic Complexity for PM6

Number of Steps	Rxn Yield Factor	No. Work Ups	No. Columns	No. Haz Chem
16	4.324	26	9	85
Cost ($/mmol)	225.07	Cost ($/g)	184.20	Synthetic Complexity	78.2
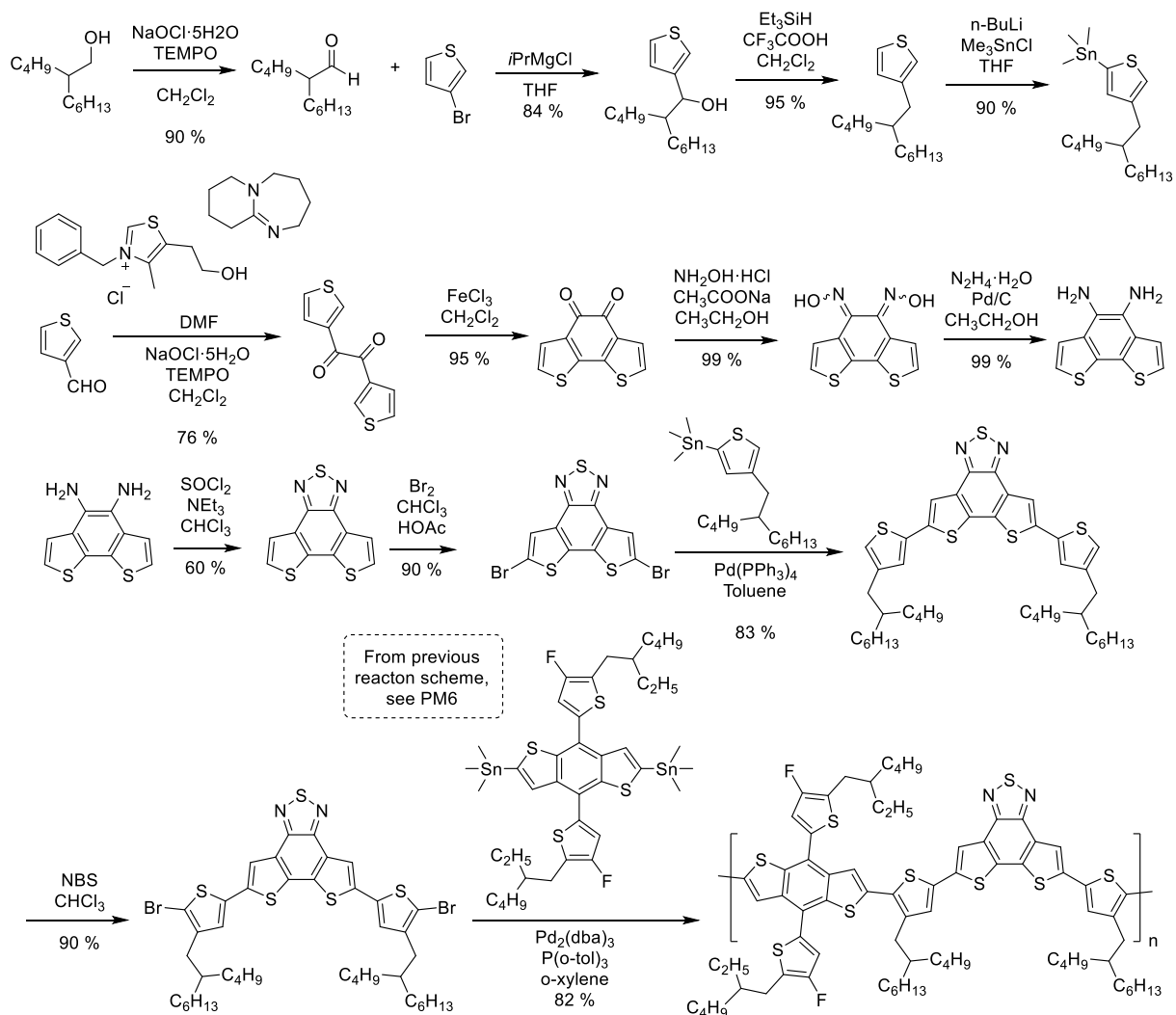
Scheme 7.11 – Synthetic Route for D18

Table 7.13 – Cost Analysis of D18

Name of Chemical	Hazards	mmol or volume (L)	Cost ($)
2-butyl-1-octanol	2	5.00	0.97
Methylene Chloride (DCM)	1	0.010 L	0.03
Sodium Hypochlorite Pentahydrate	6	10.00	0.19
TEMPO (2,2,6,6-Tetramethyl-1-piperidinyloxy)	2	0.25	0.25
3-Bromothiophene	3	5.00	1.46

Tetrahydrofuran	1	0.050 L	0.52
Isopropylmagnesium chloride solution	2	5.00	0.31
Tetrahydrofuran	1	0.025 L	0.26
Methylene Chloride (DCM)	1	0.004 L	0.01
Triethylsilane	0	25.20	0.00
Triflouroacetic Acid	2	16.80	0.00
Tetrahydrofuran	1	0.040 L	0.42
n-butyl lithium (2.5M)	4	4.79	0.18
Trimethyltin chloride (1M)	6	5.19	7.83
3-Thiophenecarboxaldehyde	0	8.54	15.62
Dimethylformamide (DMF)	2	0.017 L	0.62
Methylene Chloride (DCM)	1	0.017 L	0.05
3-Benzyl-5-(2-hydroxyethyl)-4-methylthiazolium chloride	0	0.21	0.22
1,8-Diazabicyclo[5.4.0]undec-7-ene (DBU)	4	0.43	0.02
Sodium Hypochlorite Pentahydrate	6	4.27	0.08
TEMPO (2,2,6,6-Tetramethyl-1-piperidinyloxy)	2	0.21	0.22
Methylene Chloride (DCM)	1	0.065 L	0.20
Iron (III) Chloride (FeCl3)	4	9.74	0.07
Ethanol	0	0.012 L	0.06
Hydroxylamine Hydrochloride	3	18.51	0.51
Sodium Acetate	0	18.51	0.17
Ethanol	0	0.012 L	0.06
Hydrazine monohydrate	11	61.08	0.64
10% Palladium on Carbon	0	0.15	0.22
Chloroform	3	0.015 L	0.12
Thionyl Chloride	1	9.07	0.02
Triethylamine	1	30.23	0.23
Chloroform	3	0.009 L	0.07
Acetic Acid	1	0.006 L	0.14
Liquid Bromine	3	5.44	0.59
Toluene	2	0.016 L	0.08
Tetrakis(triphenylphosphine) Palladium	0	3.59	0.00
Chloroform	3	0.007 L	0.05
N-Bromosuccinimide (NBS)	3	2.64	0.05
3-Thiophenecarboxylic acid	0	10.98	25.02
Thionyl Chloride	1	197.62	0.54
Methylene Chloride	1	0.109 L	0.34
Diethylamine	1	21.74	0.03
Tetrahydrofuran	1	0.092 L	0.96
n-butyl lithium (2.5M)	4	9.24	0.35
3-Bromothiophene	3	23.76	6.93
Tetrahydrofuran	1	0.040 L	0.41
LDA (2M) (lithium diisopropylamide)	4	28.51	3.72
2-ethylhexyl bromide	0	33.51	1.81
Tetrahydrofuran	1	0.036 L	0.37
LDA (2M) (lithium diisopropylamide)	4	21.39	2.79
Trimethylsilyl chloride	2	24.95	10.03
Tetrahydrofuran	1	0.032 L	0.33

n-butyl lithium (2.5M)	4	24.06	0.90
NFSI (N-Fluorobenzenesulfonimide)	0	28.87	126.18
Tetrahydrofuran	1	0.029 L	0.30
TBAF (tetra-n-butylammonium fluoride)	1	13.86	4.55
Tetrahydrofuran	1	0.037 L	0.39
n-butyl lithium (2.5M)	4	14.78	0.56
Tin (II) chloride dihydrate	3	31.41	272
Hydrochloric Acid	2	3.70	0.01
Tetrahydrofuran	1	0.020 L	0.21
n-butyl lithium (2.5M)	4	5.08	0.19
Trimethyltin chloride (1M)	6	6.10	9.21
o-xylene	1	0.015 L	0.62
Pd2dba3.CHCl3	1	0.04	3.66
P(o-tol)3	0	0.37	1.56

Table 7.14 – Summary and Synthetic Complexity for D18

Number of Steps	Rxn Yield Factor	No. Work Ups	No. Columns	No. Haz Chem
22	5.071	26	12	138

Cost ($/mmol)	238.39	Cost ($/g)	179.76	Synthetic Complexity	101.0
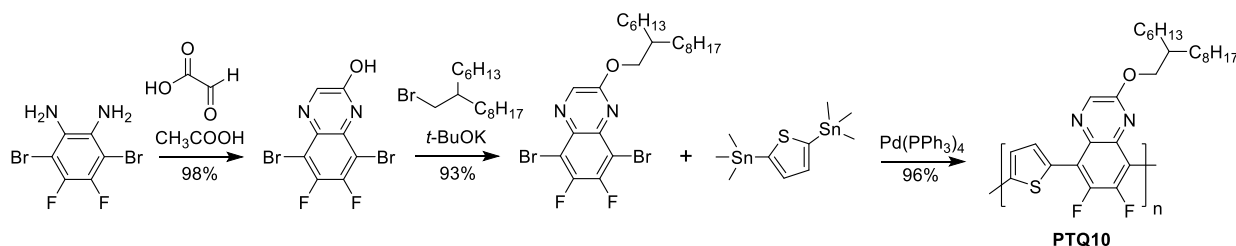
Scheme 7.12 – Synthetic Route for PTQ10 (original)

Table 7.15 – Cost Analysis of PTQ10 (original)

Name of Chemical	Hazards	mmol or volume (L)	Cost ($)
3,6-Dibromo-4,5-difluorobenzene-1,2-diamine	0	1.14	76.03
Acetic Acid (glacial)	1	0.011 L	0.27
Methanol	1	0.011 L	0.03
Glyoxylic acid	1	1.14	0.07
Potassium t-butoxide (tBuOK)	3	1.37	0.02
7-(Bromomethyl)pentadecane	0	1.14	0.31
Toluene	2	0.052 L	0.26
2,5-Bis(trimethylstannyl)thiophene	2	1.04	19.38
Tetrakis(triphenylphosphine) Palladium	0	0.04	0.59

Table 7.16 – Summary and Synthetic Complexity for PTQ10 (original)

Number of Steps	Rxn Yield Factor	No. Work Ups	No. Columns	No. Haz Chem
3	1.122	5	1	10
Cost ($/mmol)	96.96	Cost ($/g)	214.18	Synthetic Complexity	10.0
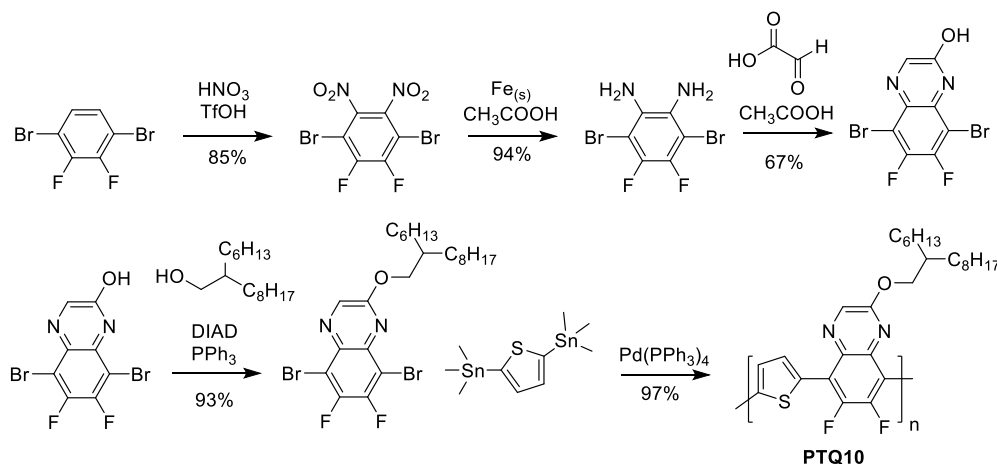
Scheme 7.13 – Synthetic Route for PTQ10 (new)

Table 7.17 – Cost Analysis of PTQ10 (new)

Name of Chemical	Hazards	mmol or volume (L)	Cost ($)
1,4-Dibromo-2,3-difluorobenzene	0	2.07	2.58
(Fuming) Nitric Acid	3	2.07	0.03
Trifluoromethanesulfonic Acid (Triflic Acid)	2	70.40	3.68
Acetic Acid	1	0.020 L	0.41
Iron (powder)	0	24.64	0.13
Sodium Hydroxide	2	98.57	0.09
Acetic Acid	1	0.010 L	0.19
Ethanol	0	0.003 L	0.01
Glyoxylic acid	1	1.74	0.11
Tetrahydrofuran	1	0.020 L	0.23
DIAD (diisopropyl azodicarboxylate)	2	1.66	0.30
Triphenylphosphine	2	1.22	0.03
2-hexyl-1-decanol	0	1.18	0.00
Thiophene	0	1.27	0.01
Tetrahydrofuran	1	0.004 L	0.03
n-butyl lithium (2.5M)	4	2.60	0.10
Trimethyltin chloride (1M)	6	2.66	4.01
Toluene	2	0.010 L	0.03
P(o-tol)3	0	0.16	0.70
Pd2dba3.CHCl3	1	0.02	2.06

Table 7.18 – Summary and Synthetic Complexity for PTQ10 (new)

Number of Steps	Rxn Yield Factor	No. Work Ups	No. Columns	No. Haz Chem
6	1.460	8	1	29
Cost ($/mmol)	14.74	Cost ($/g)	30.29	Synthetic Complexity	25.9

7.4.5 Process Mass Intensity Calculations

When considering sustainability and green chemistry, a core principle is to optimize resource use. In a chemical reaction, there are a variety of materials which include the reactants, reagents, solvents, catalysts, ligands, etc. which are used for the reaction as well as the separation and purification. For reactions with poor atom economy, there is wasted mass which contributes to loss and makes the chemistry pathway less sustainable. To provide a numerical value, the process mass intensity (PMI) can be used. PMI is a measure of the total mass of the materials used per the mass of the product. In an ideal reaction, there is no waste and the mass of the inputs is equal to the mass of the outputs, resulting in a PMI = 1. As the value of PMI decreases, more waste is generated and the reaction pathway is less sustainable.

$$PMI = \frac{total\ mass\ in\ a\ process\ (kg)}{mass\ of\ product\ (kg)}$$

To provide an example of this, the two pathways (original and our new one) for PTQ10 are investigated and corresponding PMI values are reported for each. In the original PTQ10 pathway, there are a few reaction steps and high yields, which result in a PMI of 0.25. In the case of our new PTQ10 synthetic pathway, we added additional reactions to decrease the cost, but this will increase the amount of waste generated. Furthermore, the Mitsunobu reaction has poor atom economy and decreases the PMI value. In summary, the PMI for the new PTQ10 pathway is 0.05. Note, the decrease in PMI scales with the increase

in SC demonstrated above. So while the new reaction pathway does have a significant reduction in cost, there is an increase in the complexity and waste generated.

CONCLUSION

With mounting pressure to curb greenhouse gas emissions, the drive towards clean and renewable energy continues to grow every day. In order to solve such a complex and multifaceted problem of climate change, a variety of synergetic approaches will need to be employed. While silicon solar panels offer some important benefits, organic solar cells have emerged as a complementary photovoltaic technology which can specifically address some of the shortcomings. However, in order for a polymer based solar cell to be commercially viable, they should be low cost, scalable, solution processable, high efficiency, and stable for the lifetime of the device. Throughout this dissertation, we have discussed notable contributions to the first few categories, but stability has not been effectively investigated. This highlights an important area of research which needs to be explored in order to realize this type of technology. In this section, I will offer a short summary of each chapter and then set the stage for future work in stability that should be done in the field.

Chapter Summaries: Key Takeaways

In Chapter 1, important structural modifications to fused-ring electron acceptors were summarized. Structure-property relationships were established for modifications to the donor core, the solubilizing side chains, and the acceptor end groups of FREAs. Extending the length of the donor core (either through benzene or thiophene units) was able to improve the packing, increase the electron mobility and raise the LUMO energy level – a combination which increased the solar cell efficiency. One drawback to a larger core in the decrease in solubility, so additional solubilizing side chains need to be added to the acceptor. Another

common approach is to add electron withdrawing groups to the end group of the acceptor. This approach is governed by the "Goldilocks Principle;" the electron withdrawing groups cause a red-shift in absorption and thus boost the J_{SC} of the device but also lowers the LUMO level and thus decreases the V_{OC}. Therefore, substituents need to be added with care in order to find the right balance and optimized efficiency.

Continuing with the fundamental understand of FREAs, Chapter 2 explored the impact of end group planarity. To explore this as a design rationale for electron acceptors, we synthesized a new fused-ring electron acceptor, IDTCF, which has methyl substituents out of plane to the conjugated acceptor backbone. These methyl groups hinder packing and expand the π–π stacking distance by ∼1 Å, but had little impact on the optical or electrochemical properties of the individual FREA molecule. The extra steric hindrance from the out of plane methyl substituents restricted packing and resulted in large amounts of geminate recombination, thus degrading the device performance. Our results showed that intermolecular interactions (especially π–π stacking between end groups) play a crucial role in performance of FREAs. We demonstrated that the planarity of the acceptor unit is of paramount importance as even minor deviations in end group distance are enough to disrupt crystallinity and cripple device performance.

Then transitioning over to the polymer electron donor, Chapter 3 provided insight on the polymerization of conjugated polymers. Through the Carothers equation, the molecular weight of the resulting conjugated polymer can be finely tuned, and this can have an important impact on a variety of properties. For the FTAZ polymer, once the entanglement molecular weight (~30 kg/mol) is reaches, the photovoltaic properties are generally constant. At lower molecular weights, the polymer has large and excessively pure domains, which

results in poor exciton splitting and a decrease in the J_{SC} and FF. Beyond the entanglement molecular weight, the morphology and performance stays relatively the same. When blended with a fullerene acceptor (PCBM), polymer acceptor (N2200) and small molecule acceptor (ITIC), the same general trend is seen for all systems. Additionally, the mechanical properties of the all-polymer blend of FTAZ:N2200 were investigated. At higher molecular weights, mechanically robust blends were demonstrated.

Moving on towards ways to modify the conjugated polymer, of the many different locations for functionalization on the polymer backbone, one of the least studied is the conjugated linker which connects the donor and acceptor moieties. Therefore, in Chapter 4, we synthesized and compared two conjugated polymers, HTAZ and dFT-HTAZ, which have different thiophene linkers. Compared to HTAZ, the incorporation of the dFT units maintained the optical properties while lowering the energy levels by ∼0.4 eV, which allowed for a much improved V_{OC} value of ∼1 V. Importantly, when compared with the appropriate non-fullerene acceptor, dFT-HTAZ:ITIC-Th1 blends reached an efficiency of ∼10%, which is nearly 3× that of the nonfluorinated HTAZ. As most OSC polymers have thiophene linkers, using dFT units could serve as a proficient method to increase OSC performance in many polymer systems, especially those that do not have locations for functionalization on the acceptor moiety.

In Chapter 5, we systematically explored the impact of cyano substitution on conjugated polymers by varying the amount of cyano groups, from zero to two per repeat unit, on the benzotriazole acceptor moiety of our polymers. We found that cyano substitution effectively decreases the energy levels of the polymer, leading to high V_{OC} values; however, the impact of additional cyano groups offer diminishing returns. Moreover, cyano

substitution also decreases the band gap of the polymers, inducing a shift of polymer absorption to longer wavelength. The single cyano substituent polymer, monoCNTAZ, afforded high V_{OC}, J_{SC}, and *FF* due to deep energy level, red-shifted absorption, and efficient charge transport properties, respectively. However, further additions of cyano groups degrade the performance. Overall, this work highlights the benefits and limitations of cyano functionalization on conjugated polymers for OSCs.

Next in Chapter 6, we systematically explored the impact of a variety of functional groups, including nitrogen heteroatoms, fluorine substituents, and cyano groups, on TAZ-based acceptor moieties that are incorporated into the conjugated polymers. The PyTAZ polymer suffered from low mobility and poor exciton harvesting, driven by large and excessively pure domains when blended with PCBM. The inclusion of fluorine substituents, placed strategically along the polymer backbone, can mitigate these issues, as shown with 4FT–PyTAZ. However, when this same approach is used for the cyano-functionalized polymer (CNTAZ), the resulting polymer (4FT–CNTAZ) is overfunctionalized and suffered from impure domains and recombination issues. The cyano group had a larger impact on the TAZ core compared to the nitrogen heteroatom due to the strong electron-withdrawing strength of the cyano group. Because of this, further functionalization of the cyano-based polymers had less fruitful impact on the polymer properties and resulted in deterioration of the solar cell efficiency. Overall, this work highlighted some of the benefits, thresholds, and limitations for functionalization of conjugated polymers for organic solar cells.

Finally, the synthetic complexity of OSC materials has drastically increased over the years, which makes the scalability of the highest-efficiency materials difficult. In Chapter 7, a new synthetic approach was designed towards PTQ10. The new synthetic approach to make

PTQ10 brought a significant 86% reduction in cost and could also easily accommodate different side chains to move towards green processing solvents. Furthermore, high-efficiency organic solar cells were demonstrated with a PTQ10:Y6 blend exhibiting approximately 15 % efficiency. We hope that this work helps to inspire others to consider the end goal of a scalable organic solar cell when designing their new chemistry.

<u>What makes an Organic Solar Cell Unstable: Degradation Pathways?</u>

While impressive device results have been shown throughout this dissertation and literature, for a practical application of OSCs, the device efficiency needs to be stable for a long lifetime of the device. Understanding the stressors which can cause performance degradation is the first step to preventing that loss. In real world applications of OSCs, there are a variety of everyday factors which can limit the long term stability of a cell, include mechanical stress, heat, oxygen, water, and light. This section is not designed to serve as an exhaustive list of all degradation pathways, rather, highlight the common shortcomings in blends under these various factors. Further details can be found in various articles and reviews.[307,356–362]

One of the major advantages of OSCs compared to other photovoltaic technologies is the ability to create flexible solar cells, and flexible OSCs have to withstand a variety of mechanical stresses which have various modes of failure. These include cracking, elastic strain, cohesive fracture, and debonding/decohesion. Approaches to increase the mechanical stability include increasing polymer flexibility and promote entanglements, increasing layer/layer adhesion, and decreasing crystalline components.[220,363–365] Using both a polymer donor and acceptor can help realize many of these (as we briefly discussed in Chapter 3). One struggle with mechanical properties is an apparent trend where rigid polymers have

higher stability and flexible materials have low stability.[366] This apparent tradeoff (great mechanical properties or long term stability) is an area which needs further investigation.

Continuous irradiation can cause the working temperatures of solar cells to be higher than normal ambient conditions (some over 150 °F), but these elevated temperatures are normally far below the degradation temperature of most OSC materials (many conjugated polymers have a $T_d > 300$ °C).[367–369] While this temperature change is not enough to degrade the material, it can have drastic effect on the morphology. Thermal stress can induce fullerene aggregation, small molecule crystallization, and phase separation.[370–372] A method to minimize these effects is to lock in the morphology by using a polymer that has a higher glass transition temperature (T_g) than working temperatures. This design strategy is difficult because the long alkyl side chains used for solubility lower the ductile to glass transition temperature to below room temperature for most materials. Other strategies include cross-linking, decreasing crystallinity, and removing side chains through annealing.[220,373–379] A changing morphology is one of the biggest issues facing many OSCs, because the bulk heterojunction is not the thermodynamically stable state for the active layer blend.

One of the most abundant factors which threaten OSCs is oxygen, which can cause degradation of performance through multiple pathways. First, many of the metal electrodes used have low work functions and can easily be oxidized, forming an insulating metal oxide layer. This insulting barrier will hinder transport and induce an S-shaped *J-V* curve.[380] Furthermore, in the presence of light and oxygen, both donor and acceptor materials can undergo photooxidation. This chemical reaction will change the chemical structure of the material and ruin absorption and charge transport properties.[381–384] Common methods to

minimize oxygen permeability is through encapsulation of the OSC, and further reports and reviews on this approach are available here.[385–389]

Similar to oxygen, water can cause major issues for OSCs. Just like oxygen, water is a strong enough oxidizing agent to react with low work function metal electrodes, forming an insulating barriers.[390,391] Furthermore, these defects can create pinholes allowing further addition of oxygen and water and accelerate the degradation process.[392,393] A common hole transport layer in OSCs is PEDOT:PSS which is hygroscopic and the addition of water to the solar cell can ruin extraction of charges.[394,395] Similar to stopping oxygen, appropriate encapsulation can minimize these issues.

Finally, while solar cells are designed to absorb light, even light itself (especially UV light) can degrade performance and ruin stability. As mentioned previously, in the presence of both light and oxygen, there are a variety of photooxidation chemistries that can degrade the active layer materials. In the next section, the vulnerability of vinylene bonds in PPV-based polymers while be discussed, but there are many reports that also highlight photooxidation of a variety of other structures.[396–402] The resulting materials after photooxidation have reduced visible light absorption and can serve as trap states reducing transport.[403,404] Even in the absence of oxygen, light can still be a major issue. Strong UV light can cause photobleaching, and under constant illumination, if the charge carrier transport is unbalanced, photoinduced charge accumulation can decrease V_{OC}.[405–407]

<u>What has already been Explored by the Community: History of Stability?</u>

One aspect of organic solar cell performance, long-term stability, is often ignored because of the time and efforts needed to undergo a proper exploration. The issue of stability is not new however, back in the late 1990s, Klavs Jensen and Niyazi Sarıçiftçi both reported

on the photooxidation of PPV (structure in Appendix) when exposed to light and oxygen.[404,408] Then in the early 2000s, Christoph Brabec, under the guidance of Sarıçiftçi, began to look at the degradation kinetics by accelerating lifetime measurements through temperature control.[409,410] This would eventually lead Sarıçiftçi to publish on the encapsulation techniques with low oxygen permeation rates.[411] While the number of reports focused on studying the stability was low, these aforementioned papers served as milestones in the understanding of common degradation methods for conjugated polymers.

One of the primary pathways for degradation was the oxidation at the vinylene unit of PPV; however, the field began to rapidly switch directions with the discovery of poly(3-hexylthiophene) (P3HT), which lacks the same vulnerable vinylene unit which commonly are the locations of oxidation. This lack of vinylene unit does not translate to a perfectly stable system however. In many ways, Frederik Krebs led the field in terms of scalability and stability of P3HT:PCBM blends, in part with his formation of startup companies like infinityPV. In 2007, Krebs reported the first 10,000 hour lifetime study,[412] and then in 2009, Krebs led a round robin study which looked at performance of large-area printed OSCs in eighteen labs across the world.[413] These types of experiments are less common in a small or single PI research lab, because these studies are focused on understanding the limitations of a commercializable product. With the rapidly growing excitement for OSCs and more startup companies being formed, Krebs also led the formation of the first standardized testing protocol for stability and operational lifetime of OSCs in 2011.[414] Unfortunately, many of these early startup companies would eventually file for bankruptcy, driven from the inherent instabilities present in the PCBM blends, especially with vertical phase separation (i.e. unstable morphology).[415–417] Unlike the previous PPV system, where the breakdown

mechanism was through photooxidation, these new P3HT:PCBM blends are plagued with an unstable morphology. This is an important note, as methods to minimize degradation in one system (i.e. encapsulation) might be rendered useless in a different system (i.e. poor morphology).
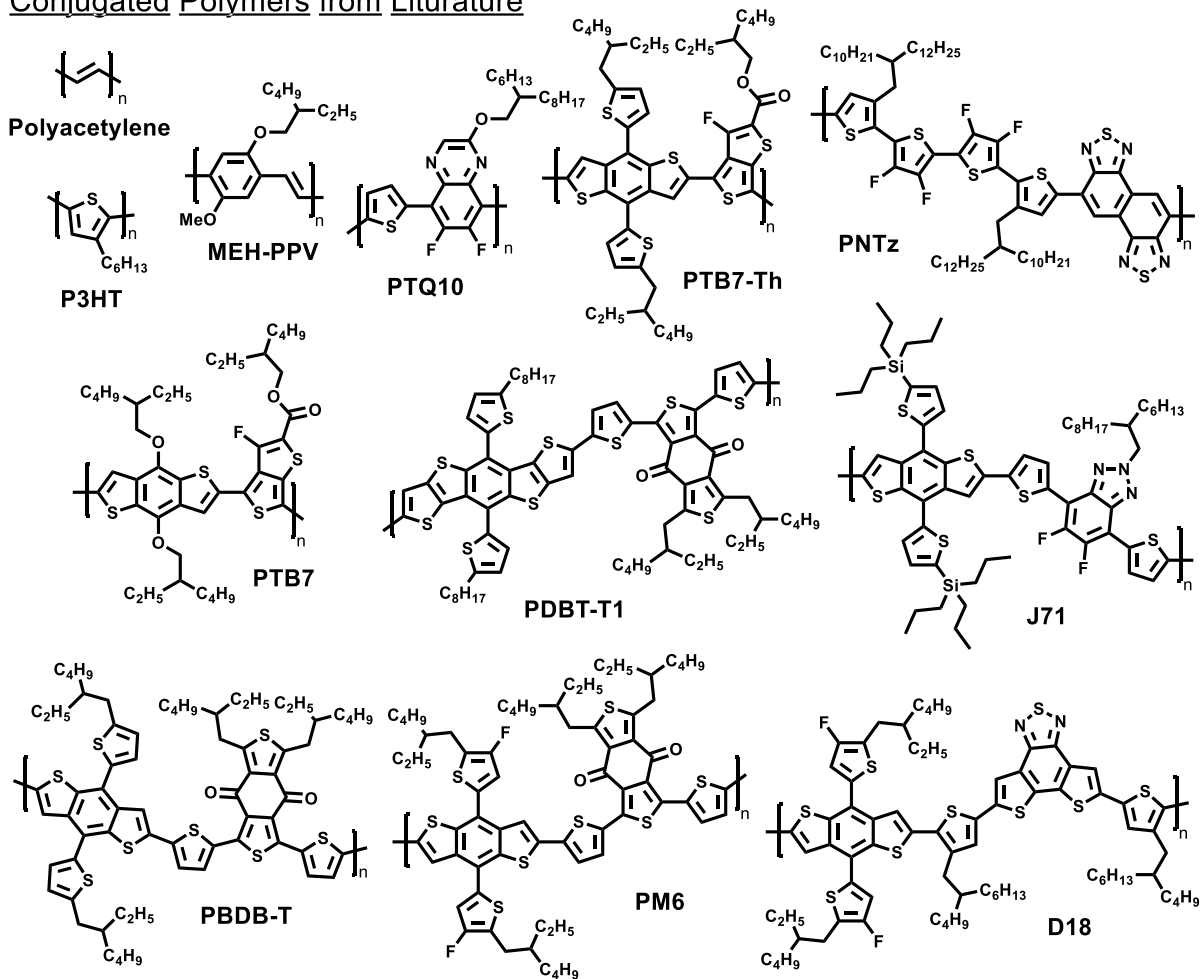
While progress was moving in the right direction for P3HT:PCBM blends, new donor polymers based on more complex donor:acceptor (D:A) copolymer approach were introduced and achieved higher efficiencies (such as those we outlined in Chapters 3-7). Furthermore, when Xiaowei Zhan published the ITIC acceptor in 2015,[38] the field was rapidly turned into a non-fullerene "gold rush" (as highlighted in Chapters 1-2). The past five years has been saturated reports of new fused ring electron acceptors (FREAs) achieving higher and higher efficiency, and this left stability on the backburner once again. More recently, there has been some projects which look at stability from a more fundamental perspective: Harald Ade and others have published multiple articles looking at the morphological stability through a polymer physics lens.[273,305,418–421] As previously mentioned, one major degradation pathway for bulk heterojunctions is the phase separation on the donor and acceptor material, which can be described through the bimodal/miscibility gap which is parameterized by the Flory-Huggins interaction parameter χ.[273,418–424] They have demonstrated correlations between factors such as the χ parameter, phase separation, fill factor, and performance.

As highlighted above, some of the initial groundwork on understanding stability has already been completed; however, researchers need to begin to think about stability as a core design principle when designing new materials. There are a variety of methods to minimize external stressors (i.e., light via a photon blocking layer or water/oxygen via encapsulation),

but intrinsic stability (i.e., stable morphology) is lagging behind. The OSC field has grown tremendously over the last 25 years, and impressive efficiencies nearing 20% are coming out all the time. If these same efficiencies can be demonstrated with a low cost polymer with high stability – then OSCs can move from a laboratory idea to a life-changing product.

APPENDIX: CHEMICAL STRUCTURES FOR MENTIONED MATERIALS

Conjugated Polymers from Liturature

Polyacetylene

P3HT

MEH-PPV

PTQ10

PTB7-Th

PNTz

PTB7

PDBT-T1

J71

PBDB-T

PM6

D18

Commonly Referenced Building Blocks

INCN

TCF

TAZ

BnDT

3FT

4FT

dFT

2TF

IDT

IDTT

Electron Acceptors

C60

PCBM

N2200

ITIC

IDIC

IHIC

F7IC (IT-4F)

F5IC

F9IC

4TIC

F11IC

CO,8DFIC

CO,6IC

F8IC

ITIC-2D

268

IDNC

CO_i6FIC

CO_i6DFIC

INIC

INIC4

F9IC

FINIC

IDTCF

ITTCF

EH-IDTBR

O-IDTBR

SIDIC

DIDIC

TIDIC

IDCIC

R = C₆H₁₃

ITIC-Th

ITIC-Th1

ITIC-Th2

ITIC-Th3

IT-M

Interlayers

PEDOT:PSS

PFN

270
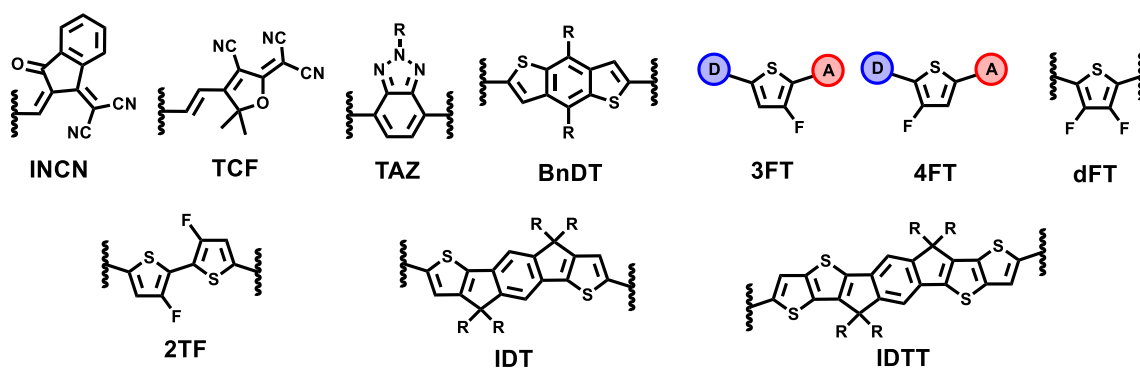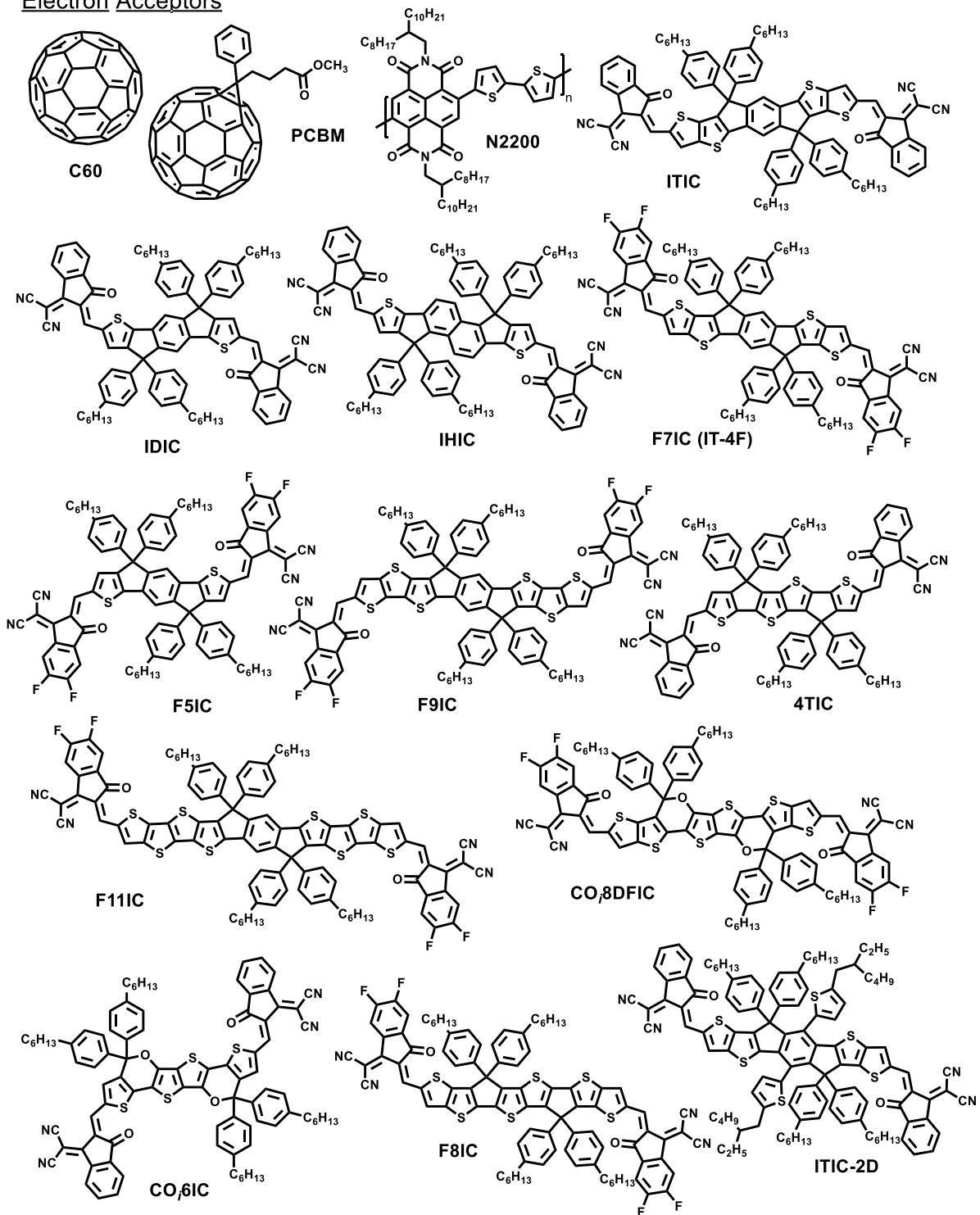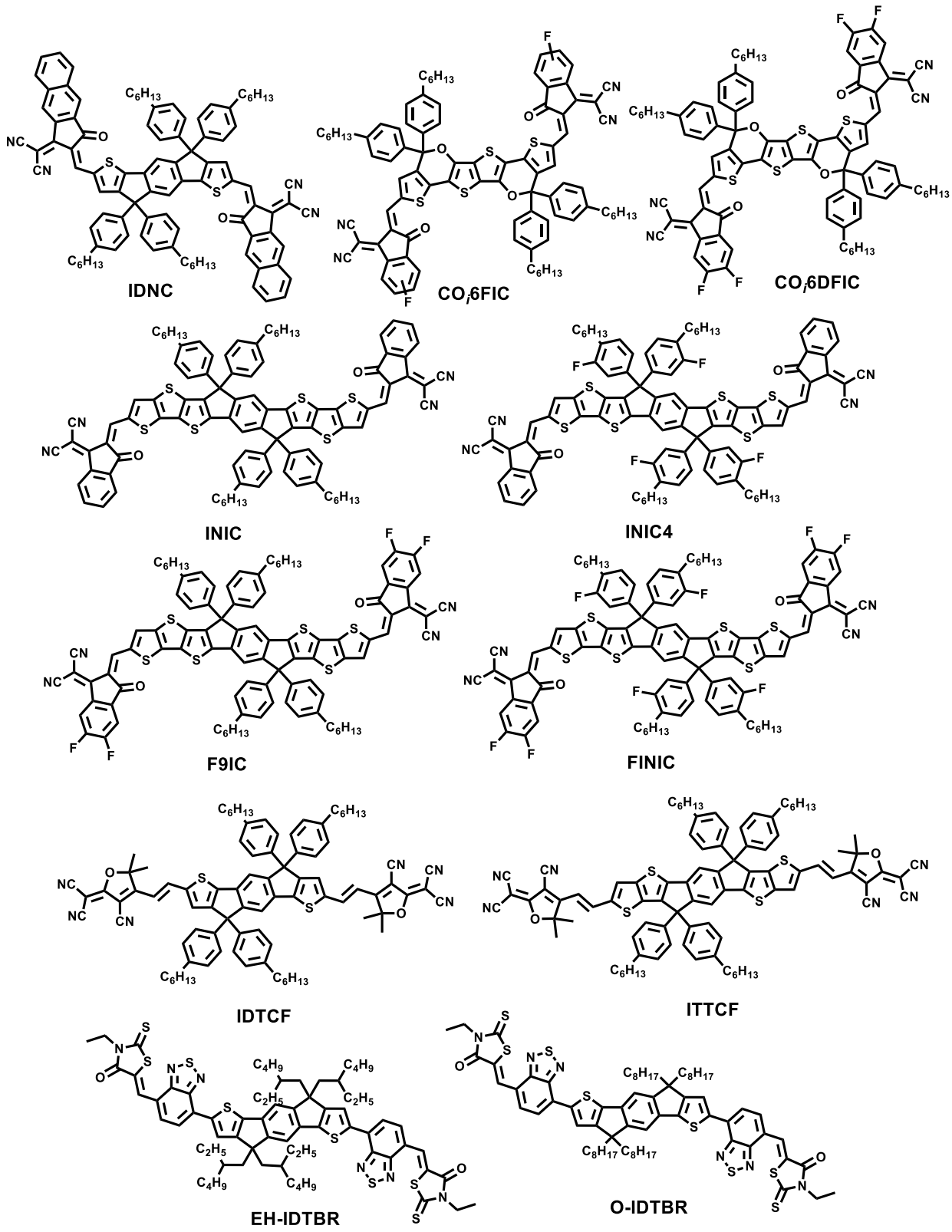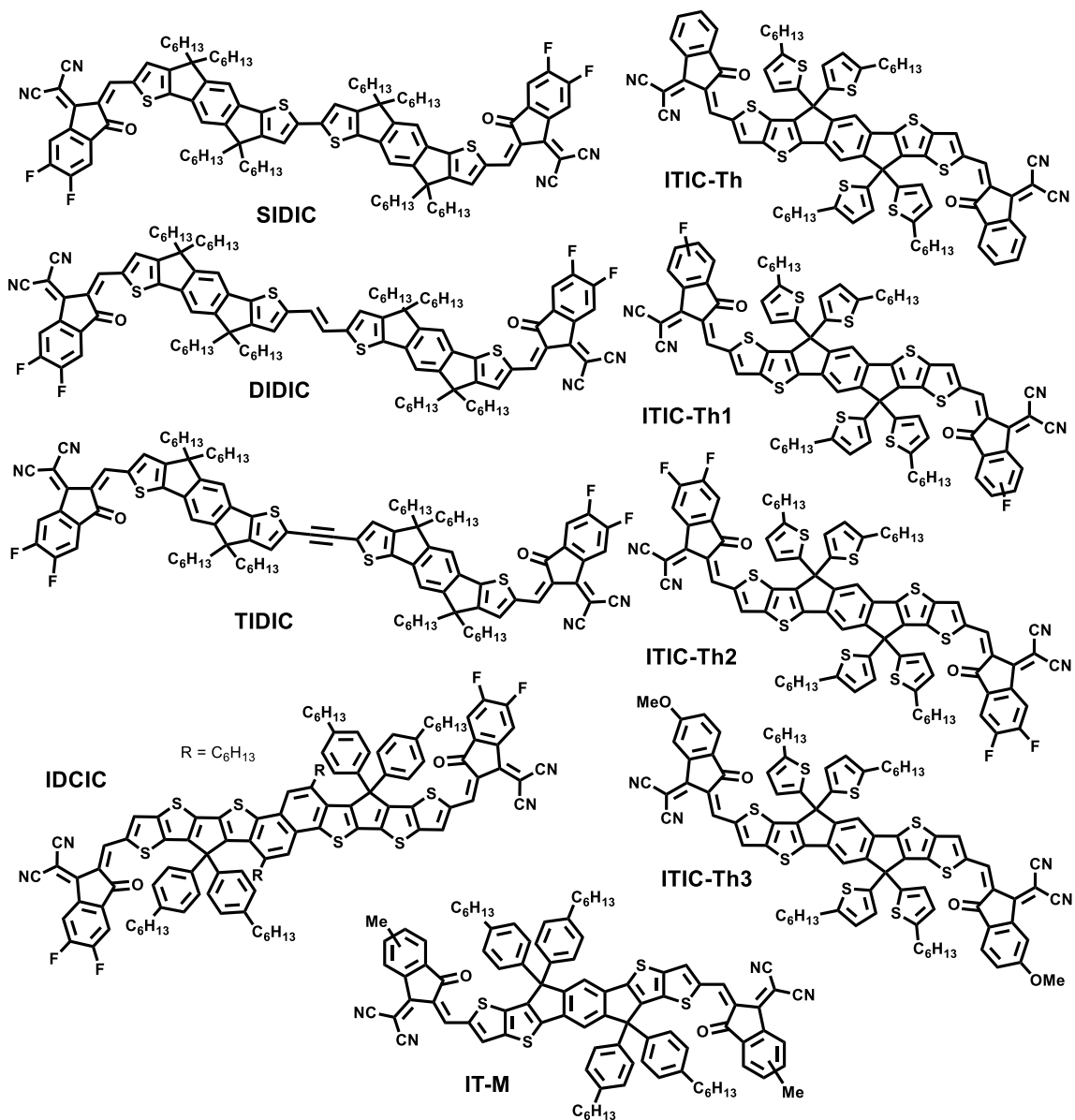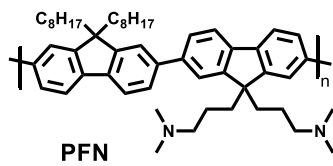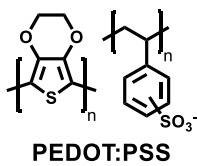
TAZ-based Conjugated Polymers
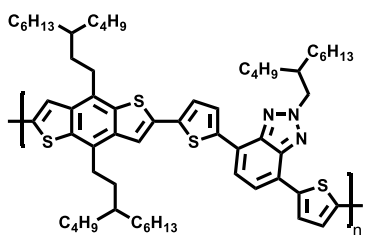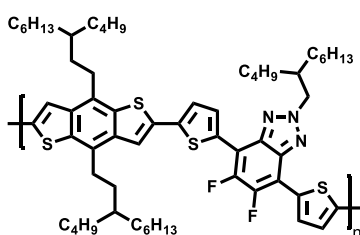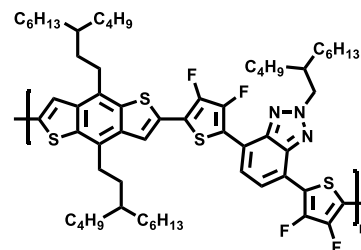
HTAZ

FTAZ

dFT-HTAZ
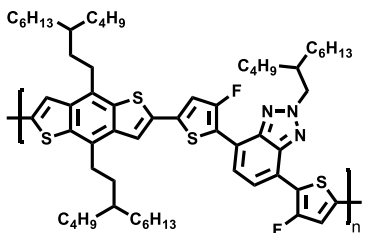
3FT-HTAZ
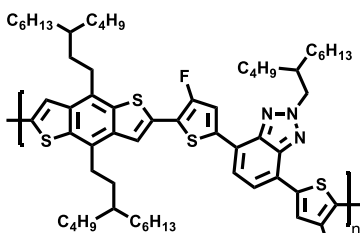
4FT-HTAZ
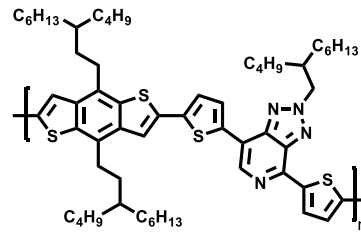
PyTAZ
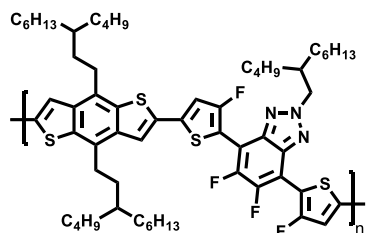
3FT-FTAZ
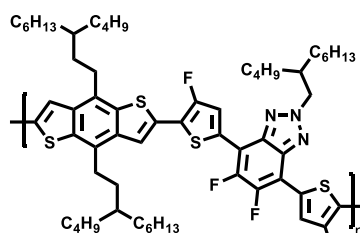
4FT-FTAZ
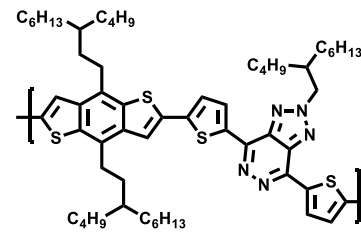
PrzTAZ
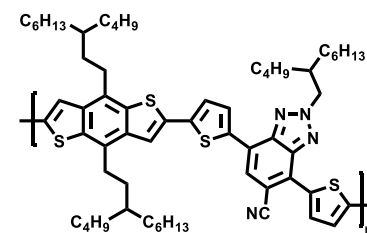
(mono)CNTAZ
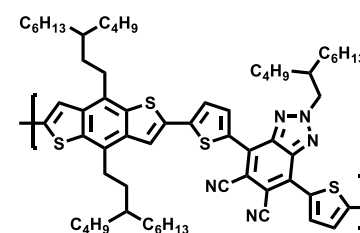
diCNTAZ
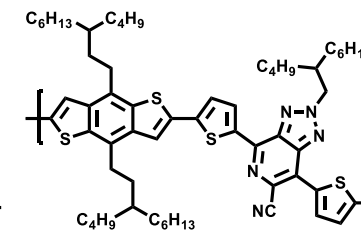
PyCNTAZ
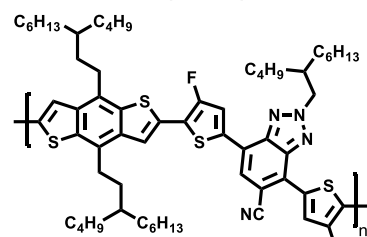
4FT-CNTAZ
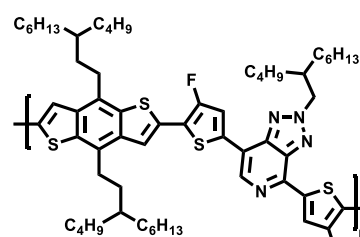
4FT-PyTAZ
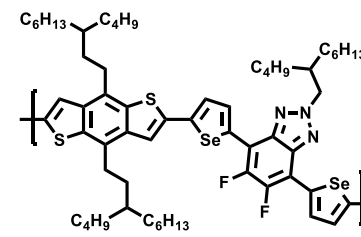
SeFTAZ

REFERENCES

[1]   J. Zhu, Y. Wu, J. Rech, J. Wang, K. Liu, T. Li, Y. Lin, W. Ma, W. You, X. Zhan, *J. Mater. Chem. C* **2018**, *6*, 66–71.

[2]   S. Dai, Y. Xiao, P. Xue, J. James Rech, K. Liu, Z. Li, X. Lu, W. You, X. Zhan, *Chem. Mater.* **2018**, *30*, 5390–5396.

[3]   T. Li, H. Zhang, Z. Xiao, J. J. Rech, H. Niu, W. You, L. Ding, *Mater. Chem. Front.* **2018**, *2*, 700–703.

[4]   J. Wang, Y. Xiao, W. Wang, C. Yan, J. Rech, M. Zhang, W. You, X. Lu, X. Zhan, *Mater. Chem. Front.* **2019**, *3*, 276–283.

[5]   G. Cai, Y. Xiao, M. Li, J. J. Rech, J. Wang, K. Liu, X. Lu, Z. Tang, J. Lian, P. Zeng, Y. Wang, W. You, X. Zhan, *J. Mater. Chem. A* **2020**, *8*, 13735–13741.

[6]   Z. Li, S. Dai, J. Xin, L. Zhang, Y. Wu, J. Rech, F. Zhao, T. Li, K. Liu, Q. Liu, W. Ma, W. You, C. Wang, X. Zhan, *Mater. Chem. Front.* **2018**, *2*, 537–543.

[7]   P. Xue, J. Zhang, J. Xin, J. Rech, T. Li, K. Meng, W. Ma, W. You, M. R. Marder, R. P. S. Han, X. Zhan, *Acta Phys. Chim. Sin.* **2018**, *35*, 275–283.

[8]   S. Dai, J. Zhou, T.-K. Lau, J. J. Rech, K. Liu, P. Xue, Z. Xie, X. Lu, W. You, X. Zhan, *Small Struct.* **2020**, *1*, 2000006.

[9]   D. He, F. Zhao, J. Xin, J. J. Rech, Z. Wei, W. Ma, W. You, B. Li, L. Jiang, Y. Li, C. Wang, *Adv. Energy Mater.* **2018**, *8*, 1802050.

[10]   J. J. Rech, N. Bauer, D. Dirkes, J. Kaplan, Z. Peng, H. Zhang, L. Ye, S. Liu, F. Gao, H. Ade, W. You, *Mater. Chem. Front.* **2019**, *3*, 1642–1652.

[11]   S. Samson, J. Rech, L. Perdigón-Toro, Z. Peng, S. Shoaee, H. Ade, D. Neher, M. Stolterfoht, W. You, *ACS Appl. Polym. Mater.* **2020**, *2*, 5300–5308.

[12]   N. Balar, J. J. Rech, R. Henry, L. Ye, H. Ade, W. You, B. T. O'Connor, *Chem. Mater.* **2019**, *31*, 5124–5132.

[13]   J. J. Rech, L. Yan, Z. Peng, S. Dai, X. Zhan, H. Ade, W. You, *Macromolecules* **2019**, *52*, 6523–6532.

[14]   Q. Zhang, J. J. Rech, L. Yan, Q. Liang, Z. Peng, H. Ade, H. Wu, W. You, *ACS Appl. Polym. Mater.* **2019**, *1*, 3313–3322.

[15] J. J. Rech, L. Yan, Z. Wang, Q. Zhang, S. Bradshaw, H. Ade, W. You, *ACS Appl. Polym. Mater.* **2021**, *3*, 30–41.

[16] J. J. Rech, J. Neu, Y. Qin, S. Samson, J. Shanahan, R. F. Josey, H. Ade, W. You, *ChemSusChem* **2021**, cssc.202100910.

[17] https://www.nobelprize.org/prizes/chemistry/2000/shirakawa/biographical/, **n.d.**

[18] https://www.sciencehistory.org/historical-profile/alan-g-macdiarmid-alan-j-heeger-and-hideki-shirakawa, **n.d.**

[19] N. S. Sariciftci, L. Smilowitz, A. J. Heeger, F. Wudl, *Synth. Met.* **1993**, *59*, 333–352.

[20] J. C. Hummelen, B. W. Knight, F. LePeq, F. Wudl, J. Yao, C. L. Wilkins, *J. Org. Chem.* **1995**, *60*, 532–538.

[21] G. Yu, J. Gao, J. C. Hummelen, F. Wudl, A. J. Heeger, *Science (80-.).* **1995**, *270*, 1789–1791.

[22] W. Zhao, S. Zhang, Y. Zhang, S. Li, X. Liu, C. He, Z. Zheng, J. Hou, *Adv. Mater.* **2018**, *30*, 1704837.

[23] J. Wang, S. Wang, C. Duan, F. J. M. Colberts, J. Mai, X. Liu, X. Jia, X. Lu, R. A. J. Janssen, F. Huang, Y. Cao, *Adv. Energy Mater.* **2017**, *7*, 1702033.

[24] J. Hou, O. Inganäs, R. H. Friend, F. Gao, *Nat. Mater.* **2018**, *17*, 119–128.

[25] Z. Xiao, X. Jia, D. Li, S. Wang, X. Geng, F. Liu, J. Chen, S. Yang, T. P. Russell, L. Ding, *Sci. Bull.* **2017**, *62*, 1494–1496.

[26] H. Feng, N. Qiu, X. Wang, Y. Wang, B. Kan, X. Wan, M. Zhang, A. Xia, C. Li, F. Liu, H. Zhang, Y. Chen, *Chem. Mater.* **2017**, *29*, 7908–7917.

[27] B. Kippelen, J.-L. Brédas, *Energy Environ. Sci.* **2009**, *2*, 251.

[28] A. Polman, M. Knight, E. C. Garnett, B. Ehrler, W. C. Sinke, *Science (80-.).* **2016**, *352*, aad4424-1–10.

[29] Y. Li, G. Xu, C. Cui, Y. Li, *Adv. Energy Mater.* **2017**, *1701791*, 1701791.

[30] W. Song, X. Fan, B. Xu, F. Yan, H. Cui, Q. Wei, R. Peng, L. Hong, J. Huang, Z. Ge, *Adv. Mater.* **2018**, *1800075*, 1–8.

[31] A. Wadsworth, M. Moser, A. Marks, M. S. Little, N. Gasparini, C. J. Brabec, D. Baran, I. McCulloch, *Chem. Soc. Rev.* **2019**, *48*, 1596–1625.

[32] H. Hu, K. Jiang, P. C. Y. Chow, L. Ye, G. Zhang, Z. Li, J. H. Carpenter, H. Ade, H. Yan, *Adv. Energy Mater.* **2018**, *8*, 1701674.

[33] B. He, Q. Yin, X. Yang, L. Liu, X. Jiang, J. Zhang, F. Huang, Y. Cao, *J. Mater. Chem. C* **2017**, *5*, 8774–8781.

[34] K. Sun, X. Tang, Y. Ran, R. He, W. Shen, M. Li, *Phys. Chem. Chem. Phys.* **2018**, *20*, 1664–1672.

[35] J. Liu, L.-K. Ma, Z. Li, H. Hu, T. Ma, C. Zhu, H. Ade, H. Yan, *J. Mater. Chem. A* **2017**, *5*, 22480–22488.

[36] J. Kim, J. B. Park, W.-H. Lee, J. Moon, J. Kim, D.-H. Hwang, I.-N. Kang, *J. Polym. Sci. Part A Polym. Chem.* **2018**, *56*, 653–660.

[37] J. Yuan, W. Guo, Y. Xia, M. J. Ford, F. Jin, D. Liu, H. Zhao, O. Inganäs, G. C. Bazan, W. Ma, *Nano Energy* **2017**, *35*, 251–262.

[38] Y. Lin, J. Wang, Z.-G. Zhang, H. Bai, Y. Li, D. Zhu, X. Zhan, *Adv. Mater.* **2015**, *27*, 1170–1174.

[39] S. Li, L. Ye, W. Zhao, S. Zhang, H. Ade, J. Hou, *Adv. Energy Mater.* **2017**, *7*, 1700183.

[40] A. Kuzmich, D. Padula, H. Ma, A. Troisi, *Energy Environ. Sci.* **2017**, *10*, 395–401.

[41] L. Zhang, B. Lin, Z. Ke, J. Chen, W. Li, M. Zhang, W. Ma, *Nano Energy* **2017**, *41*, 609–617.

[42] Z. Wang, N. Zheng, W. Zhang, H. Yan, Z. Xie, Y. Ma, F. Huang, Y. Cao, *Adv. Energy Mater.* **2017**, *7*, 1700232.

[43] B. Guo, W. Li, X. Guo, X. Meng, W. Ma, M. Zhang, Y. Li, *Adv. Mater.* **2017**, *29*, 1702291.

[44] H. Zhou, L. Yang, W. You, *Macromolecules* **2012**, *45*, 607–632.

[45] S. Xiao, Q. Zhang, W. You, *Adv. Mater.* **2017**, *29*, 1601391.

[46] N. Bauer, Q. Zhang, J. Zhu, Z. Peng, L. Yan, C. Zhu, H. Ade, X. Zhan, W. You, *J. Mater. Chem. A* **2017**, *5*, 22536–22541.

[47] J. W. Jo, S. Bae, F. Liu, T. P. Russell, W. H. Jo, *Adv. Funct. Mater.* **2015**, *25*, 120–125.

[48] O. A. Ibraikulov, C. Ngov, P. Chavez, I. Bulut, B. Heinrich, O. Boyron, K. L. Gerasimov, D. Ivanov, S. Swaraj, S. Méry, N. Leclerc, T. Heiser, P. LEVEQUE, *J. Mater. Chem. A* **2018**, DOI 10.1039/C8TA04127J.

[49] S. Zhang, Y. Qin, M. A. Uddin, B. Jang, W. Zhao, D. Liu, H. Y. Woo, J. Hou, *Macromolecules* **2016**, *49*, 2993–3000.

[50] Z.-G. Zhang, Y. Li, *Sci. China Chem.* **2015**, *58*, 192–209.

[51] H. Zhang, H. Yao, J. J. Hou, J. Zhu, J. Zhang, W. Li, R. Yu, B. Gao, S. Zhang, J. J. Hou, *Adv. Mater.* **2018**, *30*, 1800613.

[52] L. Meng, Y. Zhang, X. Wan, C. Li, X. Zhang, Y. Wang, X. Ke, Z. Xiao, L. Ding, R. Xia, H. Yip, Y. Cao, Y. Chen, *Science (80-.).* **2018**, *361*, 1094–1098.

[53] X. Che, Y. Li, Y. Qu, S. R. Forrest, *Nat. Energy* **2018**, *3*, 422–427.

[54] Y. Zhang, B. Kan, Y. Sun, Y. Wang, R. Xia, X. Ke, Y.-Q.-Q. Yi, C. Li, H.-L. Yip, X. Wan, Y. Cao, Y. Chen, *Adv. Mater.* **2018**, *30*, 1707508.

[55] Z. Xiao, X. Jia, L. Ding, *Sci. Bull.* **2017**, *62*, 1562–1564.

[56] Z. Xiao, F. Liu, X. Geng, J. Zhang, S. Wang, Y. Xie, Z. Li, H. Yang, Y. Yuan, L. Ding, *Sci. Bull.* **2017**, *62*, 1331–1336.

[57] B. Fan, D. Zhang, M. Li, W. Zhong, Z. Zeng, L. Ying, F. Huang, Y. Cao, *Sci. China Chem.* **2019**, *62*, 746–752.

[58] J. Yuan, Y. Zhang, L. Zhou, G. Zhang, H.-L. Yip, T.-K. Lau, X. Lu, C. Zhu, H. Peng, P. A. Johnson, M. Leclerc, Y. Cao, J. Ulanski, Y. Li, Y. Zou, *Joule* **2019**, 1–12.

[59] X. Xu, T. Yu, Z. Bi, W. Ma, Y. Li, Q. Peng, *Adv. Mater.* **2018**, *30*, 1703973.

[60] X. Ma, W. Gao, J. Yu, Q. An, M. Zhang, Z. Hu, J. Wang, W. Tang, C. Yang, F. Zhang, *Energy Environ. Sci.* **2018**, *11*, 2134–2141.

[61] B. Jia, S. Dai, Z. Ke, C. Yan, W. Ma, X. Zhan, *Chem. Mater.* **2018**, *30*, 239–245.

[62] F. Zhao, S. Dai, Y. Wu, Q. Zhang, J. Wang, L. Jiang, Q. Ling, Z. Wei, W. Ma, W. You, C. Wang, X. Zhan, *Adv. Mater.* **2017**, *29*, 1700144.

[63] Y. Lin, X. Zhan, *Mater. Horizons* **2014**, *1*, 470.

[64] C. Yan, S. Barlow, Z. Wang, H. Yan, A. K.-Y. Jen, S. R. Marder, X. Zhan, *Nat. Rev. Mater.* **2018**, *3*, 18003.

[65] S. Dai, X. Zhan, *Adv. Energy Mater.* **2018**, *1800002*, 1800002.

[66] T. Kietzke, *Adv. Optoelectron.* **2007**, *2007*, 1–15.

[67] D. He, F. Zhao, L. Jiang, C. Wang, *J. Mater. Chem. A* **2018**, *6*, 8839–8854.

[68] W. Huang, P. Cheng, Y. M. Yang, G. Li, Y. Yang, *Adv. Mater.* **2018**, *30*, 1705706.

[69] R. Yu, H. Yao, J. Hou, *Adv. Energy Mater.* **2018**, *1702814*, 1702814.

[70] F. Shen, J. Xu, X.-M. Li, C. Zhan, *J. Mater. Chem. A* **2018**, *6*, 15433–15455.

[71] N. Qiu, H. Zhang, X. Wan, C. Li, X. Ke, H. Feng, B. Kan, H. Zhang, Q. Zhang, Y. Lu, Y. Chen, *Adv. Mater.* **2017**, *29*, 1604964.

[72] J. Zhu, Z. Ke, Q. Zhang, J. Wang, S. Dai, Y. Wu, Y. Xu, Y. Lin, W. Ma, W. You, X. Zhan, *Adv. Mater.* **2018**, *30*, 1704713.

[73] H. Yao, Y. Cui, R. Yu, B. Gao, H. Zhang, J. Hou, *Angew. Chemie Int. Ed.* **2017**, *56*, 3045–3049.

[74] H. Lu, J. Zhang, J. Chen, Q. Liu, X. Gong, S. Feng, X. Xu, W. Ma, Z. Bo, *Adv. Mater.* **2016**, *28*, 9559–9566.

[75] Y. Lin, Y. Jin, S. Dong, W. Zheng, J. Yang, A. Liu, F. Liu, Y. Jiang, T. P. Russell, F. Zhang, F. Huang, L. Hou, *Adv. Energy Mater.* **2018**, *8*, 1701942.

[76] X. Shi, L. Zuo, S. B. Jo, K. Gao, F. Lin, F. Liu, A. K.-Y. Jen, *Chem. Mater.* **2017**, *29*, 8369–8376.

[77] Z. Luo, H. Bin, T. Liu, Z.-G. Zhang, Y. Yang, C. Zhong, B. Qiu, G. Li, W. Gao, D. Xie, K. Wu, Y. Sun, F. Liu, Y. Li, C. Yang, *Adv. Mater.* **2018**, *30*, 1706124.

[78] Y. Lin, Q. He, F. Zhao, L. Huo, J. Mai, X. Lu, C.-J. Su, T. Li, J. Wang, J. Zhu, Y. Sun, C. Wang, X. Zhan, *J. Am. Chem. Soc.* **2016**, *138*, 2973–2976.

[79] Y.-Q.-Q. Yi, H. Feng, M. Chang, H. Zhang, X. Wan, C. Li, Y. Chen, *J. Mater. Chem. A* **2017**, *5*, 17204–17210.

[80] W. Hu, X. Du, W. Zhuang, W. Su, J. Cao, A. M. Pourrahimi, N. Li, X. Shen, M. Zhang, D. Yu, W. Gruber, T. Unruh, E. Wang, C. J. Brabec, *ACS Appl. Energy Mater.* **2020**, *3*, 5734–5744.

[81] T. Umeyama, K. Igarashi, Y. Tamai, T. Wada, T. Takeyama, D. Sasada, K. Ishida, T. Koganezawa, S. Ohtani, K. Tanaka, H. Ohkita, H. Imahori, *Sustain. Energy Fuels* **2021**, *5*, 2028–2035.

[82] F.-Y. Cao, W.-C. Huang, S.-L. Chang, Y.-J. Cheng, *Chem. Mater.* **2018**, *30*, 4968–4977.

[83] J. Zhu, Y. Xiao, J. Wang, K. Liu, H. Jiang, Y. Lin, X. Lu, X. Zhan, *Chem. Mater.* **2018**, *30*, 4150–4156.

[84] J. Zhu, Z. Ke, Q. Zhang, J. Wang, S. Dai, Y. Wu, Y. Xu, Y. Lin, W. Ma, W. You, X. Zhan, *Adv. Mater.* **2018**, *30*, 1704713.

[85] Z. Xiao, X. Jia, L. Ding, *Sci. Bull.* **2017**, *62*, 1562–1564.

[86] Z. Xiao, X. Jia, D. Li, S. Wang, X. Geng, F. Liu, J. Chen, S. Yang, T. P. Russell, L. Ding, *Sci. Bull.* **2017**, *62*, 1494–1496.

[87] B. Lu, Y. Xiao, T. Li, K. Liu, X. Lu, J. Lian, P. Zeng, J. Qu, X. Zhan, *ACS Appl. Mater. Interfaces* **2019**, *11*, 33006–33011.

[88] S. Dai, T. Li, W. Wang, Y. Xiao, T.-K. Lau, Z. Li, K. Liu, X. Lu, X. Zhan, *Adv. Mater.* **2018**, *30*, 1706571.

[89] L. Meng, Y. Zhang, X. Wan, C. Li, X. Zhang, Y. Wang, X. Ke, Z. Xiao, L. Ding, R. Xia, H.-L. Yip, Y. Cao, Y. Chen, *Science (80-.).* **2018**, *361*, 1094–1098.

[90] M. Nazari, E. Cieplechowicz, T. A. Welsh, G. C. Welch, *New J. Chem.* **2019**, *43*, 5187–5195.

[91] R. Singh, M. Kim, J.-J. Lee, T. Ye, P. E. Keivanidis, K. Cho, *J. Mater. Chem. C* **2020**, *8*, 1686–1696.

[92] H. Yin, M.-Y. Sui, Q.-Q. Pan, G.-Y. Sun, Y. Geng, *Dye. Pigment.* **2018**, *148*, 394–404.

[93] H. Bristow, K. J. Thorley, A. J. P. White, A. Wadsworth, M. Babics, Z. Hamid, W. Zhang, A. F. Paterson, J. Kosco, J. Panidi, T. D. Anthopoulos, I. McCulloch, *Adv. Electron. Mater.* **2019**, *5*, 1900344.

[94] L. Ye, Y. Xiong, Q. Zhang, S. Li, C. Wang, Z. Jiang, J. Hou, W. You, H. Ade, *Adv. Mater.* **2018**, *30*, 1705485.

[95] W. Zhao, S. Li, H. Yao, S. Zhang, Y. Zhang, B. Yang, J. Hou, *J. Am. Chem. Soc.* **2017**, *139*, 7148–7151.

[96] K. Jiang, G. Zhang, G. Yang, J. Zhang, Z. Li, T. Ma, H. Hu, W. Ma, H. Ade, H. Yan, *Adv. Energy Mater.* **2018**, *8*, 1701370.

[97] X. Liu, Y. Yan, Y. Yao, Z. Liang, *Adv. Funct. Mater.* **2018**, *28*, 1802004.

[98] H. Yao, L. Ye, J. J. Hou, B. Jang, G. Han, Y. Cui, G. M. Su, C. Wang, B. Gao, R. Yu, H. Zhang, Y. Yi, H. Y. Woo, H. Ade, J. J. Hou, *Adv. Mater.* **2017**, *29*, 1700254.

[99] H. Yao, Y. Chen, Y. Qin, R. Yu, Y. Cui, B. Yang, S. Li, K. Zhang, J. Hou, *Adv. Mater.* **2016**, *28*, 1–5.

[100] S. Li, L. Ye, W. Zhao, X. Liu, J. Zhu, H. Ade, J. Hou, *Adv. Mater.* **2017**, *29*, 1704051.

[101] Y. Cui, C. Yang, H. Yao, J. Zhu, Y. Wang, G. Jia, F. Gao, J. Hou, *Adv. Mater.* **2017**, *29*, 1703080.

[102] B. Kan, H. Feng, X. Wan, F. Liu, X. Ke, Y. Wang, Y. Wang, H. Zhang, C. Li, J. Hou, Y. Chen, *J. Am. Chem. Soc.* **2017**, *139*, 4929–4934.

[103] S. Dai, F. Zhao, Q. Zhang, T.-K. Lau, T. Li, K. Liu, Q. Ling, C. Wang, X. Lu, W. You, X. Zhan, *J. Am. Chem. Soc.* **2017**, *139*, 1336–1343.

[104] J. Mai, Y. Xiao, G. Zhou, J. Wang, J. Zhu, N. Zhao, X. Zhan, X. Lu, *Adv. Mater.* **2018**, *30*, 1802888.

[105] F. Liu, Z. Zhou, C. Zhang, J. Zhang, Q. Hu, T. Vergote, F. Liu, T. P. Russell, X. Zhu, *Adv. Mater.* **2017**, *29*, 1606574.

[106] W. Gao, M. Zhang, T. Liu, R. Ming, Q. An, K. Wu, D. Xie, Z. Luo, C. Zhong, F. Liu, F. Zhang, H. Yan, C. Yang, *Adv. Mater.* **2018**, *30*, 1800052.

[107] X. Shi, J. Chen, K. Gao, L. Zuo, Z. Yao, F. Liu, J. Tang, A. K.-Y. Jen, *Adv. Energy Mater.* **2018**, *8*, 1702831.

[108] H. Bin, L. Gao, Z.-G. Zhang, Y. Yang, Y. Zhang, C. Zhang, S. Chen, L. Xue, C. Yang, M. Xiao, Y. Li, *Nat. Commun.* **2016**, *7*, 13651.

[109] J. Wang, W. Wang, X. Wang, Y. Wu, Q. Zhang, C. Yan, W. Ma, W. You, X. Zhan, *Adv. Mater.* **2017**, *29*, 1702125.

[110] W. Liu, J. Zhang, Z. Zhou, D. Zhang, Y. Zhang, S. Xu, X. Zhu, *Adv. Mater.* **2018**, *30*, 1800403.

[111] Z. Zheng, O. M. Awartani, B. Gautam, D. Liu, Y. Qin, W. Li, A. Bataller, K. Gundogdu, H. Ade, J. Hou, *Adv. Mater.* **2017**, *29*, 1604241.

[112] S. jie Xu, Z. Zhou, W. Liu, Z. Zhang, F. Liu, H. Yan, X. Zhu, *Adv. Mater.* **2017**, *29*, 1704510.

[113] Z. Zhang, M. Li, Y. Liu, J. Zhang, S. Feng, X. Xu, J. Song, Z. Bo, *J. Mater. Chem. A* **2017**, *5*, 7776–7783.

[114] Z. Liang, M. Li, X. Zhang, Q. Wang, Y. Jiang, H. Tian, Y. Geng, *J. Mater. Chem. A* **2018**, *6*, 8059–8067.

[115] Z. Zhang, J. Yu, X. Yin, Z. Hu, Y. Jiang, J. Sun, J. Zhou, F. Zhang, T. P. Russell, F. Liu, W. Tang, *Adv. Funct. Mater.* **2018**, *28*, 1705095.

[116] T. Li, S. Dai, Z. Ke, L. Yang, J. Wang, C. Yan, W. Ma, X. Zhan, *Adv. Mater.* **2018**, *30*, 1705969.

[117] L. Ye, W. Zhao, S. Li, S. Mukherjee, J. H. Carpenter, O. Awartani, X. Jiao, J. Hou, H. Ade, *Adv. Energy Mater.* **2017**, *7*, 1602000.

[118] J. Zhang, C. Yan, W. Wang, Y. Xiao, X. Lu, S. Barlow, T. C. Parker, X. Zhan, S. R. Marder, *Chem. Mater.* **2018**, *30*, 309–313.

[119] W. Wang, C. Yan, T.-K. Lau, J. Wang, K. Liu, Y. Fan, X. Lu, X. Zhan, *Adv. Mater.* **2017**, *29*, 1701308.

[120] Q. Fan, Y. Wang, M. Zhang, B. Wu, X. Guo, Y. Jiang, W. Li, B. Guo, C. Ye, W. Su, J. Fang, X. Ou, F. Liu, Z. Wei, T. C. Sum, T. P. Russell, Y. Li, *Adv. Mater.* **2018**, *30*, 1704546.

[121] Y. Chen, P. Ye, X. Jia, W. Gu, X. Xu, X. Wu, J. Wu, F. Liu, Z. Zhu, H. Huang, *J. Mater. Chem. A* **2017**, *5*, 19697–19702.

[122] X. Li, T. Yan, H. Bin, G. Han, L. Xue, F. Liu, Y. Yi, Z.-G. Zhang, T. P. Russell, Y. Li, *J. Mater. Chem. A* **2017**, *5*, 22588–22597.

[123] L. Yang, W. Gu, L. Hong, Y. Mi, F. Liu, M. Liu, Y. Yang, B. Sharma, X. Liu, H. Huang, *ACS Appl. Mater. Interfaces* **2017**, *9*, 26928–26936.

[124] M. He, T. M. Leslie, J. A. Sinicropi, *Chem. Mater.* **2002**, *14*, 2393–2400.

[125] S. C. Price, A. C. Stuart, L. Yang, H. Zhou, W. You, *J. Am. Chem. Soc.* **2011**, *133*, 4625–4631.

[126] A. Hexemer, W. Bras, J. Glossinger, E. Schaible, E. Gann, R. Kirian, A. MacDowell, M. Church, B. Rude, H. Padmore, *J. Phys. Conf. Ser.* **2010**, *247*, 012007.

[127] U. Würfel, D. Neher, A. Spies, S. Albrecht, *Nat. Commun.* **2015**, *6*, 6951.

[128] M. Stolterfoht, A. Armin, B. Philippa, D. Neher, *J. Phys. Chem. Lett.* **2016**, *7*, 4716–4721.

[129] D. Neher, J. Kniepert, A. Elimelech, L. J. A. Koster, *Sci. Rep.* **2016**, *6*, 24861.

[130] L. Lu, T. Zheng, T. Xu, D. Zhao, L. Yu, *Chem. Mater.* **2015**, *27*, 537–543.

[131] S. Solak, P. W. M. Blom, G. A. H. Wetzelaer, *Appl. Phys. Lett.* **2016**, *109*, 053302.

[132] S. R. Cowan, A. Roy, A. J. Heeger, *Phys. Rev. B* **2010**, *82*, 245207.

[133] A. K. K. Kyaw, D. H. Wang, V. Gupta, W. L. Leong, L. Ke, G. C. Bazan, A. J. Heeger, *ACS Nano* **2013**, *7*, 4569–4577.

[134] V. V. Brus, *Org. Electron.* **2016**, *29*, 1–6.

[135] Q. Zhang, L. Yan, X. Jiao, Z. Peng, S. Liu, J. J. Rech, E. Klump, H. Ade, F. So, W. You, *Chem. Mater.* **2017**, *29*, 5990–6002.

[136] N. Bauer, Q. Zhang, J. J. Rech, S. Dai, Z. Peng, H. Ade, J. Wang, X. Zhan, W. You, *Nano Res.* **2019**, *12*, 2400–2405.

[137] L. Yang, J. R. Tumbleston, H. Zhou, H. Ade, W. You, *Energy Environ. Sci.* **2013**, *6*, 316–326.

[138] H. Cha, S. Wheeler, S. Holliday, S. D. Dimitrov, A. Wadsworth, H. H. Lee, D. Baran, I. McCulloch, D. J. R., J. R. Durrant, *Adv. Funct. Mater.* **2017**, *1704389*, 1704389.

[139] H. Cha, C.-H. H. Tan, J. Wu, Y. Dong, W. Zhang, H. Chen, S. Rajaram, K. S. Narayan, I. McCulloch, J. R. Durrant, *Adv. Energy Mater.* **2018**, *8*, 1–9.

[140] J. Hong, M. J. Sung, H. Cha, C. E. Park, J. R. Durrant, T. K. An, Y.-H. H. Kim, S.-K. K. Kwon, *ACS Appl. Mater. Interfaces* **2018**, *10*, 36037–36046.

[141] W. Li, L. Yan, H. Zhou, W. You, *Chem. Mater.* **2015**, *27*, 6470–6476.

[142] S. Roland, L. Yan, Q. Zhang, X. Jiao, A. Hunt, M. Ghasemi, H. Ade, W. You, D. Neher, *J. Phys. Chem. C* **2017**, *121*, 10305–10316.

[143] D. He, F. Zhao, J. Xin, J. J. Rech, Z. Wei, W. Ma, W. You, B. Li, L. Jiang, Y. Li, C. Wang, *Adv. Energy Mater.* **2018**, *1802050*, 1–7.

[144] C. H. Y. Ho, T. Kim, Y. Xiong, Y. Firdaus, X. Yi, Q. Dong, J. J. Rech, A. Gadisa, R. Booth, B. T. O'Connor, A. Amassian, H. Ade, W. You, T. D. Anthopoulos, F. So, *Adv. Energy Mater.* **2020**, *2000823*, 2000823.

[145] M. A. Kelly, S. Roland, Q. Zhang, Y. Lee, B. Kabius, Q. Wang, E. D. Gomez, D. Neher, W. You, *J. Phys. Chem. C* **2017**, *121*, 2059–2068.

[146] Z. Chen, L. Yan, J. J. Rech, J. Hu, Q. Zhang, W. You, *ACS Appl. Polym. Mater.* **2019**, *1*, 804–814.

[147] M. A. Kelly, Q. Zhang, Z. Peng, V. Noman, C. Zhu, H. Ade, W. You, *J. Mater. Chem. A* **2018**, *6*, 19190–19200.

[148] R. L. Uy, L. Yan, W. Li, W. You, *Macromolecules* **2014**, *47*, 2289–2295.

[149] R. W. Nunes, J. R. Martin, J. F. Johnson, *Polym. Eng. Sci.* **1982**, *22*, 205–228.

[150] J. T. Seitz, *J. Appl. Polym. Sci.* **1993**, *49*, 1331–1351.

[151] J. Choi, W. Kim, D. Kim, S. Kim, J. Chae, S. Q. Choi, F. S. Kim, T. S. Kim, B. J. Kim, *Chem. Mater.* **2019**, *31*, 3163–3173.

[152] S. Savagatrup, A. D. Printz, T. F. O'Connor, A. V. Zaretski, D. J. Lipomi, *Chem. Mater.* **2014**, *26*, 3028–3041.

[153] W. Ma, J. Y. Kim, K. Lee, A. J. Heeger, *Macromol. Rapid Commun.* **2007**, *28*, 1776–1780.

[154] W. Ma, G. Yang, K. Jiang, J. H. Carpenter, Y. Wu, X. Meng, T. McAfee, J. Zhao, C. Zhu, C. Wang, H. Ade, H. Yan, *Adv. Energy Mater.* **2015**, *5*, 1–9.

[155] N. Zhou, A. S. Dudnik, T. I. N. G. N. G. Li, E. F. Manley, T. J. Aldrich, P. Guo, H.-C. C. Liao, Z. Chen, L. X. Chen, R. P. H. H. Chang, A. Facchetti, M. Olvera de la Cruz, T. J. Marks, *J. Am. Chem. Soc.* **2016**, *138*, 1240–1251.

[156] S. Savagatrup, A. D. Printz, D. Rodriquez, D. J. Lipomi, *Macromolecules* **2014**, *47*, 1981–1992.

[157] C. Grand, J. R. Reynolds, *MRS Commun.* **2015**, *5*, 155–167.

[158] W. Li, L. Yang, J. R. Tumbleston, L. Yan, H. Ade, W. You, *Adv. Mater.* **2014**, *26*, 4456–4462.

[159] J. I. Khan, R. S. Ashraf, M. A. Alamoudi, M. N. Nabi, H. N. Mohammed, A. Wadsworth, Y. Firdaus, W. Zhang, T. D. Anthopoulos, I. McCulloch, F. Laquai, *Sol. RRL* **2019**, *3*, 1900023.

[160] K. D. Deshmukh, R. Matsidik, S. K. K. Prasad, L. A. Connal, A. C. Y. Liu, E. Gann, L. Thomsen, J. M. Hodgkiss, M. Sommer, C. R. McNeill, *Adv. Funct. Mater.* **2018**, *28*, 1–13.

[161] C. Nicolet, D. Deribew, C. Renaud, G. Fleury, C. Brochon, E. Cloutet, L. Vignau, G. Wantz, H. Cramail, M. Geoghegan, G. Hadziioannou, *J. Phys. Chem. B* **2011**, *115*, 12717–12727.

[162] I. Osaka, M. Saito, H. Mori, T. Koganezawa, K. Takimiya, *Adv. Mater.* **2012**, *24*, 425–430.

[163] W. Xiong, F. Qi, T. Liu, L. Huo, X. Xue, Z. Bi, Y. Zhang, W. Ma, M. Wan, J. Liu, Y. Sun, *Sol. RRL* **2018**, *2*, 1800129.

[164] A. Wadsworth, Z. Hamid, M. Bidwell, R. S. Ashraf, J. I. Khan, D. H. Anjum, C. Cendra, J. Yan, E. Rezasoltani, A. A. Y. Y. Guilbert, M. Azzouzi, N. Gasparini, J. H. Bannock, D. Baran, H. Wu, J. C. de Mello, C. J. Brabec, A. Salleo, J. Nelson, F. Laquai, I. McCulloch, *Adv. Energy Mater.* **2018**, *8*, 1–15.

[165] J. Choi, W. Kim, S. Kim, T. S. Kim, B. J. Kim, *Chem. Mater.* **2019**, *31*, 9057–9069.

[166] R. Mauer, M. Kastler, F. Laquai, *Adv. Funct. Mater.* **2010**, *20*, 2085–2092.

[167] A. M. Ballantyne, L. Chen, J. Dane, T. Hammant, F. M. Braun, M. Heeney, W. Duffy, I. McCulloch, D. D. C. Bradley, J. Nelson, *Adv. Funct. Mater.* **2008**, *18*, 2373–2380.

[168] D. Spoltore, T. Vangerven, P. Verstappen, F. Piersimoni, S. Bertho, K. Vandewal, N. Van Den Brande, M. Defour, B. Van Mele, A. De Sio, J. Parisi, L. Lutsen, D. Vanderzande, W. Maes, J. V. Manca, *Org. Electron. physics, Mater. Appl.* **2015**, *21*, 160–170.

[169] Z. Huang, E. C. Fregoso, S. Dimitrov, P. S. Tuladhar, Y. W. Soon, H. Bronstein, I. Meager, W. Zhang, I. McCulloch, J. R. Durrant, *J. Mater. Chem. A* **2014**, *2*, 19282–19289.

[170] C. R. McNeill, A. Abrusci, J. Zaumseil, R. Wilson, M. J. McKiernan, J. H. Burroughes, J. J. M. Halls, N. C. Greenham, R. H. Friend, *Appl. Phys. Lett.* **2007**, *90*, 4–7.

[171] B. Philippa, M. Stolterfoht, P. L. Burn, G. Juška, P. Meredith, R. D. White, A. Pivrikas, *Sci. Rep.* **2014**, *4*, 1–7.

[172] R. Noriega, J. Rivnay, K. Vandewal, F. P. V. Koch, N. Stingelin, P. Smith, M. F. Toney, A. Salleo, *Nat. Mater.* **2013**, *12*, 1038–1044.

[173] X. Jiao, L. Ye, H. Ade, *Adv. Energy Mater.* **2017**, *7*, 1–22.

[174] A. Hexemer, P. Müller-Buschbaum, *IUCrJ* **2015**, *2*, 106–125.

[175] P. Müller-Buschbaum, *Adv. Mater.* **2014**, *26*, 7692–7709.

[176] J. R. Reynolds, B. C. Thompson, T. A. Skotheim, L. Ye, S. J. Stuard, H. Ade, in *Conjug. Polym.*, **2019**, pp. 427–458.

[177] J. J. M. Halls, K. Pichler, R. H. Friend, S. C. Moratti, A. B. Holmes, *Appl. Phys. Lett.* **1996**, *68*, 3120–3122.

[178] W. Huang, E. Gann, N. Chandrasekaran, L. Thomsen, S. K. K. Prasad, J. Hodgkiss, D. Kabra, Y.-B. Cheng, C. R. McNeill, *Energy Environ. Sci.* **2017**, 0–21.

[179] S. Mukherjee, X. Jiao, H. Ade, *Adv. Energy Mater.* **2016**, *6*, 1600699.

[180] W. Ma, L. Ye, S. Zhang, J. Hou, H. Ade, *J. Mater. Chem. C* **2013**, *1*, 5023.

[181] W. Ma, J. R. Tumbleston, M. Wang, E. Gann, F. Huang, H. Ade, *Adv. Energy Mater.* **2013**, *3*, 864–872.

[182] H. Gaspar, F. Figueira, L. Pereira, A. Mendes, J. Viana, G. Bernardo, H. Gaspar, F. Figueira, L. Pereira, A. Mendes, J. C. Viana, G. Bernardo, *Materials (Basel).* **2018**, *11*, 2560.

[183] J. Benduhn, K. Tvingstedt, F. Piersimoni, S. Ullbrich, Y. Fan, M. Tropiano, K. A. McGarry, O. Zeika, M. K. Riede, C. J. Douglas, S. Barlow, S. R. Marder, D. Neher, D. Spoltore, K. Vandewal, *Nat. Energy* **2017**, *2*, 17053 (in press).

[184] N. K. Elumalai, A. Uddin, *Energy Environ. Sci.* **2016**, *9*, 391–410.

[185] L. J. A. Koster, M. Kemerink, M. M. Wienk, K. Maturová, R. A. J. Janssen, *Adv. Mater.* **2011**, *23*, 1670–1674.

[186] M. Stolterfoht, A. Armin, B. Philippa, R. D. White, P. L. Burn, P. Meredith, G. Juška, A. Pivrikas, *Sci. Rep.* **2015**, *5*, 9949.

[187] L. J. A. Koster, V. D. Mihailetchi, R. Ramaker, H. Xie, P. W. Blom, *Org. Optoelectron. Photonics II* **2006**, *6192*, 61922G.

[188] U. Würfel, L. Perdigón-Toro, J. Kurpiers, C. M. Wolff, P. Caprioglio, J. J. Rech, J. Zhu, X. Zhan, W. You, S. Shoaee, D. Neher, M. Stolterfoht, *J. Phys. Chem. Lett.* **2019**, *10*, 3473–3480.

[189] W. Tress, M. Yavari, K. Domanski, P. Yadav, B. Niesen, J. P. Correa Baena, A. Hagfeldt, M. Graetzel, *Energy Environ. Sci.* **2018**, *11*, 151–165.

[190] K. Vandewal, J. Benduhn, V. C. Nikolis, *Sustain. Energy Fuels* **2018**, *2*, 538–544.

[191] K. Vandewal, K. Tvingstedt, A. Gadisa, O. Inganäs, J. V. Manca, *Phys. Rev. B* **2010**, *81*, 125204.

[192] Z. Liu, L. Krückemeier, B. Krogmeier, B. Klingebiel, J. A. Márquez, S. Levcenko, S. Öz, S. Mathur, U. Rau, T. Unold, T. Kirchartz, *ACS Energy Lett.* **2019**, *4*, 110–117.

[193] J. Yao, T. Kirchartz, M. S. Vezie, M. A. Faist, W. Gong, Z. He, H. Wu, J. Troughton, T. Watson, D. Bryant, J. Nelson, *Phys. Rev. Appl.* **2015**, *4*, 1–10.

[194] M. Kotova, G. Londi, J. Junker, S. Dietz, A. Privitera, K. Tvingstedt, D. Beljonne, A. Sperlich, V. Dyakonov, *Mater. Horizons* **2020**, *7*, 1641–1649.

[195] D. J. Lipomi, H. Chong, M. Vosgueritchian, J. Mei, Z. Bao, *Sol. Energy Mater. Sol. Cells* **2012**, *107*, 355–365.

[196] Z. Tang, J. Wang, A. Melianas, Y. Wu, R. Kroon, W. Li, W. Ma, M. R. Andersson, Z. Ma, W. Cai, W. Tress, O. Inganäs, *J. Mater. Chem. A* **2018**, *6*, 12574–12581.

[197] M. Azzouzi, J. Yan, T. Kirchartz, K. Liu, J. Wang, H. Wu, J. Nelson, *Phys. Rev. X* **2018**, *8*, 31055.

[198] F. D. Eisner, M. Azzouzi, Z. Fei, X. Hou, T. D. Anthopoulos, T. J. S. Dennis, M. Heeney, J. Nelson, *J. Am. Chem. Soc.* **2019**, *141*, 6362–6374.

[199] D. Rodriquez, S. Savagatrup, E. Valle, C. M. Proctor, C. McDowell, G. C. Bazan, T.-Q. Nguyen, D. J. Lipomi, *ACS Appl. Mater. Interfaces* **2016**, *8*, 11649–11657.

[200] C. Müller, *Chem. Mater.* **2015**, *27*, 2740–2754.

[201] C. Bruner, F. Novoa, S. Dupont, R. Dauskardt, *ACS Appl. Mater. Interfaces* **2014**, *6*, 21474–21483.

[202] N. R. Tummala, C. Risko, C. Bruner, R. H. Dauskardt, J. L. Bredas, J.-L. Brédas, **2015**, *53*, 934–942.

[203] T. Kim, J.-H. Kim, T. E. Kang, C. Lee, H. Kang, M. Shin, C. Wang, B. Ma, U. Jeong, T.-S. Kim, & Bumjoon, J. Kim, *Nat. Commun.* **2015**, *6*, 8547.

[204] J.-H. Kim, J. Noh, H. Choi, J.-Y. Lee, T.-S. Kim, *Chem. Mater.* **2017**, *29*, 3954–3961.

[205] B. Fan, L. Ying, P. Zhu, F. Pan, F. Liu, J. Chen, F. Huang, Y. Cao, *Adv. Mater.* **2017**, *1703906*, 1–7.

[206] N. Balar, Y. Xiong, L. Ye, S. Li, D. Nevola, D. B. Dougherty, J. Hou, H. Ade, B. T. O'Connor, *ACS Appl. Mater. Interfaces* **2017**, *9*, DOI 10.1021/acsami.7b13719.

[207] C. Bruner, R. Dauskardt, *Macromolecules* **2014**, *47*, 1117–1121.

[208] H. Kang, M. A. Uddin, C. Lee, K.-H. Kim, T. L. Nguyen, W. Lee, Y. Li, C. Wang, H. Y. Woo, B. J. Kim, *J. Am. Chem. Soc.* **2015**, *137*, 2359–2365.

[209] A. Sharma, X. Pan, J. A. Campbell, M. R. Andersson, D. A. Lewis, *Macromolecules* **2017**, *50*, 3347–3354.

[210] R. Xie, Y. Lee, M. P. Aplan, N. J. Caggiano, C. Müller, R. H. Colby, E. D. Gomez, *Macromolecules* **2017**, *50*, 5146–5154.

[211] N. R. Tummala, C. Risko, C. Bruner, R. H. Dauskardt, J. L. Bredas, *J. Polym. Sci. Part B-Polymer Phys.* **2015**, *53*, 934–942.

[212] D. Rodriquez, J.-H. Kim, S. E. Root, Z. Fei, P. Boufflet, M. Heeney, T.-S. Kim, D. J. Lipomi, *ACS Appl. Mater. Interfaces* **2017**, *9*, 8855–8862.

[213] N. Balar, B. T. O'Connor, *Macromolecules* **2017**, *50*, DOI 10.1021/acs.macromol.7b01282.

[214] S. Dey, *Small* **2019**, *15*, 1900134.

[215] P. Bi, X. Hao, *Sol. RRL* **2019**, *3*, 1970011.

[216] N. Gasparini, A. Salleo, I. McCulloch, D. Baran, *Nat. Rev. Mater.* **2019**, *4*, 229–242.

[217] G. Liu, J. Jia, K. Zhang, X. Jia, Q. Yin, W. Zhong, L. Li, F. Huang, Y. Cao, *Adv. Energy Mater.* **2019**, *9*, 1803657.

[218] R. S. Gurney, D. G. Lidzey, T. Wang, *Reports Prog. Phys.* **2019**, *82*, 036601.

[219] H. J. Son, W. Wang, T. Xu, Y. Liang, Y. Wu, G. Li, L. Yu, *J. Am. Chem. Soc.* **2011**, *133*, 1885–1894.

[220] Z. Li, T. Zhang, Y. Xin, X. Zhao, D. Yang, F. Wu, X. Yang, *J. Mater. Chem. A* **2016**, *4*, 18598–18606.

[221] J. Oh, K. Kranthiraja, C. Lee, K. Gunasekar, S. Kim, B. Ma, B. J. Kim, S.-H. Jin, *Adv. Mater.* **2016**, *28*, 10016–10023.

[222] Z. Du, X. Bao, Y. Li, D. Liu, J. Wang, C. Yang, R. Wimmer, L. W. Städe, R. Yang, D. Yu, *Adv. Energy Mater.* **2018**, *8*, 1701471.

[223] C. Roy, T. Bura, S. Beaupré, M.-A. Légaré, J.-P. Sun, I. G. Hill, M. Leclerc, *Macromolecules* **2017**, *50*, 4658–4667.

[224] I.-B. Kim, S.-Y. Jang, Y.-A. Kim, R. Kang, I.-S. Kim, D.-K. Ko, D.-Y. Kim, *ACS Appl. Mater. Interfaces* **2017**, *9*, 24011–24019.

[225] K. Feng, G. Yang, X. Xu, G. Zhang, H. Yan, O. Awartani, L. Ye, H. Ade, Y. Li, Q. Peng, *Adv. Energy Mater.* **2018**, *8*, 1602773.

[226] H. Huang, L. Yang, A. Facchetti, T. J. Marks, *Chem. Rev.* **2017**, *117*, 10291–10318.

[227] C. J. Mueller, E. Gann, C. R. Singh, M. Thelakkat, C. R. McNeill, *Chem. Mater.* **2016**, *28*, 7088–7097.

[228] R. Singh, J. Lee, M. Kim, P. E. Keivanidis, K. Cho, *J. Mater. Chem. A* **2016**, *270*, 1789–1791.

[229] Y. Cheng, Y. Qi, Y. Tang, C. Zheng, Y. Wan, W. Huang, R. Chen, *J. Phys. Chem. Lett.* **2016**, *7*, 3609–3615.

[230] B. Carsten, J. M. Szarko, H. J. Son, W. Wang, L. Lu, F. He, B. S. Rolczynski, S. J. Lou, L. X. Chen, L. Yu, *J. Am. Chem. Soc.* **2011**, *133*, 20468–20475.

[231] D. Xia, Y. Wu, Q. Wang, A. Zhang, C. Li, Y. Lin, F. J. M. Colberts, J. J. van Franeker, R. A. J. Janssen, X. Zhan, W. Hu, Z. Tang, W. Ma, W. Li, *Macromolecules* **2016**, *49*, 6445–6454.

[232] A. Zhang, C. Xiao, Y. Wu, C. Li, Y. Ji, L. Li, W. Hu, Z. Wang, W. Ma, W. Li, *Macromolecules* **2016**, *49*, 6431–6438.

[233] J. W. Jo, J. W. Jung, E. H. Jung, H. Ahn, T. J. Shin, W. H. Jo, *Energy Environ. Sci.* **2015**, *8*, 2427–2434.

[234] J. W. Jo, J. W. Jung, H. Wang, P. Kim, T. P. Russell, W. H. Jo, *Chem. Mater.* **2014**, *26*, 4214–4220.

[235] H. Zhang, S. Li, B. Xu, H. Yao, B. Yang, J. Hou, *J. Mater. Chem. A* **2016**, *4*, 18043–18049.

[236] D. He, X. Geng, L. Ding, *Polym. Chem.* **2016**, *7*, 4993–4997.

[237] Z. Wang, Z. Li, J. Liu, J. Mei, K. Li, Y. Li, Q. Peng, *ACS Appl. Mater. Interfaces* **2016**, *8*, 11639–11648.

[238] E. H. Jung, H. Ahn, W. H. Jo, J. W. Jo, J. W. Jung, *Dye. Pigment.* **2019**, *161*, 113–118.

[239] J. J.-H. Kim, J. Baek Park, W.-H. Lee, J. J.-H. Kim, D.-H. Hwang, I. Kang, *J. Polym. Sci. Part A Polym. Chem.* **2017**, *55*, 2506–2512.

[240] S. Cho, W. Lee, J. B. Park, J. Kim, D. Hwang, I. Kang, *Synth. Met.* **2015**, *210*, 273–281.

[241] Q. Fan, W. Su, X. Guo, Y. Wang, J. Chen, C. Ye, M. Zhang, Y. Li, *J. Mater. Chem. A* **2017**, *5*, 9204–9209.

[242] L. Xue, Y. Yang, J. Xu, C. Zhang, H. Bin, Z. Zhang, B. Qiu, X. Li, C. Sun, L. Gao, J. Yao, X. Chen, Y. Yang, M. Xiao, Y. Li, *Adv. Mater.* **2017**, *29*, 1703344.

[243] K. Feng, J. Yuan, Z. Bi, W. Ma, X. Xu, G. Zhang, Q. Peng, *iScience* **2019**, *12*, 1–12.

[244] J. Yang, P. Cong, L. Chen, X. Wang, J. Li, A. Tang, B. Zhang, Y. Geng, E. Zhou, *ACS Macro Lett.* **2019**, *8*, 743–748.

[245] H.-C. Chen, Y. Chen, C. Liu, Y. Chien, S.-W. Chou, P. Chou, *Chem. Mater.* **2012**, *24*, 4766–4772.

[246] Z. Wang, J. Zhao, Y. Li, Q. Peng, *Polym. Chem.* **2014**, *5*, 4984–4992.

[247] H. Bronstein, J. M. Frost, A. Hadipour, Y. Kim, C. B. Nielsen, R. S. Ashraf, B. P. Rand, S. Watkins, I. McCulloch, *Chem. Mater.* **2013**, *25*, 277–285.

[248] H. Zhou, L. Yang, A. C. Stuart, S. C. Price, S. Liu, W. You, *Angew. Chemie Int. Ed.* **2011**, *50*, 2995–2998.

[249] D. Qian, L. Ye, M. Zhang, Y. Liang, L. Li, Y. Huang, X. Guo, S. Zhang, Z. Tan, J. Hou, *Macromolecules* **2012**, *45*, 9611–9617.

[250] T. Bura, S. Beaupré, O. A. Ibraikulov, M.-A. Légaré, J. Quinn, P. Lévêque, T. Heiser, Y. Li, N. Leclerc, M. Leclerc, *Macromolecules* **2017**, *50*, 7080–7090.

[251] K. Guo, J. Bai, Y. Jiang, Z. Wang, Y. Sui, Y. Deng, Y. Han, H. Tian, Y. Geng, *Adv. Funct. Mater.* **2018**, *28*, 1801097.

[252] C. Yang, W. Jin, J. Wang, Y. Ding, S. Nong, K. Shi, Y. Lu, Y. Dai, F. Zhuang, T. Lei, C. Di, D. Zhu, J. Wang, J. Pei, *Adv. Mater.* **2018**, *30*, 1802850.

[253] C. J. Mueller, C. R. Singh, M. Fried, S. Huettner, M. Thelakkat, *Adv. Funct. Mater.* **2015**, *25*, 2725–2736.

[254] Y. Gao, Y. Deng, H. Tian, J. Zhang, D. Yan, Y. Geng, F. Wang, *Adv. Mater.* **2017**, *29*, 1–7.

[255] L. Zhang, Z. Wang, C. Duan, Z. Wang, Y. Deng, J. Xu, F. Huang, Y. Cao, *Chem. Mater.* **2018**, *30*, 8343–8351.

[256] H. Chen, M. Nikolka, A. Wadsworth, W. Yue, A. Onwubiko, M. Xiao, A. J. P. White, D. Baran, H. Sirringhaus, I. McCulloch, *Macromolecules* **2018**, *51*, 71–79.

[257] Z. Ni, H. Dong, H. Wang, S. Ding, Y. Zou, Q. Zhao, Y. Zhen, F. Liu, L. Jiang, W. Hu, *Adv. Mater.* **2018**, *30*, 1704843.

[258] F. Chen, Y. Jiang, Y. Sui, J. Zhang, H. Tian, Y. Han, Y. Deng, W. Hu, Y. Geng, *Macromolecules* **2018**, *51*, 8652–8661.

[259] D. J. Crouch, D. Sparrowe, M. Heeney, I. McCulloch, P. J. Skabara, *Macromol. Chem. Phys.* **2010**, *211*, 2642–2648.

[260] Z. Ni, H. Dong, H. Wang, S. Ding, Y. Zou, Q. Zhao, Y. Zhen, F. Liu, L. Jiang, W. Hu, *Adv. Mater.* **2018**, *1704843*, 1704843.

[261] K. Kawashima, T. Fukuhara, Y. Suda, Y. Suzuki, T. Koganezawa, H. Yoshida, H. Ohkita, I. Osaka, K. Takimiya, *J. Am. Chem. Soc.* **2016**, *138*, 10265–10275.

[262] Z. Fei, M. Shahid, N. Yaacobi-Gross, S. Rossbauer, H. Zhong, S. E. Watkins, T. D. Anthopoulos, M. Heeney, *Chem. Commun.* **2012**, *48*, 11130.

[263] E. Collado-Fregoso, P. Boufflet, Z. Fei, E. Gann, S. Ashraf, Z. Li, C. R. McNeill, J. R. Durrant, M. Heeney, *Chem. Mater.* **2015**, *27*, 7934–7944.

[264] J. Wolf, F. Cruciani, A. El Labban, P. M. Beaujuge, *Chem. Mater.* **2015**, *27*, 4184–4187.

[265] S. Liu, X. Song, S. Thomas, Z. Kan, F. Cruciani, F. Laquai, J.-L. Bredas, P. M. Beaujuge, *Adv. Energy Mater.* **2017**, *7*, 1602574.

[266] S. Liu, Z. Kan, S. Thomas, F. Cruciani, J.-L. Brédas, P. M. Beaujuge, *Angew. Chemie Int. Ed.* **2016**, *55*, 12996–13000.

[267] J. Zhang, H. S. Tan, X. Guo, A. Facchetti, H. Yan, *Nat. Energy* **2018**, *3*, 720–731.

[268] P. Cheng, G. Li, X. Zhan, Y. Yang, *Nat. Photonics* **2018**, *12*, 131–142.

[269] P. Pattanasattayavong, N. Yaacobi-Gross, K. Zhao, G. O. N. Ndjawa, J. Li, F. Yan, B. C. O'Regan, A. Amassian, T. D. Anthopoulos, *Adv. Mater.* **2013**, *25*, 1504–1509.

[270] W. Li, S. Albrecht, L. Yang, S. Roland, J. R. Tumbleston, T. McAfee, L. Yan, M. A. Kelly, H. Ade, D. Neher, W. You, *J. Am. Chem. Soc.* **2014**, *136*, 15566–15576.

[271] E. Gann, A. T. Young, B. A. Collins, H. Yan, J. Nasiatka, H. A. Padmore, H. Ade, A. Hexemer, C. Wang, *Rev. Sci. Instrum.* **2012**, *83*, 045110.

[272] L. Ye, S. J. Stuard, H. Ade, in *Conjug. Polym.*, CRC Press, **2019**, pp. 427–458.

[273] L. Ye, H. Hu, M. Ghasemi, T. Wang, B. A. Collins, J.-H. Kim, K. Jiang, J. H. Carpenter, H. Li, Z. Li, T. McAfee, J. Zhao, X. Chen, J. L. Y. Lai, T. Ma, J.-L. Bredas, H. Yan, H. Ade, *Nat. Mater.* **2018**, *17*, 253–260.

[274] Q. Zhang, M. A. Kelly, A. Hunt, H. Ade, W. You, *Macromolecules* **2016**, *49*, 2533–2540.

[275] Q. Zhang, M. A. Kelly, N. Bauer, W. You, *Acc. Chem. Res.* **2017**, *50*, 2401–2409.

[276] F. Meyer, *Prog. Polym. Sci.* **2015**, *47*, 70–91.

[277] N. Leclerc, P. Chávez, O. Ibraikulov, T. Heiser, P. Lévêque, *Polymers (Basel).* **2016**, *8*, 11.

[278] M. Qiu, R. G. Brandt, Y. Niu, X. Bao, D. Yu, N. Wang, L. Han, L. Yu, S. Xia, R. Yang, *J. Phys. Chem. C* **2015**, *119*, 8501–8511.

[279] H. Cha, H. N. Kim, T. K. An, M. S. Kang, S.-K. Kwon, Y.-H. Kim, C. E. Park, *ACS Appl. Mater. Interfaces* **2014**, *6*, 15774–15782.

[280] H. G. Kim, M. Kim, J. A. Clement, J. Lee, J. Shin, H. Hwang, D. H. Sin, K. Cho, *Chem. Mater.* **2015**, *27*, 6858–6868.

[281] A. Casey, S. D. Dimitrov, P. Shakya-Tuladhar, Z. Fei, M. Nguyen, Y. Han, T. D. Anthopoulos, J. R. Durrant, M. Heeney, *Chem. Mater.* **2016**, *28*, 5110–5120.

[282] A. Casey, J. P. Green, P. Shakya Tuladhar, M. Kirkus, Y. Han, T. D. Anthopoulos, M. Heeney, *J. Mater. Chem. A* **2017**, *5*, 6465–6470.

[283] J. Wudarczyk, G. Papamokos, V. Margaritis, D. Schollmeyer, F. Hinkel, M. Baumgarten, G. Floudas, K. Müllen, *Angew. Chemie Int. Ed.* **2016**, *55*, 3220–3223.

[284] R. Hamilton, C. G. Shuttle, B. O'Regan, T. C. Hammant, J. Nelson, J. R. Durrant, *J. Phys. Chem. Lett.* **2010**, *1*, 1432–1436.

[285] Z. He, C. Zhong, X. Huang, W.-Y. Wong, H. Wu, L. Chen, S. Su, Y. Cao, *Adv. Mater.* **2011**, *23*, 4636–4643.

[286] H. Yao, Y. Li, H. Hu, P. C. Y. Chow, S. Chen, J. Zhao, Z. Li, J. H. Carpenter, J. Y. L. Lai, G. Yang, Y. Liu, H. Lin, H. Ade, H. Yan, *Adv. Energy Mater.* **2018**, *8*, 1701895.

[287] C. Duan, K. Gao, J. J. van Franeker, F. Liu, M. M. Wienk, R. A. J. Janssen, *J. Am. Chem. Soc.* **2016**, *138*, 10782–10785.

[288] ab Y.-C. L. Yu-Wei Su, and Kung-Hwa Wei*a, *J. Mat. Chem. A.* **2017**, *4*, 1–330.

[289] H. Zhang, X. Wang, L. Yang, S. Zhang, Y. Zhang, C. He, W. Ma, J. Hou, *Adv. Mater.* **2017**, *29*, 1703777.

[290] J. Rivnay, S. C. B. Mannsfeld, C. E. Miller, A. Salleo, M. F. Toney, *Chem. Rev.* **2012**, *112*, 5488–5519.

[291] M. A. Faist, T. Kirchartz, W. Gong, R. S. Ashraf, I. McCulloch, J. C. de Mello, N. J. Ekins-Daukes, D. D. C. Bradley, J. Nelson, *J. Am. Chem. Soc.* **2012**, *134*, 685–692.

[292] E. T. Hoke, K. Vandewal, J. A. Bartelt, W. R. Mateker, J. D. Douglas, R. Noriega, K. R. Graham, J. M. J. Fréchet, A. Salleo, M. D. McGehee, *Adv. Energy Mater.* **2013**, *3*, 220–230.

[293] C. G. Shuttle, B. O'Regan, A. M. Ballantyne, J. Nelson, D. D. C. Bradley, J. de Mello, J. R. Durrant, *Appl. Phys. Lett.* **2008**, *92*, 093311.

[294] P. R. F. Barnes, K. Miettunen, X. Li, A. Y. Anderson, T. Bessho, M. Gratzel, B. C. O'Regan, *Adv. Mater.* **2013**, *25*, 1881–1922.

[295] D. Credgington, R. Hamilton, P. Atienzar, J. Nelson, J. R. Durrant, *Adv. Funct. Mater.* **2011**, *21*, 2744–2753.

[296] C. G. Shuttle, R. Hamilton, J. Nelson, B. C. O'Regan, J. R. Durrant, *Adv. Funct. Mater.* **2010**, *20*, 698–702.

[297] C. G. Shuttle, A. Maurano, R. Hamilton, B. O'Regan, J. C. de Mello, J. R. Durrant, *Appl. Phys. Lett.* **2008**, *93*, 183501.

[298] C. G. Shuttle, R. Hamilton, B. C. O'Regan, J. Nelson, J. R. Durrant, *Proc. Natl. Acad. Sci.* **2010**, *107*, 16448–16452.

[299] J. Yan, G. Luo, B. Xiao, H. Wu, Z. He, Y. Cao, *Org. Electron.* **2015**, *24*, 125–130.

[300] D. Bartesaghi, I. D. C. Pérez, J. Kniepert, S. Roland, M. Turbiez, D. Neher, L. J. A. Koster, *Nat. Commun.* **2015**, *6*, 7083.

[301] D. Baran, R. S. Ashraf, D. A. Hanifi, M. Abdelsamie, N. Gasparini, J. A. Röhr, S. Holliday, A. Wadsworth, S. Lockett, M. Neophytou, C. J. M. Emmott, J. Nelson, C. J. Brabec, A. Amassian, A. Salleo, T. Kirchartz, J. R. Durrant, I. McCulloch, *Nat. Mater.* **2017**, *16*, 363–369.

[302] G. Wang, M. A. Adil, J. Zhang, Z. Wei, *Adv. Mater.* **2018**, *1805089*, 1805089.

[303] M. Zhang, X. Guo, W. Ma, H. Ade, J. Hou, *Adv. Mater.* **2015**, *27*, 4655–4660.

[304] Q. Fan, W. Su, Y. Wang, B. Guo, Y. Jiang, X. Guo, F. Liu, T. P. Russell, M. Zhang, Y. Li, *Sci. China Chem.* **2018**, *61*, 531–537.

[305] M. Ghasemi, H. Hu, Z. Peng, J. J. Rech, I. Angunawela, J. H. Carpenter, S. J. Stuard, A. Wadsworth, I. McCulloch, W. You, H. Ade, *Joule* **2019**, *3*, 1328–1348.

[306] H. K. H. Lee, A. M. Telford, J. A. Röhr, M. F. Wyatt, B. Rice, J. Wu, A. de Castro Maciel, S. M. Tuladhar, E. Speller, J. McGettrick, J. R. Searle, S. Pont, T. Watson, T. Kirchartz, J. R. Durrant, W. C. Tsoi, J. Nelson, Z. Li, *Energy Environ. Sci.* **2018**, *11*, 417–428.

[307] M. Jørgensen, K. Norrman, S. A. Gevorgyan, T. Tromholt, B. Andreasen, F. C. Krebs, *Adv. Mater.* **2012**, *24*, 580–612.

[308] W. R. Mateker, M. D. McGehee, *Adv. Mater.* **2017**, *29*, 1603940.

[309] N. Y. Doumon, G. Wang, R. C. Chiechi, L. J. A. Koster, *J. Mater. Chem. C* **2017**, *5*, 6611–6619.

[310] G. Wang, F. S. Melkonyan, A. Facchetti, T. J. Marks, *Angew. Chemie Int. Ed.* **2019**, *58*, 4129–4142.

[311] L. Yang, H. Zhou, A. C. Stuart, W. You, *Molecular Design of Conjugated Polymers for High-Efficiency Solar Cells*, **2014**.

[312] Y. Ma, Z. Kang, Q. Zheng, *J. Mater. Chem. A* **2017**, *5*, 1860–1872.

[313] M. Schnürch, M. Spina, A. F. Khan, M. D. Mihovilovic, P. Stanetty, *Chem. Soc. Rev.* **2007**, *36*, 1046–1057.

[314] K. J. Thorley, I. McCulloch, *J. Mater. Chem. C* **2018**, *6*, 12413–12421.

[315] E. Gann, A. T. Young, B. A. Collins, H. Yan, J. Nasiatka, H. A. Padmore, H. Ade, A. Hexemer, C. Wang, *Rev. Sci. Instrum.* **2012**, *83*, DOI 10.1063/1.3701831.

[316] J. Rivnay, R. Noriega, R. J. Kline, A. Salleo, M. F. Toney, *Phys. Rev. B* **2011**, *84*, 045203.

[317] Z. Peng, L. Ye, Harald Ade, *Understanding, Quantifying, and Controlling the Molecular Ordering of Semi-Conducting Polymers: From Novices to Experts and Amorphous to Perfect Crystals*, **2020**.

[318] J. A. Bartelt, Z. M. Beiley, E. T. Hoke, W. R. Mateker, J. D. Douglas, B. A. Collins, J. R. Tumbleston, K. R. Graham, A. Amassian, H. Ade, J. M. J. Fréchet, M. F. Toney, M. D. McGehee, *Adv. Energy Mater.* **2013**, *3*, 364–374.

[319] B. A. Collins, Z. Li, J. R. Tumbleston, E. Gann, C. R. Mcneill, H. Ade, *Adv. Energy Mater.* **2013**, *3*, 65–74.

[320] T. Wang, X.-K. Chen, A. Ashokan, Z. Zheng, M. K. Ravva, J.-L. Brédas, *Adv. Funct. Mater.* **2018**, *28*, 1705868.

[321] A. Tang, B. Xiao, Y. Wang, F. Gao, K. Tajima, H. Bin, Z.-G. Zhang, Y. Li, Z. Wei, E. Zhou, *Adv. Funct. Mater.* **2018**, *28*, 1704507.

[322] S. Athanasopoulos, F. Schauer, V. Nádaždy, M. Weiß, F. Kahle, U. Scherf, H. Bässler, A. Köhler, *Adv. Energy Mater.* **2019**, *9*, 1900814.

[323] Q. Liu, Y. Jiang, K. Jin, J. Qin, J. Xu, W. Li, J. Xiong, J. Liu, Z. Xiao, K. Sun, S. Yang, X. Zhang, L. Ding, *Sci. Bull.* **2020**, *65*, 272–275.

[324] J. Yuan, Y. Zhang, L. Zhou, G. Zhang, H.-L. Yip, T.-K. Lau, X. Lu, C. Zhu, H. Peng, P. A. Johnson, M. Leclerc, Y. Cao, J. Ulanski, Y. Li, Y. Zou, *Joule* **2019**, *3*, 1140–1151.

[325] F. Zhao, S. Dai, Y. Wu, Q. Zhang, J. Wang, L. Jiang, Q. Ling, Z. Wei, W. Ma, W. You, C. Wang, X. Zhan, *Adv. Mater.* **2017**, *29*, 1700144.

[326] Y. Liang, Z. Xu, J. Xia, S.-T. Tsai, Y. Wu, G. Li, C. Ray, L. Yu, *Adv. Mater.* **2010**, *22*, E135–E138.

[327] G. Li, V. Shrotriya, J. Huang, Y. Yao, T. Moriarty, K. Emery, Y. Yang, *Nat. Mater.* **2005**, *4*, 864–868.

[328] H. Zhou, L. Yang, W. You, *Macromolecules* **2012**, *45*, 607–632.

[329] Z. Zhang, J. Wang, *J. Mater. Chem.* **2012**, *22*, 4178.

[330] R. S. Kularatne, H. D. Magurudeniya, P. Sista, M. C. Biewer, M. C. Stefan, *J. Polym. Sci. Part A Polym. Chem.* **2013**, *51*, 743–768.

[331] P. Ertl, A. Schuffenhauer, *J. Cheminform.* **2009**, *1*, 8.

[332] C. W. Coley, L. Rogers, W. H. Green, K. F. Jensen, *J. Chem. Inf. Model.* **2018**, *58*, 252–261.

[333] R. Po, G. Bianchi, C. Carbonera, A. Pellegrino, *Macromolecules* **2015**, *48*, 453–461.

[334] G. Marzano, C. V. Ciasca, F. Babudri, G. Bianchi, A. Pellegrino, R. Po, G. M. Farinola, *European J. Org. Chem.* **2014**, *2014*, 6583–6614.

[335] C. Jimenez-Gonzalez, C. S. Ponder, Q. B. Broxterman, J. B. Manley, *Org. Process Res. Dev.* **2011**, *15*, 912–917.

[336] D. J. C. Constable, A. D. Curzons, V. L. Cunningham, *Green Chem.* **2002**, *4*, 521–527.

[337] A. D. Curzons, D. N. Mortimer, D. J. C. Constable, V. L. Cunningham, *Green Chem.* **2001**, *3*, 1–6.

[338] B. Azzopardi, C. J. M. Emmott, A. Urbina, F. C. Krebs, J. Mutale, J. Nelson, *Energy Environ. Sci.* **2011**, *4*, 3741.

[339] F. C. Krebs, T. Tromholt, M. Jørgensen, *Nanoscale* **2010**, *2*, 873.

[340] F. C. Krebs, M. Hösel, M. Corazza, B. Roth, M. V. Madsen, S. A. Gevorgyan, R. R. Søndergaard, D. Karg, M. Jørgensen, *Energy Technol.* **2013**, *1*, 378–381.

[341] F. Machui, M. Hösel, N. Li, G. D. Spyropoulos, T. Ameri, R. R. Søndergaard, M. Jørgensen, A. Scheel, D. Gaiser, K. Kreul, D. Lenssen, M. Legros, N. Lemaitre, M. Vilkman, M. Välimäki, S. Nordman, C. J. Brabec, F. C. Krebs, *Energy Environ. Sci.* **2014**, *7*, 2792.

[342] C. Sun, F. Pan, H. Bin, J. Zhang, L. Xue, B. Qiu, Z. Wei, Z.-G. Zhang, Y. Li, *Nat. Commun.* **2018**, *9*, 743.

[343] Y. Wu, Y. Zheng, H. Yang, C. Sun, Y. Dong, C. Cui, H. Yan, Y. Li, *Sci. China Chem.* **2020**, *63*, 265–271.

[344] P.-O. Morin, T. Bura, M. Leclerc, *Mater. Horizons* **2016**, *3*, 11–20.

[345] J. A. Carrillo, M. L. Turner, M. J. Ingleson, *J. Am. Chem. Soc.* **2016**, *138*, 13361–13368.

[346] K. B. Seo, I. H. Lee, J. Lee, I. Choi, T. L. Choi, *J. Am. Chem. Soc.* **2018**, *140*, 4335–4343.

[347] S. Zhang, L. Ye, H. Zhang, J. Hou, *Mater. Today* **2016**, *19*, 533–543.

[348] S. Lee, D. Jeong, C. Kim, C. Lee, H. Kang, H. Y. Woo, B. J. Kim, *ACS Nano* **2020**, *14*, 14493–14527.

[349] T. L. Nguyen, C. Lee, H. Kim, Y. Kim, W. Lee, J. H. Oh, B. J. Kim, H. Y. Woo, *Macromolecules* **2017**, *50*, 4415–4424.

[350] R. Kroon, R. Gehlhaar, T. T. Steckler, P. Henriksson, C. Müller, J. Bergqvist, A. Hadipour, P. Heremans, M. R. Andersson, *Sol. Energy Mater. Sol. Cells* **2012**, *105*, 280–286.

[351] T. Y. S. But, P. H. Toy, *J. Am. Chem. Soc.* **2006**, *128*, 9636–9637.

[352] D. Hirose, T. Taniguchi, H. Ishibashi, *Angew. Chemie Int. Ed.* **2013**, *52*, 4613–4617.

[353] J. A. Buonomo, C. C. Aldrich, *Angew. Chemie Int. Ed.* **2015**, *54*, 13041–13044.

[354] R. H. Beddoe, K. G. Andrews, V. Magné, J. D. Cuthbertson, J. Saska, A. L. Shannon-Little, S. E. Shanahan, H. F. Sneddon, R. M. Denton, *Science (80-.).* **2019**, *365*, 910–914.

[355] J. J. Rech, L. Yan, Z. Wang, Q. Zhang, S. Bradshaw, H. Ade, W. You, *ACS Appl. Polym. Mater.* **2021**, *3*, 30–41.

[356] S. K. Hau, H.-L. Yip, A. K. Y. Jen, *Polym. Rev.* **2010**, *50*, 474–510.

[357] D. Angmo, F. C. Krebs, *Energy Technol.* **2015**, *3*, 774–783.

[358] M. Jørgensen, K. Norrman, F. C. Krebs, *Sol. Energy Mater. Sol. Cells* **2008**, *92*, 686–714.

[359] A. Moliton, J.-M. Nunzi, *Polym. Int.* **2006**, *55*, 583–600.

[360] S. E. Shaheen, in *2007 IEEE Int. Reliab. Phys. Symp. Proceedings. 45th Annu.*, IEEE, **2007**, pp. 248–252.

[361] D. Baran, R. S. Ashraf, D. A. Hanifi, M. Abdelsamie, N. Gasparini, J. A. Röhr, S. Holliday, A. Wadsworth, S. Lockett, M. Neophytou, C. J. M. Emmott, J. Nelson, C. J. Brabec, A. Amassian, A. Salleo, T. Kirchartz, J. R. Durrant, I. McCulloch, *Nat. Mater.* **2017**, *16*, 363–369.

[362] P. Cheng, X. Zhan, *Chem. Soc. Rev.* **2016**, *45*, 2544–2582.

[363] A. Gumyusenge, D. T. Tran, X. Luo, G. M. Pitch, Y. Zhao, K. A. Jenkins, T. J. Dunn, A. L. Ayzner, B. M. Savoie, J. Mei, *Science (80-.).* **2018**, *362*, 1131–1134.

[364] G. Feng, J. Li, F. J. M. Colberts, M. Li, J. Zhang, F. Yang, Y. Jin, F. Zhang, R. A. J. Janssen, C. Li, W. Li, *J. Am. Chem. Soc.* **2017**, *139*, 18647–18656.

[365] Y. Liang, S. Lan, P. Deng, D. Zhou, Z. Guo, H. Chen, H. Zhan, *ACS Appl. Mater. Interfaces* **2018**, *10*, 32397–32403.

[366] M. Ghasemi, N. Balar, Z. Peng, H. Hu, Y. Qin, T. Kim, J. J. Rech, M. Bidwell, W. Mask, I. McCulloch, W. You, A. Amassian, C. Risko, B. T. O'Connor, H. Ade, *Nat. Mater.* **2021**, DOI 10.1038/s41563-020-00872-6.

[367] P. Cheng, Q. Shi, Y. Lin, Y. Li, X. Zhan, *Org. Electron.* **2013**, *14*, 599–606.

[368] L. Dou, C.-C. Chen, K. Yoshimura, K. Ohya, W.-H. Chang, J. Gao, Y. Liu, E. Richard, Y. Yang, *Macromolecules* **2013**, *46*, 3384–3390.

[369] X. Zhan, Z. Tan, B. Domercq, Z. An, X. Zhang, S. Barlow, Y. Li, D. Zhu, B. Kippelen, S. R. Marder, *J. Am. Chem. Soc.* **2007**, *129*, 7246–7247.

[370] C. Lindqvist, A. Sanz-Velasco, E. Wang, O. Bäcke, S. Gustafsson, E. Olsson, M. R. Andersson, C. Müller, *J. Mater. Chem. A* **2013**, *1*, 7174.

[371] J. Jo, S.-S. Kim, S.-I. Na, B.-K. Yu, D.-Y. Kim, *Adv. Funct. Mater.* **2009**, *19*, 866–874.

[372] A. Swinnen, I. Haeldermans, M. vande Ven, J. D'Haen, G. Vanhoyland, S. Aresu, M. D'Olieslaeger, J. Manca, *Adv. Funct. Mater.* **2006**, *16*, 760–765.

[373] S. Li, L. Zhan, F. Liu, J. Ren, M. Shi, C. Z. Li, T. P. Russell, H. Chen, *Adv. Mater.* **2017**, *1705208*, 1–8.

[374] S. Ben Dkhil, M. Pfannmöller, R. R. Schröder, R. Alkarsifi, M. Gaceur, W. Köntges, H. Heidari, S. Bals, O. Margeat, J. Ackermann, C. Videlot-Ackermann, *ACS Appl. Mater. Interfaces* **2018**, acsami.7b17021.

[375] I. Osaka, M. Saito, I. Osaka, *J. Mater. Chem. C* **2017**, DOI 10.1039/C7TC04721E.

[376] K.-E. Hung, C.-E. Tsai, S.-L. Chang, Y.-Y. Lai, U.-S. Jeng, F.-Y. Cao, C.-S. Hsu, C.-J. Su, Y.-J. Cheng, *ACS Appl. Mater. Interfaces* **2017**, acsami.7b13426.

[377] C. H. Y. Ho, H. Cao, Y. Lu, T.-K. Lau, S. H. Cheung, H.-W. LI, H. Yin, K. L. Chiu, L.-K. Ma, Y. Cheng, S. W. TSANG, X. Lu, S.-K. So, B. S. Ong, *J. Mater. Chem. A* **2017**, DOI 10.1039/C7TA06530B.

[378] Y. Gong, K. Chang, C. Chen, M. Han, X. Zhan, J. Min, X. Jiao, Q. Li, Z. Li, *Mater. Chem. Front.* **2018**, DOI 10.1039/C8QM00486B.

[379] Y. Zhang, Y. Xu, M. J. Ford, F. Li, J. Sun, X. Ling, Y. Wang, J. Gu, J. Yuan, W. Ma, *Adv. Energy Mater.* **2018**, *8*, 1800029.

[380] M. Glatthaar, M. Riede, N. Keegan, K. Sylvester-Hvid, B. Zimmermann, M. Niggemann, A. Hinsch, A. Gombert, *Sol. Energy Mater. Sol. Cells* **2007**, *91*, 390–393.

[381] K. Norrman, F. C. Krebs, *Sol. Energy Mater. Sol. Cells* **2006**, *90*, 213–227.

[382] M. O. Reese, A. M. Nardes, B. L. Rupert, R. E. Larsen, D. C. Olson, M. T. Lloyd, S. E. Shaheen, D. S. Ginley, G. Rumbles, N. Kopidakis, *Adv. Funct. Mater.* **2010**, *20*, 3476–3483.

[383] J. Schafferhans, A. Baumann, A. Wagenpfahl, C. Deibel, V. Dyakonov, *Org. Electron.* **2010**, *11*, 1693–1700.

[384] A. Seemann, T. Sauermann, C. Lungenschmied, O. Armbruster, S. Bauer, H.-J. Egelhaaf, J. Hauch, *Sol. Energy* **2011**, *85*, 1238–1249.

[385] S. Sarkar, J. H. Culp, J. T. Whyland, M. Garvan, V. Misra, *Org. Electron.* **2010**, *11*, 1896–1900.

[386] I. A. Channa, A. Distler, M. Zaiser, C. J. Brabec, H. Egelhaaf, *Adv. Energy Mater.* **2019**, *9*, 1900598.

[387] G. Dennler, C. Lungenschmied, H. Neugebauer, N. S. Sariciftci, M. Latrèche, G. Czeremuszkin, M. R. Wertheimer, *Thin Solid Films* **2006**, *511–512*, 349–353.

[388] C. Lungenschmied, G. Dennler, G. Czeremuzskin, M. Latrèche, H. Neugebauer, N. S. Sariciftci, in *Photonics Sol. Energy Syst.* (Ed.: A. Gombert), **2006**, p. 619712.

[389] S. Cros, R. de Bettignies, S. Berson, S. Bailly, P. Maisse, N. Lemaitre, S. Guillerez, *Sol. Energy Mater. Sol. Cells* **2011**, *95*, S65–S69.

[390] K. Norrman, S. A. Gevorgyan, F. C. Krebs, *ACS Appl. Mater. Interfaces* **2009**, *1*, 102–112.

[391] H. Klumbies, M. Karl, M. Hermenau, R. Rösch, M. Seeland, H. Hoppe, L. Müller-Meskamp, K. Leo, *Sol. Energy Mater. Sol. Cells* **2014**, *120*, 685–690.

[392] K. Feron, T. J. Nagle, L. J. Rozanski, B. B. Gong, C. J. Fell, *Sol. Energy Mater. Sol. Cells* **2013**, *109*, 169–177.

[393] S. Züfle, M. T. Neukom, S. Altazin, M. Zinggeler, M. Chrapa, T. Offermans, B. Ruhstaller, *Adv. Energy Mater.* **2015**, *5*, 1500835.

[394] B. Xu, J. Hou, *Adv. Energy Mater.* **2018**, *1800022*, 1–22.

[395] M. O. Reese, A. J. Morfa, M. S. White, N. Kopidakis, S. E. Shaheen, G. Rumbles, D. S. Ginley, *Sol. Energy Mater. Sol. Cells* **2008**, *92*, 746–752.

[396] L. Córcoles, J. Abad, J. Padilla, A. Urbina, *Sol. Energy Mater. Sol. Cells* **2015**, *141*, 423–428.

[397] M. V. Madsen, T. Tromholt, K. Norrman, F. C. Krebs, *Adv. Energy Mater.* **2013**, *3*, 424–427.

[398] A. Rivaton, S. Chambon, M. Manceau, J.-L. Gardette, N. Lemaître, S. Guillerez, *Polym. Degrad. Stab.* **2010**, *95*, 278–284.

[399] M. Manceau, A. Rivaton, J.-L. Gardette, S. Guillerez, N. Lemaître, *Polym. Degrad. Stab.* **2009**, *94*, 898–907.

[400] A. Tournebize, P.-O. Bussière, P. Wong-Wah-Chung, S. Thérias, A. Rivaton, J.-L. Gardette, S. Beaupré, M. Leclerc, *Adv. Energy Mater.* **2013**, *3*, 478–487.

[401] A. Tournebize, P.-O. Bussière, A. Rivaton, J.-L. Gardette, H. Medlej, R. C. Hiorns, C. Dagron-Lartigau, F. C. Krebs, K. Norrman, *Chem. Mater.* **2013**, *25*, 4522–4528.

[402] R. Grisorio, G. Allegretta, P. Mastrorilli, G. P. Suranna, *Macromolecules* **2011**, *44*, 7977–7986.

[403] C. H. Peters, I. T. Sachs-Quintana, W. R. Mateker, T. Heumueller, J. Rivnay, R. Noriega, Z. M. Beiley, E. T. Hoke, A. Salleo, M. D. McGehee, *Adv. Mater.* **2012**, *24*, 663–668.

[404] B. H. Cumpston, K. F. Jensen, *J. Appl. Polym. Sci.* **1998**, *69*, 2451–2458.

[405] A. Kumar, R. Devine, C. Mayberry, B. Lei, G. Li, Y. Yang, *Adv. Funct. Mater.* **2010**, *20*, 2729–2736.

[406] K. Kawano, R. Pacios, D. Poplavskyy, J. Nelson, D. D. C. Bradley, J. R. Durrant, *Sol. Energy Mater. Sol. Cells* **2006**, *90*, 3520–3530.

[407] G. Dennler, M. C. Scharber, C. J. Brabec, *Adv. Mater.* **2009**, *21*, 1323–1338.

[408] H. Neugebauer, C. Brabec, J. C. Hummelen, N. S. Sariciftci, *Sol. Energy Mater. Sol. Cells* **2000**, *61*, 35–42.

[409] E. A. Katz, D. Faiman, S. M. Tuladhar, J. M. Kroon, M. M. Wienk, T. Fromherz, F. Padinger, C. J. Brabec, N. S. Sariciftci, *J. Appl. Phys.* **2001**, *90*, 5343–5350.

[410] S. Schuller, P. Schilinsky, J. Hauch, C. J. Brabec, *Appl. Phys. A* **2004**, *79*, 37–40.

[411] G. Dennler, C. Lungenschmied, H. Neugebauer, N. S. Sariciftci, A. Labouret, *J. Mater. Res.* **2005**, *20*, 3224–3233.

[412] F. C. Krebs, K. Norrman, *Prog. Photovoltaics Res. Appl.* **2007**, *15*, 697–712.

[413] F. C. Krebs, S. A. Gevorgyan, B. Gholamkhass, S. Holdcroft, C. Schlenker, M. E. Thompson, B. C. Thompson, D. Olson, D. S. Ginley, S. E. Shaheen, H. N. Alshareef, J. W. Murphy, W. J. Youngblood, N. C. Heston, J. R. Reynolds, S. Jia, D. Laird, S. M. Tuladhar, J. G. A. Dane, P. Atienzar, J. Nelson, J. M. Kroon, M. M. Wienk, R. A. J. Janssen, K. Tvingstedt, F. Zhang, M. Andersson, O. Inganäs, M. Lira-Cantu, R. de Bettignies, S. Guillerez, T. Aernouts, D. Cheyns, L. Lutsen, B. Zimmermann, U. Würfel, M. Niggemann, H.-F. Schleiermacher, P. Liska, M. Grätzel, P. Lianos, E. A. Katz, W. Lohwasser, B. Jannon, *Sol. Energy Mater. Sol. Cells* **2009**, *93*, 1968–1977.

[414] M. O. Reese, S. A. Gevorgyan, M. Jørgensen, E. Bundgaard, S. R. Kurtz, D. S. Ginley, D. C. Olson, M. T. Lloyd, P. Morvillo, E. A. Katz, A. Elschner, O. Haillant, T. R. Currier, V. Shrotriya, M. Hermenau, M. Riede, K. R. Kirov, G. Trimmel, T. Rath, O. Inganäs, F. Zhang, M. Andersson, K. Tvingstedt, M. Lira-Cantu, D. Laird, C. McGuiness, S. (Jimmy) Gowrisanker, M. Pannone, M. Xiao, J. Hauch, R. Steim, D. M. DeLongchamp, R. Rösch, H. Hoppe, N. Espinosa, A. Urbina, G. Yaman-Uzunoglu, J.-B. Bonekamp, A. J. J. M. van Breemen, C. Girotto, E. Voroshazi, F. C. Krebs, *Sol. Energy Mater. Sol. Cells* **2011**, *95*, 1253–1267.

[415] B. Watts, W. J. Belcher, L. Thomsen, H. Ade, P. C. Dastoor, *Macromolecules* **2009**, *42*, 8392–8397.

[416] J. Zhao, A. Swinnen, G. Van Assche, J. Manca, D. Vanderzande, B. Van Mele, *J. Phys. Chem. B* **2009**, *113*, 1587–1591.

[417] C.-Y. Chen, C.-S. Tsao, Y.-C. Huang, H.-W. Liu, W.-Y. Chiu, C.-M. Chuang, U.-S. Jeng, C.-J. Su, W.-R. Wu, W.-F. Su, L. Wang, *Nanoscale* **2013**, *5*, 7629.

[418] L. Ye, B. A. Collins, X. Jiao, J. Zhao, H. Yan, H. Ade, *Adv. Energy Mater.* **2018**, *8*, 1703058.

[419] Y. Zhu, A. Gadisa, Z. Peng, M. Ghasemi, L. Ye, Z. Xu, S. Zhao, H. Ade, *Adv. Energy Mater.* **2019**, *9*, 1900376.

[420] H. Hu, L. Ye, M. Ghasemi, N. Balar, J. J. Rech, S. J. Stuard, W. You, B. T. O'Connor, H. Ade, *Adv. Mater.* **2019**, *31*, 1808279.

[421] L. Ye, S. Li, X. Liu, S. Zhang, M. Ghasemi, Y. Xiong, J. Hou, H. Ade, *Joule* **2019**, *3*, 443–458.

[422] L. Ye, B. A. Collins, X. Jiao, J. Zhao, H. Yan, H. Ade, *Adv. Energy Mater.* **2018**, *1703058*, 1703058.

[423] Y. Zhu, A. Gadisa, Z. Peng, M. Ghasemi, L. Ye, Z. Xu, S. Zhao, H. Ade, *Adv. Energy Mater.* **2019**, *9*, 1900376.

[424] M. Ghasemi, H. Hu, Z. Peng, J. J. Rech, I. Angunawela, J. H. Carpenter, S. J. Stuard,
       A. Wadsworth, I. McCulloch, W. You, H. Ade, *Joule* **2019**, *3*, 1328–1348.